

Search for the Mini Black Hole  
in the Multijet Final State  
in  $pp$  Collisions at  $\sqrt{s} = 7$  TeV

by

Michiru Kaneda

A Thesis submitted to the Department of Physics  
for the degree of Doctor of Philosophy

The University of Tokyo

December 2010



# Abstract

A mini black hole search is motivated by theories of extra dimensions. ADD model is one of extra dimensions theories in which all extra dimensions are compactified in cylinder shape. In the model, only gravitational field can propagate into additional  $n$  dimensions. Hence, the fundamental gravitational force is stronger than that measured in  $3+1$  space-time dimensions. This could lead the fundamental Planck scale,  $M_D$ , of  $O(1)$  TeV in  $n+4$  dimensions, and solve the hierarchy problem where the Planck scale is vastly large compared with the electroweak scale. On the assumption of  $M_D \sim O(1)$  TeV, mini black holes with masses of  $O(1)$  TeV could be produced at the Large Hadron Collider (LHC) at CERN.

In this thesis, mini black holes were searched for in a multijet final state in proton-proton collisions at center of mass energy of 7 TeV, produced by LHC. The collision data collected by the ATLAS detector in 2010, corresponding to the integrated luminosity of  $36.3 \text{ pb}^{-1}$ , were used in the search.

The mini black hole signals for  $n = 2$  to 7 and  $M_D = 0.8$  GeV to 2 TeV are searched for. For each  $n$  and  $M_D$ , the mass thresholds of the mini black holes were set by the assumptions that colliding particles collapse in a black hole if the Compton wavelength is equal to or less than the Schwarzschild radius or horizon radius. In case  $M_D = 1$  TeV, the assumption with Schwarzschild (horizon) radius gives mass thresholds of about 2 (3) TeV to 4 (5) TeV for  $n = 7$  to 2. Mini black holes are decayed mainly by the Hawking radiation. The model of no graviton emission is used for the decay of mini black holes. The burst model, in which mini black hole decay into multi-body, is adopted for the Planck Phase when the mass of mini black holes become smaller than the Planck Scale.

Observed events are consistent with Standard Model predictions and upper limits on the mini black hole production cross sections are set. This result can be interpreted to the lower limits on  $M_D$  for each  $n$  by comparing with theoretical cross sections. On the assumption using Schwarzschild (horizon) radius, a lower limit on  $M_D$  for  $n = 4$  (5) is placed as

$$M_D > 1.26 (1.06) \text{ TeV},$$

at 95% confidence level, which is the most stringent limit obtained by the collider experiments.

# Acknowledgements

First, I would like to express my appreciation to my supervisor, Prof. Tomio Kobayashi for providing the chance to do this work. He gave me many advices and supports both on the physics and the research life. I will keep his advices in mind for my research life.

I would like to thank Prof. Shoji Asai for giving me the ideas of studies. I was given much knowledge and many experiences about physics and experiments by him. I am grateful to Prof. Junichi Tanaka for supporting my studies. I could start a study at the ATLAS experiment smoothly with his kind supports and I had many helpful discussions with him. I wish to express my gratitude to Dr. Shimpei Yamamoto. He gave me many suggestions and helped on this thesis. I could write up this thesis with his warm advices and guidance.

I am thankful to Dr. Junichi Kanzaki for supporting me especially when I started the study at the ATLAS experiment. I am thankful to Dr. Toshio Namba for teaching basics of the physics experiments. I wish to thank Prof. Naoko Kanaya, Prof. Osamu Jinnouchi, Dr. Koji Terashi, Dr. Soushi Tsuno, Dr. Yosuke Kataoka, Dr. Taiki Yamamura, Dr. Tatsuya Masubuchi and Dr. Koji Nakamura for helpful discussions at the ATLAS experiments. I also wish to thank all professors, staffs and students at the International Center for Elementary Particle Physics at the University of Tokyo for supporting my research.

I am especially thankful to the member of analysis group of the black hole in ATLAS: Prof. Ian Hinchliffe, Prof. Cidem Issever, Prof. Victor Lendermann, Prof. Douglas Gingrich, Prof. Andy Parker, Dr. James Frost, Dr. Haiping Peng, Dr. Thorsten Diezsch, Mr. Haoshuang Ji, and all members who are working in the group. I wish to thank all people who have been working for the ATLAS experiment and LHC. My thesis is completed based on all of their works.

Finally, I am indebted to my parents for their understanding and support for all of my life.

# Contents

<b>List of Figures</b>	<b>vi</b>
<b>Table of Contents</b>	<b>xi</b>
<b>1 Introduction</b>	<b>1</b>
<b>2 Physics Beyond the Standard Model</b>	<b>3</b>
2.1 The Standard Model . . . . .	3
2.2 Hierarchy Problem . . . . .	4
2.3 Supersymmetry . . . . .	6
2.4 Extra Dimensions . . . . .	7
2.4.1 Kaluza-Klein theory . . . . .	7
2.4.2 ADD model . . . . .	9
2.4.3 RS model . . . . .	12
2.5 Mini Black Hole . . . . .	13
2.5.1 Production of Mini Black Hole . . . . .	14
2.5.2 Production of Black Hole at LHC . . . . .	18
2.5.3 Decay of Black Hole . . . . .	18
2.6 Searched Model . . . . .	21
2.6.1 Mass Threshold of Black Hole . . . . .	21
2.6.2 Decay Model . . . . .	24
<b>3 The LHC and the ATLAS Detector</b>	<b>25</b>
3.1 The Large Hadron Collider . . . . .	25
3.2 A Toroidal LHC ApparatuS . . . . .	27
3.3 Coordinate System in the ATLAS experiment . . . . .	27
3.4 Magnet system . . . . .	28
3.4.1 Central Solenoid Magnet . . . . .	29
3.4.2 Toroid Magnets . . . . .	30
3.5 Inner detector . . . . .	30
3.5.1 Pixel detector . . . . .	31

3.5.2	Semiconductor Tracker . . . . .	34
3.5.3	Transition Radiation Tracker . . . . .	34
3.6	Calorimeter . . . . .	34
3.6.1	Hadronic calorimeter . . . . .	36
3.6.2	Muon system . . . . .	43
3.7	Luminosity Monitor . . . . .	43
3.8	Trigger . . . . .	45
3.8.1	L1 Calorimeter Trigger . . . . .	47
3.8.2	The Jet Trigger . . . . .	47
<b>4</b>	<b>Monte Carlo Simulation</b>	<b>49</b>
4.1	ATLAS Simulation . . . . .	49
4.2	BlackMax, A Generator for the Mini Black Hole Events . . . . .	49
4.3	Characteristics of Mini Black Hole Events . . . . .	50
4.4	Generators for Background Events . . . . .	58
4.4.1	PYTHIA . . . . .	58
4.4.2	HERWIG and JIMMY . . . . .	58
4.4.3	ALPGEN . . . . .	58
4.4.4	MC@NLO . . . . .	59
4.4.5	Tuning for Underlying Events and Minimum Bias Events . . . . .	59
4.4.6	Summary of Standard Model MC samples . . . . .	60
<b>5</b>	<b>Jet Reconstruction</b>	<b>61</b>
5.1	Clustering of calorimeter cells . . . . .	61
5.2	Jet Finding Algorithm . . . . .	64
5.3	Hadronic Calibration . . . . .	66
5.4	Uncertainties on Jet Energy Scale . . . . .	69
5.4.1	Jet Energy Resolution Uncertainty . . . . .	69
5.4.2	Jet Energy Scale Uncertainty . . . . .	71
<b>6</b>	<b>Data Samples and Event Preselection</b>	<b>78</b>
6.1	Data Period . . . . .	78
6.2	Trigger . . . . .	78
6.3	Data Quality . . . . .	80
6.4	Event Preselection . . . . .	81
6.4.1	Jet Selection . . . . .	81
6.4.2	Trigger and the leading jet transverse momentum selection . . . . .	81
6.4.3	Event Cleaning . . . . .	82
6.4.4	Pile-up effect and transverse momentum cut on Jets . . . . .	89
6.4.5	Summary of Preselection . . . . .	90

<b>7</b>	<b>Characteristics of Signal and Background Events</b>	<b>93</b>
7.1	QCD Background . . . . .	93
7.2	Discriminant Observables . . . . .	95
7.3	Characteristics of QCD background . . . . .	97
<b>8</b>	<b>Search for the Mini Black Hole</b>	<b>106</b>
8.1	Jets in Observed Events . . . . .	106
8.2	Extraction of Signal Yield . . . . .	109
8.3	Incorporating Systematic Uncertainties . . . . .	111
8.4	Systematic Uncertainties . . . . .	111
	8.4.1 Uncertainties of background shape . . . . .	111
	8.4.2 Uncertainties in Signal Normalization . . . . .	116
8.5	Validation of Signal Extraction Method with Pseudo Data . .	128
<b>9</b>	<b>Constraint on the Mini Black Hole Production</b>	<b>130</b>
9.1	Limits on the Mini Black Hole Production Cross Sections . . .	130
9.2	Lower Limits on the Planck Scale . . . . .	141
<b>10</b>	<b>Discussion</b>	<b>143</b>
10.1	Setting Limits with Different $\sum p_T$ Range . . . . .	143
10.2	Comparison with Astrophysical Results . . . . .	147
10.3	Expected limits with increased statistics . . . . .	147
<b>11</b>	<b>Conclusions</b>	<b>152</b>
<b>A</b>	<b>Parameters for BlackMax</b>	<b>154</b>
<b>B</b>	<b>Mass Reconstruction of the Mini Black Hole</b>	<b>157</b>
<b>C</b>	<b>Further Validation of Signal Extraction</b>	<b>161</b>

# List of Figures

2.1	The discovery potential of the Higgs boson at the ATLAS experiment . . . . .	5
2.2	One-loop corrections to the Higgs boson mass by a fermion (a) and by a scalar particle (b) . . . . .	5
2.3	Gauge coupling constants . . . . .	7
2.4	Particles of the SM can propagate only in (3 + 1) space-time dimensional “SM Brane”, while the graviton can propagate into “Bulk” . . . . .	8
2.5	95 % CL lower limits on $M_D$ in the ADD model obtained by the LEP and the CDF experiments . . . . .	11
2.6	95 % CL lower limits on $M_D$ in the ADD model obtained by the LEP and the Tevatron experiments . . . . .	11
2.7	Formation of the mini black hole . . . . .	14
2.8	The ATLAS detector side view with a simulated mini black hole event . . . . .	15
2.9	The cross section of the mini black hole . . . . .	19
2.10	The Hawking temperature . . . . .	20
2.11	The threshold of black hole production with the condition: $\lambda < r_s$ . Each line represents each $n$ . For example, $M_{\text{BHth}} = 4.26\text{TeV}$ (2.08TeV) for $n = 2$ (7) at $M_D = 1$ TeV. . . . .	22
2.12	Mass thresholds . . . . .	22
2.13	The threshold of black hole production on the assumption of $\lambda < r_h$ . Each line represents each $n$ . For example, $M_{\text{BHth}} = 6.38\text{TeV}$ (2.92TeV) for $n = 2$ (7) at $M_D = 1$ TeV. . . . .	23
3.1	An aerial photo of LHC . . . . .	26
3.2	Accelerators at CERN . . . . .	26
3.3	The ATLAS Detector . . . . .	28
3.4	Geometry of magnets . . . . .	29
3.5	Barrel toroid . . . . .	30
3.6	Integral magnetic field . . . . .	31
3.7	Structure of the inner detector in the barrel region . . . . .	32

3.8	Structure of the inner detector in the end-cap region . . . . .	32
3.9	Plan view of a quarter-section of the ATLAS inner detector . . .	33
3.10	Pixel detector . . . . .	33
3.11	The ATLAS calorimeter . . . . .	35
3.12	The amount of materials of the EM calorimeter . . . . .	35
3.13	Interaction length of the ATLAS detector . . . . .	36
3.14	The LAr EM calorimeter in the barrel region . . . . .	37
3.15	The tile calorimeter module . . . . .	39
3.16	Segmentation in depth and $\eta$ of the tile calorimeter . . . . .	40
3.17	HEC Calorimeter . . . . .	41
3.18	The forward calorimeter . . . . .	42
3.19	The overview of the ATLAS muon system . . . . .	43
3.20	The LUCID detector . . . . .	44
3.21	Flow of L1 trigger . . . . .	46
3.22	Architecture of the L1 calorimeter trigger . . . . .	48
3.23	The illustration of the jet trigger algorithms . . . . .	48
4.1	ATLAS simulation . . . . .	49
4.2	Mass spectra of the mini black holes produced with BlackMax for four different points. All the distributions are normalized to a unit area. . . . .	53
4.3	Number of particles emitted by a mini black hole for four different points. All the distributions are normalized to a unit area. . . . .	54
4.4	PDG id distribution in the decay particles from the mini black hole for four different points. All the distributions are normal- ized to a unit area. . . . .	54
4.5	The number of jets (a) and transverse momentum spectra of all jets (b) in the black hole event for four different points. All the distributions are normalized to a unit area. . . . .	56
4.6	Transverse momentum spectra of the leading jets (a) and the second leading jet (b) in the black hole event for four different points. All the distributions are normalized to a unit area. . . .	56
4.7	Transverse momentum spectra of the third leading jets (b) and the forth leading jet (b) in the black hole event for four different points. All the distributions are normalized to a unit area. . . . .	57
4.8	Transverse momentum spectra of the fifth leading jets in the black hole event for four different points. All the distributions are normalized to a unit area. . . . .	57

5.1	Overview of jet reconstruction in ATLAS . . . . .	62
5.2	The illustration of topological clustering . . . . .	63
5.3	Sketch of Cone v.s. Anti-Kt algorithm for a collinear splitting . . . . .	65
5.4	Sketch of Cone v.s. Anti-Kt algorithm for a infrared radiation . . . . .	65
5.5	Distributions for energy ratios of $E^{\text{EM}}$ to $E^{\text{true}}$ for the range of $56\text{GeV} < p_{\text{T}}^{\text{EM}} < 60\text{GeV}$ (a) and $80\text{GeV} < p_{\text{T}}^{\text{true}} < 85\text{GeV}$ (b) . . . . .	66
5.6	Illustration of the process for energy calibration . . . . .	68
5.7	Calibration factors as a function of jet $p_{\text{T}}^{\text{EM}}$ in EM scale for the central (circles) and end-cap (triangles) regions [118]. . . . .	68
5.8	The coordination system for the bisector method . . . . .	70
5.9	Jet energy resolution . . . . .	71
5.10	Relative jet energy scale systematic uncertainty as a function of jet $p_{\text{T}}$ for $0 <  \eta  < 0.3$ (a) and $0.3 <  \eta  < 0.8$ (b) . . . . .	75
5.11	Relative jet energy scale systematic uncertainty as a function of jet $p_{\text{T}}$ for $0.8 <  \eta  < 1.2$ . . . . .	76
5.12	Relative jet energy scale systematic uncertainty as a function of jet $p_{\text{T}}$ for $1.2 <  \eta  < 2.1$ (a) and $2.1 <  \eta  < 2.8$ (b) . . . . .	77
6.1	Total integrated luminosity at $\sqrt{s} = 7\text{TeV}$ . . . . .	79
6.2	Trigger efficiencies . . . . .	81
6.3	Distributions of $f_{\text{EM}}$ (a) and $f_{\text{quality}}$ (b) . . . . .	84
6.4	Distributions of $n_{90}$ (a) and $f_{\text{HEC}}$ (b) . . . . .	85
6.5	Distributions of $t_{\text{jet}}$ (a) and $f_{\text{max}}$ (b) . . . . .	86
6.6	Distributions of $f_{\text{cha}}$ . . . . .	87
6.7	Distributions of $f_{\text{TG3}}$ (a) and $f_{\text{corr}}$ (b) . . . . .	87
6.8	Event display of a cosmic-ray event . . . . .	88
6.9	Inclusive jet $p_{\text{T}}$ distributions before and after jet cleaning . . . . .	89
6.10	Number of primary vertexes of the data . . . . .	90
6.11	The transverse momentum distribution of jets in minimum bias events of the MC samples. The histogram is normalized to unity. . . . .	91
7.1	$p_{\text{T}}$ distributions of the leading (a) and fifth leading jet (b) for QCD, $t\bar{t}$ , $Z$ + jets and $W$ + jets processes . . . . .	94
7.2	Distributions of the number of jets with $p_{\text{T}} > 50\text{GeV}$ for QCD MC events and black hole signals with various parameters . . . . .	95
7.3	The number of jets for the events with $1000\text{GeV} < \sum p_{\text{T}} < 1500\text{GeV}$ (a) and $2000\text{GeV} < \sum p_{\text{T}} < 3000\text{GeV}$ (b) . . . . .	96
7.4	$\sum p_{\text{T}}$ distributions of signal and background events . . . . .	96
7.5	$N_{\text{J}} - \sum p_{\text{T}}$ distribution for QCD background events after applying preselection. The histogram is normalized to $36.3\text{pb}^{-1}$ . . . . .	97

7.6	$N_J$ - $\sum p_T$ distributions for signal point rs_2_1000 (a) and rs_4_1000 (b). The histograms are normalized to $36.3 \text{ pb}^{-1}$ . . . . .	98
7.7	Leading jet $p_T$ distributions of QCD MC events in $1000 \text{ GeV} < \sum p_T < 1500 \text{ GeV}$ (a) and $2000 \text{ GeV} < \sum p_T < 3000 \text{ GeV}$ (b) . . .	101
7.8	Fifth leading jet $p_T$ distributions of QCD MC events in $1000 \text{ GeV} < \sum p_T < 1500 \text{ GeV}$ (a) in $2000 \text{ GeV} < \sum p_T < 3000 \text{ GeV}$ (b) . . .	102
7.9	$\sum p_T$ distributions of QCD background for $N_J = 2 - 5$ . In (b), histograms are normalized by the number of events in $\sum p_T > 1000 \text{ GeV}$ . . . . .	102
7.10	$\sum p_T$ distributions of QCD PYTHIA MC (a) for $N_J < 5$ (red rectangles) and $N_J \geq 5$ (black circles), and the ratio of them: $\sum p_T (N_J \geq 5) / \sum p_T (N_J < 5)$ (b) . . . . .	103
7.11	$\sum p_T$ distributions of QCD PYTHIA MC for $N_J < 5$ (circles) and $N_J \geq 5$ (histogram) . . . . .	105
8.1	$p_T$ distributions of leading jet (a) and second leading jet (b) for data and QCD MC events. Yellow error bands represent statistical uncertainties of MC events. . . . .	107
8.2	$p_T$ distributions of third leading jet (a) and fourth leading jet (b) for data and QCD MC events. Yellow error bands represent statistical uncertainties of MC events. . . . .	107
8.3	$p_T$ distribution of fifth leading jet (a) and $N_J$ distribution for data and QCD MC events. Yellow error bands represent statistical uncertainties of MC events. . . . .	108
8.4	$\sum p_T$ distributions of $N_J < 5$ for data and QCD PYTHIA MC events. Yellow error bands represent statistical uncertainties of MC events. . . . .	108
8.5	Illustration of four regions in $N_J - \sum p_T$ plane . . . . .	109
8.6	$\sum p_T$ distributions of QCD ALPGEN MC for the event in $N_J < 5$ (circles) and $N_J \geq 5$ (histogram) . . . . .	114
8.7	$\sum p_T$ distributions in $N_J < 5$ (a) and $N_J \geq 5$ of QCD PYTHIA sample . . . . .	114
8.8	$\sum p_T$ distributions in $N_J < 5$ (a) and $N_J \geq 5$ (b) for QCD, $t\bar{t}$ , $Z + \text{jets}$ and $W + \text{jets}$ processes . . . . .	115
8.9	Test statistics, $-\log \lambda(s')$ , as a function of $s'$ for pseudo data without signal events . . . . .	128
8.10	Test statistics, $-\log \lambda(s')$ , as a function of $s'$ for pseudo data with signal events . . . . .	129
9.1	$\sum p_T$ distributions of observed events for $N_J \geq 5$ (filled circles) and $N_J < 5$ (histogram) . . . . .	131

9.2	Test statistics ( $-\log \lambda(s')$ ) as a function of $s'$ for observed events	131
9.3	95% CL upper limit on the cross section for $n = 2$ (a) and $n = 3$ (b) on the assumption of $\lambda < r_s$	135
9.4	95% CL upper limit on the cross section for $n = 4$ (a) and $n = 5$ (b) on the assumption of $\lambda < r_s$	136
9.5	95% CL upper limit on the cross section for $n = 6$ (a) and $n = 7$ (b) on the assumption of $\lambda < r_s$	137
9.6	95% CL upper limit on the cross section for $n = 2$ (a) and $n = 3$ (b) on the assumption of $\lambda < r_h$	138
9.7	95% CL upper limit on the cross section for $n = 4$ (a) and $n = 5$ (b) on the assumption of $\lambda < r_h$	139
9.8	95% CL upper limit on the cross section for $n = 6$ (a) and $n = 7$ (b) on the assumption of $\lambda < r_h$	140
9.9	95% CL lower limit on $M_D$ as a function of number of extra dimension	141
10.1	95% CL upper limit on the cross section for $n = 4$ (a) and $n = 6$ (b) on the assumption of $\lambda < r_s$	144
10.2	Expected 95% CL upper limit on cross section with theoretical cross section for $n = 4$ on the assumption $\lambda < r_s$ (a) and on the assumption $\lambda < r_h$ (b)	148
10.3	Expected lower limits on $M_D$ for on the assumption of $\lambda < r_s$ (a) and $\lambda < r_h$ (b)	149
10.4	Cross sections for three different parameter sets of $(M_D, M_{\text{BHth}})$ as a function of $\sqrt{s}$	151
B.1	The mass spectrum (a) and the resolution (b) of the mini black hole	158
B.2	$\sum p_T$ distributions (a) and $M_{\text{BH}}$ distributions (b) for the events required all preselection cut and the second leading jet $p_T > 50\text{GeV}$	159
B.3	$M_{\text{BH}}$ distributions for events of $N_J \geq 5$ with $\sum p_T$ cut of 1500 GeV (a) and 2000 GeV (b)	160
C.1		162

# List of Tables

2.1	The degrees of freedom of the standard model particles . . . . .	20
3.1	Design Parameters of LHC . . . . .	27
4.1	Mini Black Hole signal MC samples on the assumption $\lambda < r_s$	51
4.2	Mini Black Hole signal MC samples on the assumption $\lambda < r_h$	52
4.3	PGD ids for each particle. Anti-particles are assigned negative PDG ids corresponding to the particles. . . . .	55
4.4	Event generators and cross sections of each process. The $p_T$ cut represent the cut on the leading parton $p_T$ . . . . .	60
6.1	Summary of the data recorded in 2010 . . . . .	79
6.2	Emission probability of jets in minimum bias events . . . . .	90
6.3	Data reduction summary of each preselection cut . . . . .	91
7.1	Expected number of events after applying preselection. The numbers correspond to $36.3 \text{ pb}^{-1}$ . . . . .	94
7.2	Expected number of events and acceptance for background events with $N_J \geq 5$ and $\sum p_T > 1500(2000)\text{GeV}$ . The numbers are normalized to $36.3 \text{ pb}^{-1}$ . . . . .	98
7.3	Expected number of events and acceptance for the mini black hole signals with $N_J \geq 5$ and $\sum p_T > 1500(2000)\text{GeV}$ for samples on the assumption $\lambda < r_s$ . The numbers are normalized to $36.3 \text{ pb}^{-1}$ . . . . .	99
7.4	Expected number of events and acceptance for the mini black hole signals with $N_J \geq 5$ and $\sum p_T > 1500(2000)\text{GeV}$ for samples on the assumption $\lambda < r_h$ . The numbers are normalized to $36.3 \text{ pb}^{-1}$ . . . . .	100
7.5	The numbers of QCD MC events with $N_J \geq 5$ and $N_J < 5$ , and the ratio between them for each $\sum p_T$ bin. The errors indicate statistical uncertainties of MC events. . . . .	104

7.6	Number of expected events in each region for PYTHIA MC events. The errors represent statistical uncertainties of MC events. . . . .	104
8.1	Number of events in four regions estimated with the negative jet energy shift. The errors represent statistical uncertainties of MC events. . . . .	112
8.2	Number of events in four regions estimated with the positive jet energy shift. The errors represent statistical uncertainties of MC events. . . . .	112
8.3	Number of events in four regions estimated with additional 14% resolution. The errors represent statistical uncertainties of MC events. . . . .	113
8.4	Number of events in four regions of QCD ALPGEN MC sample. The errors represent statistical error of MC events. . . . .	113
8.5	Number of events in four regions of QCD PYTHIA MC events with CTEQ66. The errors represent statistical errors of MC events. . . . .	115
8.6	Number of events in four regions. The MC events of QCD PYTHIA, $t\bar{t}$ , $Z + \text{jets}$ and $W + \text{jets}$ are summed. . . . .	116
8.7	Systematic uncertainties of the background shape . . . . .	116
8.8	Number of expected events in $\mathcal{R}_0$ for each signal models on the assumption $\lambda < r_s$ . . . . .	117
8.9	Number of expected events in $\mathcal{R}_1$ for each signal models on the assumption $\lambda < r_s$ . . . . .	118
8.10	Number of expected events in $\mathcal{R}_2$ for each signal models on the assumption $\lambda < r_s$ . . . . .	119
8.11	Number of expected events in $\mathcal{R}_3$ for each signal models on the assumption $\lambda < r_s$ . . . . .	120
8.12	Number of expected events in $\mathcal{R}_0$ for each signal models on the assumption $\lambda < r_h$ . . . . .	121
8.13	Number of expected events in $\mathcal{R}_1$ for each signal models on the assumption $\lambda < r_h$ . . . . .	122
8.14	Number of expected events in $\mathcal{R}_2$ for each signal models on the assumption $\lambda < r_h$ . . . . .	123
8.15	Number of expected events in $\mathcal{R}_3$ for each signal models on the assumption $\lambda < r_h$ . . . . .	124
8.16	Systematic uncertainties of signal cross sections for signal points on the assumption $\lambda < r_s$ estimated by CTEQ66 error set . . .	126
8.17	Systematic uncertainties of signal cross sections for signal points on the assumption $\lambda < r_h$ estimated by CTEQ66 error set . .	127

9.1	Numbers of observed events for each $\sum p_T$ - $N_J$ region . . . . .	130
9.2	95 % CL limits on cross sections for each signal point on the assumption $\lambda < r_s$ . . . . .	132
9.3	95 % CL limits on cross sections for each signal point on the assumption $\lambda < r_h$ . . . . .	133
9.4	The highest $M_D$ of excluded signal points at 95 % CL in same $n$ and same assumption for $M_{\text{BHth}}$ . . . . .	134
9.5	Lower limits on $M_D$ [TeV] at 95 % CL on the assumption of $\lambda < r_s$ ( $r_h$ ) . . . . .	142
10.1	Number of events in each region of the data . . . . .	143
10.2	95 % CL limits on cross sections for signal point on the assumption $\lambda < r_s$ . . . . .	145
10.3	95 % CL limits on cross sections for signal point on the assumption $\lambda < r_h$ . . . . .	146
10.4	Expected 95 % CL Limits on $M_D$ [TeV] on the assumption $\lambda < r_s$	150
10.5	Expected 95 % CL Limits on $M_D$ [TeV] on the assumption $\lambda < r_h$	150

# Chapter 1

## Introduction

The Standard Model (SM) for particle physics has made striking successes over the last few decades. Three fundamental forces called strong, weak and electromagnetic are involved in SM. They are described with the quantum field theory. The past experimental data that explored these forces are well described by SM. There is another fundamental force, gravitational force, which is not included in SM. The scale where quantum effects of the gravity is called the Planck scale, which is  $O(10^{19})$  GeV <sup>1</sup>. This scale is too large to conduct the experimental tests. Therefore, the quantum effects of the gravity are little-known. In the SM framework, the electromagnetic and weak forces are unified to “electroweak” force at the energy scale of  $O(100)$  GeV. There is large difference between the Planck scale and electroweak scale and it is called “hierarchy problem”. The parameters in SM measured by experiments are calculated from the fundamental parameters by the quantum correction. The large difference between the Planck scale and the electroweak scale makes the problem that the electroweak force of  $O(100)$  GeV must be tuned at an accuracy of  $O(10^{-17})$  GeV at the Planck scale. This is called “fine-tuning” problem, which is a part of the hierarchy problem.

The theory of supersymmetry resolves this fine-tuning problem by introducing the super partners for particles in SM. The quantum corrections by the particles in SM and by the super partners are cancelled out.

Another attempt is the theory introducing extra spacial dimensions. By introducing extra dimensions in which the gravitational force can propagate, only a part of gravitational force can be felt by the observers in four space-time dimensions. Consequently the observers in four space-time dimensions feel only a part of the gravitational force. Hence the fundamental Planck scale would not be as large as  $O(10^{19})$  GeV. If the gravity scale is close to

---

<sup>1</sup>In this thesis, natural units,  $c = \hbar = 1$  is adopted.

the electroweak scale, the hierarchy problem is resolved. If the gravity scale is close to  $O(1)$  TeV, mini black holes with the mass of  $O(1)$  TeV can exist.

The Large Hadron Collider (LHC) is designed to explore the TeV energy range by producing the proton-proton collisions at the center of mass energy of 14 TeV, and it is capable of producing mini black holes with the mass of  $O(1)$  TeV. The mini black hole decays immediately into many particles with high energies. The ATLAS detector is one of the general purpose detectors placed at a collision point of LHC and has a detection capability for the mini black hole events.

The LHC achieved the proton-proton collision at the center-of-mass energy,  $\sqrt{s} = 2.36$  TeV in 2009. This was the highest energy of particle collision by accelerators. The LHC raised the energy of the proton-proton collision up to  $\sqrt{s} = 7$  TeV in 2010 and has been in operation since March 2010. In this thesis, the search for mini black holes using proton-proton collisions at  $\sqrt{s} = 7$  TeV recorded with the ATLAS detector in 2010 is presented. The signal yields show zero consistent and the cross section upper limits for the mini black hole productions are set. With the cross section limits, the lower limits on the fundamental Planck scale are set.

This thesis consists of eleven chapters.

Chapter 2 describes the physics beyond the SM. The details of the mini black hole production and decay are described in this chapter.

Chapter 3 presents an overview of the LHC and the ATLAS detector. The Monte Carlo (MC) simulations used in this thesis are described in Chapter 4. The mini black hole model which is used in this thesis is given in this chapter. Chapter 5 shows the jet reconstruction algorithm for this thesis. The uncertainties for the jet energy are also given in this chapter.

The data set used in this thesis is explained in Chapter 6. Preselection criteria for an analysis of the searching mini black hole are given in this chapter. Chapter 7 shows characteristics of the mini black hole and Standard Model background events. Discriminant observables for the mini black hole events are discussed in this chapter. Chapter 8 describes the analysis method for the mini black hole search. The result for the cross sections of the mini black hole is given in Chapter 9. The lower limits on the Planck Scale obtained from the results of the cross sections are summarized in this chapter. In Chapter 10, comparison with the limits on the Planck scale obtained by Astrophysical experiments, and expected limits with increased statistics and high energy collisions are discussed.

Finally, Chapter 11 concludes this thesis.

# Chapter 2

## Physics Beyond the Standard Model

This chapter is a summary of particle physics relevant to this thesis. First, SM and its problems are summarized. Supersymmetry is described as one of solutions for the problems in SM. The theory of extra dimension is described as another solution. Finally, the mini black hole phenomenon with the existence of extra dimensions in the collider experiment is described.

### 2.1 The Standard Model

The goal of particle physics is to describe all phenomena in nature with simple theory. Nature looks like very complex. However it is believed that there is a fundamental rule by which all phenomena can be described. There are many theoretical and experimental approaches to find it out. The experimental and theoretical results suggest that nature can be described with the quantum field theory in which there are only small numbers of fundamental particles and they behave according to the interactions associated to the symmetries. Such symmetry is called as the gauge symmetry.

The theory of a unification of the electromagnetic and the weak interactions was established in 1960's [1, 2]. It is called the electroweak theory which is described with  $SU(2)_L \otimes U(1)_Y$  gauge symmetry. The strong interaction can be also described with the gauge symmetry of  $SU(3)_C$ . The theory of the strong interaction is called the quantum chromodynamics (QCD) [3, 4, 5]. The SM consists of the electroweak theory and QCD.

In SM, quarks and leptons are elementary particles which form matter. There are six types of quarks:  $u$ ,  $d$ ,  $c$ ,  $s$ ,  $t$  and  $b$ . They have non-zero electric charge, weak isospin, and color charge which are related to the electromag-

netic, weak, and strong interactions, respectively. Leptons consist of three charged leptons:  $e$ ,  $\mu$ ,  $\tau$  and three neutrinos;  $\nu_e$ ,  $\nu_\mu$ ,  $\nu_\tau$ . They do not have color charge and neutrinos do not have electric charge. Therefore, neutrinos interact only via weak interaction in SM.

The interactions in SM are associated with the exchange of particles; photon,  $W^\pm/Z^0$  and gluon, which are called gauge bosons.

Photon is associated to the electromagnetic interaction which is described by  $U(1)_{em}$ , the subgroup of  $SU(2)_L \otimes U(1)_Y$ . Photon is massless, thus the electromagnetic interaction has infinite range. The weak interaction can reach only  $\sim 10^{-16}$  cm. It means that the gauge bosons for the weak interaction,  $W^\pm/Z^0$ , should have mass of  $O(100)$  GeV. The Higgs mechanism [6] gives them non-zero mass through the spontaneous symmetry breaking [7]. The electroweak gauge symmetry is broken by this mechanism and particles in SM can have masses. These massive bosons were predicted in 1968 and observed by UA1 and UA2 experiments in 1983 [8, 9, 10, 11]. The strong interaction can reach only  $\sim 10^{-13}$  cm because of the color confinement which does not allow that color charged particles, quarks and gluons, exist alone. Gluons are massless, hence the gauge symmetry works out strictly in QCD.

The Higgs boson has not been observed, yet. The LEP experiments reported the limit on the Higgs mass,  $m_H$ . The lower and upper limits at 95% confidence level (CL) on  $m_H$  are set to be 114.4 GeV and 193 GeV, respectively [12, 13]. The Tevatron experiments excluded the high mass region of  $158 < m_H < 175$  GeV at 95% CL [14].

Figure 2.1 shows the sensitivity for the Higgs boson at the ATLAS experiment. The evidence at  $3\sigma$  is expected in the region of  $139 < m_H < 180$  GeV with an integrated luminosity of  $1 \text{ fb}^{-1}$ .

## 2.2 Hierarchy Problem

One of the problems in SM is that the Planck scale,  $M_{\text{Pl}} = 1.2 \times 10^{19}$  GeV, where quantum effects of gravity cannot be negligible, is  $10^{17}$  times larger than the electroweak scale of  $O(100)$  GeV. In other words, the gravitational interaction is very weak compared with the electroweak interaction. This problem is called the hierarchy problem.

The Higgs boson is expected to have a mass of  $O(100)$  GeV. The Higgs boson mass receives radiative corrections by a fermion,  $f$ , as shown in Figure 2.2(a). The coupling of a fermion to the Higgs field is given by the Yukawa coupling constant  $\lambda_f$  with the term  $-\lambda_f H f f$ . This correction can

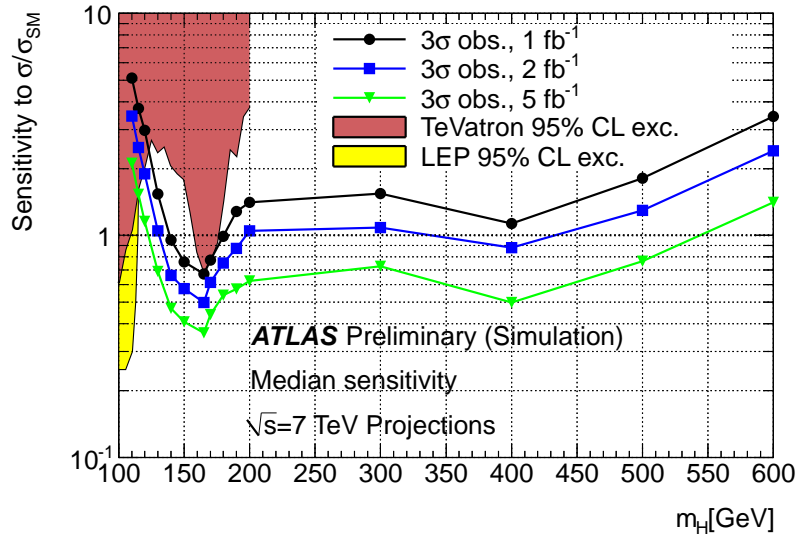


Figure 2.1: The discovery potential of the Higgs boson at the ATLAS experiment. Lines represent  $3\sigma$  sensitivities at  $\sqrt{s} = 7$  TeV with integrated luminosities of 1, 2 and  $5\text{fb}^{-1}$  [15]. The filled area represents the excluded region with 95% CL set by the LEP and the Tevatron experiments.

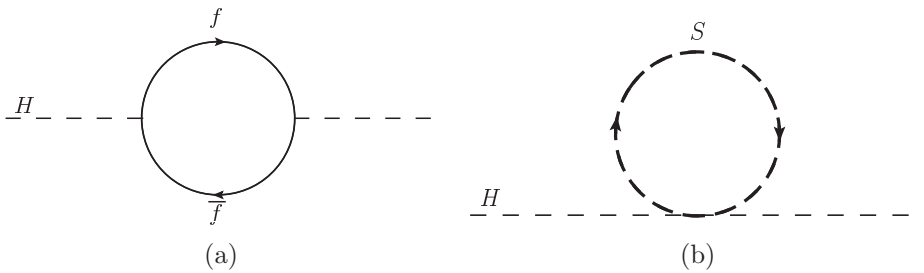


Figure 2.2: One-loop corrections to the Higgs boson mass by a fermion (a) and by a scalar particle (b)

be written as

$$\Delta m_H^2 = -\frac{|\lambda_f|^2}{8\pi^2}\Lambda^2 + \dots, \quad (2.1)$$

where  $\Lambda$  is ultraviolet cutoff where the SM is valid up to. If there is no new physics up to the Planck scale, this cut-off is the same order as  $M_{\text{Pl}}$ , which results in an extremely large correction compared with  $m_H$ ; an incredible fine tuning cancellation between the radiative corrections and the bare mass needs to be employed.

The theories introducing Supersymmetry and extra dimensions can resolve this issue with different approaches.

## 2.3 Supersymmetry

Supersymmetry (SUSY) [16, 17, 18] can provide a solution of the fine-tuning not of the hierarchy problem. The SUSY is symmetry between two particles whose spins differ by 1/2. All fermions have their scalar particle (boson) partners.

Figure 2.2(b) shows a Feynman diagram for a radiative correction by a scalar particle,  $S$ . The coupling for this scalar particle is assigned as  $\lambda_S$ . The coupling term corresponding to Figure 2.2(b) is given as  $-\lambda_S |H|^2 |S|^2$ . The correction is written as

$$\Delta m_H^2 = \frac{\lambda_S}{16\pi^2}\Lambda^2 + \dots \quad (2.2)$$

If there are two complex scalars with  $\lambda_S \sim |\lambda_f|^2$  corresponding to right-handed and left-handed fermions, the radiative term for  $\Lambda^2$  is canceled out. This symmetry between fermions and bosons is called SUSY.

The SUSY makes it possible to unify the coupling constants of the electroweak and the strong interactions naturally [20]. Figure 2.3 shows the demonstration of the running coupling constants for SM and SUSY[19]. Here,  $\alpha_{1-3}$  is the fine structure constant which is defined as

$$\begin{aligned} \alpha_1 &= (5/3) g'^2 / (4\pi), \\ \alpha_2 &= g^2 / (4\pi), \\ \alpha_3 &= g_s^2 / (4\pi), \end{aligned} \quad (2.3)$$

where  $g'$ ,  $g$ , and  $g_s$  represent coupling constants for  $U(1)$ ,  $SU(2)$  and  $SU(3)$ , respectively. MSSM is the one of the SUSY models which is minimal extension to the Standard Model. The three coupling constants do not meet at one point for the SM case, but on the assumption of SUSY, they meet at one point.

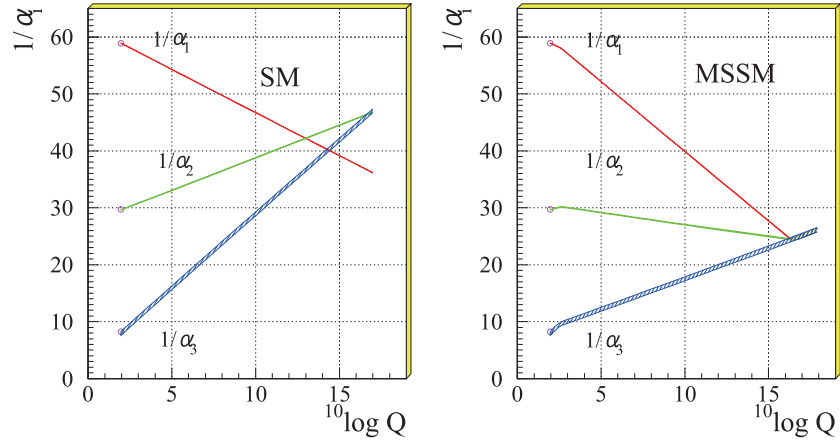


Figure 2.3: Gauge coupling constants as a function of the energy scale,  $Q$ , in the SM (left) and in Supersymmetry (right) [19].  $\alpha_{1-3}$  is the fine structure constant defined in Eq 2.3.

The SUSY models adopt R-parity, which is 1 for all SM particles and -1 for SUSY particles. In most of SUSY models, R-parity is conserved. This leads to the fact that the SUSY particles cannot decay into only SM particles. Hence, the lightest SUSY particle (LSP) exists stably. The LSP is a good candidate of the dark matter [21]. The LSP is expected to have mass of  $O(1)$  TeV and the search for SUSY particles is important in the LHC experiment.

## 2.4 Extra Dimensions

The idea of extra dimensions is another approach to resolve the hierarchy problem. A new fundamental Planck scale is introduced, which is not far from the electroweak scale. Therefore, the fine-tuning is not necessary.

In this thesis, ADD model, in which extra dimensions are compactified in cylinder shape, are considered. In the following subsections, Kaluza-Klein theory which is the origin of the ADD model is described at first. Next ADD model is summarized. Finally, RS model which is another theory of the extra dimensions is also given.

### 2.4.1 Kaluza-Klein theory

In 1914, Nordstöm published a paper of Maxwell-Nordstöm electromagnetic-gravitational theory in which the Einstein equations and Maxwell equations

in four dimensions are unified in a five dimensional space-time [22]. In 1920's, after the general relativity was established [23], Kaluza proposed to extend the general relativity to the five-dimensional space-time [24] and Klein explained the mechanism with fourth space dimension which is compactified in a very small circle as the size of the Planck length [25]. This is called the Kaluza-Klein (KK) theory.

Though it had some problems and had been dismissed once, it was catapulted back into the spotlight after 1970's with the supergravity [26] and superstring [27] theories. The supergravity is the gauge theory of the supersymmetry in which gravitino, the super partner of graviton, works as a gauge field. The superstring theory is one of the hopeful candidates of quantum theory of the gravity. These theories are constructed with higher dimensions, 10 or 11 dimensions.

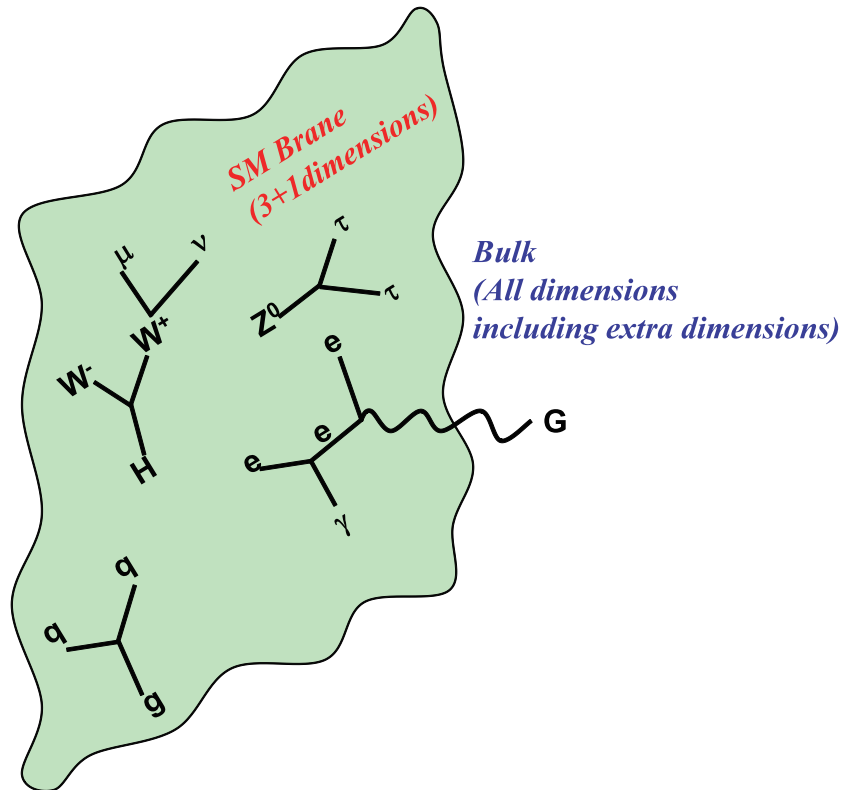


Figure 2.4: Particles of the SM can propagate only in  $(3 + 1)$  space-time dimensional “SM Brane”, while the graviton can propagate into “Bulk”.

Recently, theories of TeV scale extra dimensions with the brane [28] have been investigated. These theories describe that the SM particles are local-

ized in the three space dimension, called the brane, while the graviton can propagate into the all space dimensions, called the bulk, as the illustration of Figure 2.4.

### 2.4.2 ADD model

Arkani-Hamed, Dimopoulos, and Dvali (ADD) proposed the large extra dimensions (LED) [29, 30, 31].

The gravitational force,  $F$ , between two materials with masses  $m_1$  and  $m_2$  is known to follow the Gauss's law in three space dimensions and it is written as

$$F(r) = G \frac{m_1 m_2}{r^2}, \quad (2.4)$$

where  $r$  is the distance between the two materials and  $G$  is the Newton's constant. The relationship between  $G$  and  $M_{\text{Pl}}$  is given as [32]

$$M_{\text{Pl}}^2 = \frac{1}{G}. \quad (2.5)$$

If there are  $n$  extra dimensions (the total space-time dimension  $D = 4 + n$ ), the gravity force follows the Gauss's law in the  $3 + n$  dimensions in the range of smaller than extra dimensions size. Here, all dimensions are assumed to be compactified in cylinder shape of which radius equal  $R$ . A linear size of extra dimension is  $2\pi R$ . The gravity force in the range of  $R$  is given as

$$F_{(D)}(r) = G_D \frac{m_1 m_2}{(2\pi r)^n r^2} (r < R), \quad (2.6)$$

where  $G_D$  is the Newton's constant in  $D$  dimensions. Namely, the gravitational interaction becomes rapidly large in the range smaller than  $R$  by the effect of additional term,  $1/(2\pi r)^n$ .

Here, a fundamental Planck scale,  $M_D$ , is defined by

$$M_D^{n+2} = \frac{(2\pi)^n}{8\pi G_D}. \quad (2.7)$$

This definition is called PDG convention which is used in Particle Data Group [32] and is originally defined in [33]. There are other conventions; Giddings and Thomas's convention:  $M_p^{n+2} = (2\pi)^n / (4\pi G_D)$  [34, 35] and Dimopolous and Landsberg's convention:  $M_{DL}^{n+2} = 1/G_D$  [36] which was used in previous ATLAS results [37]. In this thesis, PDG definition is used to compare with previous collider results for  $M_D$ .

Eq. 2.4 and Eq. 2.6 must be identical at  $r = R$ . Hence, a following equation is obtained:

$$M_{\text{Pl}}^2 = 8\pi R^n M_D^{n+2}. \quad (2.8)$$

If  $M_D = 1$  TeV,  $R = 10^{12}$  m for  $n = 1$ . If there is such an extra dimension, it affects the Solar System. However the Solar System obeys the Gauss's law of three space dimensions, therefore the case of  $n = 1$  with TeV-scale Planck scale in ADD model is rejected. In case  $n = 2(7)$ , the size becomes  $10^{-4}(10^{-15})$  m. This size can be tested directly by the precise measurement of the gravitational interaction. If there is a deviation from the three space dimensional Gauss's law, it would suggest the presence of extra dimensions. Washington group reported a result of the interaction force in submillimeter range with a torsion-pendulum detector. Their result shows that there is no new force and set the limit  $R < 37 \mu\text{m}$ ,  $M_D > 3.6$  TeV at 95 % CL for  $n = 2$  [38].

The gravitational field makes a series of states as a result of the compactification of extra dimensions. The  $i$ -th state with the momentum for extra dimensions,  $\vec{p}_i^2$ , seems like a particle with mass  $m_i^2 = \vec{p}_i^2$  for an observer trapped in the brane. It is called KK graviton. KK graviton search is one of the possibilities to observe the LED effects at the collider experiments. KK graviton interacts via the gravitational force. Consequently, it hardly interacts with matter and is observed as an unbalance of momenta in a detector. It is called missing energy. The LEP experiments searched for KK graviton with  $e^+e^- \rightarrow \gamma/Z +$  missing energy signatures. The virtual graviton exchanges in  $e^+e^- \rightarrow \gamma\gamma$  signatures is another signature of extra dimensions and the LEP experiments searched for. In proton-proton collisions, momenta of two collision partons along the beam axis are not known. Therefore missing energy in transverse direction to the beam axis,  $E_T^{\text{miss}}$ , is used. The Tevatron experiments (the CDF and D0 experiments) searched for KK graviton with  $p\bar{p} \rightarrow \text{jet} + E_T^{\text{miss}}$  and  $p\bar{p} \rightarrow \gamma + E_T^{\text{miss}}$  signatures. There are no signal events and current best 95 % CL limits from above two experiments are  $M_D > 1.60, 1.20, 1.04, 0.98, 0.94, 0.80, 0.78$  TeV for each  $n = 2, \dots, 8$ , respectively [39, 40, 41]. Figure 2.5 and 2.6 show the current limit on  $M_D$  as a function of  $n$ .

Astrophysical experiments reported results of extra dimensions. One of the methods is to check the energy emission from the supernova. If KK gravitons exist, they carry much energy and the energy spectra from the supernova are changed by KK graviton [42]. These KK gravitons change the  $\gamma$  ray background generated by graviton decays [43]. Another possibility is the observation of a halo of KK gravitons which are trapped by the neutron star and decay into photons [44]. The last one reported the most stringent limits on  $M_D$  in astrophysical experiments: 1760, 76.8, 9.43, 2.12, 0.67, and 0.29 TeV for  $n = 2, \dots, 7$ , respectively.

Ultra high-energy cosmic-rays interacting with the atmosphere could produce the mini black hole. If black holes are produced by the interactions of

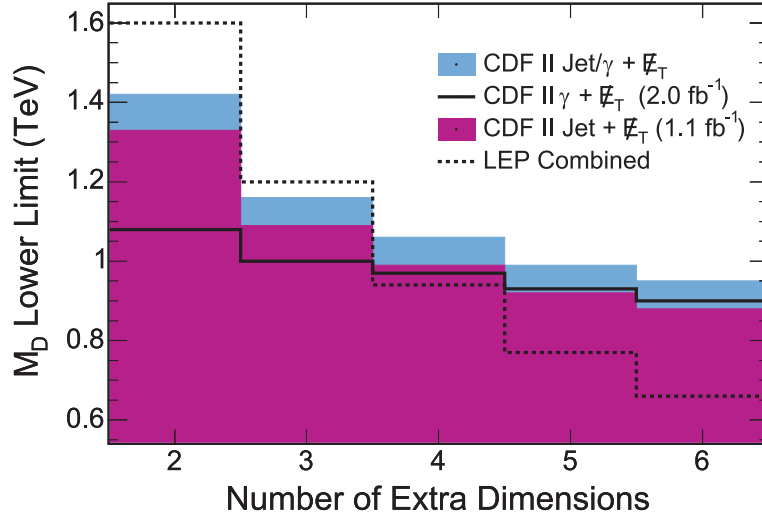


Figure 2.5: 95 % CL lower limits on  $M_D$  in the ADD model obtained by the LEP and the CDF experiments[40]

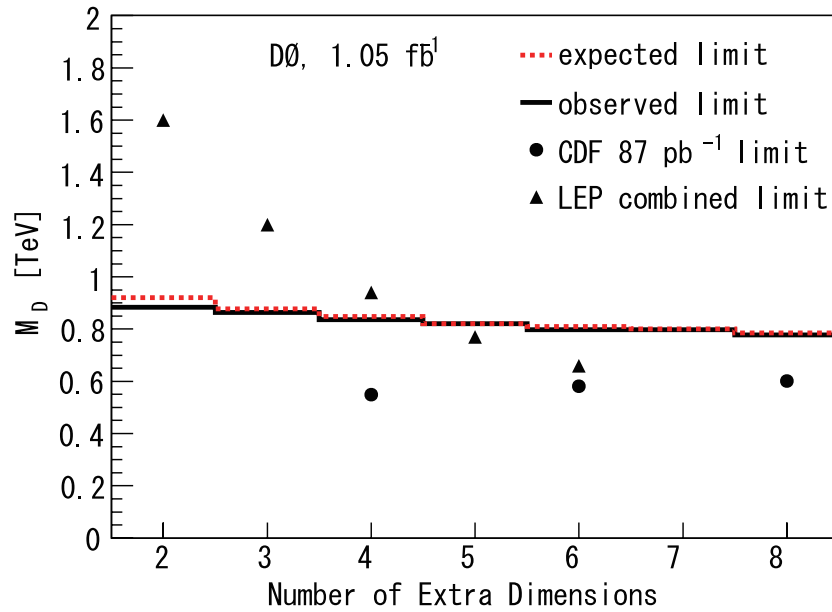


Figure 2.6: 95 % CL lower limits on  $M_D$  in the ADD model obtained by the LEP and the Tevatron experiments[41]

neutrinos with the atmosphere, the light descendants of the black hole may initiate quasi-horizontal showers. The lack of observed events with such showers results in limits of  $M_D > 1.0 - 1.4$  TeV for  $n \geq 5$  [45].

### 2.4.3 RS model

The alternative theory of extra dimensions proposed by Randall and Sundrum, called the RS model, is the model adopting one warped extra dimension [46]. In this model, two branes exist in the fifth dimensional geometry. They are separated by a slice of AdS space-time of curvature  $k$ . The background metric of the model is described as

$$ds^2 = e^{(-2kr_c\phi)} \eta_{\mu\nu} dx^\mu dx^\nu - r_c^2 d\phi^2 (0 \leq \phi \leq \pi), \quad (2.9)$$

where  $x^\mu$  is the coordination of 4-dimensional space-time,  $\phi$  is the coordinate along the fifth dimension, and  $r_c$  is the radius of the compactification of the fifth dimension. Two branes exist at the point  $\phi = 0$  and  $\phi = \pi$ . The brane at the point  $\phi = 0$  is called ‘‘Planck brane’’, where gravitational force is originated. The brane at  $\phi = \pi$  is called ‘‘Weak brane’’ where SM fields are localized. A Planck scale in five dimensions,  $M$ , is related to  $M_{\text{Pl}}$  as [46]

$$(M_{\text{Pl}})^2 = \frac{M^3}{k} (1 - e^{-2\pi kr_c}), \quad (2.10)$$

where  $kr_c > 1$  and  $M_{\text{Pl}} \sim k \sim M$ . Therefore, Eq. 2.10 can be approximated as

$$(M_{\text{Pl}})^2 = \frac{M^3}{k}. \quad (2.11)$$

In this convention, any mass parameter at Weak brane,  $m_{\text{weak}}$ , is given as

$$m_{\text{weak}} = m_0 e^{-\pi kr_c}, \quad (2.12)$$

where  $m_0$  is the mass parameter at Plank brane. The mass parameter at Weak brane is exponentially reduced by the factor  $e^{-2\pi kr_c}$ , which is called ‘‘warp factor’’. Thus, the energy scale at Weak brane,  $\tilde{M}$ , is given as

$$\tilde{M} = M e^{-\pi kr_c}. \quad (2.13)$$

In case  $kr_c \sim 11$ , the energy scale of  $O(1)$  TeV at Weak brane are generated from the energy scale  $\sim M \sim M_{\text{Pl}} = 1.2 \times 10^{19}$  GeV. The value  $kr_c \sim 11$  is naturally obtained by minimizing the potential for the modulus field that sets the size of the fifth dimension [47].

In RS model, the mass of  $n$ -th excited KK graviton,  $M_n$ , is written as

$$M_n = kx_n e^{-kr_c \pi}, \quad (2.14)$$

where  $x_n$  is the  $n$ -th root of the Bessel function ( $x_1 = 3.83$ ). With Eq. 2.11, 2.13 and 2.14,  $\tilde{M}$  is written as

$$\tilde{M} = \frac{(8\pi)^{1/3} M_1}{x_1 c^{2/3}}, \quad (2.15)$$

where

$$c = \frac{\sqrt{8\pi} k}{M_{\text{Pl}}}. \quad (2.16)$$

To solve the fine-tuning problem,  $M_1$  should be  $O(1)$  TeV and  $c$  should satisfies  $0.01 < c < 0.1$  [48].

The observables  $M_1$  and  $c$  are usually chosen as independent parameters in the experiments. The stringent results on this KK graviton mass with dielectron and diphoton final states reported in [49]. The 95% CL lower limit on  $M_1$  was reported as 1050 (560) GeV for  $c = 0.1(0.01)$ . These limits give the limit on  $\tilde{M}$  as

$$\tilde{M} \gtrsim 3.7 \text{ TeV}. \quad (2.17)$$

Hereafter, only extra dimensions theory of ADD model is considered unless otherwise noted.

## 2.5 Mini Black Hole

If extra dimensions exist and a fundamental Planck scale is TeV scale, the mini black hole with TeV scale mass can exist. It can be produced by two particles collision at TeV scale.

The mini black hole is formed in a two particle collision with the center-of-mass energy  $\sqrt{\hat{s}} = M_{\text{BH}}$  if their impact parameter,  $b$ , is smaller than twice of the horizon radius,  $r_h$ , of the black hole. Figure 2.7 shows the illustration of a formation of the mini black hole.

The cross section of such a collision can be simply considered as a disk with radius  $2r_h$ :

$$\sigma = \pi (2r_h)^2. \quad (2.18)$$

In case of  $M_{\text{BH}} = 1$  TeV,  $r_h$  is  $O(10^{-35})$  m and the cross section is  $O(10^{-41})$  b. Such a small cross section comes from large  $M_{\text{Pl}}$  because  $r_h$  is given as [36, 50]:

$$r_h \sim \frac{1}{M_{\text{Pl}}} \frac{M_{\text{BH}}}{M_{\text{Pl}}}. \quad (2.19)$$



Figure 2.7: Formation of the mini black hole

However if there are extra dimensions and the fundamental Planck scale is  $O(\text{TeV})$ , the horizon radius is written as

$$r_h \sim \frac{1}{M_D} \left( \frac{M_{\text{BH}}}{M_D} \right)^{1/(n+1)}. \quad (2.20)$$

If  $M_D \sim M_{\text{BH}} \sim O(\text{TeV})$ , the cross section is  $O(100)$  pb. The mini black hole immediately (in a Planck time  $1/M_{\text{Pl}} \sim 10^{-27}$  s) decays into many particles mainly by the Hawking radiation.

The LHC is designed to collide two proton beams at  $\sqrt{s} = 14$  TeV. It has a capacity to produce the mini black holes. The mini black hole has very large cross section and decays into many high energy particles. Figure 2.8 shows an event display of simulated mini black hole event in the ATLAS detector. The mini black hole events could be produced at LHC in an early stage of the experiment and it can be discriminated from the Standard Model processes with the high multiplicity topology.

The following subsections describe the details of the production and the decay of the mini black hole.

### 2.5.1 Production of Mini Black Hole

A Black hole is produced when an impact parameter,  $b$ , of two colliding particles is smaller than the horizon radius,  $r_h$ , of the  $n+4$  space-time dimensions:

$$b < 2r_h(n, M_{\text{BH}}, J), \quad (2.21)$$

where  $M_{\text{BH}}$  and  $J$  are the mass and the angular momentum of the mini black hole, respectively. The interaction area is considered as the cross section:

$$\sigma = \pi (2r_h)^2. \quad (2.22)$$

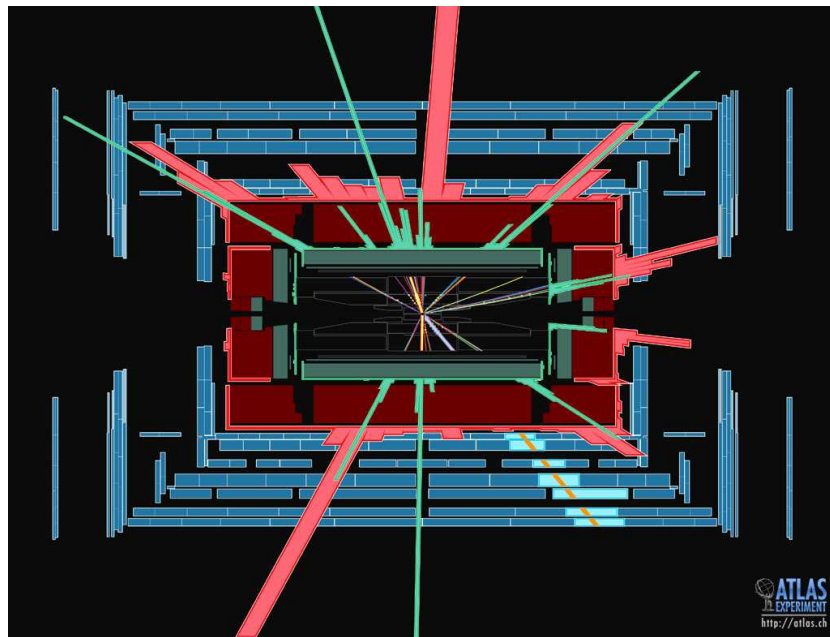


Figure 2.8: The ATLAS detector side view with a simulated mini black hole event. The beam axis is horizontal in center. The black center region is the inner detector and many tracks are shown. The green and red area show electromagnetic and hadronic calorimeters, respectively. The green and red histograms show the energies deposited in electromagnetic and hadronic calorimeters, respectively. Outer blue areas show muon system and the yellow line in it shows muon.

The metric of a rotating black hole for the  $n + 4$  dimensions in the Boyer-Lindquist coordinates <sup>1</sup> is given as [51]

$$ds^2 = \left(1 - \frac{\mu}{r^{n-1}\Sigma}\right) dt^2 - \sin^2 \theta \left(r^2 + a^2 + \frac{a^2 \mu \sin^2 \theta}{r^{n-1}\Sigma}\right) d\phi^2 + 2a \sin^2 \theta \frac{\mu}{r^{n-1}\Sigma} dt d\phi - \frac{\Sigma}{\Delta} dr^2 - \Sigma d\theta^2 - r^2 \cos^2 \theta d\Omega_n^2, \quad (2.24)$$

where

$$\Delta = r^2 + a^2 - \mu r^{n-1}, \quad (2.25)$$

$$\Sigma = r^2 + a^2 \cos^2 \theta, \quad (2.26)$$

and  $d\Omega_n^2$  is the metric on an  $n$ -sphere. The parameter  $\mu$  is related to the mass of the black hole as

$$M_{\text{BH}} = \frac{(n+2) A_{n+2}}{16\pi G_D} \mu, \quad (2.27)$$

where  $G_D$  is the Newton's constant in  $D (= n + 4)$  dimensions. In this thesis, PDG convention for ADD model is used for the relation between  $G_D$  and fundamental Planck scale,  $M_D$ , in  $n + 4$  dimensions as described in Subsection 2.4.2. It is defined as [33]

$$G_D = \frac{(2\pi)^n}{8\pi M_D^{n+2}}. \quad (2.28)$$

$A_{n+2}$  is the area of an  $(n + 2)$  dimensional unit sphere and it is given by

$$A_{n+2} = \frac{2\pi^{\frac{n+3}{2}}}{\Gamma\left(\frac{n+3}{2}\right)}. \quad (2.29)$$

The angular momentum of the black hole is written as

$$J = \frac{2}{n+2} M_{\text{BH}} a. \quad (2.30)$$

---

<sup>1</sup> The Boyer-Lindquist coordinates,  $r$ ,  $\theta$ ,  $\phi$  are related to Cartesian  $xyz$  coordinates as

$$\begin{aligned} x &= \sqrt{r^2 + a^2} \sin \theta \cos \phi, \\ y &= \sqrt{r^2 + a^2} \sin \theta \sin \phi, \\ z &= r \cos \theta, \end{aligned} \quad (2.23)$$

where  $a$  is the parameter of the spin.

The horizon radius is given as the solution of  $\Delta = 0$ . Hence, the horizon radius is written as

$$r_h = \left( \frac{\mu}{1 + \left(\frac{a}{r_h}\right)^2} \right)^{\frac{1}{n-1}} = \frac{r_s}{\left(1 + \left(\frac{a}{r_h}\right)^2\right)^{\frac{1}{n-1}}}, \quad (2.31)$$

where  $r_s \equiv \mu^{1/(n+1)}$  is the Schwarzschild radius. It is the horizon radius for a non-rotating black hole. With  $r_s$ ,  $M_{\text{BH}}$  is rewritten as

$$M_{\text{BH}} = \frac{2\pi^{\frac{n+3}{2}} (n+2) M_D^{n+2}}{\Gamma\left(\frac{n+3}{2}\right) 2(2\pi)^n r_s^{n+1}}. \quad (2.32)$$

In case of the collision of two massless particles with center-of-mass energy  $\sqrt{\hat{s}} = E = M_{\text{BH}}$  and impact parameter  $b$ , the angular momentum in the center-of-mass frame before the collision is written as

$$J = bM_{\text{BH}}/2. \quad (2.33)$$

Hence, the angular momentum is increased if the impact parameter becomes larger for a fixed mass. On the other hand, from Eq. 2.31, the horizon radius becomes smaller if the angular momentum becomes larger. As a result, there is a maximum value of the impact parameter,  $b_{\text{max}}$ , for each parameter set of  $n$ ,  $M_D$  and  $M_{\text{BH}}$ . The condition of the mini black hole formation can be rewritten:

$$b < b_{\text{max}} \equiv 2r_h(n, M_{\text{BH}}, J = b_{\text{max}}M_{\text{BH}}/2), \quad (2.34)$$

and this can be rewritten with  $r_s$  as [52]

$$b_{\text{max}} = 2 \frac{r_s}{\left[1 + \left(\frac{n+2}{2}\right)^2\right]^{\frac{1}{n+1}}}. \quad (2.35)$$

As a result, the cross section of the mini black hole is written as

$$\sigma = 4\pi (r_h)^2 = 4\pi \frac{r_s^2}{\left[1 + \left(\frac{n+2}{2}\right)^2\right]^{\frac{2}{n+1}}}. \quad (2.36)$$

## 2.5.2 Production of Black Hole at LHC

In the proton-proton collision of LHC, partons in the protons collide. Therefore parton densities in proton have to be considered to calculate a differential cross section of mini black hole events. The differential cross section is given by

$$\frac{d\sigma(pp \rightarrow \text{BH} + X)}{dM_{\text{BH}}} = \frac{dL}{dM_{\text{BH}}} \hat{\sigma}(ab \rightarrow \text{BH}) |_{\hat{s}=M_{\text{BH}}^2}, \quad (2.37)$$

where  $a$  and  $b$  are partons in protons, and  $dL/dM_{\text{BH}}$  is the parton luminosity which is a sum of the integral of all the parton possibilities. It can be written with the Parton Distribution Functions (PDFs),  $f_i(x_i)$ :

$$\frac{dL}{dM_{\text{BH}}} = \frac{2M_{\text{BH}}}{s} \sum_{a,b} \int_{M_{\text{BH}}^2/s}^1 \frac{dx_a}{x_a} f_a(x_a) f_b\left(\frac{M_{\text{BH}}^2}{sx_a}\right). \quad (2.38)$$

The mini black hole is produced with the continuous mass distribution above a threshold,  $M_{\text{BHth}}$ . This threshold is one of parameters of the mini black hole events. The simulated black holes in this thesis have the mass distribution from  $M_{\text{BHth}}$  to the proton proton collision energy, 7 TeV. Figure 2.9 shows the cross sections as a function of  $M_{\text{BHth}}$ . Each color represents different value of the Planck scale and each line type (solid, dash, dash-dot) represents the number of extra dimensions. Though the cross section of the mini black hole events depends on  $n$  and  $M_D$ , a typical cross section is roughly 100(10) pb for  $M_{\text{BHth}} = 2(3)$  TeV.

## 2.5.3 Decay of Black Hole

The mini black hole of  $O(1)$  TeV mass evaporates immediately. There are three stages in the decay of the black hole:

- Balding Phase: this phase is the formation process of the black hole. In this phase, the black hole loses all “hair” (characteristics other than mass, charge and angular momentum) and multipole moments by the gravitational radiation and the Hawking radiation.
- Evaporation Phase: this phase employs the Hawking radiation.
- Planck Phase: Planck phase is the phase when the black hole mass becomes about  $M_D$ . This phase is governed by the theory of quantum gravity.

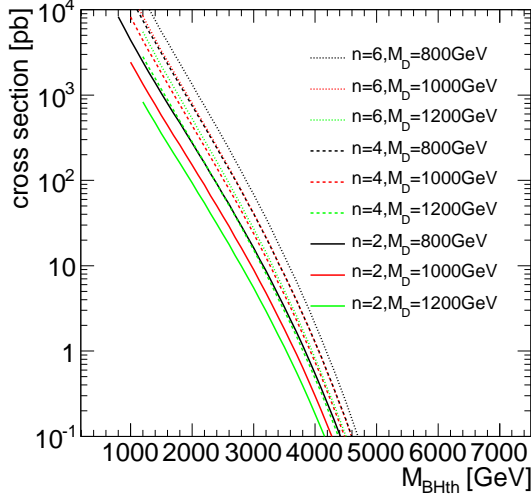


Figure 2.9: The cross section of the mini black hole as a function of black hole mass threshold. Each line shows each value of  $n$  and  $M_D$  parameters.

The gravitational emission is not known well especially for rotating black hole. The fraction of the gravitational emission depends on the models.

The Hawking radiation [53] is defined with the Hawking temperature,  $T_H$ , which is obtained as

$$T_H = \frac{n + 1}{4\pi r_h} \quad (2.39)$$

in the  $n + 4$  dimensions. Figure 2.10 shows  $T_H$  for each parameter of  $M_D$  and  $M_{BH}$  as a function of  $n$ . The higher  $M_D$  and the lower  $M_{BH}$  parameters show the higher temperature.

The flux of particles emitted by the black hole is given by [54]

$$\frac{d^2 N}{dt d\omega} = \frac{1}{2\pi} \sum_{j=|h|}^{\infty} \sum_{m=-j}^j \frac{1}{\exp((\omega - m\Omega)/T_H) + c} \Gamma_{(h,j,m,\omega)}^{(n)}(\omega, a_*), \quad (2.40)$$

where  $\omega$  is energy of the emitted particle,  $h$  is helicity, and  $\Omega$  is called the horizon angular velocity defined as:

$$\begin{aligned} \Omega &= a_* / ((1 + a_*^2) r_h), \\ a_* &= a / r_h. \end{aligned}$$

The value of  $c$  is -1 (+1) for the bosons (fermions).  $\Gamma_{(h,j,m,\omega)}^{(n)}$  is the gray body factor [55, 56, 57, 58, 59]. This factor is the suppression factor from the

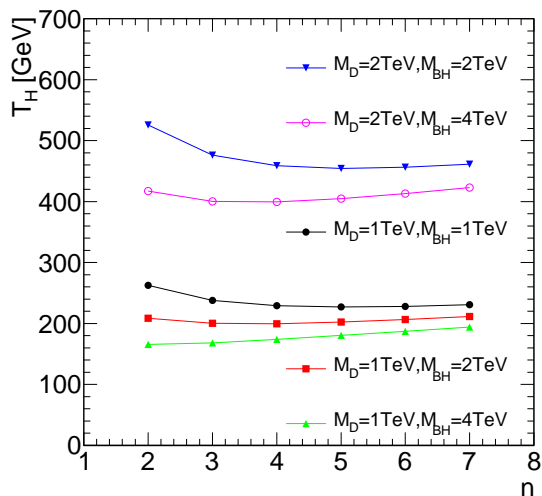


Figure 2.10: The Hawking temperature as a function of the number of extra dimensions. The lower  $M_{\text{BH}}$  shows the higher temperature for the same  $M_D$ . And higher  $M_D$  shows higher temperature.

perfect black body radiation and depends on physical quantities. Because of the term  $1/(\exp((\omega - m\Omega)/T_H))$  in Eq. 2.40, the mini black hole of higher  $T_H$  emits the higher energy particles.

The fraction of the particles emitted by the Hawking radiation is defined by the degrees of freedom. Table 2.1 summarizes the degrees of freedom for the all standard model particles.

Table 2.1: The degrees of freedom of the standard model particles

Particle type	Degree of freedom
Quarks	6
Leptons	2
Gluons	16
Photons	2
$Z$	2
$W^\pm$	2
Higgs	1

When the black hole mass becomes near the Planck scale after emission of particles, the classical theories cannot be used to describe the decay. This

phase is Planck Phase. The quantum gravity theory is needed to treat a remnant of the black hole. There are some possibilities in the Planck Phase:

- Burst Model: the burst model makes multi-body decay at the Planck Phase. Fixed and unfixed models can be considered [60]. The Hawking radiation flux is usually employed to determine the decay particles. One of the examples for the unfixed model follows a Poisson distribution [61]. Another scenario minimizes the number of particles [54].
- Boiling Model: this model continues the Hawking radiation in the Planck Phase. Finally, it makes multi-body decay at decided threshold of a mass.
- Stable Remnant: the remnant of the black hole could remain stably [62, 63, 64]. This stable remnant does not interact in the brane. Therefore, this is one of the candidates of the dark matter.

## 2.6 Searched Model

This subsection describes a model of the mini black hole which is searched for in this thesis. Section 4.2 also gives the model descriptions especially for technical descriptions in an event generator for Monte Carlo studies.

### 2.6.1 Mass Threshold of Black Hole

In classical idea [65], it is considered that the black hole is formed when the Compton wave length of the  $M_{\text{BH}}$ ,  $\lambda$ , becomes smaller than the Schwarzschild radius with center-of-mass collision energy  $E = M_{\text{BH}}$ :

$$\lambda = \frac{2\pi}{E} = \frac{2\pi}{M_{\text{BH}}} < r_s(n, M_D, M_{\text{BH}}). \quad (2.41)$$

From this condition  $M_{\text{BHth}}$  can be obtained as a function of  $M_D$ . Figure 2.11 shows  $M_{\text{BHth}}$  as a function of  $M_D$  with this condition. On the assumption of Eq. 2.41, the higher number of extra dimensions shows the lower threshold. Figure 2.12(a) shows  $M_{\text{BHth}}$  calculated with Eq. 2.41 for each  $n$ ,  $M_D$ . Corresponding cross sections are shown in Figure 2.12(b). Another assumption based on  $r_h$  at  $b = b_{\text{max}}$  instead of  $r_s$  is considered:

$$\lambda < r_h(n, M_D, M_{\text{BH}}, J = b_{\text{max}}M_{\text{BH}}/2). \quad (2.42)$$

In this thesis, signal points are defined with these assumptions for  $n = 2 - 7$  and  $M_D = 800 - 2000$  GeV. Figure 2.13 shows  $M_{\text{BHth}}$  as a function of

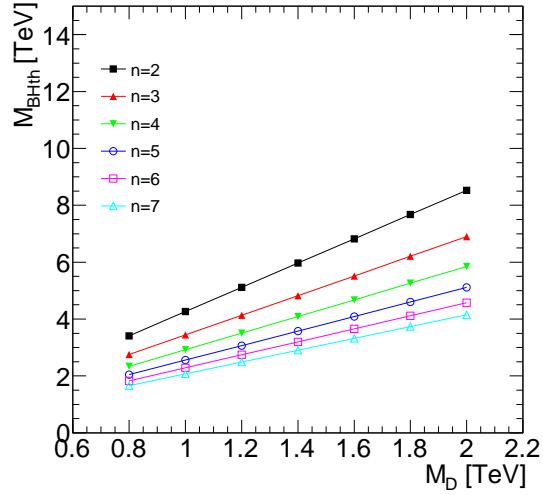


Figure 2.11: The threshold of black hole production with the condition:  $\lambda < r_s$ . Each line represents each  $n$ . For example,  $M_{\text{BHth}} = 4.26$  TeV (2.08 TeV) for  $n = 2$  (7) at  $M_D = 1$  TeV.

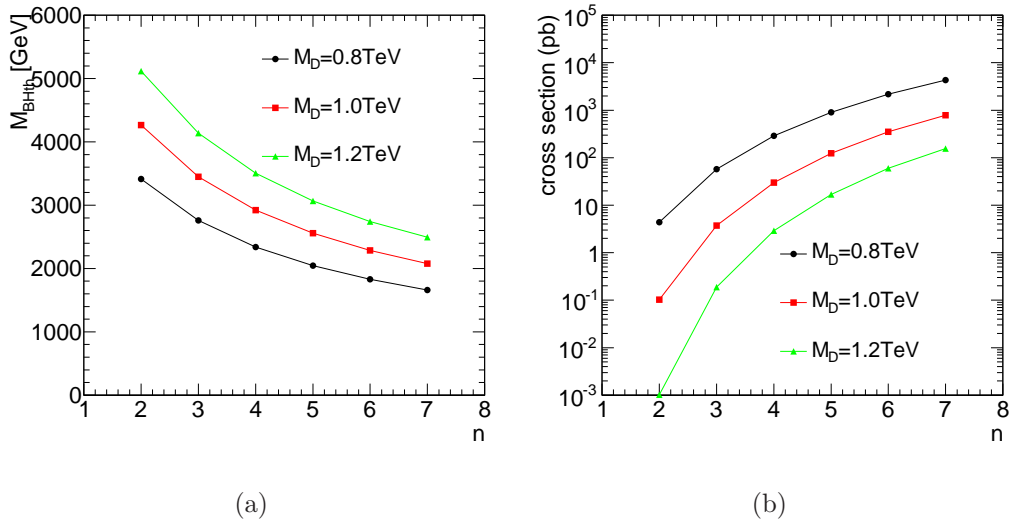


Figure 2.12: Mass thresholds calculated with Eq. 2.41 (a) and cross sections for them (b) for each  $M_D$  as a function of  $n$ .

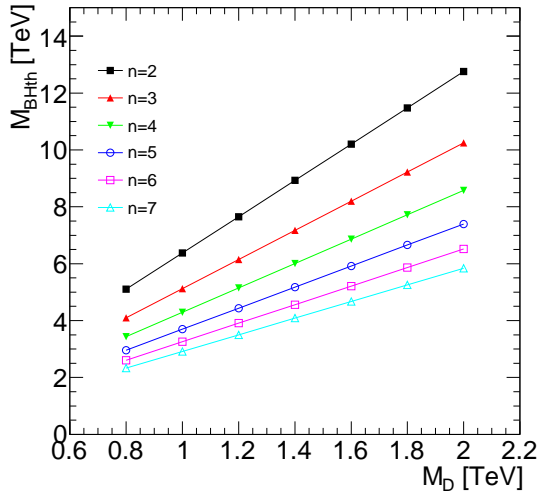


Figure 2.13: The threshold of black hole production on the assumption of  $\lambda < r_h$ . Each line represents each  $n$ . For example,  $M_{\text{BHth}} = 6.38$  TeV (2.92 TeV) for  $n = 2$  (7) at  $M_D = 1$  TeV.

$M_D$  under this assumption. The  $M_{\text{BHth}}$  values are larger than that obtained on the assumption of Eq. 2.41 by factor about 1.5.

There are some discussions for  $M_{\text{BHth}}$  [35, 45, 66, 67, 68]. The assumptions in these papers mainly require enough thermalized black holes for assuring that the black holes evaporate by the Hawking radiation. Following requirements are considered for thermal black holes:

- [66] shows that the entropy of the black hole should be large. The entropy,  $S$ , of the black hole is defined as [68]

$$S = \frac{4\pi M_{\text{BH}} r_s}{n+2} \gg 1. \quad (2.43)$$

On the above assumptions of mass thresholds, the signal points based on the Schwarzschild radius and  $n = 7$  show minimum  $S$ , which equal to 8.77. Hence, all signal points can be considered to satisfy Eq. 2.43.

- The life time of the mini black hole,  $\tau$ , should be large compared to  $1/M_{\text{BH}}$  to ensures that the mini black hole process is considered as  $s$ -channel process which intermediate the mini black hole [35]. This criterion requires  $M_{\text{BHth}}/M_D \gtrsim 1.3$  [68]. All signal points in this thesis satisfy this criterion.

In summary, the assumptions on  $M_{\text{BHth}}$  used in this thesis satisfy the requirements of the thermal black hole.

In case of RS model, the Schwarzschild radius is given as [68]

$$r_s = \left( \frac{M_{\text{BH}}}{3\pi^2 \tilde{M}^3} \right)^{1/2}. \quad (2.44)$$

The lower limit on  $\tilde{M}$  is estimated in Subsection 2.4.3 is 3.7 TeV. The lowest  $M_{\text{BHth}}$  for RS model obtained from Eq. 2.41 and 2.44 is 39 TeV. Therefore, the mini black hole production based on RS model is not possible at LHC and it is not considered in this thesis.

## 2.6.2 Decay Model

Mini black holes immediately go to Evaporation Phase and decay with the Hawking radiation. No graviton emission model is used in this thesis. In case of the Planck Phase, burst model is adopted for  $M_{\text{BH}} < M_D$ . The burst model follows below criteria:

1. The numbers of decay particles are defined as:  $N_{-1/3}$  for down-type quarks,  $N_{2/3}$  for up-type quarks,  $N_{-1}$  for charged lepton and  $W$  bosons,  $N_{gl}$  for gluons, and  $N_n$  for non-charged particle,  $\nu, \gamma, Z, h$ .
2. On the constraint of conserving the charge and the color, all possible combinations of  $N$  except for  $N_n$  are searched.
3. The combination which has minimum number of particles is selected.
4. If the total number of particles of the combination is less than 2, the number is added to  $N_n$  to keep the total number of particles equal to 2.
5. In this combination, decay particles are selected randomly according to the degrees of freedom.
6. Momenta and energies are assigned randomly to conserve the momenta and energies of the mini black hole.

In this thesis, BlackMax [54, 69], a black hole generator, is used to generate the MC events of the mini black hole. BlackMax can provide events based on above descriptions. Details of the generator and MC events are described in Section 4.2.

# Chapter 3

## The LHC and the ATLAS Detector

This chapter describes an overview of the LHC and the ATLAS detector.

### 3.1 The Large Hadron Collider

The Large Hadron Collider (LHC) [70] is a proton-proton collider which is constructed at the European Organization for Nuclear Research (CERN) in Geneva, Switzerland. The LHC is placed in the tunnel where the Large Electron-Positron Collider (LEP) had been placed. This tunnel's circumferential length is 26.7 km. It lies 45-170 m below the surface and runs through both Switzerland and France (Figure 3.1).

Before injecting proton beams into the LHC, protons are accelerated up to an injection energy, 450 GeV by four accelerators at CERN (LINAC, PSB, PS, SPS) (Figure 3.2). Two proton beams are injected into LHC and they run in opposite directions.

The LHC ring consists of eight arcs and eight straight sections. In the arc regions, dipole magnets are used to bend the beams. They produce a magnetic field strength 8.33 T which operated at 1.9 K. The cooling is achieved by super-fluid liquid helium. In the straight sections, 400 MHz superconducting cavity system accelerates the beams up to 7 TeV.

The design center-of-mass energy of a proton-proton collision of LHC is 14 TeV. In 2010, LHC ran at the center-of-mass energy of 7 TeV. It is the current highest energy of particle collisions by a collider. This energy is significantly higher than the energy of Tevatron, which is a proton-antiproton collider with center-of-mass energy = 1.96 TeV.

The main design parameters of LHC for proton-proton collisions are sum-



Figure 3.1: An aerial photo of LHC

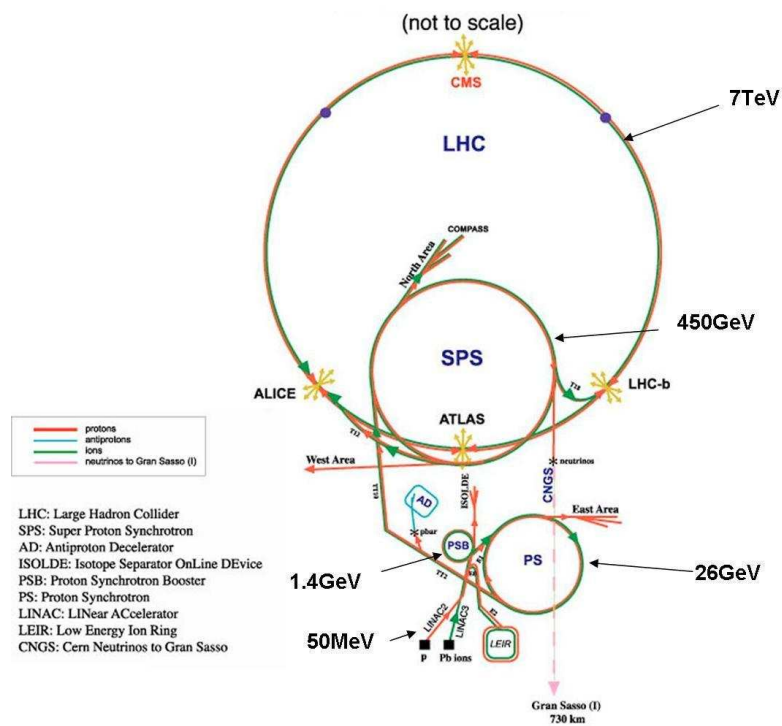


Figure 3.2: Accelerators at CERN

marized in Table 3.1.

Table 3.1: Design Parameters of LHC

Maximum Energy	7.0 TeV
Injection Energy	450 GeV
Luminosity	$10^{34} \text{ cm}^{-2}\text{s}^{-1}$
Beam Life Time	15 h
Number of Bunches	2808
Bunch Crossing Interval	24.95 ns
Proton Intensity per Bunch	$1.14 \times 10^{11}$

There are eight beam crossing points at LHC and the following detectors are placed at four of them. ATLAS (A Toroidal LHC Apparatus) [71] and CMS (Compact Muon Solenoid) [72] are the general purpose detectors. LHCb (Large Hadron Collider beauty experiment) [73] is the detector especially for B-physics. ALICE (A Large Ion Collider Experiment) [74] is made for the physics of heavy ion collisions.

## 3.2 A Toroidal LHC Apparatus

The ATLAS (A Toroidal LHC Apparatus) detector [75, 76] (Figure 3.3) is a multi-purpose detector placed at one of the beam crossing points of LHC. The height of the detector is 25 m and the length is 44 m. Total weight of the detector is about 7000 tonnes. The ATLAS detector is designed as symmetry in both forward and backward sides and has coverage almost  $4\pi$  in solid angle.

The ATLAS detector consists of the magnet system, the inner detectors, the calorimeters and the muon system. In the following sections, the coordinate system used at the ATLAS detector is given at first. Second, each sub-detector system is summarized. The luminosity monitor system and the trigger system are described after that.

## 3.3 Coordinate System in the ATLAS experiment

The coordinate system used in the ATLAS experiment is summarized in this section. The origin of the coordinate system is defined at the proton-proton

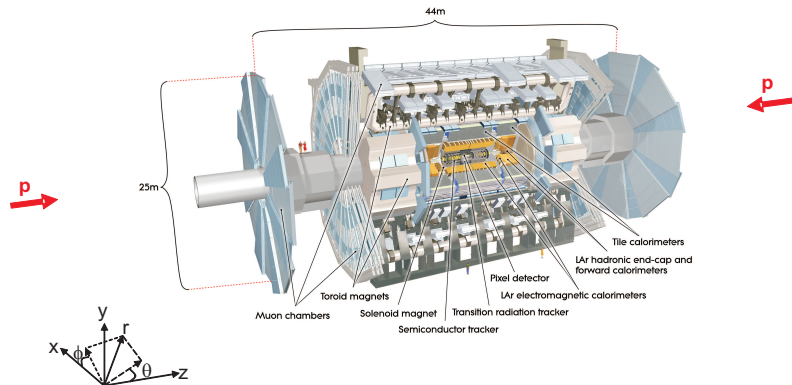


Figure 3.3: The ATLAS Detector

collision point. The direction of  $x$ -axis is defined to point to the center of the LHC ring and  $y$ -axis positive direction is upward. The  $z$ -axis is defined as the beam direction. Following a right-handed coordinate system, the positive direction of the  $z$ -axis points in a counterclockwise direction. The polar angle  $\theta$  is defined as an angle from the beam axis and the azimuthal angle  $\phi$  is the angle around the beam axis. The pseudo rapidity,  $\eta$ :

$$\eta \equiv -\ln \tan \left( \frac{\theta}{2} \right) \quad (3.1)$$

is useful for highly Lorentz boosted collision experiment and it is used instead of  $\theta$  in hadron collider experiments. The distance between two points in the pseudorapidity-azimuthal angle space is defined as  $\Delta R = \sqrt{(\Delta\eta)^2 + (\Delta\phi)^2}$ . The transverse direction is defined on  $x$ - $y$  plane. The momentum (energy) in the transverse plane is denoted as  $p_T$  ( $E_T$ ). The missing transverse energy is  $E_T^{\text{miss}}$ .

### 3.4 Magnet system

The ATLAS detector has four superconducting magnets, one central solenoid magnet and three toroid magnets. The solenoid magnet is set between the inner detector and the electromagnetic calorimeter. The toroid magnets are set in the outer side of the detector. Each magnet is set in barrel region and in each end-cap region. Figure 3.4 shows the geometry of magnets. Red lines

and red filled area represent the toroid magnets and the solenoid magnet, respectively.

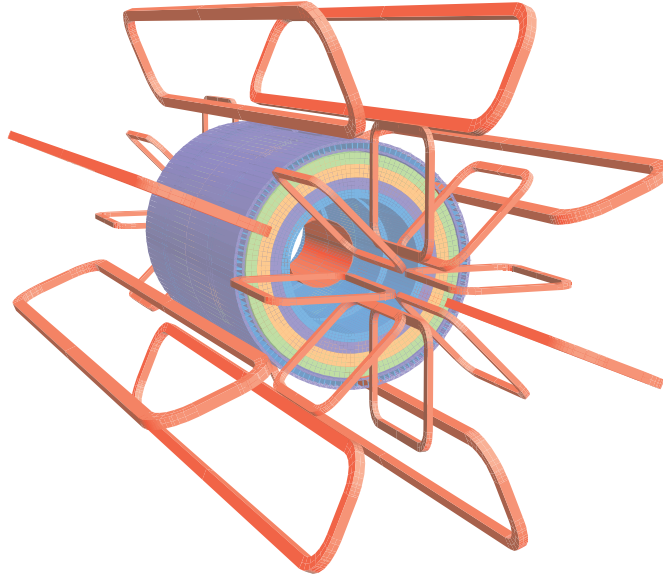


Figure 3.4: Geometry of magnets. Red lines show the toroid magnets and red filled component represents the solenoid magnet. Four layers around the solenoid magnet represent calorimeters.

In the following two subsections, the central solenoid magnet and the toroid magnet are described.

### 3.4.1 Central Solenoid Magnet

The central solenoid magnet [77, 78] provides a 2 T magnetic field along the beam axis. This magnet is placed in front of calorimeters and thereby it should be optimized to minimize the materials to achieve good performance in the calorimeters. Therefore, the cryostat is shared with the liquid argon (LAr) calorimeter to reduce the material. Its total radiation length ( $X_0$ ) of the coil is about  $0.66 X_0$ . The inner (outer) diameter is 2.46 m (2.56 m). The length along beam axis is 5.8 m. The coil mass is 5.4 tonnes. The operation temperature is 4.5 K. It can be re-cooled within one day in case of a quench.

### 3.4.2 Toroid Magnets

The toroid magnets are divided in three regions, one barrel and two end-cap regions. They are air core coils and eight coils are set as rotational symmetry around the beam axis for each region. Figure 3.5 shows barrel toroid installed in the underground cavern.

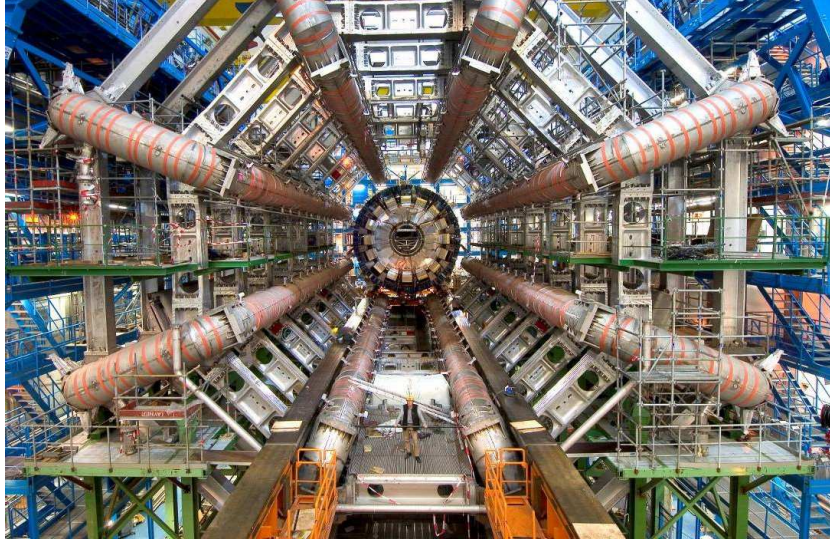


Figure 3.5: Barrel toroid

The size of the barrel toroid is 25.3 m in length, and 9.4 m and 25.3 m of inner and outer diameters, respectively. The size of the end-cap toroid is 5.0 m in length, and 1.65 m and 10.7 m of inner and outer diameters, respectively.

Figure 3.6 shows the integral magnetic field provided by the toroid magnets as a function of  $|\eta|$ . The longitudinal axis shows the bending power which is characterized by the integral magnetic field calculated for infinite momentum muons.

## 3.5 Inner detector

The inner detector covers the region of  $|\eta| < 2.5$  to measure the momentum of charged particles. It consists of Pixel Detector (Pixel), Semiconductor Tracker (SCT) and Transition Radiation Tracker (TRT) in a cylindrical envelope of length 6.2 m and diameter of 1.15 m. Figure 3.7 and 3.8 show the each detector with tracks of  $p_T = 10$  GeV for barrel and end-cap region,

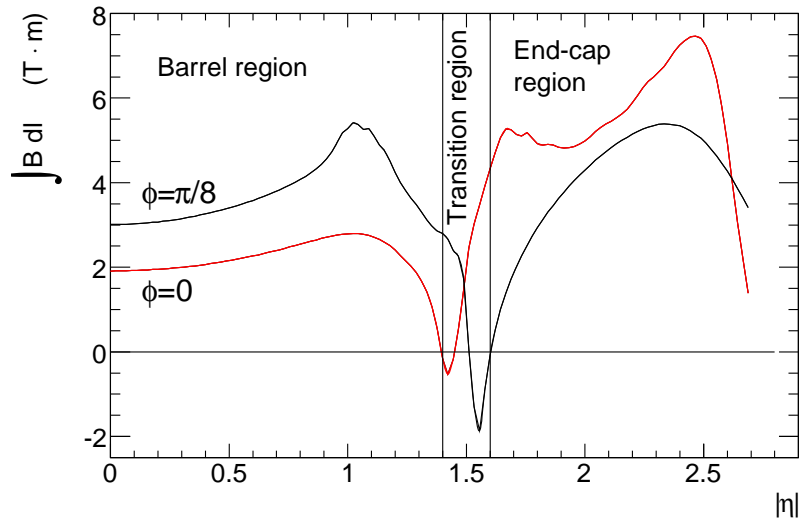


Figure 3.6: Integral magnetic field as a function of  $|\eta|$  provided by the toroid magnets

respectively. Figure 3.9 is the plan view of a quarter-section of the inner detector. It is in a 2 T magnetic field provided by the central solenoid magnet.

Pixel and SCT cover the region  $|\eta| < 2.5$ . They are designed cylindrical in the barrel region while they have a disk architecture in the end-cap region as shown in Figure 3.7 and 3.8. TRT provides a large number of hits and makes continuous tracking. The performance of the inner detector for  $p_T$  measurement of tracks is

$$\frac{\sigma_{p_T}}{p_T} = 0.05\% \cdot p_T \cdot \text{GeV}^{-1} \oplus 1\%. \quad (3.2)$$

### 3.5.1 Pixel detector

Pixel detector [79] is designed to provide high granularity measurements in the closest position to the interaction point. It adopts the semiconductor technology and covers  $|\eta| < 2.5$ . Figure 3.10 shows the illustration of the Pixel detector. The nominal pixel size is  $50 \times 400 \mu\text{m}^2$ . There are about 80.4 million readout channels. The position resolution of a single hit is  $10 \mu\text{m}$  in  $R - \phi$  and  $115 \mu\text{m}$  in  $z$ .

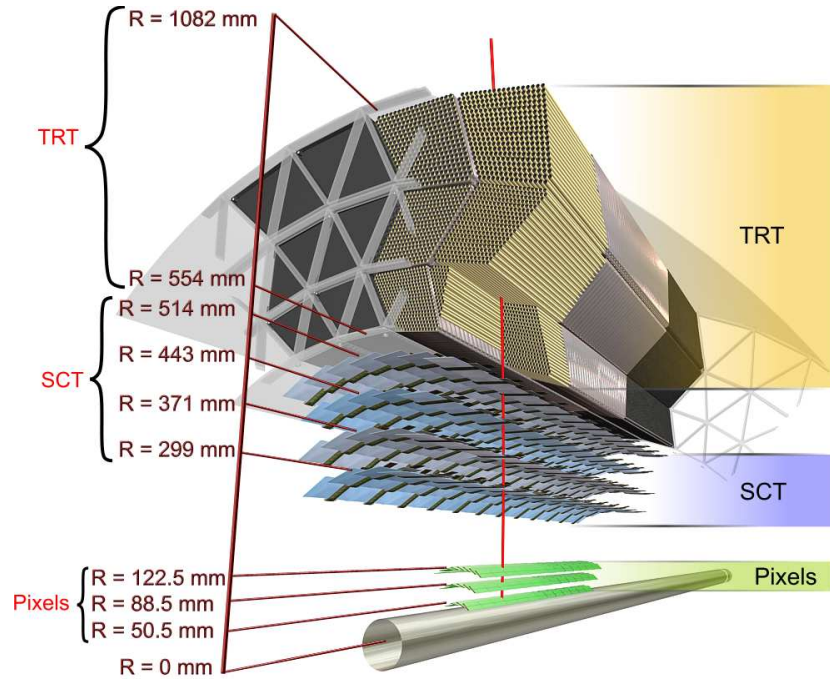


Figure 3.7: Structure of the inner detector in the barrel region. A red line represents  $10$  GeV track at  $\eta = 0.3$ .

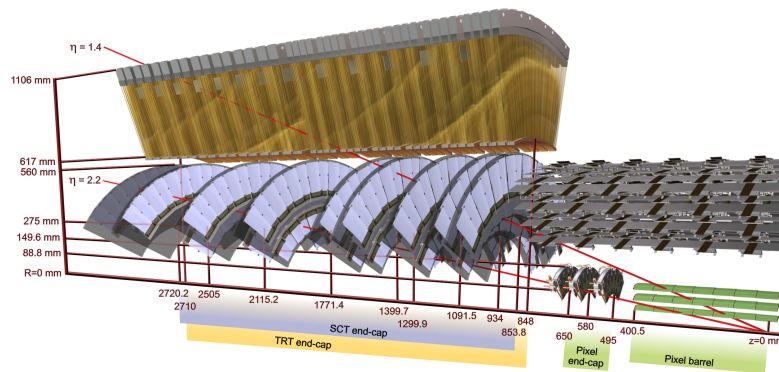


Figure 3.8: Structure of the inner detector in the end-cap region. Two red lines represent tracks at  $\eta = 1.4$  and  $2.2$ .

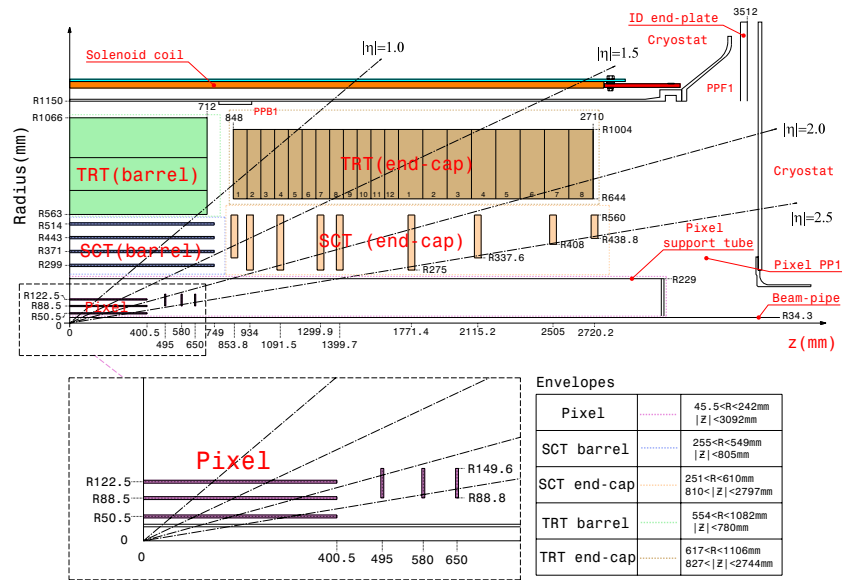


Figure 3.9: Plan view of a quarter-section of the ATLAS inner detector

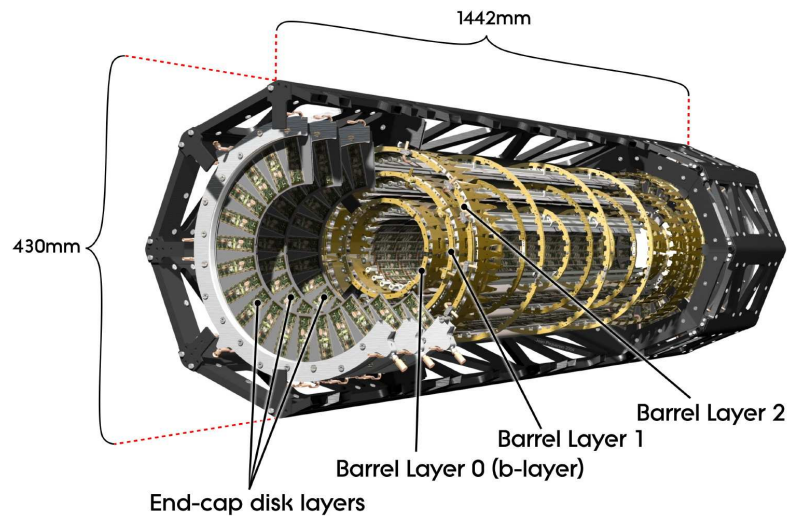


Figure 3.10: Pixel detector

### 3.5.2 Semiconductor Tracker

SCT [80] adopts single-sided p-in-n silicon microstrip sensors. Eight layers are expected to be crossed by tracks. One sensor has about  $60 \times 60 \text{mm}^2$  size and 768 active strips of  $80 \mu\text{m}$  pitches. The SCT in the barrel region uses 40 mrad stereo strips. The total number of SCT readout channels is about 6.3 millions. The resolution of the barrel region is  $17 \mu\text{m}$  in  $R - \phi$  and  $580 \mu\text{m}$  in  $z$ . The resolution of the end-cap region is  $17 \mu\text{m}$  in  $R - \phi$  and  $580 \mu\text{m}$  in  $R$ .

### 3.5.3 Transition Radiation Tracker

TRT [81] uses straw drift tubes of 4 mm diameter. TRT is the outermost part of inner detector as shown in Figure 3.7.

TRT has about 351,000 readout channels and 73 layers of straws interleaved with fibers in the barrel region. There are 160 straw planes foils in the end-cap region. The coverage of the TRT is  $|\eta| < 2.0$ . TRT provides only  $R - \phi$  plane information. The typical number of hits is 36 per track.

## 3.6 Calorimeter

Figure 3.11 shows the cut-away view of the ATLAS calorimeter system. The ATLAS calorimeter system consists of liquid argon (LAr) electromagnetic (EM) calorimeter, Tile calorimeter, LAr hadronic end-cap calorimeter and LAr forward calorimeter [82, 83].

Figure 3.12 shows the radiation length of the EM calorimeter for the barrel region (a) and for the end-cap region (b) as a function of pseudo rapidity. The radiation length of the EM calorimeter is  $> 22 X_0$  for the barrel region and  $> 24 X_0$  for the end-cap region.

Figure 3.13 shows the interaction length ( $\lambda$ ) of calorimeters as a function of pseudo rapidity. The total interaction length of calorimeters is about  $9.7 \lambda$  for the barrel region and  $10 \lambda$  for the end-cap region. They cover the range of  $|\eta|$  up to 4.9.

### The LAr EM calorimeter

The LAr EM calorimeter is divided into two regions, the barrel region (EMB,  $|\eta| < 1.475$ ) and the end-cap regions (EMEC,  $1.375 < |\eta| < 3.2$ ). The EMB is separated at  $\eta = 0$  and there is a 4 mm gap.

The LAr EM calorimeter is a sampling calorimeter composed of liquid argon as an active layer and lead as an absorber. Figure 3.14 shows the LAr

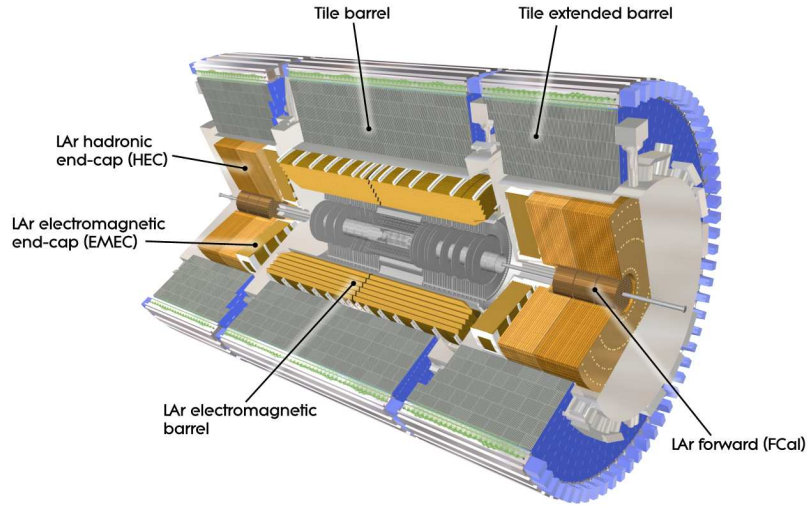


Figure 3.11: The ATLAS calorimeter

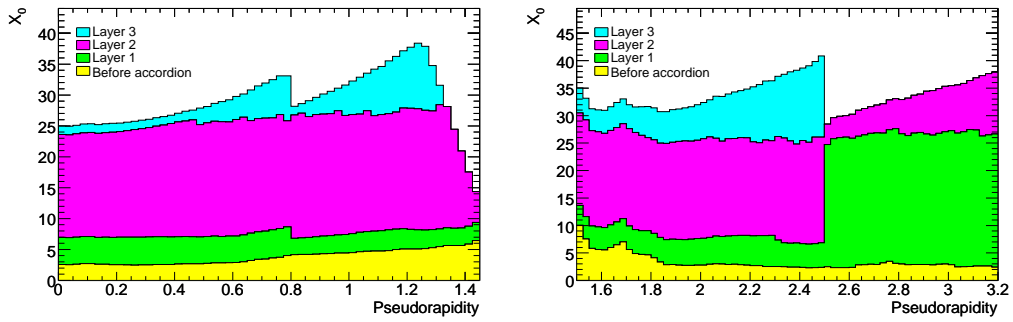


Figure 3.12: The amount of materials of the EM calorimeter in units of radiation length for the barrel region (a) and for the end-cap region (b) as a function of pseudo rapidity. Layer 1-3 mean the layers of the EM calorimeter. “Before accordion” represents materials of the inside of the EM calorimeter.

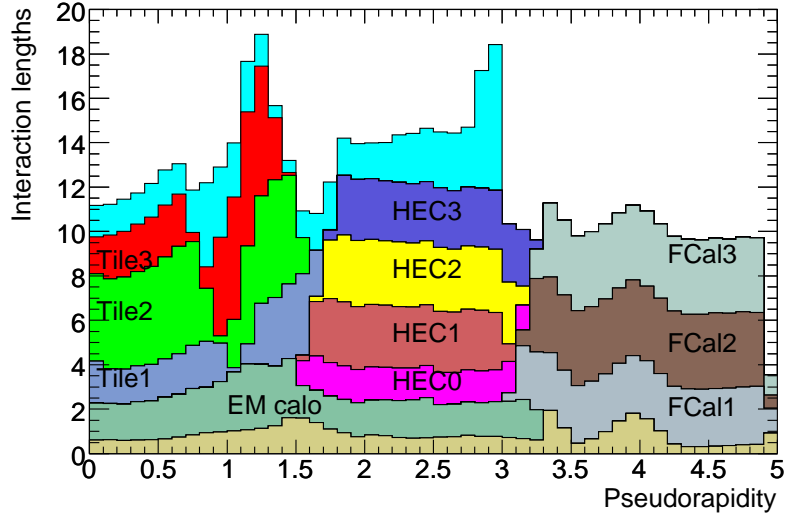


Figure 3.13: Interaction length of the ATLAS detector as a function of  $|\eta|$ . The undermost histogram represents the total material of the inside of the calorimeters. The histogram on the top without a legend represents the muon system. Other histograms are calorimeter components.

EM calorimeter in the barrel region. The LAr EM calorimeter is designed as accordion shape. This shape does not make cracks in any  $\phi$  region and the extraction of the signals can be fast at the rear or the front of the EM calorimeter.

It consists of three layers. The nominal granularity is  $\sim 0.025 \times 0.025$  in  $\Delta\eta \times \Delta\phi$ . As shown in Figure 3.14, the first layer in the barrel region is finely divided in  $\eta$  direction and its granularity is  $0.025/8 \times 0.1$  of  $\Delta\eta \times \Delta\phi$ .

The presampler is placed in the region  $|\eta| < 1.8$  for the correction of the energy loss by electrons and photons in front of the calorimeter.

An energy resolution was measured with the electron test beam [84]. The energy range of the beam is between 15 GeV and 180 GeV. The result of the test beam is:

$$\frac{\sigma_E}{E} = \frac{10\% \cdot \sqrt{\text{GeV}}}{\sqrt{E}} \oplus 0.17\%. \quad (3.3)$$

### 3.6.1 Hadronic calorimeter

The hadronic calorimeters of the ATLAS detector consist of three different components. There is the tile calorimeter (Tile) in the barrel region, the

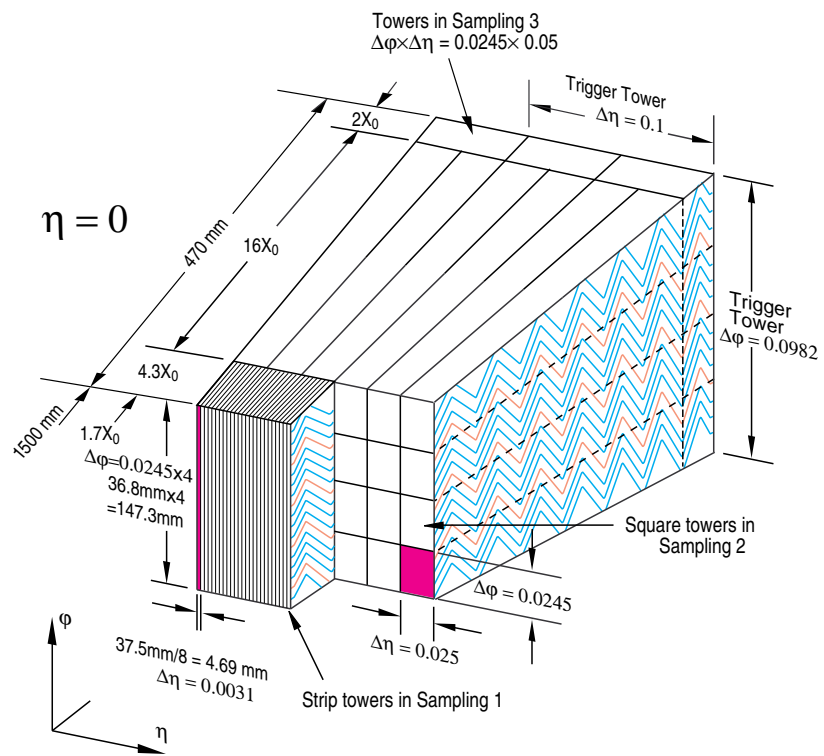


Figure 3.14: The LAr EM calorimeter in the barrel region

LAr hadronic end-cap calorimeter (HEC) in end-cap region and Forward calorimeter (FCAL) in range of  $|\eta|(> 3.1)$ .

### Tile calorimeter

The tile calorimeter [83] is a sampling calorimeter which adopts steel as an absorber and scintillator as an active material. The tile calorimeter covers the region of  $|\eta| < 1.7$ . It consists of three regions: one central barrel region ( $|\eta| < 1.0$ ) and two extended barrel region ( $0.8 < |\eta| < 1.7$ ). It is located behind the LAr EM calorimeter. The depth in the interaction length of it is about  $7.4 \lambda$ . There are a 600 mm gaps between central barrel and extended barrel regions. These gaps are needed for the cables and services of the inner detector and the LAr detector. The intermediate tile calorimeter (ITC) is placed to cover the gaps as an extension of the extended barrel. The scintillator of ITC is installed in  $1.0 < |\eta| < 1.6$ . The scintillators in  $1.0 < |\eta| < 1.6$  consists of gap scintillators in  $1.0 < |\eta| < 1.2$  and crack scintillators in  $1.2 < |\eta| < 1.6$ .

Figure 3.15 shows the sketch of a tile calorimeter module. The scintillator tiles are installed perpendicularly to the beam axis. Each tile has two wavelength-shifting fibers in both sides for readout and they are connected to the photomultiplier tubes (PMTs). The module can work even if one fiber is broken.

The tile calorimeter consists of three layers as shown in Figure 3.16. The granularity in  $\Delta\eta \times \Delta\phi$  is  $0.1 \times 0.1$  for the first two layers, and  $0.2 \times 0.1$  for the last layer.

The energy resolution was measured with hadron beams [71]. The energy range is between 20 GeV and 180 GeV, and at 350 GeV. The energy resolution for jets is estimated as

$$\frac{\sigma_E}{E} = \frac{56.4\% \cdot \sqrt{\text{GeV}}}{\sqrt{E}} \oplus 5.5\% \quad (3.4)$$

for  $\eta = 0.35$ . It depends on  $\eta$  because the effective depth is increased as  $\eta$  increases. As representative examples, the energy resolution at energy of 20 GeV is 14.2%, 13.7%, 13.0% for  $\eta = 0.25, 0.35, 0.55$ , respectively. The energy resolution at energy of 350 GeV is 6.6%, 6.3%, 5.9% for  $\eta = 0.25, 0.35, 0.55$ , respectively.

### LAr hadronic end-cap calorimeter

In the end-cap region, the LAr calorimeter with copper as an absorber is placed as the hadronic end-cap calorimeter (HEC) [85] behind EMEC and

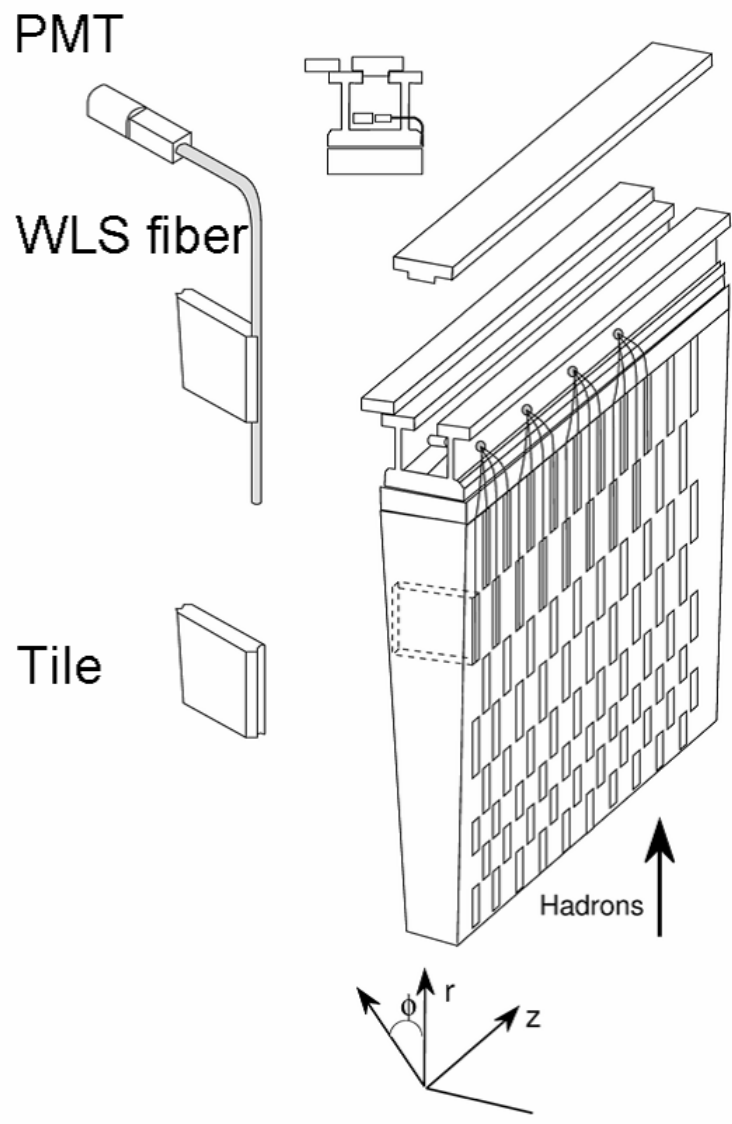


Figure 3.15: The tile calorimeter module

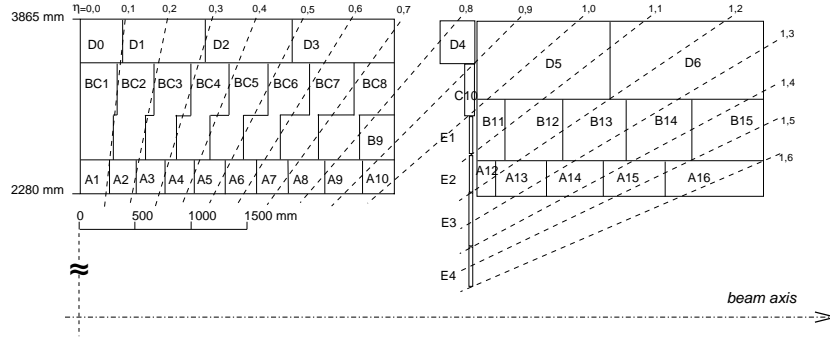


Figure 3.16: Segmentation in depth and  $\eta$  of the tile calorimeter. Left shows the barrel region and right shows the extended barrel region. The vertical axis represents the distance from the beam axis.

it covers the range of  $1.5 < |\eta| < 3.2$ . It consists of three electrodes in the 8.5 mm gaps of copper as shown in Figure 3.17. The readout cell size in  $\Delta\eta \times \Delta\phi$  is  $0.1 \times 0.1 (0.2 \times 0.2)$  for the region  $1.5 < |\eta| < 2.5 (2.5 < |\eta| < 3.2)$ .

The energy resolution for pions was estimated with the test beam of pion with energies up to 200 GeV [86]. The energy resolution of the HEC for pions is estimated as

$$\frac{\sigma_E}{E} = \frac{70.6\% \cdot \sqrt{\text{GeV}}}{\sqrt{E}} \oplus 5.8\%. \quad (3.5)$$

### Forward calorimeter

The forward calorimeter (FCAL) is a LAr calorimeter. It covers the range  $3.1 < |\eta| < 4.9$ . It is composed of three layers. The first layer is the electromagnetic layer adopting copper as an absorber. The second and third layers use tungsten which can reduce the spread of hadronic showers. The forward calorimeter has a tube structure set parallel to the beam direction. Figure 3.18 shows the structure of the forward calorimeter. The electrodes are the tube and the rod. The LAr is filled in the gap between the rod and the tube.

The energy resolution of this detector is estimated as followings [87]:

$$\frac{\sigma_E}{E} = \frac{28.5\% \cdot \sqrt{\text{GeV}}}{\sqrt{E}} \oplus 3.5\% \quad \text{forelectron}, \quad (3.6)$$

$$\frac{\sigma_E}{E} = \frac{70.0\% \cdot \sqrt{\text{GeV}}}{\sqrt{E}} \oplus 3.0\% \quad \text{forhadron}. \quad (3.7)$$

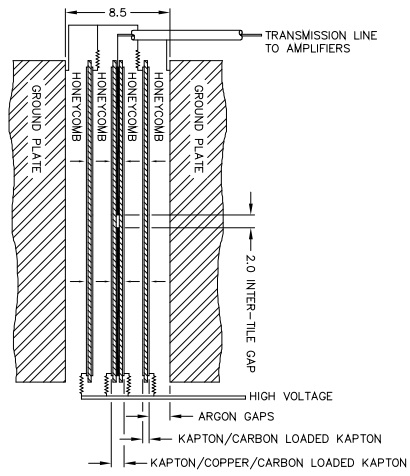
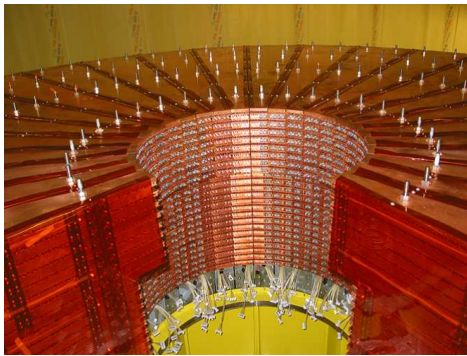


Figure 3.17: Left is the picture of the HEC and right shows the sketch of readout structure of the HEC. The HEC module has 8.5 mm gap between the copper ground plates. There are three electrodes. The middle one is for the read out and the high-voltage is applied between the middle one and others. The LAr is filled between the electrodes. A honeycomb sheet is placed to keep the space.

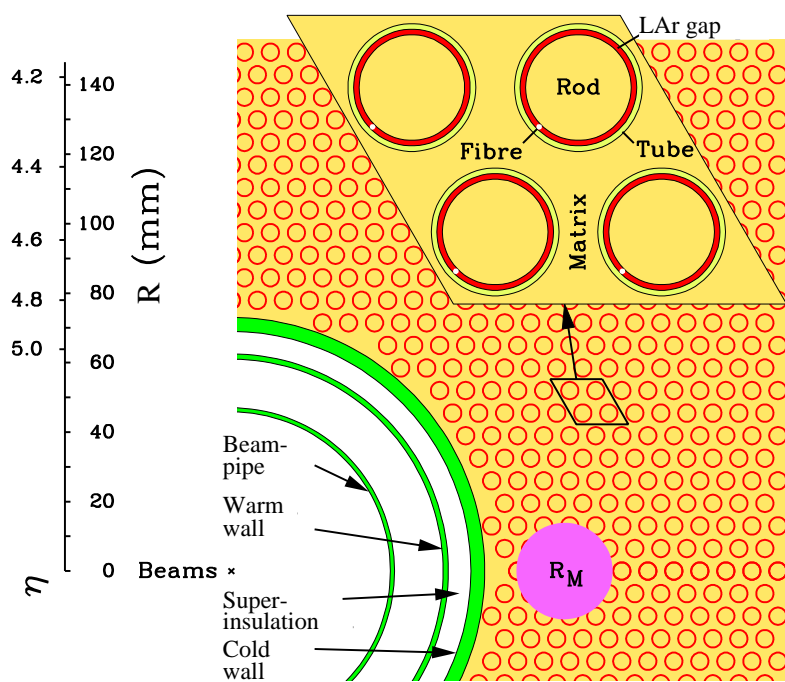


Figure 3.18: The sketch of the forward calorimeter's structure.  $R_M$  represent Moliere radius.

### 3.6.2 Muon system

High energy muons (above  $O(\text{GeV})$ ) hardly interact in materials and pass through the calorimeters with a small loss of energy. Hence momentum of muons can be measured in outer side of the calorimeters. Muon system of the ATLAS detector [88] consists of two precision measurement tracking chambers: Monitored Drift Tube chamber (MDT) and Cathode-Strip Chamber (CSC), and two trigger chambers: Resistive Plate Chambers (RPC) and Thin Gap Chambers (TGC) and toroid magnets (Figure 3.19).

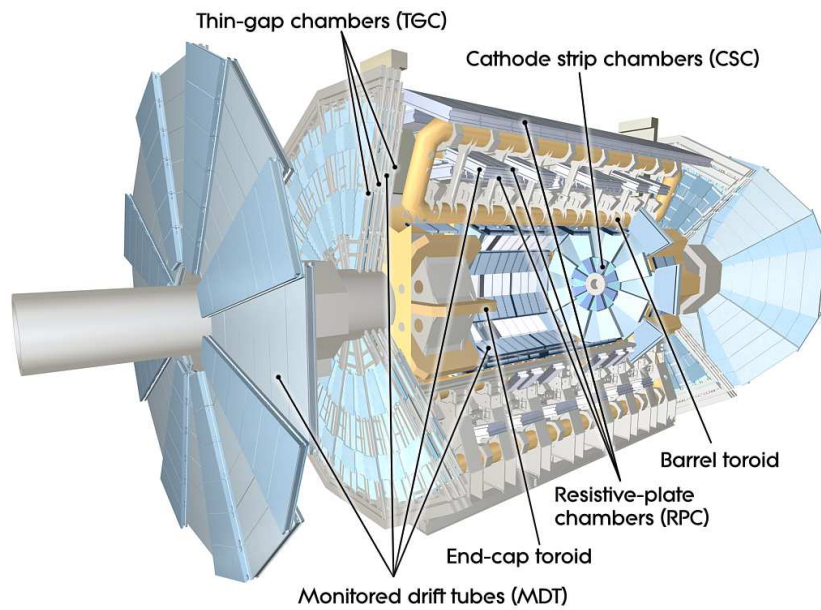


Figure 3.19: The overview of the ATLAS muon system

### 3.7 Luminosity Monitor

LUCID (LUMinosity measurement using Cherenkov integrating Detector) [89] is placed at  $\pm 17\text{ m}$  away from interaction point of the ATLAS detector. LUCID measures the inelastic proton-proton scattering in the forward direction to determine the integrated luminosity for the ATLAS detector. The detector consists of Cherenkov tubes. The tube is 1.5 m long and 15 mm diameter aluminum tube (Figure 3.20).

The tube is filled with  $\text{C}_4\text{F}_{10}$  gas at constant pressure of 1.1 bar.  $\text{C}_4\text{F}_{10}$  provides Cherenkov threshold of 10 MeV for electrons and 2.8 MeV for pions.

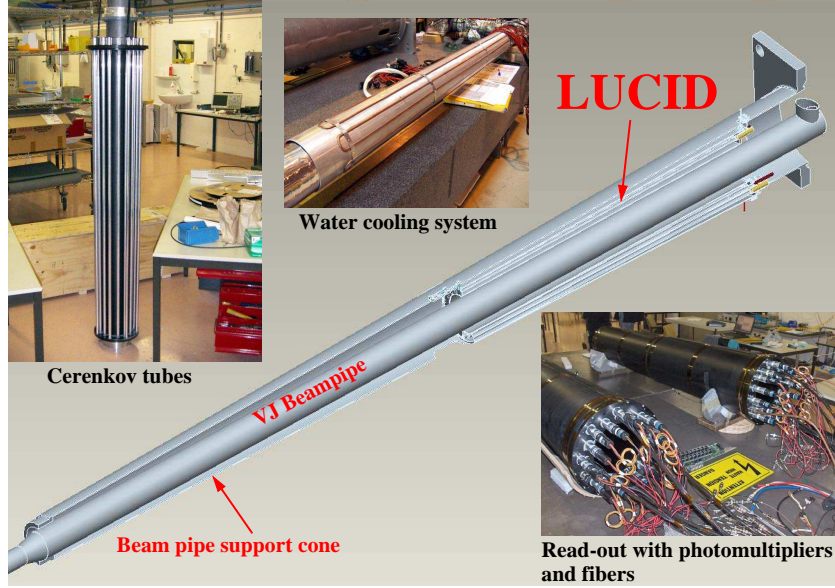


Figure 3.20: The LUCID detector

Each side has 20 tubes. The tubes are installed around the beam-pipe and pointed to the interaction point.

The calibration of the LUCID is done with Van der Meer (vdM) scans [90] which is sometimes called as beam-separation or luminosity scans. The scans are done as follows.

The luminosity  $\mathcal{L}$  is parameterized as

$$\mathcal{L} = n_b f_r I_1 I_2 \int \rho_1(x, y) \rho_2(x, y) dx dy, \quad (3.8)$$

where  $n_b$  is the number of colliding bunches,  $f_r$  is the machine revolution frequency,  $I_{1(2)}$  is the number of particles per bunch in beam 1 (2), and  $\rho_{1(2)}$  is the particle density in the transverse plane ( $x-y$ ) of the beam 1 (2) at the interaction point. The particle density is assumed that there is no correlation between  $x$  and  $y$ . Therefore, the particle density term can be divided into the terms of  $x$  and  $y$  as

$$\begin{aligned} \int \rho_1(x, y) \rho_2(x, y) dx dy &= \int \rho_1(x) \rho_2(x) dx \int \rho_1(y) \rho_2(y) dy \\ &= \Omega_x(\rho_1, \rho_2) \Omega_y(\rho_1, \rho_2), \end{aligned} \quad (3.9)$$

where  $\Omega_{x(y)}(\rho_1, \rho_2)$  is the beam overlap integral in the  $x$  ( $y$ ) direction. The

beam overlap integral is calculated as

$$\Omega_x(\rho_1, \rho_2) = \frac{R_x(0)}{\int R_x(h) dh}, \quad (3.10)$$

where  $R_x(h)$  is the rate measured by a beam monitor when the beam separation is  $h$  in  $x$  direction. This rate is scanned by changing  $h$ . The distribution of  $R_x(h)$  is fitted by a function of a double Gaussian and a flat background to estimate  $\int R_x(h) dh$ . A beam size is defined as

$$\sum_x \equiv \frac{1}{\sqrt{2\pi}} \frac{\int R_x(h) dh}{R_x(0)}. \quad (3.11)$$

With the beam size, the luminosity is rewritten as

$$\mathcal{L} = \frac{n_b f_r I_1 I_2}{2\pi \sum_x \sum_y}. \quad (3.12)$$

The main uncertainty for the luminosity measurement comes from beam intensities which are estimated by measuring the total charge in the bunches. This uncertainty is estimated as 10%. Another uncertainty comes from the growth of the transverse emittance. The uncertainty of 3% is estimated for the non-reproducibility of this growth effect. In total, the uncertainty of the luminosity measurement by the LUCID is estimated as 11.0% [91].

### 3.8 Trigger

The ATLAS detector has three distinct levels in trigger, Level-1 (L1), Level-2 (L2) and Event Filter (EF). The L1 trigger can use limited information of the detector and must make triggers within  $2.5 \mu\text{s}$  to reduce the rate at the L1 trigger less than 75 kHz. L2 and EF are called High Level Trigger (HLT) and they refine the lower level trigger decisions to reduce the final rate up to 200 Hz.

The L1 triggers are made if the calorimeters have more energy than the energy threshold in the reduced-granularity region or muon is identified by muon trigger chambers. They are collected to the Central Trigger Processor (CTP) (Figure 3.21). The combination of triggers or prescale is applied here. If the event passed the L1 trigger, it is passed to HLT. L1 trigger defines Regions-of-Interests (RoIs) which makes triggers and it is used in HLT.

In this thesis, non-prescaled single jet triggers are used. The data taking by single jet triggers have used only the L1 trigger information especially for the lowest non-prescaled single jet triggers in 2010. Following subsections describe the information about the overview of L1 calorimeter triggers and jet trigger in the L1 calorimeter trigger.

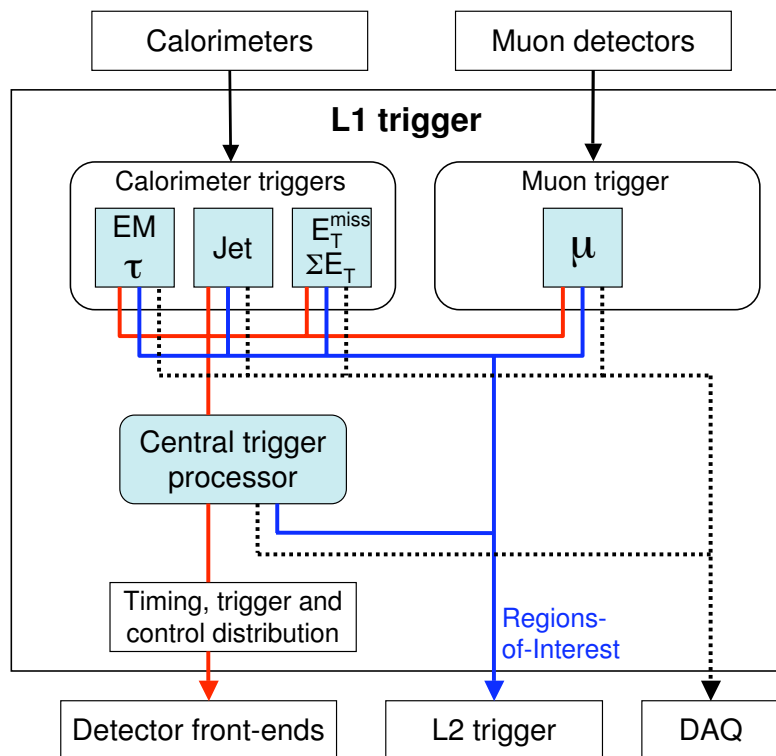


Figure 3.21: Flow of L1 trigger

### 3.8.1 L1 Calorimeter Trigger

The ATLAS Level-1 Calorimeter Trigger (L1Calo) [92] is made by the calorimeters. Seeds of the triggers are high  $p_T$  electron, photons,  $\tau$ -leptons, jets and  $E_T^{\text{miss}}$ . L1Calo uses 7000 analogue trigger towers of granularity of  $0.1 \times 0.1$  in most parts, and larger at the higher  $|\eta|$ . The signal reaches CTP about  $1.5 \mu\text{s}$  after the bunch-crossing. A total latency for the L1Calo chain is about  $2.1 \mu\text{s}$ .

The L1Calo system can be divided into the three sub-systems, the Pre-Processor Module (PPM), the Cluster Processor (CP) and the Jet Energy sum Processor (JEP). Figure 3.22 shows the architecture of the L1 calorimeter trigger. The PPM digitizes the analogue calorimeter trigger-tower signals. The signals are transmitted to the CP and the JEP. The CP is used for identification of electrons, photons and  $\tau$ -leptons. The JEP makes jet triggers, triggers of sum of  $E_T$  and missing transverse energy.

### 3.8.2 The Jet Trigger

The Jet Trigger [93] operates on jet elements which are made by summing over  $2 \times 2$  trigger towers corresponding to the granularity  $\phi = 0.2 \times 0.2$  in  $\Delta\eta \times \Delta\phi$ . All components of calorimeters in the towers are summed up. This trigger covers the region of  $|\eta|$  up to 3.2.

Jet trigger sums  $E_T$  in the window size of  $2 \times 2$ ,  $3 \times 3$  or  $4 \times 4$  jet elements, corresponding to the size of  $0.4 \times 0.4$ ,  $0.6 \times 0.6$  or  $0.8 \times 0.8$  in  $\Delta\eta \times \Delta\phi$  as shown in Figure 3.23.

The window is required to surround  $2 \times 2$  jet elements which has local maximum. This local maximum location is defined as the coordinate of the jet RoIs. The  $E_T$  for each window is calculated and compared with the predefined energy thresholds of jet triggers.

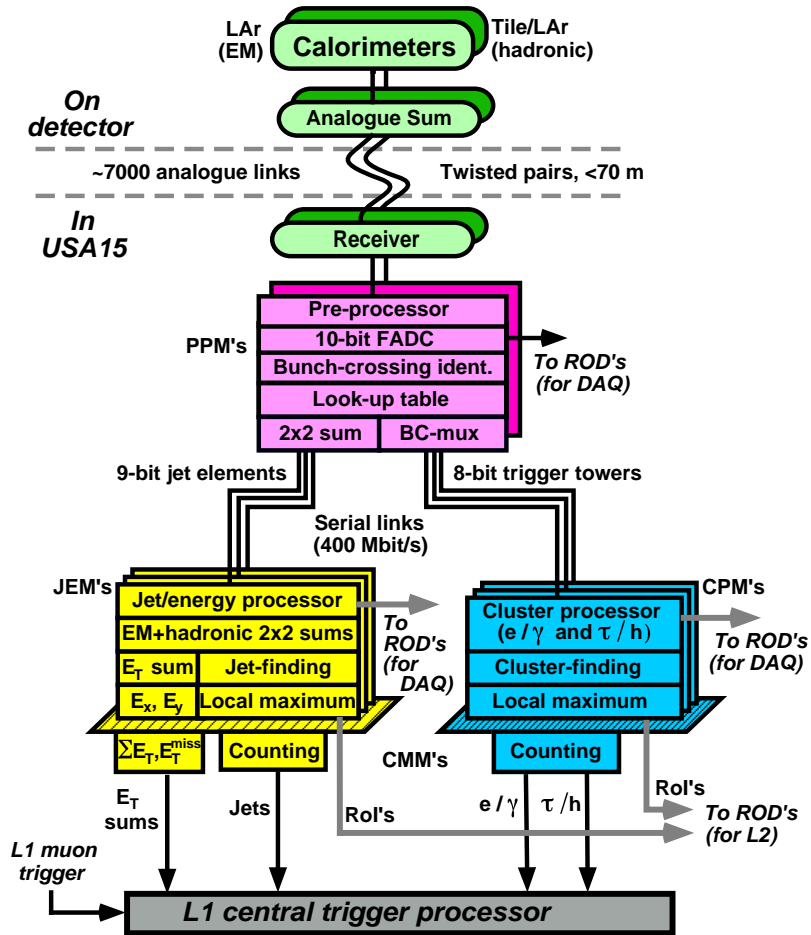


Figure 3.22: Architecture of the L1 calorimeter trigger

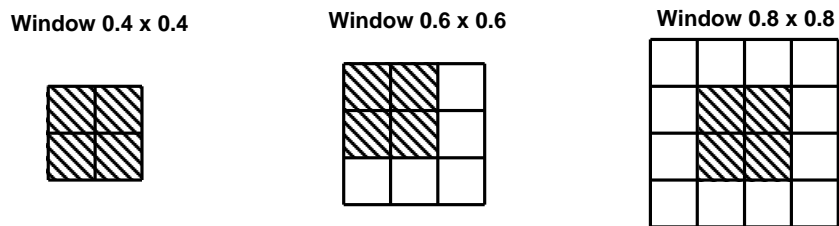


Figure 3.23: The illustration of the jet trigger algorithms based on jet elements of which size is  $0.2 \times 0.2$  in  $\Delta\eta \times \Delta\phi$ . Shaded regions represent RoIs. It can be seen that there are four possibilities of windows in  $0.6 \times 0.6$  case.

# Chapter 4

## Monte Carlo Simulation

### 4.1 ATLAS Simulation

The simulation for ATLAS is implemented to the framework called Athena [94]. It is also used for the real data reconstruction.

The flow of the simulation and reconstruction is illustrated in Figure 4.1. Physics events are produced by event generators. Several generators are used

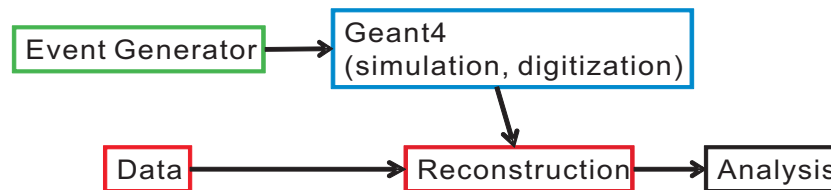


Figure 4.1: ATLAS simulation

depending on the physics processes. The detector simulation is performed with the GEANT4 simulation [95, 96]. Finally, reconstruction algorithms are applied.

The following sections summarize the event generators which are used for this thesis.

### 4.2 BlackMax, A Generator for the Mini Black Hole Events

BlackMax [54, 69] is used to generate the mini black hole events in this thesis. BlackMax provides the events up to the decay of the mini black hole.

The shower evolution and hadronization are simulated with PYTHIA which is described in Section 4.4.1. A version used in this thesis is BlackMax 2.01.3.

The parameter settings of the model used in this thesis are follows:

- The definition of Planck Scale follows the PDG definition [33](See Subsection 2.4.2)
- CTEQ66 [97] is used for the PDFs
- Both baryon number and lepton number are conserved through the mini black hole production and decay.
- Graviton is not emitted.
- Burst model is employed for the Planck Phase.
- The number of extra dimension is varied from 2 to 7.
- The Planck scale is set as  $M_D = 0.8 \text{ TeV} - 2.0 \text{ TeV}$ .
- The mass threshold is calculated on assumption of  $\lambda < r_s$  and  $\lambda < r_h$ .

All parameters which are used for this thesis can be found in Appendix A.

Table 4.1 (4.2) gives the MC data sets of signals for which  $M_{\text{BHth}}$  is calculated with Eq. 2.41 (2.42).

### 4.3 Characteristics of Mini Black Hole Events

In this section, the characteristics of mini black hole events produced with BlackMax are described. The following signal points in Table 4.1 are used as benchmark in this section:

- rs.2\_1000 ( $n = 2$ ,  $M_D = 1000 \text{ GeV}$ ,  $M_{\text{BHth}} = 4266 \text{ GeV}$ )
- rs.4\_1000 ( $n = 4$ ,  $M_D = 1000 \text{ GeV}$ ,  $M_{\text{BHth}} = 2923 \text{ GeV}$ )
- rs.7\_1000 ( $n = 7$ ,  $M_D = 1000 \text{ GeV}$ ,  $M_{\text{BHth}} = 2078 \text{ GeV}$ )
- rs.4\_1200 ( $n = 4$ ,  $M_D = 1200 \text{ GeV}$ ,  $M_{\text{BHth}} = 3507 \text{ GeV}$ )

where first column, “rs”, represents the assumption of  $M_{\text{BHth}}$  based on the Schwarzschild radius in Eq. 2.41. Second and third columns represent the number of extra dimension and the Planck scale, respectively.

The mass spectra of the mini black holes produced with BlackMax generator are shown in Figure 4.2 for four different points. The mini black

Table 4.1: Mini Black Hole signal MC samples on the assumption  $\lambda < r_s$ . First column, “rs”, represents the assumption of  $M_{\text{BHth}}$  based on the Schwarzschild radius. Second and third columns represent the number of extra dimension and the Planck scale, respectively. PDFs of CTEQ66 are used for these samples. Other common settings are seen in Appendix A.

Signal point	Parameters	Cross section [pb]
rs_2_800	$n = 2, M_D = 800 \text{ GeV}, M_{\text{BHth}} = 3412 \text{ GeV}$	4.40
rs_2_1000	$n = 2, M_D = 1000 \text{ GeV}, M_{\text{BHth}} = 4266 \text{ GeV}$	$1.02 \times 10^{-1}$
rs_2_1200	$n = 2, M_D = 1200 \text{ GeV}, M_{\text{BHth}} = 5117 \text{ GeV}$	$1.02 \times 10^{-3}$
rs_3_800	$n = 3, M_D = 800 \text{ GeV}, M_{\text{BHth}} = 2758 \text{ GeV}$	$5.76 \times 10^1$
rs_3_1000	$n = 3, M_D = 1000 \text{ GeV}, M_{\text{BHth}} = 3448 \text{ GeV}$	3.72
rs_3_1200	$n = 3, M_D = 1200 \text{ GeV}, M_{\text{BHth}} = 4137 \text{ GeV}$	$1.88 \times 10^{-1}$
rs_3_1500	$n = 3, M_D = 1500 \text{ GeV}, M_{\text{BHth}} = 5171 \text{ GeV}$	$7.34 \times 10^{-4}$
rs_4_800	$n = 4, M_D = 800 \text{ GeV}, M_{\text{BHth}} = 2338 \text{ GeV}$	$2.89 \times 10^2$
rs_4_1000	$n = 4, M_D = 1000 \text{ GeV}, M_{\text{BHth}} = 2923 \text{ GeV}$	29.9
rs_4_1200	$n = 4, M_D = 1200 \text{ GeV}, M_{\text{BHth}} = 3507 \text{ GeV}$	2.89
rs_4_1500	$n = 4, M_D = 1500 \text{ GeV}, M_{\text{BHth}} = 4384 \text{ GeV}$	$5.74 \times 10^{-2}$
rs_4_2000	$n = 4, M_D = 2000 \text{ GeV}, M_{\text{BHth}} = 5845 \text{ GeV}$	$4.37 \times 10^{-6}$
rs_5_800	$n = 5, M_D = 800 \text{ GeV}, M_{\text{BHth}} = 2045 \text{ GeV}$	$9.02 \times 10^2$
rs_5_1000	$n = 5, M_D = 1000 \text{ GeV}, M_{\text{BHth}} = 2557 \text{ GeV}$	$1.24 \times 10^2$
rs_5_1200	$n = 5, M_D = 1200 \text{ GeV}, M_{\text{BHth}} = 3068 \text{ GeV}$	$1.68 \times 10^1$
rs_5_1500	$n = 5, M_D = 1500 \text{ GeV}, M_{\text{BHth}} = 3835 \text{ GeV}$	$7.29 \times 10^{-1}$
rs_5_2000	$n = 5, M_D = 2000 \text{ GeV}, M_{\text{BHth}} = 5113 \text{ GeV}$	$1.05 \times 10^{-3}$
rs_6_800	$n = 6, M_D = 800 \text{ GeV}, M_{\text{BHth}} = 1829 \text{ GeV}$	$2.17 \times 10^3$
rs_6_1000	$n = 6, M_D = 1000 \text{ GeV}, M_{\text{BHth}} = 2286 \text{ GeV}$	$3.51 \times 10^2$
rs_6_1200	$n = 6, M_D = 1200 \text{ GeV}, M_{\text{BHth}} = 2743 \text{ GeV}$	$5.97 \times 10^1$
rs_6_1500	$n = 6, M_D = 1500 \text{ GeV}, M_{\text{BHth}} = 3429 \text{ GeV}$	3.96
rs_6_2000	$n = 6, M_D = 2000 \text{ GeV}, M_{\text{BHth}} = 4572 \text{ GeV}$	$2.23 \times 10^{-2}$
rs_7_800	$n = 7, M_D = 800 \text{ GeV}, M_{\text{BHth}} = 1662 \text{ GeV}$	$4.30 \times 10^3$
rs_7_1000	$n = 7, M_D = 1000 \text{ GeV}, M_{\text{BHth}} = 2078 \text{ GeV}$	$7.81 \times 10^2$
rs_7_1200	$n = 7, M_D = 1200 \text{ GeV}, M_{\text{BHth}} = 2493 \text{ GeV}$	$1.55 \times 10^2$
rs_7_1500	$n = 7, M_D = 1500 \text{ GeV}, M_{\text{BHth}} = 3116 \text{ GeV}$	$1.40 \times 10^1$
rs_7_2000	$n = 7, M_D = 2000 \text{ GeV}, M_{\text{BHth}} = 4155 \text{ GeV}$	$1.71 \times 10^{-1}$

Table 4.2: Mini Black Hole signal MC samples on the assumption  $\lambda < r_h$ . First column, “rh”, represents the assumption of  $M_{\text{BHth}}$  based on horizon radius. Second and third columns represent the number of extra dimension and the Planck scale, respectively. PDFs of CTEQ66 is used for these samples. Other common settings are seen in Appendix A.

Signal point	parameters	Cross section [pb]
rh_2_800	$n = 2, M_D = 800 \text{ GeV}, M_{\text{BHth}} = 5102 \text{ GeV}$	$3.27 \times 10^{-3}$
rh_3_800	$n = 3, M_D = 800 \text{ GeV}, M_{\text{BHth}} = 4099 \text{ GeV}$	$6.03 \times 10^{-1}$
rh_3_1000	$n = 3, M_D = 1000 \text{ GeV}, M_{\text{BHth}} = 5124 \text{ GeV}$	$2.66 \times 10^{-3}$
rh_4_800	$n = 4, M_D = 800 \text{ GeV}, M_{\text{BHth}} = 3432 \text{ GeV}$	9.88
rh_4_1000	$n = 4, M_D = 1000 \text{ GeV}, M_{\text{BHth}} = 4290 \text{ GeV}$	$2.27 \times 10^{-1}$
rh_4_1200	$n = 4, M_D = 1200 \text{ GeV}, M_{\text{BHth}} = 5148 \text{ GeV}$	$2.11 \times 10^{-3}$
rh_5_800	$n = 5, M_D = 800 \text{ GeV}, M_{\text{BHth}} = 2959 \text{ GeV}$	61.1
rh_5_1000	$n = 5, M_D = 1000 \text{ GeV}, M_{\text{BHth}} = 3698 \text{ GeV}$	3.09
rh_5_1200	$n = 5, M_D = 1200 \text{ GeV}, M_{\text{BHth}} = 4438 \text{ GeV}$	$1.04 \times 10^{-1}$
rh_5_1500	$n = 5, M_D = 1500 \text{ GeV}, M_{\text{BHth}} = 5547 \text{ GeV}$	$1.26 \times 10^{-4}$
rh_6_800	$n = 6, M_D = 800 \text{ GeV}, M_{\text{BHth}} = 2606 \text{ GeV}$	$2.28 \times 10^2$
rh_6_1000	$n = 6, M_D = 1000 \text{ GeV}, M_{\text{BHth}} = 3258 \text{ GeV}$	18.0
rh_6_1200	$n = 6, M_D = 1200 \text{ GeV}, M_{\text{BHth}} = 3909 \text{ GeV}$	1.18
rh_6_1500	$n = 6, M_D = 1500 \text{ GeV}, M_{\text{BHth}} = 4886 \text{ GeV}$	$9.14 \times 10^{-3}$
rh_7_800	$n = 7, M_D = 800 \text{ GeV}, M_{\text{BHth}} = 2334 \text{ GeV}$	$6.18 \times 10^2$
rh_7_1000	$n = 7, M_D = 1000 \text{ GeV}, M_{\text{BHth}} = 2918 \text{ GeV}$	65.4
rh_7_1200	$n = 7, M_D = 1200 \text{ GeV}, M_{\text{BHth}} = 3501 \text{ GeV}$	6.41
rh_7_1500	$n = 7, M_D = 1500 \text{ GeV}, M_{\text{BHth}} = 4377 \text{ GeV}$	$1.27 \times 10^{-1}$
rh_7_2000	$n = 7, M_D = 2000 \text{ GeV}, M_{\text{BHth}} = 5835 \text{ GeV}$	$1.03 \times 10^{-5}$

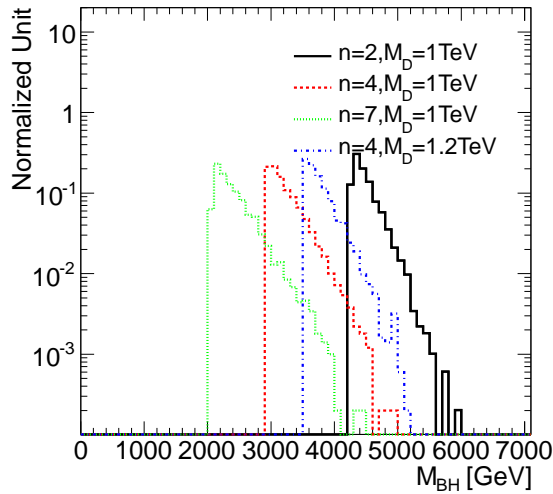


Figure 4.2: Mass spectra of the mini black holes produced with BlackMax for four different points. All the distributions are normalized to a unit area.

hole signal events have sharp cut-off due to the production threshold and a continuous spectrum to higher mass region.

Figure 4.3 shows a number of particles emitted by the mini black hole. Generally, the mini black hole emits a very large number of particles. The point with a smaller number of dimensions shows the higher number of particles mainly because the smaller number of dimensions makes the higher  $M_{\text{BHth}}$  which results in a larger fraction of high mass black holes. On the other hand, the signal rs\_4\_1200 ( $M_{\text{BHth}} = 3.50$  TeV) shows the almost same number of particles as rs\_4\_1000 ( $M_{\text{BHth}} = 2.92$  TeV) even though the former case has a higher mass. This is because the higher Planck scale makes the Hawking temperature higher as shown in Figure 2.10, that leads to a higher energy particles emitted by the black hole. Consequently, the total number of emitted particles becomes smaller and the two effects are cancelled out.

The relative composition of emitted particles is shown in Figure 4.4. The horizontal axis represents particle numbers called PDG id [32], which is summarized in Table 4.3. In principle, they are emitted by the Hawking radiation and the rate depends on the degrees of freedom of each type. The unbalances between the quarks and anti-quarks or between the up-type and down-type quark comes from the conservation of the electric charge.

The signal rs\_2\_1000 shows more uniformity than others because it produces more particles that tend to wash out the effect. The signal rs\_7\_1000

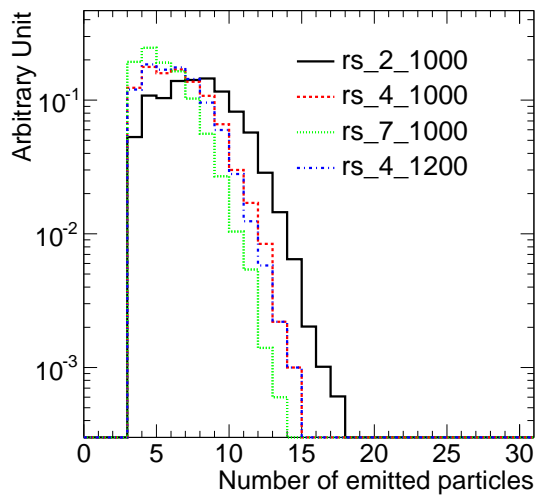


Figure 4.3: Number of particles emitted by a mini black hole for four different points. All the distributions are normalized to a unit area.

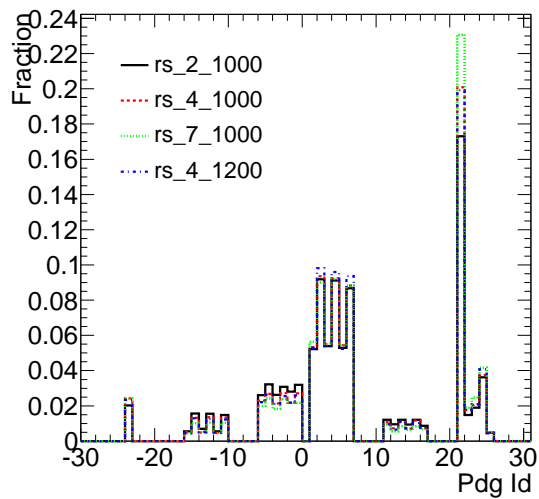


Figure 4.4: PDG id distribution in the decay particles from the mini black hole for four different points. All the distributions are normalized to a unit area.

Table 4.3: PGD ids for each particle. Anti-particles are assigned negative PDG ids corresponding to the particles.

Quarks						
Particle	$d$	$u$	$s$	$c$	$b$	$t$
PDG id	1	2	3	4	5	6
Leptons						
Particle	$e^-$	$\mu^-$	$\tau^-$	$\nu_e$	$\nu_\mu$	$\nu_\tau$
PDG id	11	12	13	14	15	16
Gauge Bosons						
Particle	$g$	$\gamma$	$Z$	$W^+$	$h$	
PDG id	21	22	23	24	25	

has the largest gluon fraction. This behavior can be explained by considering that this signal has a smaller black hole mass (see Figure 4.2) and hence more easily produced by collisions of low- $x$  partons in the proton. Therefore, more gluons can participate in the hard process compared to, e.g., the signal of rs\_4\_1000, which has a similar number of decay particles but a higher mass. In general, quarks and gluons have a dominant contribution. Therefore, the mini black hole events are dominated by multijet events.

The number of jets and transverse momentum spectra of all jets in the mini black hole events are shown in Figure 4.5. The signal rs\_4\_1200 shows a harder spectrum than others except rs\_2\_1000 and the lower  $n$  shows the higher energies. This is because the lower  $n$  leads to the higher temperature especially for  $M_D \sim M_{\text{BH}}$  case as Figure 2.10. The very hard spectrum of rs\_2\_1000 comes from its highest  $M_{\text{BHth}}$ .

Figure 4.6-4.8 show the  $p_T$  distributions of the first five highest  $p_T$  jets in the black hole event. For all signal points, the leading jets have a very high  $p_T$  about 500 GeV - 1 TeV. The mini black hole events have a few hundreds GeV even for the fifth leading jet  $p_T$ .

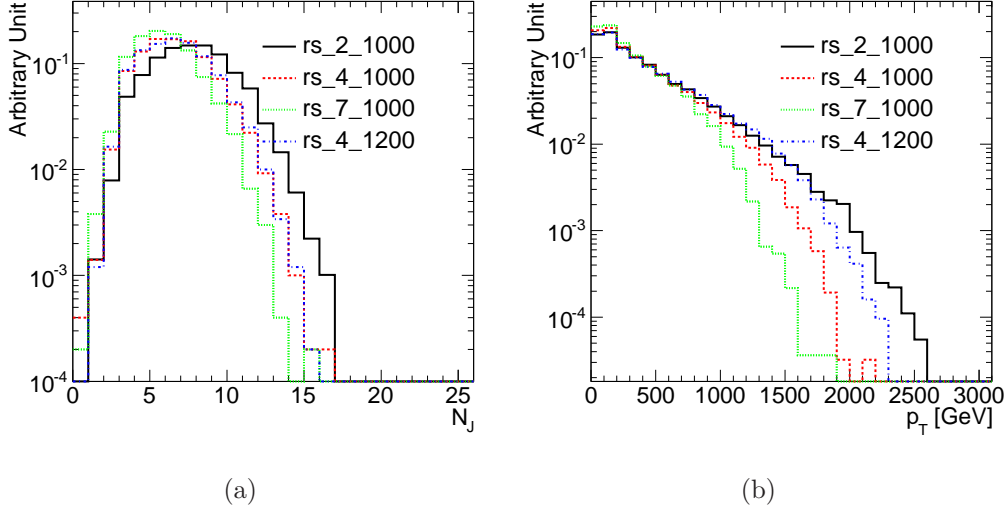


Figure 4.5: The number of jets (a) and transverse momentum spectra of all jets (b) in the black hole event for four different points. All the distributions are normalized to a unit area.

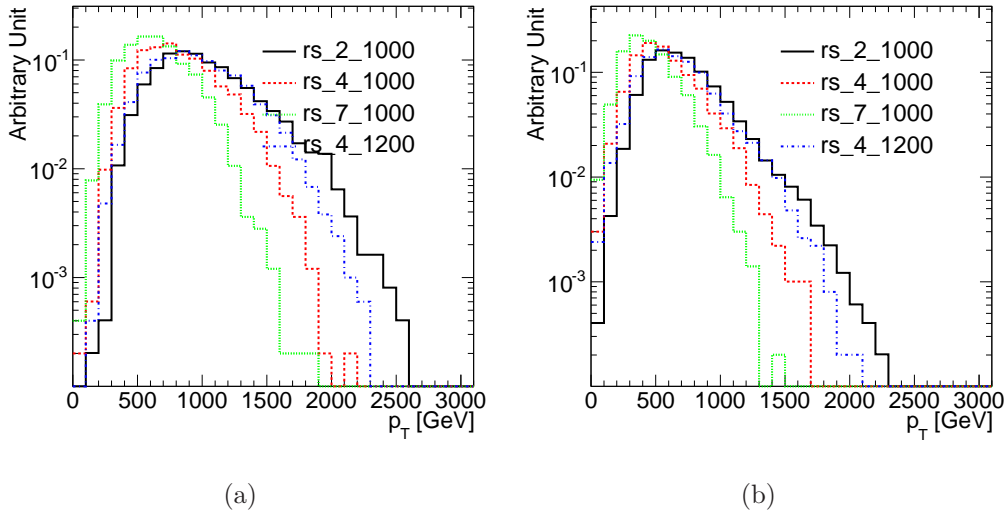


Figure 4.6: Transverse momentum spectra of the leading jets (a) and the second leading jet (b) in the black hole event for four different points. All the distributions are normalized to a unit area.

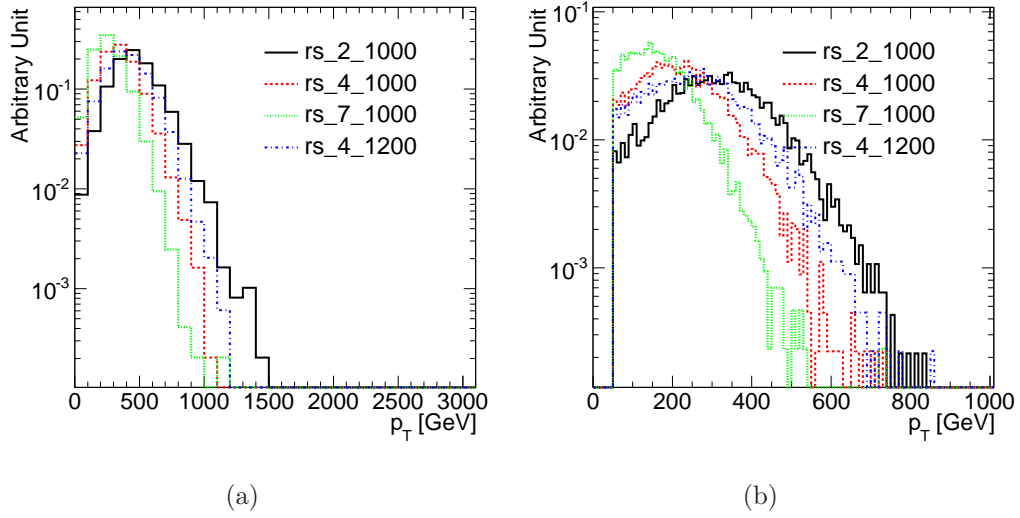


Figure 4.7: Transverse momentum spectra of the third leading jets (a) and the fourth leading jet (b) in the black hole event for four different points. All the distributions are normalized to a unit area.

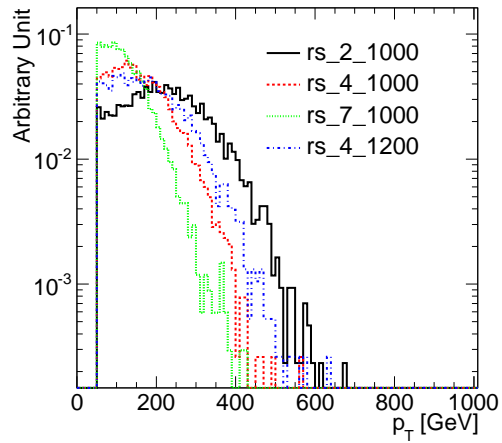


Figure 4.8: Transverse momentum spectra of the fifth leading jets in the black hole event for four different points. All the distributions are normalized to a unit area.

## 4.4 Generators for Background Events

This section summarizes event generators used to simulate Standard Model background processes. The characteristics of background events are described in Chapter 7.

### 4.4.1 PYTHIA

PYTHIA [98] is the leading order event generator widely used in particle physics. It can generate about 240 different hard processes which are calculated with the leading order matrix element (ME) derived from Feynman diagrams. Higher order QCD processes are reproduced by the parton shower which is based on the leading log approximation. PYTHIA adopts the string hadronization model [99, 100, 101, 102]. PYTHIA 6.421 is used in this work. The main QCD and minimum bias samples are produced by PYTHIA. The proton parton density functions (PDFs) are provided by LHAPDF [103], and the PYTHIA samples used in this analysis are generated with modified leading order MRST2007 [104].

### 4.4.2 HERWIG and JIMMY

HERWIG [105] is the leading order generator adopting the cluster model [106] for the hadronization. JIMMY [107] is the generator which can generate multiple parton scattering events. Versions used in this thesis are HERWIG 6.510 and JIMMY 4.1. The HERWIG 6.510 and JIMMY 4.1 are used to generate  $Z/W + \text{jets}$  events as well as for the parton shower and hadronization in events produced by ALPGEN [108] and MC@NLO [109, 110] generators. The LO PDF CTEQ6L1 [111] has been used in the HERWIG event generation.

### 4.4.3 ALPGEN

ALPGEN [108] is the tree level ME calculator for multi parton final states. It uses the exact leading order ME for the calculation. ALPGEN version 2.13 is used in this thesis. One of the QCD background samples is made with ALPGEN for systematic uncertainty studies. ALPGEN generates hard process events and parton shower evolution and hadronization are governed by HERWIG. This two-step event generation causes a double counting of events with multi partons in the final state, due to additional partons produced by HERWIG parton shower processes. These double countings are removed by the MLM matching method [112]. The MLM matching uses jets made from final-state particles. Partons generated by ALPGEN and jets are then

matched based on their distance  $\Delta R$  in  $\eta - \phi$  plane. If all partons made by ALPGEN match jets in  $\Delta R$  and there are no jets left over which do not match partons of ALPGEN, the event is accepted. Otherwise, the event is rejected.

ALPGEN sample adopts PDFs of CTEQ6L1.

#### 4.4.4 MC@NLO

MC@NLO [109, 110] is the next to the leading order (NLO) generator. MC@NLO 3.41 is used in this thesis. It was used for  $t\bar{t}$  MC sample production. MC@NLO sample adopts PDFs of CTEQ66.

#### 4.4.5 Tuning for Underlying Events and Minimum Bias Events

The parameters in PYTHIA and HERWIG (JIMMY) are tuned inside ATLAS to reproduce the underlying event and minimum bias event data publicly available [113]. The main parameters used in the tuning for PYTHIA are:

- A cut-off scale in multi interaction,
- Rescale exponent of multi interaction cut-off,
- A size of the matter fraction,
- A amount of color reconnection in the final state,
- A probability of the color partons which are kicked out for the beam remnant,
- A running  $\alpha_S$  value for the parton showers.

The main parameters of the tuning for HERWIG (JIMMY) are:

- A minimum  $p_T$  in hadronic jet production,
- A minimum transverse momentum of secondary scatters,
- An inverse proton radius squared,
- A probability of a soft underlying event.

The tuning is done with the data sets of underlying events and minimum bias events, which are published by the Tevatron experiments. One parameter is varied at a time and the parameter which has most impact on the observable under the study is identified. This procedure is repeated until the result shows agreement with the data sets.

#### 4.4.6 Summary of Standard Model MC samples

Table 4.4 summarizes event generators and the cross sections of the Standard Model background processes considered in this analysis.

Table 4.4: Event generators and cross sections of each process. The  $p_T$  cut represent the cut on the leading parton  $p_T$ .

Process	Event Generator	Cross Section [pb]
QCD ( $p_T > 8$ GeV)	PYTHIA	$1.06 \times 10^{10}$
QCD ( $p_T > 15$ GeV)	ALPGEN	$3.14 \times 10^8$
$t\bar{t}$	MC@NLO	$1.65 \times 10^2$
$Z$ +jets ( $p_T > 250$ GeV)	HERWIG	3.90
$W$ +jets ( $p_T > 250$ GeV)	HERWIG	9.21
Minimum Bias	PYTHIA	$5.84 \times 10^{10}$

# Chapter 5

## Jet Reconstruction

This chapter describes the jet reconstruction algorithm and energy calibration procedures for the offline analysis employed in the black hole search.

The jet reconstruction is performed by the following steps;

1. Clustering of calorimeter cells to build inputs for jets,
2. Running jet identification algorithm,
3. Calibration to hadronic energy scale.

Figure 5.1 shows an overview of jet reconstruction in ATLAS. The detailed descriptions of each step are given in the following sections.

### 5.1 Clustering of calorimeter cells

While a wide variety of inputs can be used in the ATLAS jet reconstruction, calorimeter clusters dynamically built by using a three-dimensional clustering algorithm, called “topological clustering” [114], are used in this thesis. The topological clustering classifies the calorimeter cells as “seeds”, “neighbors”, and “others” based on the significance of their energy deposits with respect to electronic noise in the calorimeters.

- First, calorimeter cells with  $|E_{\text{cell}}| > 4\sigma_{\text{noise}}$  are defined as “seeds”, where  $E_{\text{cell}}$  is the measured energy in the calorimeter cell, and  $\sigma_{\text{noise}}$  is the RMS of the cell energy distributions taken from random events.
- Second, “neighbor” cells with  $|E_{\text{cell}}| > 2\sigma_{\text{noise}}$ , adjacent to the seeds, are added to form clusters.

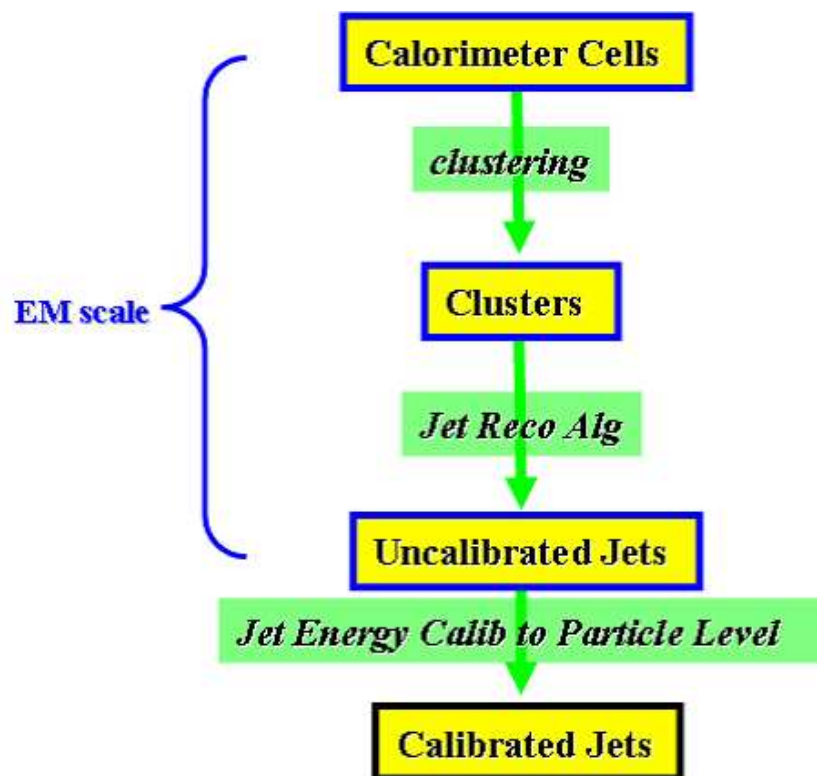


Figure 5.1: Overview of jet reconstruction in ATLAS

- In a final step, all cells surrounding the neighbors are added to the clusters.

Figure 5.2 is the illustration of topological clustering performed on the grid of calorimeter cells.

Finally, in order to separate clusters associated with different incident particles, but overlapping in the calorimeter due to shower development, the reconstructed clusters are processed by the split algorithm based on the position of local maxima and minima within the clusters. The splitting algorithm works by

- Finding the local maxima, which is a cell in the cluster with  $p_T$  of at least 500 MeV and higher than the  $p_T$  of neighbors. The number of neighbor cells is required to be larger than 3.
- Forming new clusters by adding cells around the local maxima.

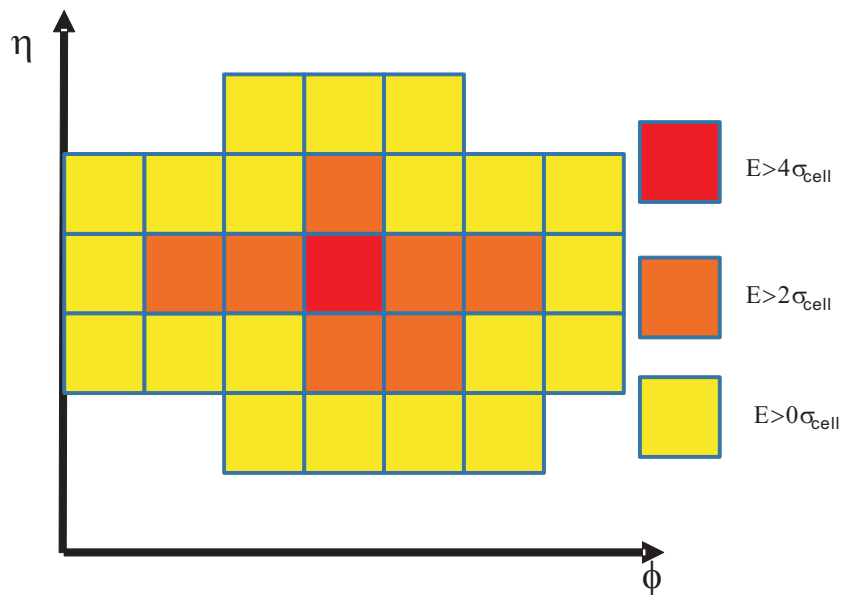


Figure 5.2: The illustration of topological clustering

The energies of clusters are calibrated based on the test-beam measurements for electrons and muons [115, 116, 117]. Therefore, the clusters are calibrated to the EM scale. The calorimeter response for the hadron interaction is different from the EM interaction due to non-compensating nature of the calorimeter and non-uniform response over different rapidity coverage. Hence, this energy should be calibrated into the hadronic scale. This calibration is done after jet finding as described in the following section.

## 5.2 Jet Finding Algorithm

Anti-Kt algorithm [116] is adopted for the jet reconstruction with the topological clusters as inputs. The algorithm uses following variables:

$$\begin{aligned} d_{ii} &= p_{Ti}^{-2}, \\ d_{ij} &= \min(p_{Ti}^{-2}, p_{Tj}^{-2}) \times \frac{\Delta R_{ij}^2}{D^2}, \\ d_{min} &= \min(d_{ii}, d_{ij}), \end{aligned}$$

where  $p_{Ti(j)}$  is transverse momentum of  $i$  ( $j$ )-th cluster and  $\Delta R_{ij}$  is the distance between  $i$ -th and  $j$ -th clusters. Different values of  $D$  result in different size of jets and  $D = 0.4$  is used in this thesis. All combinations of clusters are computed from the highest  $p_T$  cluster. If  $d_{min} = d_{ij}$ ,  $i$ - and  $j$ -th clusters are combined and defined as new cluster. In case of  $d_{min} = d_{ii}$ , it is defined as a jet and removed from the cluster list. Once it is done for the all clusters, the algorithm is applied for the cluster list repeatedly until the list becomes empty.

For comparison, a cone algorithm is introduced below. The cone algorithm sorts the clusters in decreasing order in  $p_T$ . The highest cluster is defined as “seed cluster” and makes proto-jets from clusters within a cone  $\Delta R < 0.4$  around the “seed cluster”. This procedure is re-applied on the clusters except for the clusters which are used for proto-jets. A centroid of the proto-jet is calculated from the  $E_T$  weighted position of clusters in the proto-jet. With this centroid, new proto-jets are constructed from the clusters within a cone  $\Delta R < 0.4$  around the centroid. This procedure is repeated until these proto-jets are stable. Finally, if two jets are overlapped, energies are divided based on the distance from the center of the jets. If overlap energy is greater than half of total energy of two jets, they are merged.

The two clustering algorithm are known to have different sensitivity to collinear and infrared safety, and hence produce different list of jets when those additional radiations are present in the events. Figure 5.3 shows the illustration of Anti-Kt and cone algorithms in the case of two hard partons accompanied by an additional parton in the middle. When the middle parton splits into two softer collinear partons, the Anti-Kt algorithm still finds the same jet while the cone algorithm may find more jets due to different seeding algorithms.

Figure 5.4 shows the illustration of Anti-Kt algorithm and the cone algorithm for an infrared radiation. The infrared radiation between two partons is considered. Cone algorithm would find new centroid by the effect of the infrared radiation and would change the number of jets.

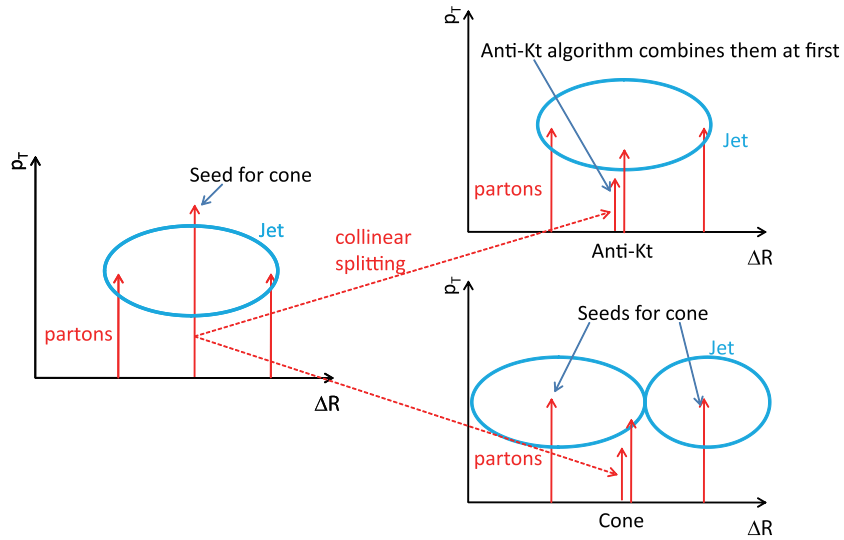


Figure 5.3: Sketch of Cone v.s. Anti-Kt algorithm. In the left picture, both algorithms collect three partons. In the right two figures, the parton in the middle is split into two partons by a collinear splitting. A number of jets by Anti-Kt algorithm is not changed while that of the cone algorithm is changed.

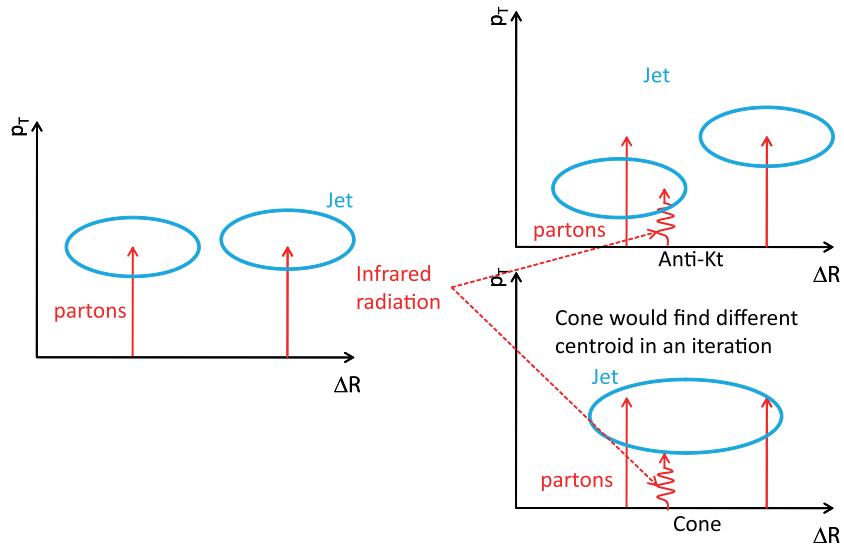


Figure 5.4: Sketch of Cone v.s. Anti-Kt algorithm. In the left picture, both algorithms make two jets. In the right two figures, the infrared radiation between two partons is considered. Cone algorithm finds new centroid and makes only one jet.

These effects are changed by the higher order calculation. Therefore, Anti-Kt algorithms allows more robust comparison with theory predictions because it is stable in the presence of collinear splitting and infrared radiation.

### 5.3 Hadronic Calibration

Jets reconstructed from calorimeter clusters found at the electromagnetic scale are subject to hadronic energy scale calibration because of several detector effects such as lower calorimeter response for hadronic than the electromagnetic particles due to non-compensating calorimeters, energy loss in inactive detector regions, etc.

The current ATLAS jet calibration is based on jet response measured in the MC simulation. This calibration uses truth jets, which is reconstructed from stable particles with the lifetime less than 10 ps, generated by the MC generator. The calibration factor is estimated by comparing reconstructed jet energy (at EM scale,  $E^{\text{EM}}$ ) with the truth jet energy,  $E^{\text{true}}$  in bins of truth jet  $p_{\text{T}}$ ,  $p_{\text{T}}^{\text{true}}$ , and reconstructed jet  $\eta$ . An observable is reconstructed jet  $p_{\text{T}}$  at EM scale,  $p_{\text{T}}^{\text{EM}}$ , instead of  $E^{\text{true}}$ . Therefore, the calibration factor should be rewritten as a function of  $p_{\text{T}}^{\text{EM}}$ .

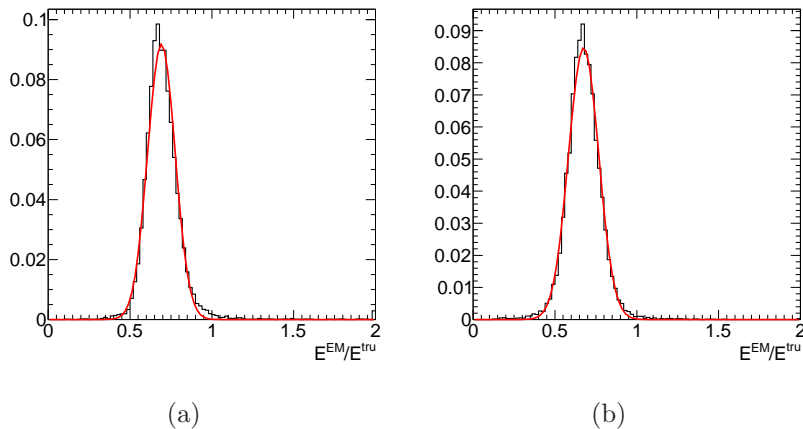


Figure 5.5: Distributions for energy ratios of  $E^{\text{EM}}$  to  $E^{\text{true}}$  for the range of  $56 \text{ GeV} < p_{\text{T}}^{\text{EM}} < 60 \text{ GeV}$  (a) and  $80 \text{ GeV} < p_{\text{T}}^{\text{true}} < 85 \text{ GeV}$  (b). An energy scale of jets at the EM scale is about 0.7 times of energy scale of truth jets. Therefore, the range for  $p_{\text{T}}^{\text{EM}}$  is defined lower to use same  $p_{\text{T}}$  region of truth jets.

Figure 5.5(a) and 5.5(b) show energy ratios of the EM scale jet to the

truth jet for the range of  $56 \text{ GeV} < p_{\text{T}}^{\text{EM}} < 60 \text{ GeV}$  and  $80 \text{ GeV} < p_{\text{T}}^{\text{true}} < 85 \text{ GeV}$ , respectively. Both distributions are fitted by a Gaussian function. The distribution of  $E^{\text{EM}}/E^{\text{true}}$  in the fixed  $p_{\text{T}}^{\text{EM}}$  bin is not a Gaussian shape because there are more contributions from the events in low  $p_{\text{T}}^{\text{true}}$  than events in high  $p_{\text{T}}^{\text{true}}$  due to falling jet  $p_{\text{T}}$  spectrum and detector resolution effects. The same distribution in the fixed  $p_{\text{T}}^{\text{true}}$  bin shows better agreement with a Gaussian shape. The width of the distribution corresponds to a jet resolution. Taking this into consideration, a following procedure is adopted to obtain the calibration function.

First, the pair of the reconstructed jet and the truth jet which satisfies the following conditions is selected:

- $\Delta R_{\text{EMtrue}} < 0.3$ , where  $\Delta R_{\text{EMtrue}}$  is a distance between the jets of a pair.
- There are no jets with  $p_{\text{T}} > 7 \text{ GeV}$  within  $\Delta R = 2.5 \times R$  around each jet, where  $R$  is the size of the jet.

Second, the calibration factor is obtained as follows:

- Dividing the pairs in bins of  $p_{\text{T}}^{\text{true}}$ .
- Fitting  $p_{\text{T}}^{\text{EM}}$  distributions in each bin by a Gaussian and obtaining the means,  $\langle p_{\text{T}}^{\text{EM}} \rangle$  for each bin.
- Fitting  $\langle E^{\text{EM}} \rangle / E^{\text{true}}$  with a function,  $R(p_{\text{T}}^{\text{true}})$ :

$$R(p_{\text{T}}^{\text{true}}) = \sum_{i=0}^4 \frac{a_i}{\ln(p_{\text{T}}^{\text{true}})^i}, \quad (5.1)$$

where  $a_0 = 1$  and other  $a_i$  are free parameters.

- Refitting the  $\langle E^{\text{EM}} \rangle / E^{\text{true}}$  with  $p_{\text{T,est}}^{\text{EM}} \equiv R(p_{\text{T}}^{\text{true}}) \cdot p_{\text{T}}^{\text{true}}$  instead of  $p_{\text{T}}^{\text{EM}}$ . The function obtained by this fitting is the calibration function of  $p_{\text{T}}^{\text{EM}}$ .

Figure 5.6 shows the procedure of fittings in the second step. The horizontal axis is changed from  $p_{\text{T}}^{\text{true}}$  to  $p_{\text{T,est}}^{\text{EM}}$  ( $=p_{\text{T}}^{\text{reco}}$  in the figure).

Figure 5.7 shows the calibration factors as a function of jet  $p_{\text{T}}^{\text{EM}}$  for the central and end-cap regions. This calibration factor is applied for the jets produced by Anti-Kt algorithm.

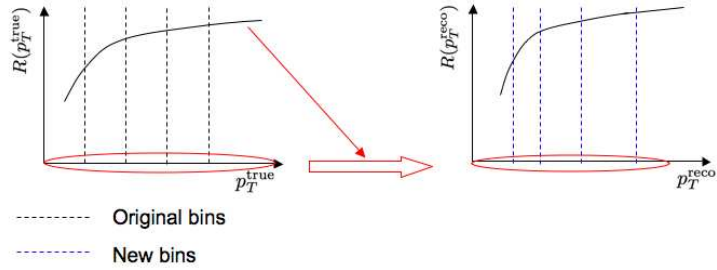


Figure 5.6: Illustration of the process. The horizontal axis is changed from  $p_T$  of truth jets to  $p_T$  of estimated reconstructed jets.

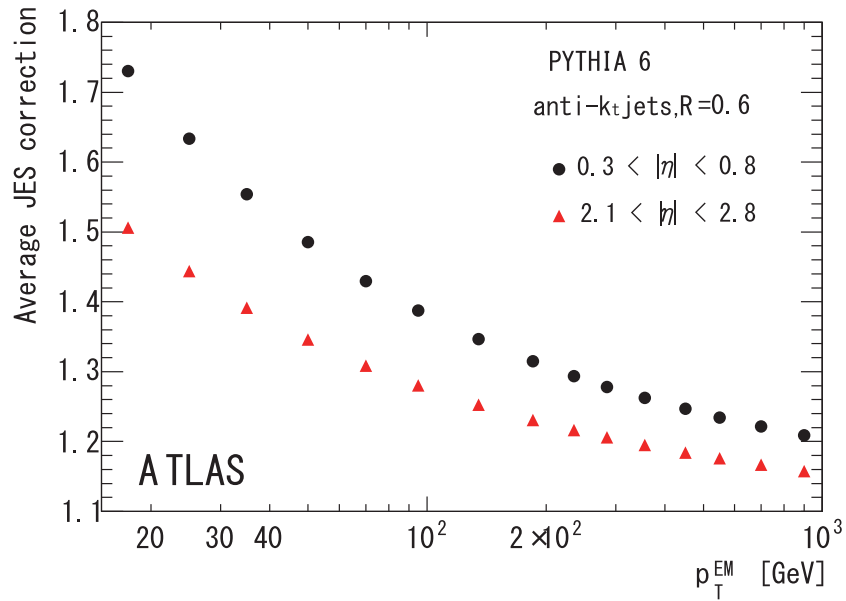


Figure 5.7: Calibration factors as a function of jet  $p_T^{\text{EM}}$  in EM scale for the central (circles) and end-cap (triangles) regions [118].

## 5.4 Uncertainties on Jet Energy Scale

### 5.4.1 Jet Energy Resolution Uncertainty

The jet energy resolution is estimated by the two methods from data events [119].

One uses dijet balance as follows. Two jets are required to satisfy  $\Delta\phi \geq 2.8$  between them and are required to be in the same  $\eta$  region. The asymmetry between  $p_T$  of two leading jets  $A$  is defined as

$$A(p_{\text{TJ1}}, p_{\text{TJ2}}) \equiv \frac{p_{\text{TJ1}} - p_{\text{TJ2}}}{p_{\text{TJ1}} + p_{\text{TJ2}}} = \frac{p_{\text{TJ1}} - p_{\text{TJ2}}}{2\bar{p}_T}, \quad (5.2)$$

where  $p_{\text{TJ1(2)}}$  is  $p_T$  of the leading (second leading) jet, and  $\bar{p}_T = (p_{\text{TJ1}} + p_{\text{TJ2}})/2$ . Assuming the transverse momentum balance, the mean value of  $p_T$  of two jets,  $p_{\text{TJ1}}, p_{\text{TJ2}}$ , can be written as

$$\langle p_{\text{TJ1}} \rangle = \langle p_{\text{TJ2}} \rangle = \frac{p_{\text{TJ1}} + p_{\text{TJ2}}}{2} = \bar{p}_T, \quad (5.3)$$

Since two jets are required in the same  $\eta$  region, they have same resolution:  $\sigma_1 = \sigma_2 = \bar{\sigma}$ , where  $\sigma_{1(2)}$  is the energy resolution of the jets and  $\bar{\sigma}$  is the resolution at  $p_T = \bar{p}_T$ . These assumptions give the relation between the resolution of  $A$ ,  $\sigma_A$ , and  $\sigma_{1,2}$  as

$$\sigma_A = \frac{\sqrt{\sigma_1^2 + \sigma_2^2}}{\langle p_{\text{TJ1}} + p_{\text{TJ2}} \rangle} = \frac{\bar{\sigma}}{\sqrt{2}\bar{p}_T}. \quad (5.4)$$

As a result, the resolution at  $p_T = \bar{p}_T$  is given by  $\sigma_A$ .

Another method is based on an imbalance vector,  $\vec{p}_T = \vec{p}_{\text{TJ1}} + \vec{p}_{\text{TJ2}}$ . This is called the bisector method. This method uses a coordinate system described in Figure 5.8. In a perfect dijet balance system,  $\vec{p}_T$  equals to zero, but there are a number of sources that rise fluctuations. Variance by the fluctuations,  $\text{Var}(p_T)$ , in  $\zeta$  and  $\psi$  directions are denoted as  $\sigma_\zeta^2 \equiv \text{Var}(p_{T\zeta})$  and  $\sigma_\psi^2 \equiv \text{Var}(p_{T\psi})$ , respectively. The fluctuation at the particle level,  $\sigma^{\text{part}}$ , comes mostly from initial state radiation. This effect expected to be same in both  $\zeta$  and  $\psi$  directions:

$$(\sigma_\zeta^{\text{part}})^2 = (\sigma_\psi^{\text{part}})^2, \quad (5.5)$$

where  $\sigma_\zeta^{\text{part}}$  and  $\sigma_\psi^{\text{part}}$  are the fluctuations at the particle level for  $\zeta$  and  $\psi$  directions, respectively. The fluctuation for  $\psi$  at the reconstructed jet level is sensitive to the energy resolution because  $p_{T\psi}$  is the difference of large transverse momentum in  $x - y$  plane while the fluctuation for  $\zeta$  at the

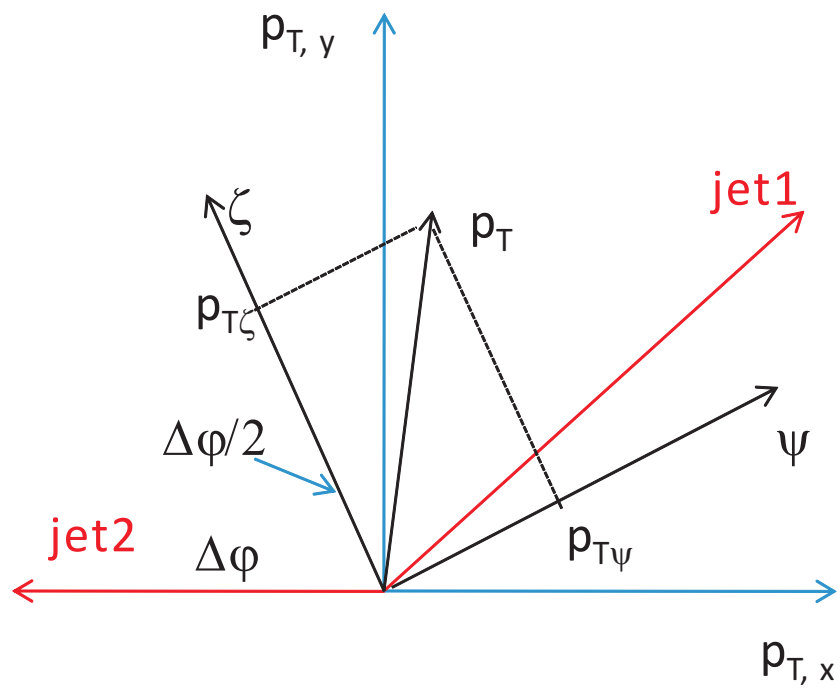


Figure 5.8: The coordination system for the bisector method.  $\Delta\phi_{1,2}$  is the angle between two jets in the  $x - y$  plane.  $\zeta$ -axis directs to the direction of the center of two jets in  $\phi$ .  $\psi$ -axis is defined as the orthogonal to the  $\zeta$ -axis.

reconstructed jet level is small. If two jets are in same  $\eta$  and have the same resolution value, the resolution at  $p_T = \bar{p}_T$ , which is the same definition of Eq. 5.3, is given as

$$\frac{\sigma_{\bar{p}_T}}{\bar{p}_T} = \frac{\sqrt{\text{Var}(p_T - p_T^{\text{part}})}}{\bar{p}_T} = \frac{\sqrt{(\sigma_\psi)^2 - (\sigma_\zeta)^2}}{\sqrt{2}\bar{p}_T |\cos \Delta\phi_{12}|} \quad (5.6)$$

This method can remove the soft radiation effect by subtraction in quadrature  $\sigma_\zeta$  from  $\sigma_\psi$

Figure 5.9 shows the jet energy resolution for the dijet balance and bisector methods as a function of the  $\bar{p}_T$ . It shows agreement with the MC simulation within 14 %.

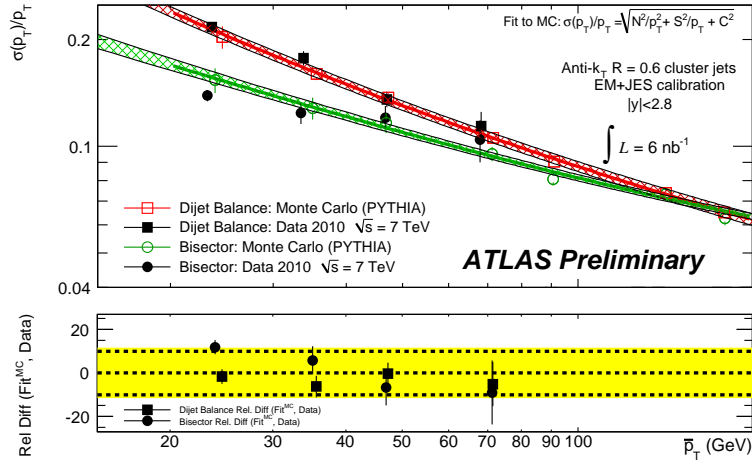


Figure 5.9: Jet energy resolution for the dijet balance and bisector methods as a function of the  $\bar{p}_T$ . The lower plot shows the relative difference between data and MC events.

## 5.4.2 Jet Energy Scale Uncertainty

The uncertainty of the jet energy scale (JES) calibrated by this procedure is estimated by the MC events and the data [120]. The basic procedure to evaluate the uncertainty is to check jet response after applying the calibration in various Monte Carlo samples produced with different parameter conditions varied from the nominal settings (by the amount of parameter uncertainties) and compare it with the nominal jet response. The nominal MC sample is

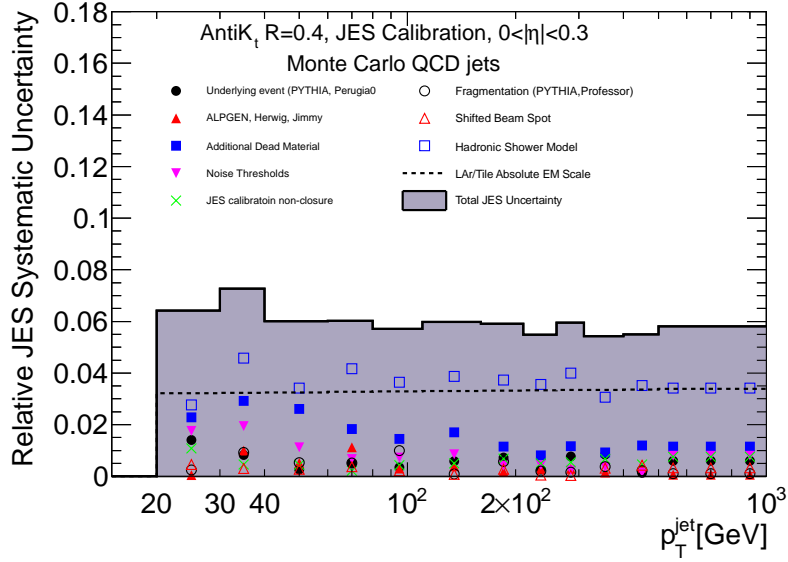
QCD events generated by PYTHIA with tunes described in Subsection 4.4.5. The uncertainty sources are the follows:

- Underlying event: This uncertainty is evaluated by comparing the nominal response to jet response obtained in a sample of PYTHIA events in which the soft-QCD part is tuned with only minimum bias event data from the Tevatron and CERN proton-anti-proton collider experiments.
- ALPGEN, HERWIG, JIMMY: Overall MC tune and generator dependence on the jet response is estimated by comparing the response in the nominal PYTHIA QCD and ALPGEN +JIMMY QCD sample.
- Additional Dead Material: The extra radiation length ( $X_0$ ) is added as the dead material to the detector simulation. The additional materials are as follows:
  - The dead material of  $0.05 X_0$  between the presampler and the EM calorimeter for the barrel region.
  - The dead material of  $0.2 X_0$  in the cryostat before the EM calorimeter.
  - The dead material of  $0.2 X_0$  in the cryostat between the EM and hadron calorimeters.
  - An increased density of the material of the barrel-endcap cryostat gap by a factor 1.5.
- Noise Thresholds: The noise thresholds in the topological clustering are changed by  $\pm 10\%$  and the jets are re-reconstructed with the new topological clusters to estimate the effect on noise thresholds.
- JES calibration non-closure: The calibration constants are derived from isolated jets while the JES uncertainty is evaluated using inclusive jets (containing non-isolated jets), and this leads to a non-closure of jet response. Other differences in deriving and applying the calibrations, such as cross section weights on the Monte Carlo samples, also cause the non-closure in jet response. Since this non-closure jet response is fully correlated and almost constant at a given jet  $p_T$  and  $\eta$ , the uncertainty due to non-closure is added linearly.
- Fragmentation: This uncertainty is estimated from PYTHIA QCD sample with tuning the parameters to LEP data using Professor software [121].

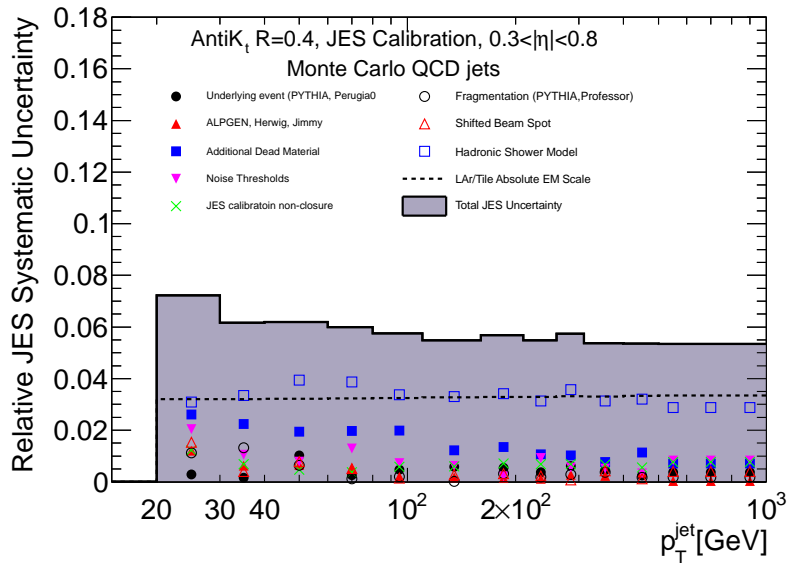
- Shifted Beam Spot: The nominal beam spot in MC is set as  $(x, y, z) = (-0.15, 1, 0)$  mm, and this nominal sample is used to derive the calibration. Any shifted beam spots may affect the  $p_T$  measurement of the jets. The effect on JES is estimated from the sample in which the beam spot is set as  $(x, y, z) = (1.5, 2.5, -9)$  mm. The current average shift of the beams spot in the data is estimated as  $(x, y, z) = (-0.4, 0.62, -1.3)$  mm. Therefore, this shifted sample covers the shift of the data.
- Hadronic Shower Model: This uncertainty comes from the description of hadronic interaction in the GEANT4 detector simulation. The nominal sample is based on the Quark Gluon String model [122] for the fragmentation of the nucleus, and Bertini cascade model [123] for the interactions of the hadrons in the medium of the nucleus. The uncertainty is estimated by two samples. One sample does not simulate Bertini nucleon cascades. Another sample uses the Fritiof model [122] instead of the Quark Gluon String fragmentation model.
- LAr/Tile Absolute EM Scale: This uncertainty is estimated from the conditions of the test beam setup and the full ATLAS detector. The LAr temperature, pulse reconstruction methods, calibration corrections, time stability are considered for the EM calorimeter. For the hadronic calorimeter, the electromagnetic scale uncertainty is estimated from the ratio of the response of the muons in the test beam and the MC events, and in the cosmic ray and the MC events.
- $\eta$  Intercalibration (Relative, Data/MC): The detector material in the end-cap region is less known than the barrel region. The transition region between the barrel and end-cap calorimeters have lower response to the jets at the EM scale, hence, larger JES uncertainty than that in other regions. Therefore the JES uncertainty for the higher rapidity regions is determined using the uncertainty in the central barrel region ( $0.3 < |\eta| < 0.8$ ) as a reference, and evaluating additional uncertainty in jet response on top of it. This determination of additional JES uncertainty is performed by measuring relative  $p_T$  balance of forward jet in dijet events with respect to the central reference jet. The uncertainty comes from the difference between data and MC events in the relative energy scale, and the deviation from the one of the relative energy scale in the data.

Applying each uncertainty component evaluated above to the jet four-vectors, the largest deviation from unity measured in jet response can be considered

as a JES uncertainty for each systematic effect. All of these systematic uncertainties are added in quadrature (except for non-closure systematic uncertainty being added linearly) to evaluate the total JES systematic uncertainties shown in Figure 5.10-5.12. Filled area shows total uncertainty of JES and it is about 7%. The marks and the lines represent each uncertainty source.



(a)



(b)

Figure 5.10: Relative jet energy scale systematic uncertainty as a function of jet  $p_T$  for  $0 < |\eta| < 0.3$  (a) and  $0.3 < |\eta| < 0.8$  (b). Filled histogram shows the total uncertainty. Each point and line shows each uncertainty source.

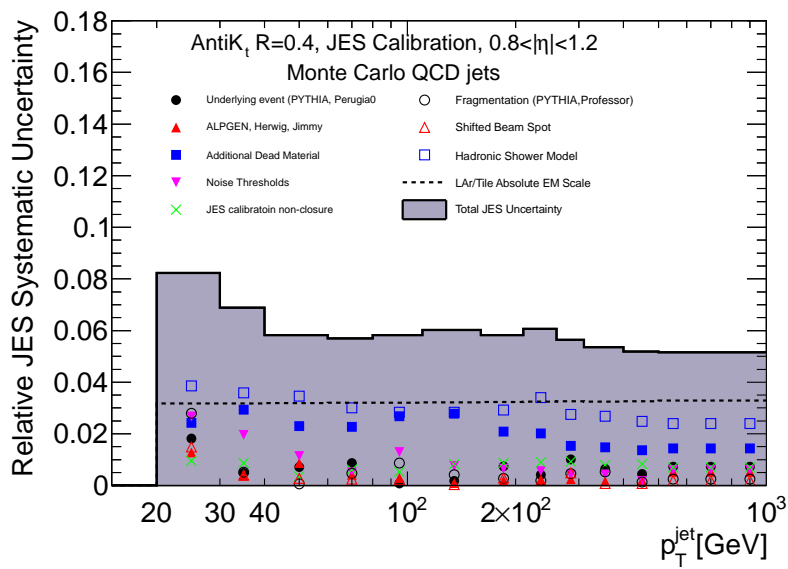
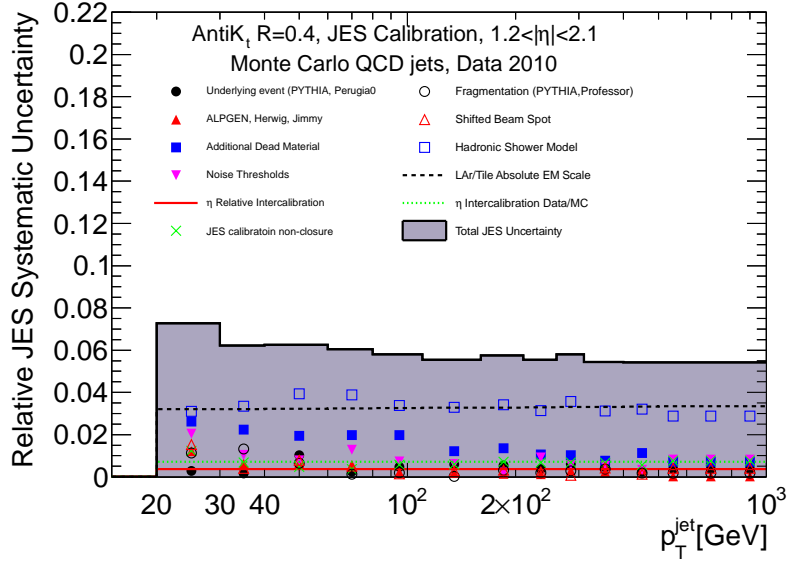
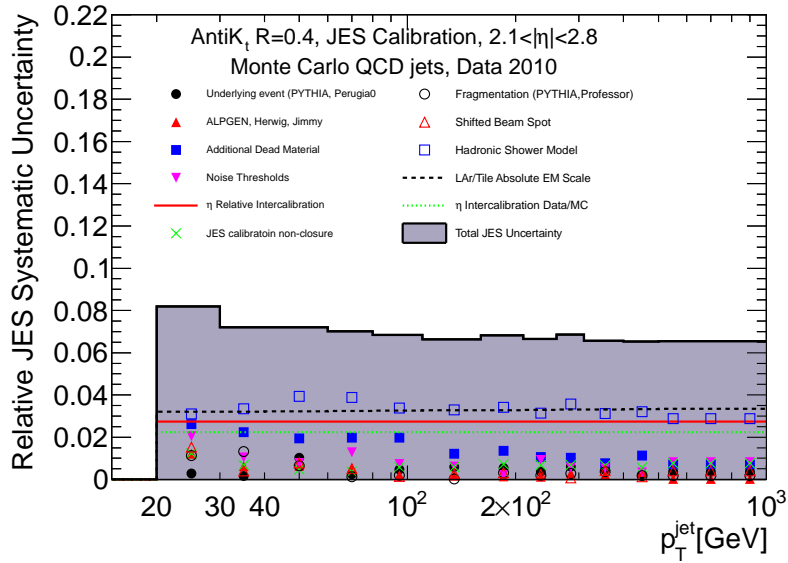


Figure 5.11: Relative jet energy scale systematic uncertainty as a function of jet  $p_T$  for  $0.8 < |\eta| < 1.2$ . Filled histogram shows the total uncertainty. Each point and line shows each uncertainty source.



(a)



(b)

Figure 5.12: Relative jet energy scale systematic uncertainty as a function of jet  $p_T$  for  $1.2 < |\eta| < 2.1$  (a) and  $2.1 < |\eta| < 2.8$  (b). Filled histogram shows the total uncertainty. Each point and line shows each uncertainty source. In the end-cap region,  $|\eta| > 2.1$ , the uncertainty is derived from the uncertainty in the barrel region,  $|\eta| < 2.1$ , by the  $\eta$  inter-calibration [124]. The contribution from the  $\eta$  inter-calibration is added to the end-cap region.

# Chapter 6

## Data Samples and Event Preselection

The ATLAS detector accumulated the data of proton-proton collisions at the center-of-mass energy  $\sqrt{s} = 7$  TeV provided by LHC in 2010. The LHC delivered a total integrated luminosity of  $48.9 \text{ pb}^{-1}$ . The ATLAS detector recorded that of  $45.0 \text{ pb}^{-1}$ . Figure 6.1 shows the integrated luminosity as a function of the day in 2010.

This chapter describes the data samples to be analyzed for the mini black hole search. Details of the event preselection are described in this chapter.

### 6.1 Data Period

The ATLAS experiment has started the physics program with proton-proton collisions at  $\sqrt{s} = 7$  TeV since March 2010. During the data taking, the trigger configurations had been changed according to the instantaneous luminosity. There are eight periods corresponding to the beam and the detector conditions and the data samples are separately defined for each period. The integrated luminosities, the trigger configurations and numbers of recorded events for each period are summarized in Table 6.1. Eight periods are categorized by the trigger configurations. The integrated luminosities are calculated after applying the data quality selection which is described later.

### 6.2 Trigger

This search uses a non-prescaled single jet trigger. Level-1 hardware (L1) triggers are used. There are some single jet triggers with different energy thresholds. The single jet triggers with lower  $E_T$  thresholds are prescaled to

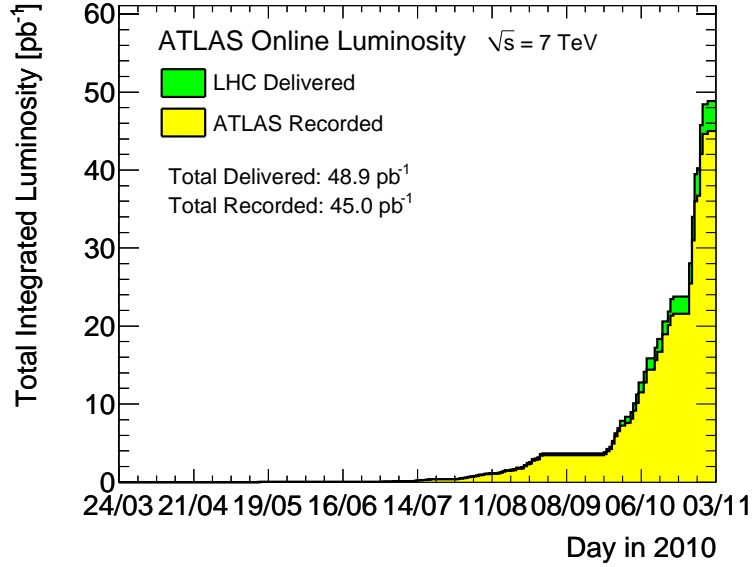


Figure 6.1: Total integrated luminosity at  $\sqrt{s} = 7$  TeV as a function of the day. The green and yellow filled histograms represent one which was delivered by LHC and one which was recorded at ATLAS, respectively.

Table 6.1: Summary of the data recorded in 2010

Period	Integrated Luminosity [pb <sup>-1</sup> ]	Used Trigger	Events
A	$3.80 \times 10^{-4}$	L1, single jet 55GeV	378
B	$8.07 \times 10^{-3}$	L1, single jet 55GeV	6744
C	$8.46 \times 10^{-3}$	L1, single jet 55GeV	5932
D	0.298	L1, single jet 55GeV	158918
E	1.00	L1, single jet 55GeV	478211
F	1.81	L1, single jet 55GeV	859477
G	6.87	L1, single jet 95GeV	430608
H	7.25	L1, single jet 95GeV	449263
I	19.1	L1, single jet 95GeV	1221161
Sum	36.3	-	3610692

keep the data acquisition rate up to 200 Hz. The lowest non-prescaled single jet trigger had been changed depending on the instantaneous luminosity. The following summarizes the trigger definitions for each period:

- Period A-F: A single jet L1 trigger with threshold 55 GeV on  $E_T$  of jet (L1\_J55)
- Period G-I: A single jet L1 trigger with threshold 95 GeV on  $E_T$  of jet (L1\_J95)

The energy defined in L1 trigger is EM scale which corresponds to  $2/3 \sim 1/2$  of hadronic scale. The lowest non-prescaled single jet trigger in Period F is L1\_J55 which has the  $E_T$  threshold of 55 GeV; L1\_J55 is prepared in all the periods up to F, and used for the analysis with data of A-F.

In Period G-I, the threshold of the lowest non-prescaled single jet trigger is set to be 95 GeV. This trigger is named L1\_J95 and used for the analysis.

## 6.3 Data Quality

The recorded data contain the events affected by the instrumental issues which arose during the data taking. In order to reject such events, the data quality selection cuts are applied. In the ATLAS experiment, a certain amount of the data is collectively saved into a single file; this file unit is called “Luminosity Block”. Each sub-detector is checked both online and offline on luminosity block basis. During the procedure, the data quality flag, which indicates whether the corresponding luminosity block is suitable for physics analysis, is labeled for each sub-detector.

The following requirements are applied to reject events which are affected by the problems on the ATLAS detector:

- Data recorded in the stable beam conditions.
- The magnet system is in good operation and the field strength is set to be the nominal value.
- All sub-detectors are fully operational during the data taking.
- There is no problematic peak or deficit in the distributions of jet and  $E_T^{\text{miss}}$  which is potentially caused by the trips of power supplies and the high noise rates.

With these requirements, the integrated luminosity of the data becomes  $36.3 \text{ pb}^{-1}$ ; this is the total amount of the data used in this thesis. In table 6.1, the integrated luminosities for each different trigger period are summarized.

## 6.4 Event Preselection

This section gives the details of the event preselection. Trigger efficiencies and the selection criterion on the leading jet, the cleaning of events, and  $p_T$  cut on jets to remove the pile-up effect are described.

### 6.4.1 Jet Selection

Reconstructed jets are selected with the following criteria:

$$\begin{aligned} |\eta| &< 2.8, \\ p_T &> 20 \text{ GeV}. \end{aligned} \tag{6.1}$$

### 6.4.2 Trigger and the leading jet transverse momentum selection

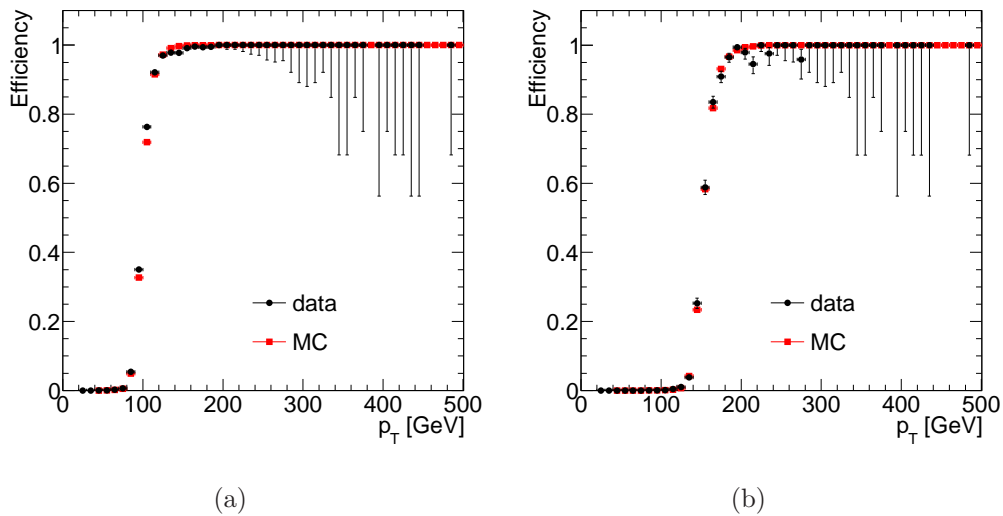


Figure 6.2: Trigger efficiencies for L1\_J55 (a) and L1\_J95 (b). Circles (rectangles) show the efficiency for the data (MC) events.

Figure 6.2 shows the efficiencies of L1\_J55 and L1\_J95 as a function of the leading jet transverse momentum,  $p_{TJ1}$ , for data and MC events. The MC events are generated by PYTHIA. The efficiencies are calculated from two single jet triggers with energy threshold of 5 GeV and 55 GeV (95 GeV)

as follows:

$$\epsilon_{L1\_J55} = \frac{N_{L1\_J55 \& \& L1\_J5}}{N_{L1\_J5}}, \quad (6.2)$$

$$\epsilon_{L1\_J95} = \frac{N_{L1\_J95 \& \& L1\_J5}}{N_{L1\_J5}}, \quad (6.3)$$

where  $\epsilon_{L1\_J55}$  ( $\epsilon_{L1\_J95}$ ) is the trigger efficiency for L1\_J55 (L1\_J95). The number of events which passed both L1\_J55 (L1\_J95) is defined as  $N_{L1\_J55 \& \& L1\_J5}$  ( $N_{L1\_J95 \& \& L1\_J5}$ ). The number of events which passed L1\_J5 is shown as  $N_{L1\_J5}$ .

As shown in Figure 6.2, the trigger efficiency reaches 100% at  $p_T = 250$  GeV for L1\_J95. An inefficiency of the trigger makes difficulties to retrieve the cross section and also results in biases on the event selection. To reject  $p_T$  dependence of trigger biases,  $p_{TJ1}$  is required as

$$p_{TJ1} > 250 \text{ GeV} \quad (6.4)$$

in preselection cuts for all the data. With this requirement, the trigger efficiency shows almost 100% in both data and MC events.

### 6.4.3 Event Cleaning

This section describes the details of the event cleaning.

#### Primary Vertex Requirement

The primary vertex is an interaction point estimated from tracks for an event. The primary vertex requirement is applied to remove non-collision background events. Sources of non-collision background are listed below:

- The interactions of proton beam with the residual gas in the beam pipe
- Beam halo: Muons or pions which come from the upper stream of the beam line
- Bremsstrahlung of cosmic-ray muons in the calorimeters

These background events can be removed with the requirement where the primary vertex should be near the beam collision spot which is estimated from the primary vertices for each Luminosity Block.

The beam spot size is  $\sigma_{xy} = 15 \mu\text{m}$  and  $\sigma_z = 5.6 \text{ cm}$ [125] at LHC. Hence, the primary vertex requirements are set as follows:

$$\begin{aligned} N_{\text{tracks}} &\geq 5, \\ |z_{\text{vertex}} - z_{\text{beamspot}}| &< 15 \text{ cm}, \end{aligned} \quad (6.5)$$

where  $N_{\text{tracks}}$  is the number of tracks with  $p_T > 150$  MeV associated to the primary vertex and  $z_{\text{vertex}}$  and  $z_{\text{beamspot}}$  are the positions of the vertex and the beam spot along to  $z$ -axis, respectively.

## Jet Cleaning

There are several sources which make up fake jets such as a spiky noise in the calorimeter and a bremsstrahlung of muons in cosmic-rays. The following variables are used for the fake jet cleaning:

- $f_{\text{EM}}$ : The EM calorimeter energy in a jet divided by total energy of the jet
- $f_{\text{quality}}$ : The LAr calorimeter measures the energy depositions of particles with the pulse shapes of the cells. Each cell in the LAr has a quality factor which indicates the difference of the measured pulse shape with the predicted one. The LAr quality fraction,  $f_{\text{quality}}$ , is defined as the fraction of cells which have quality factors greater than 4000, with respect to the total number of cells associated to the jet.
- $n_{90}$ : The number of calorimeter cells where the sum of cell energies exceeds 90 % of jet energy. The cell energies are summed in decreasing order of energy.
- $f_{\text{HEC}}$ : The fraction of HEC energy in a jet.
- $t_{\text{jet}}$ : The jet time which is calculated by the energy weighted mean of the cells timing.
- $f_{\text{max}}$ : The maximum fraction of energy in one calorimeter layer.
- $f_{\text{cha}}$ : The ratio of  $\sum p_T^{\text{tracks}}$  to the jet  $p_T$ , where  $\sum p_T^{\text{tracks}}$  is the scalar  $p_T$  sum of tracks associated to the jet. The associated tracks are selected by requiring  $\Delta R(\text{jet}, \text{track}) < 0.4$ , where  $\Delta R(\text{jet}, \text{track})$  is the distance between the jet axis and a track in the  $\eta - \phi$  plane.
- $f_{\text{TG3}}$ : The fraction of energy in the third tile gap scintillator layer.
- $f_{\text{cor}}$ : Some problematic cells are masked while the data taking. The energies of these masked cells are estimated from neighboring cells when jets are reconstructed. The fraction of energy of these problematic cells is defined as  $f_{\text{cor}}$ .

Figures 6.3-6.7 show distributions of jet cleaning variables for data and MC events. The quality factor in the LAr is not emulated in the MC events and only the data is shown in Figure 6.3(b).

Excesses of data events can be observed in Figures 6.3(a), 6.4(a) and 6.5(a) in which the contribution of fake jets is dominant.

With these variables, the fake jets are categorized into:

- EM coherent noise: The fake jets are induced by the noise burst and coherent noise in the electromagnetic calorimeter. Fake jets have a large energy fraction in the electromagnetic calorimeter and consist of a single or a few cells with bad qualities. As a consequence of these features, the fake jets from EM noise are defined as:

$$- f_{EM} > 0.95 \text{ and } |f_{quality}| > 0.8$$

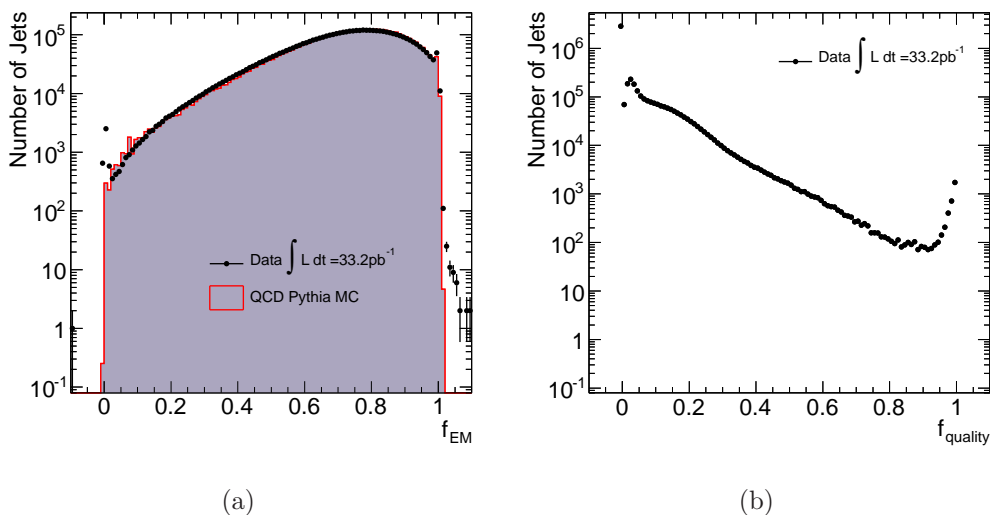


Figure 6.3: Distributions of  $f_{EM}$  (a) and  $f_{quality}$  (b). Filled circles show the data of period G-I. The histogram shows the MC events. The MC events are normalized to the number of events in the data. The L1\_J95 trigger and the primary vertex requirements are applied.

- HEC spike: The noise burst in the hadron end-cap detectors are one of the main sources of fake jets. Fake jets can be tagged with a large fraction of HEC energy and a small number of cells in the jet or bad quality of the LAr pulse shapes. The fake jet originating from HEC spike is defined as:

- $f_{\text{HEC}} > 0.8$  and  $n_{90} \leq 5$
- $f_{\text{HEC}} > 0.5$  and  $|f_{\text{quality}}| > 0.5$

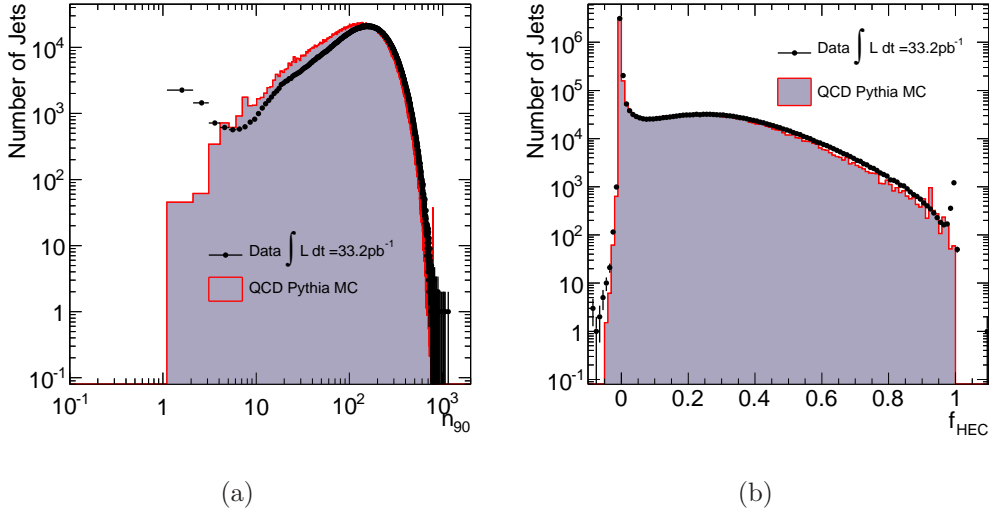


Figure 6.4: Distributions of  $n_{90}$  (a) and  $f_{\text{HEC}}$  (b). Filled circles show the data of period G-I. The histogram shows the MC events. The MC events are normalized to the number of events in the data. The L1\_J95 trigger and the primary vertex requirements are applied.

- Cosmic-ray and beam background: The background events induced by cosmic-rays and beam halos can be removed with the timing difference of the jet from the collision. In addition, the fake jets originating from cosmic-rays give a small fraction of EM calorimeter energy because most of cosmic-ray muons would pass the large volume of hadron calorimeters. A high energy deposit of cosmic-ray muon in the hadron calorimeter would reach to the EM calorimeter. This fake jet can be removed by requiring an associated track which comes from the collision point. Beam halo muon traveling along  $z$ -axis is also reconstructed as a jet. In this case, one calorimeter layer has most of jet energy in the central region.

Therefore, the followings give the definitions of these fake jets:

- $t_{\text{jet}} > 25\text{ns}$
- $f_{\text{EM}} < 0.05$

- $f_{\max} > 0.9$  and  $|\eta|$  of jet  $< 2$
- $f_{\text{cha}} > 0.02$  and  $p_T$  of jet  $> 250\text{GeV}$

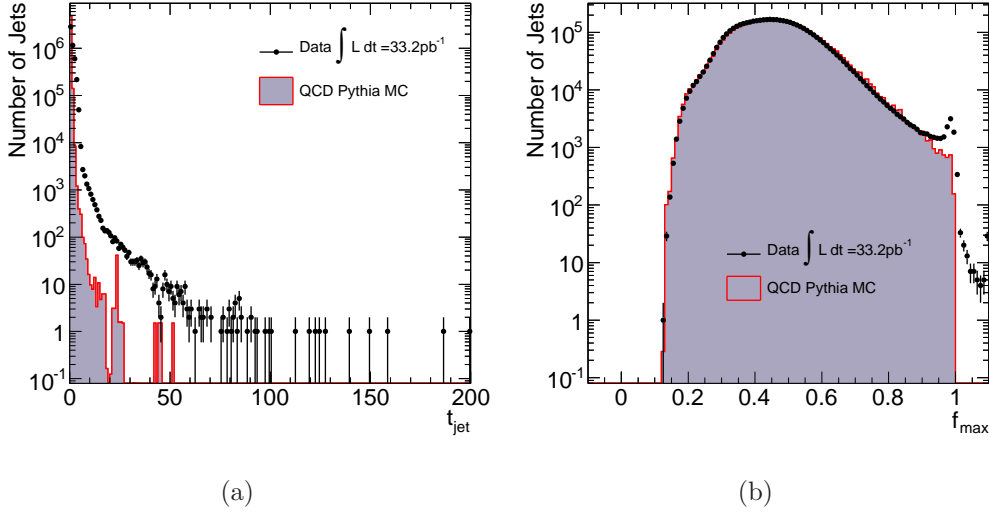


Figure 6.5: Distributions of  $t_{\text{jet}}$  (a) and  $f_{\max}$  (b). Filled circles show the data of period G-I. The histogram shows the MC events. The MC events are normalized to the number of events in the data. The L1\_J95 trigger and the primary vertex requirements are applied.

- Jet with a large energy fraction in the third tile-gap layer: The third layer of tile-gap scintillator is not fully calibrated. Therefore, the jet which has a large fraction of energy in this layer is rejected by the following criterion:

- $f_{\text{TG3}} > 0.5$

- The correction of masked cells possibly causes a mis-measurement of the jet energy. The rejection cut to reject mis-measured jets is set as

- $f_{\text{cor}} > 0.5$

In summary, the events containing fake jets or potentially mis-measured jets are rejected by applying the criteria described above to all jets with  $p_T > 20\text{ GeV}$  in the events.. Figure 6.8 shows an event display of cosmic-ray

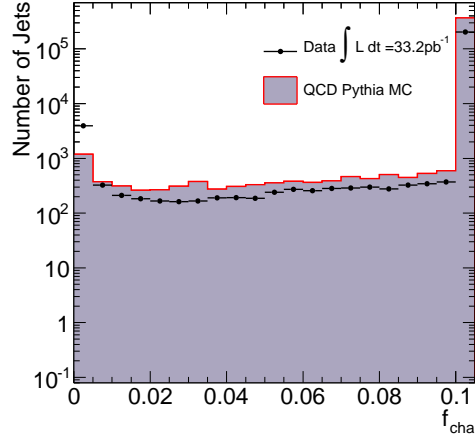


Figure 6.6: Distributions of  $f_{\text{cha}}$ . Filled circles show the data of period G-I. The histogram shows the MC events. The MC events are normalized to the number of events in the data. The L1\_J95 trigger and the primary vertex requirements are applied. The overflow events are added in the last bin.

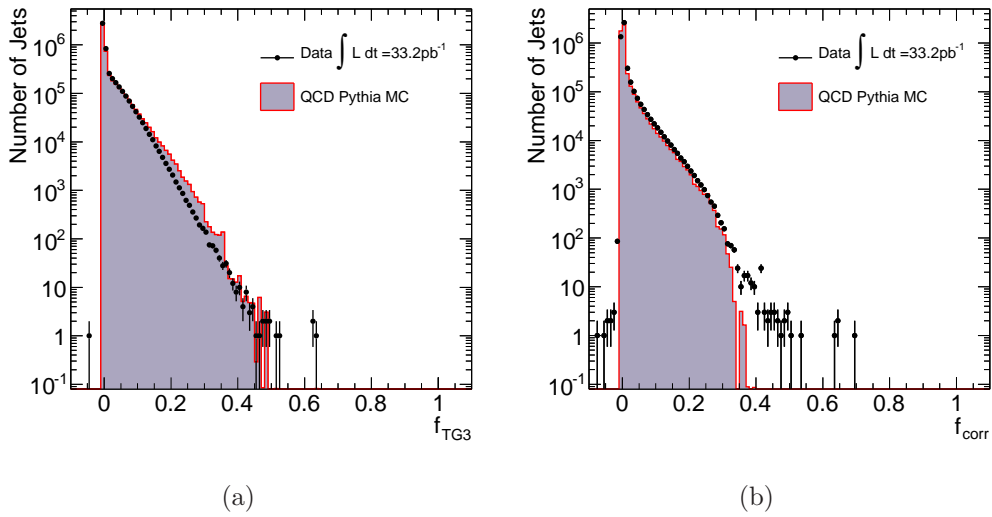


Figure 6.7: Distributions of  $f_{\text{TG3}}$  (a) and  $f_{\text{corr}}$  (b). Filled circles show the data of period G-I. The histogram shows the MC events. The MC events are normalized to the number of events in the data. The L1\_J95 trigger and the primary vertex requirements are applied.

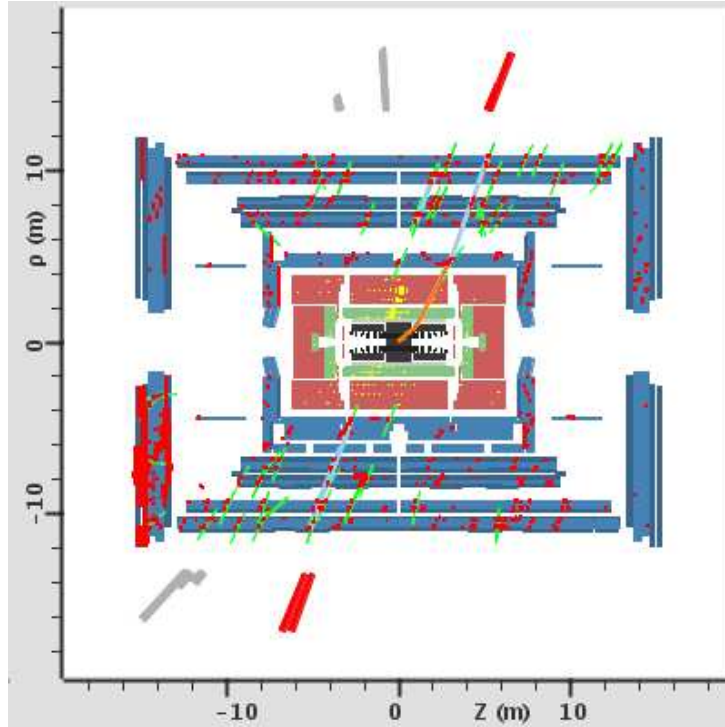


Figure 6.8: Event display of a cosmic-ray event. A sectional side view of the ATLAS detector in  $y - z$  plane is shown. Black region in the center represents the inner tracker. Green and red regions represent the EM and hadron calorimeters, respectively. Blue regions represent the muon system. Yellow segments show the energy deposits in the calorimeters. Red points in the muon system show the hits in the muon system. Lines show reconstructed tracks. All tracks direct same direction and are not pointing the collision point. Consequently, this event is concluded to be originated from cosmic-rays. In the event, there are two high  $p_T$  jets of  $p_T = 2.08$  TeV and  $p_T = 120$  GeV. The group of yellow segments in the upper region of the calorimeter represents 2.80 TeV jet which is not pointing to the collision point and does not have any associated tracks.

event. The leading jet in this event has  $p_T$  of 2.08 TeV, which does not have tracks and removed by the criterion on  $f_{cha}$ .

Figure 6.9 shows distributions of  $p_T$  of all jets for data and MC events. Filled rectangles and circles show the data before and after applying the jet cleaning, respectively. The histograms show QCD PYTHIA MC events. There is an excess of events in high  $p_T$  region before the jet cleaning; they are

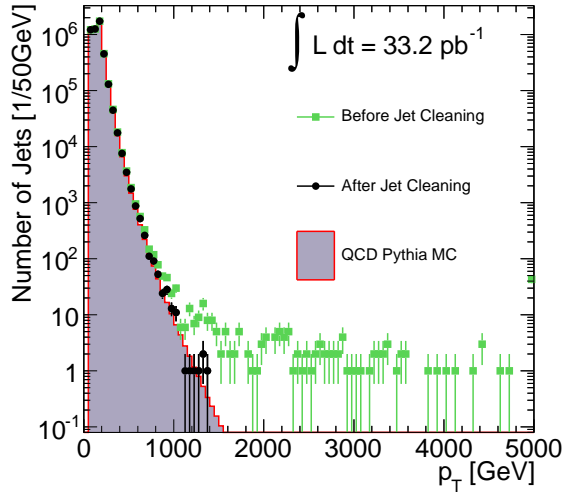


Figure 6.9: Inclusive jet  $p_T$  distributions. Filled rectangles and circles show the data before and after the jet cleaning, respectively. The data corresponds to period G-I with the selection criteria of trigger and primary vertex. The histogram shows the MC events. The MC events are normalized by the total number of the data events.

removed with the criteria described in this section. The rejection efficiency for real jet events is estimated to be 0.6% from the MC events.

#### 6.4.4 Pile-up effect and transverse momentum cut on Jets

In the data, multiple collisions could take place in an event; the mean number of vertices measured to be 2.63. Figure 6.10 shows the number of vertices in the data with the requirements of trigger and the event cleaning. The most probable process of collisions other than hard one is the minimum bias interaction.

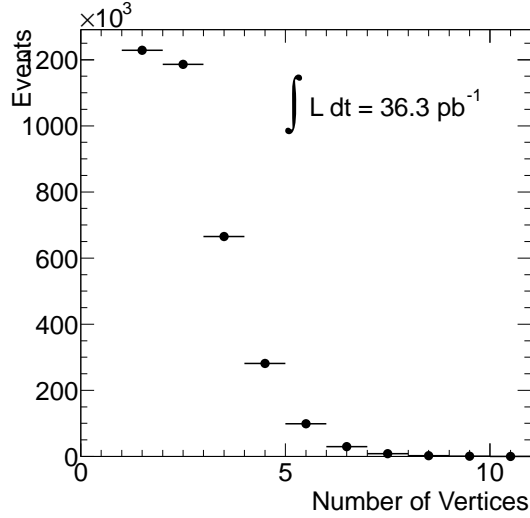


Figure 6.10: Number of primary vertexes of the data after requiring the single jet trigger and the event cleaning cuts. The vertices satisfying Eq. 6.5 are counted.

Figure 6.11 shows the transverse momentum distribution of jets in minimum bias events. The histogram is normalized to unity, which gives the emission probability of single jet per collision as a function of jet  $p_T$ . Table 6.2 shows the emission probabilities with different cuts on  $p_T$ . By requiring  $p_T > 50$  GeV, the probability of observing a jet in minimum bias collisions is 0.0367%. Even if there are more than five pile-up collisions, the probability of observing pile-up jets is estimated to be less than 0.2%. Consequently, the pile-up effect could be negligible by requiring a threshold of 50 GeV on jets. Hereafter, jets which have  $p_T > 50$  GeV are used in the analysis.

Table 6.2: Emission probability of jets in minimum bias events

$p_T$ cut	20 GeV	30 GeV	40 GeV	50 GeV
Probability [%]	1.41	0.284	0.0902	0.0357

### 6.4.5 Summary of Preselection

Table 6.3 shows the data reduction summary of each preselection cut. The

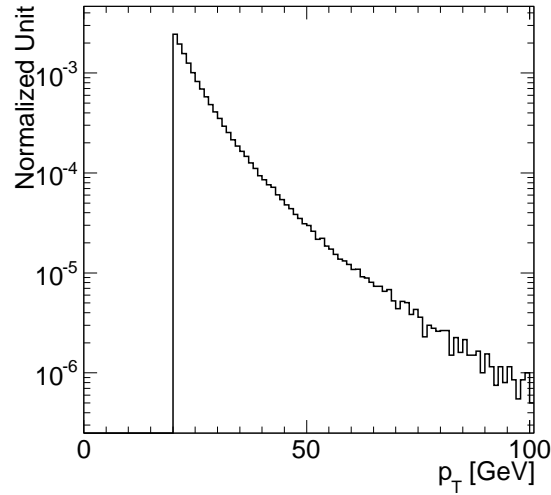


Figure 6.11: The transverse momentum distribution of jets in minimum bias events of the MC samples. The histogram is normalized to unity.

Table 6.3: Data reduction summary of each preselection cut

Selection	Events
Trigger	3610692
Vertex Requirement	3582452
Jet Cleaning	3537534
The Leading Jet Requirement	171902

primary vertex requirement and jet cleaning cuts removed 2% of triggered events. After all preselection cuts, 171902 events remain.

# Chapter 7

## Characteristics of Signal and Background Events

Characteristics of mini black hole events observed in the ATLAS detector are determined in mainly Hawking radiation phase. Mini black hole events are expected to have a high-multiplicity final state with high  $p_T$  particles and could be identified by the appearance of multiple high  $p_T$  jets, electrons, muons and photons and also by the large  $E_T^{\text{miss}}$  due to energetic neutrinos emitted in the evaporation phase. It takes relatively a long time to assess performance of high  $p_T$  electrons, muons, photons and large  $E_T^{\text{miss}}$  compared with high  $p_T$  jets at an early stage of the experiment. Therefore, the mini black hole events are searched for in the multijet final state.

In this chapter, characteristics of signal and background events are described. Discriminant observables are also discussed.

### 7.1 QCD Background

After requiring the criteria on the leading jets given in Section 6.4, the main background is QCD process. Figure 7.1 shows  $p_T$  distributions of the leading and fifth leading jet for the remaining events after preselection cuts. The numbers of MC events for each process are listed in Table 7.1. The table shows that QCD process dominates and the number of QCD events is larger than that of other SM processes by three orders of magnitudes. The  $p_T$  distributions also show that QCD process is dominant even in high  $p_T$  region. Thus, only QCD events are considered in background studies and the contribution of other processes is incorporated as a systematic uncertainty in this analysis.

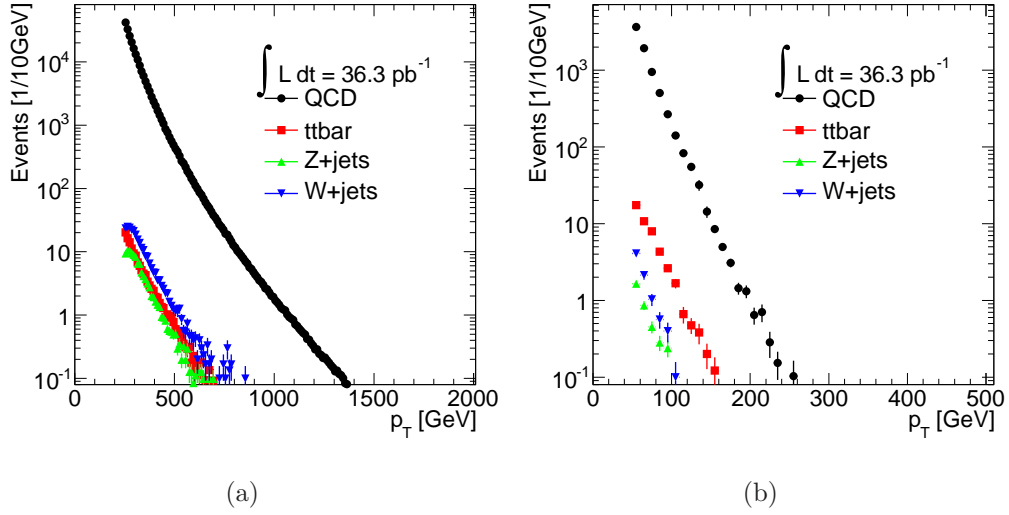


Figure 7.1:  $p_T$  distributions of the leading (a) and fifth leading jet (b) for QCD,  $t\bar{t}$ ,  $Z + \text{jets}$  and  $W + \text{jets}$  processes

Table 7.1: Expected number of events after applying preselection. The numbers correspond to  $36.3 \text{ pb}^{-1}$

Process	Number of events
QCD	$2.15 \times 10^5$
$t\bar{t}$	$1.36 \times 10^2$
$Z + \text{jets}$	$1.06 \times 10^2$
$W + \text{jets}$	$2.58 \times 10^2$

## 7.2 Discriminant Observables

Black hole signal events have high multiplicity of high  $p_T$  jets. Therefore, following variables give a good discrimination between signal and background events:

- $N_J$ : Number of jets with  $p_T > 50$  GeV, and  $|\eta| < 2.8$
- $\sum p_T$ : Sum of  $p_T$  of jets in an event. Jets are required to have  $p_T > 50$  GeV.

The cut of  $p_T > 50$  GeV on jets is applied to remove the pile-up effect as mentioned in Section 6.4.4.

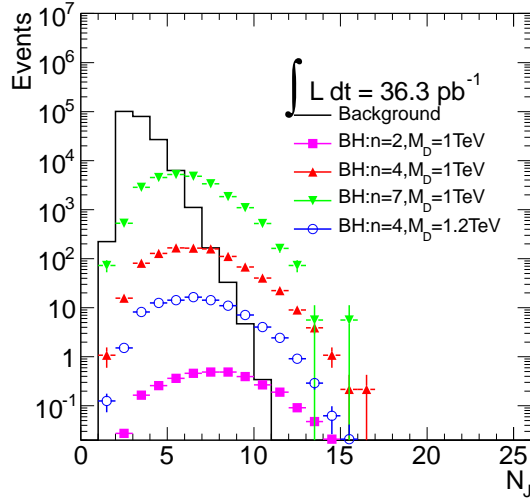


Figure 7.2: Distributions of the number of jets with  $p_T > 50$  GeV for QCD MC events and black hole signals with various parameters.

Figures 7.2 and 7.3 show  $N_J$  distributions for signal and QCD background events. Most of background events go in the dijet topology and cluster around  $N_J = 2$ . On the other hand, signal events give peaks at  $N_J = 5$  or higher.

The  $\sum p_T$  distributions for signal and background events are shown in Figure 7.4. They are divided into two region of  $1 < N_J < 5$  and  $N_J \geq 5$ ; signal events dominate and give high  $\sum p_T$  in the latter. The QCD events dominate in the region of  $N_J > 1$ . Events with single jet could be observed due to the cosmic-rays or calorimeter noises. Therefore single jet events are not used hereafter. The criterion “ $1 < N_J < 5$ ” is indicated by “ $N_J < 5$ ” unless otherwise noted.

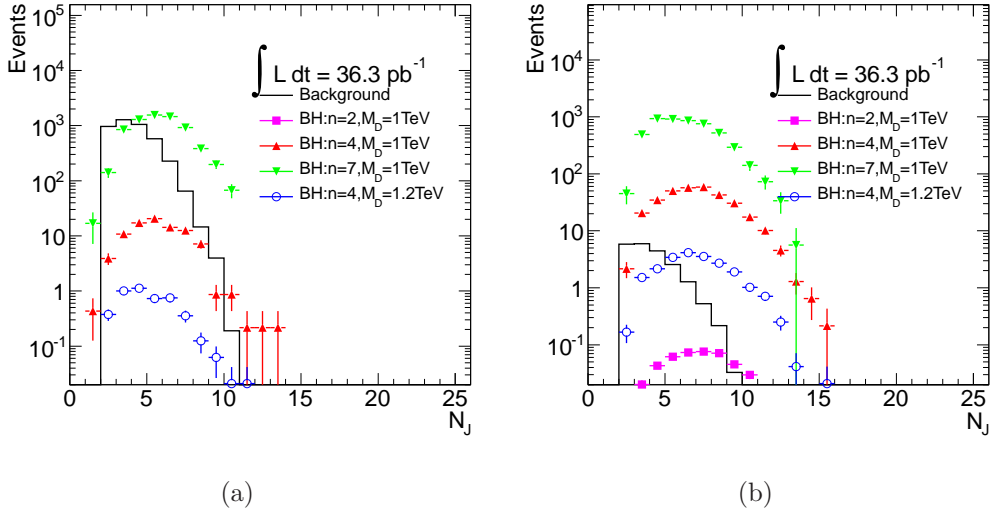


Figure 7.3: The number of jets for the events with  $1000 \text{ GeV} < \sum p_T < 1500 \text{ GeV}$  (a) and  $2000 \text{ GeV} < \sum p_T < 3000 \text{ GeV}$  (b).

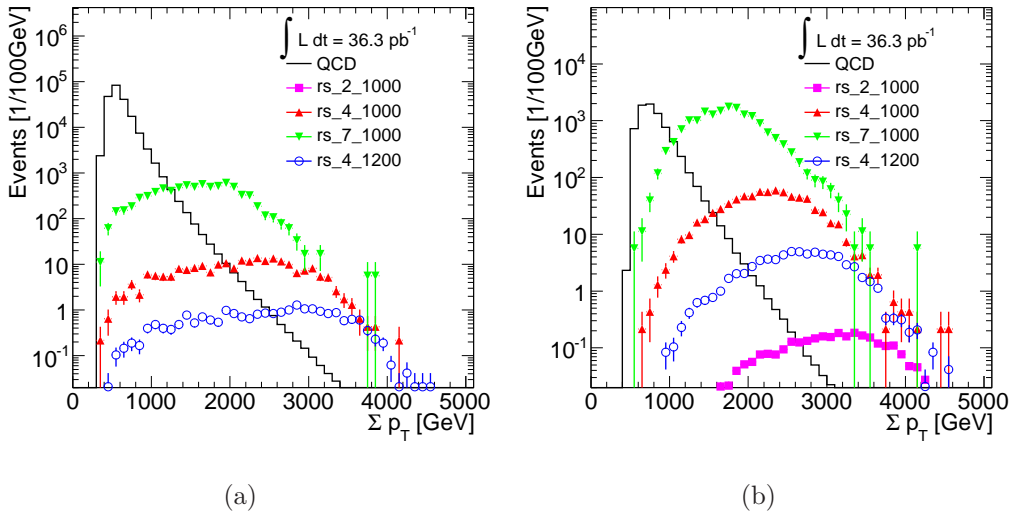


Figure 7.4:  $\sum p_T$  distributions of signal and background events in regions of  $N_J < 5$  (a) and  $N_J \geq 5$  (b)

Figures 7.5 and 7.6 show two-dimensional distributions of  $\sum p_T$  and  $N_J$  for QCD background and signal events. The signal events give larger values

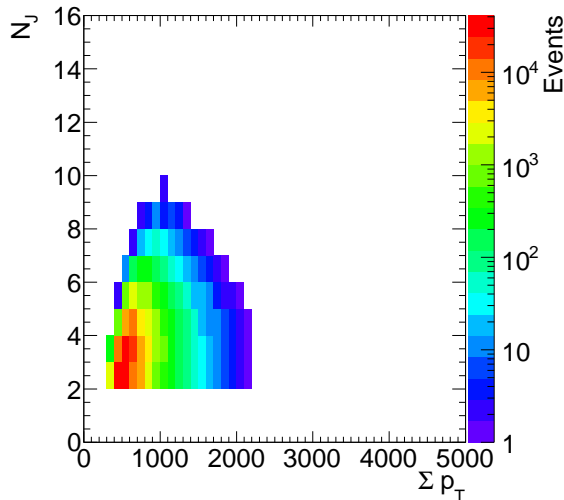


Figure 7.5:  $N_J$ - $\sum p_T$  distribution for QCD background events after applying preselection. The histogram is normalized to  $36.3 \text{ pb}^{-1}$ .

of  $\sum p_T$  and  $N_J$ , which is different from QCD background events.

Tables 7.2, 7.3 and 7.4 summarize the expected numbers of events in a region of  $N_J \geq 5$  and  $\sum p_T > 1500$  (2000) GeV for background and signal events. Signal events show high efficiencies even in  $\sum p_T > 2000$  GeV while only a few events of QCD background events remain. Hence, the signal region is set as follows:

$$\begin{aligned} N_J &\geq 5, \\ \sum p_T &> 2000 \text{ GeV}. \end{aligned} \tag{7.1}$$

### 7.3 Characteristics of QCD background

In order to estimate the background contamination and to determine the signal yield in the later, characteristics of QCD background events are discussed.

Typical QCD events show dijet-like topology and  $p_T$  of fifth leading jet is expected to be small compared with that of signal events. Figure 7.7

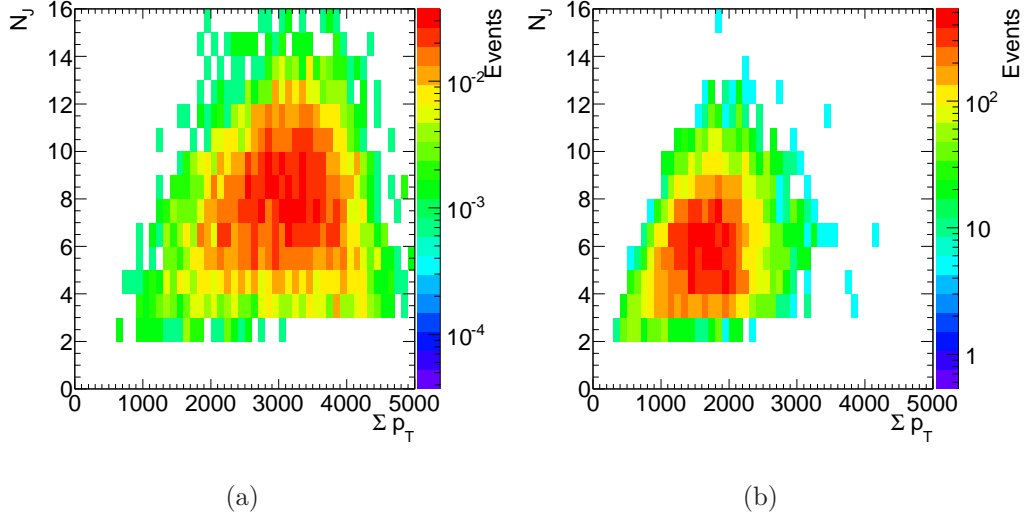


Figure 7.6:  $N_J$ - $\sum p_T$  distributions for signal point rs\_2\_1000 (a) and rs\_4\_1000 (b). The histograms are normalized to  $36.3 \text{ pb}^{-1}$ .

Table 7.2: Expected number of events and acceptance for background events with  $N_J \geq 5$  and  $\sum p_T > 1500(2000) \text{ GeV}$ . The numbers are normalized to  $36.3 \text{ pb}^{-1}$ .

Process	$\sum p_T > 1500 \text{ GeV}$ (acceptance [%])	$\sum p_T > 2000 \text{ GeV}$ (acceptance [%])
QCD	59.5 ( $\sim 10^{-8}$ )	5.17 ( $\sim 10^{-9}$ )
$t\bar{t}$	0.633 (0.02)	0.097 (0.003)
$Z + \text{jets}$	0.084 (0.06)	0.014 (0.01)
$W + \text{jets}$	0.166 (0.05)	<0.001 (-)

Table 7.3: Number of expected events and acceptance for the mini black hole signals with  $N_J \geq 5$  and  $\sum p_T > 1500(2000)$  GeV for signal points on the assumption  $\lambda < r_s$ . The numbers are normalized to  $36.3 \text{ pb}^{-1}$ . The models corresponding to the abbreviations are summarized in Table 4.1.

Signal point	$\sum p_T > 1500 \text{ GeV}$ (acceptance [%])	$\sum p_T > 2000 \text{ GeV}$ (acceptance [%])
rs_2_800	$1.20 \times 10^2$ (75.6)	$1.02 \times 10^2$ ( 64.3 )
rs_2_1000	2.8 (75.9)	2.65 ( 71.9 )
rs_2_1200	$2.74 \times 10^{-2}$ (74.7)	$2.68 \times 10^{-2}$ ( 73.1 )
rs_3_800	$1.34 \times 10^3$ (64.6)	$9.10 \times 10^2$ ( 43.8 )
rs_3_1000	94.1 (70.2)	81.8 ( 61.1 )
rs_3_1200	4.9 (72.4)	4.63 ( 68.4 )
rs_3_1500	$1.86 \times 10^{-2}$ (70.4)	$1.82 \times 10^{-2}$ ( 68.8 )
rs_4_800	$5.76 \times 10^3$ (55.4)	$2.84 \times 10^3$ ( 27.4 )
rs_4_1000	$6.83 \times 10^2$ (63.4)	$5.09 \times 10^2$ ( 47.2 )
rs_4_1200	68.7 (66)	61.2 ( 58.8 )
rs_4_1500	1.38 (66.7)	1.31 ( 63.6 )
rs_4_2000	$1.04 \times 10^{-4}$ (66.1)	$1.03 \times 10^{-4}$ ( 65.5 )
rs_5_800	$1.46 \times 10^4$ (44.9)	$5.11 \times 10^3$ ( 15.7 )
rs_5_1000	$2.61 \times 10^3$ (58.5)	$1.59 \times 10^3$ ( 35.7 )
rs_5_1200	$3.68 \times 10^2$ (60.9)	$2.93 \times 10^2$ ( 48.4 )
rs_5_1500	16.9 (64.4)	15.6 ( 59.3 )
rs_5_2000	$2.37 \times 10^{-2}$ (62.6)	$2.32 \times 10^{-2}$ ( 61.2 )
rs_6_800	$2.71 \times 10^4$ (34.8)	$6.68 \times 10^3$ ( 8.56 )
rs_6_1000	$6.36 \times 10^3$ (50.3)	$3.07 \times 10^3$ ( 24.3 )
rs_6_1200	$1.25 \times 10^3$ (58.0)	$8.78 \times 10^2$ ( 40.8 )
rs_6_1500	88.5 (62.2)	77.9 ( 54.7 )
rs_6_2000	0.492 (61.4)	0.474 ( 59.1 )
rs_7_800	$3.95 \times 10^4$ (25.5)	$8.98 \times 10^3$ ( 5.81 )
rs_7_1000	$1.20 \times 10^4$ (42.7)	$4.51 \times 10^3$ ( 16.0 )
rs_7_1200	$2.93 \times 10^3$ (52.5)	$1.77 \times 10^3$ ( 31.6 )
rs_7_1500	$2.96 \times 10^2$ (58.8)	$2.46 \times 10^2$ ( 48.9 )
rs_7_2000	3.75 (60.9)	3.54 ( 57.5 )

Table 7.4: Number of expected events and acceptance for the mini black hole signals with  $N_J \geq 5$  and  $\sum p_T > 1500(2000)$  GeV for signal points on the assumption  $\lambda < r_s$ . The numbers are normalized to  $36.3 \text{ pb}^{-1}$ . The models corresponding to the abbreviations are summarized in Table 4.2.

Signal point	$\sum p_T > 1500$ GeV (acceptance [%])	$\sum p_T > 2000$ GeV (acceptance [%])
rh_2_800	$9.82 \times 10^{-2}$ (83.4)	$9.68 \times 10^{-2}$ ( 82.2 )
rh_3_800	17.3 (79.6)	16.2 ( 74.7 )
rh_3_1000	$7.58 \times 10^{-2}$ (79.1)	$7.44 \times 10^{-2}$ ( 77.6 )
rh_4_800	$2.59 \times 10^2$ (72.8)	$2.21 \times 10^2$ ( 62.1 )
rh_4_1000	6.15 (75.4)	5.88 ( 72.1 )
rh_4_1200	$5.61 \times 10^{-2}$ (74)	$5.52 \times 10^{-2}$ ( 72.8 )
rh_5_800	$1.53 \times 10^3$ (69.4)	$1.15 \times 10^3$ ( 52.2 )
rh_5_1000	78.5 (70.6)	71.7 ( 64.4 )
rh_5_1200	2.66 (70.9)	2.56 ( 68.3 )
rh_5_1500	$3.13 \times 10^{-3}$ (69.1)	$3.09 \times 10^{-3}$ ( 68.2 )
rh_6_800	$5.10 \times 10^3$ (62)	$3.28 \times 10^3$ ( 39.9 )
rh_6_1000	$4.35 \times 10^2$ (67.2)	$3.67 \times 10^2$ ( 56.8 )
rh_6_1200	29.1 (68.6)	26.9 ( 63.4 )
rh_6_1500	0.227 (68.9)	0.221 ( 67.3 )
rh_7_800	$1.20 \times 10^4$ (53.7)	$6.08 \times 10^3$ ( 27.3 )
rh_7_1000	$1.48 \times 10^3$ (63.1)	$1.12 \times 10^3$ ( 47.5 )
rh_7_1200	$1.54 \times 10^2$ (66.6)	$1.36 \times 10^2$ ( 59.0 )
rh_7_1500	3.05 (66.6)	2.93 ( 64 )
rh_7_2000	$2.40 \times 10^{-4}$ (64.9)	$2.37 \times 10^{-4}$ ( 64.2 )

shows the leading jet  $p_T$  distributions of QCD events in  $1000 \text{ GeV} < \sum p_T < 1500 \text{ GeV}$  and  $2000 \text{ GeV} < \sum p_T < 3000 \text{ GeV}$ . The dijet-like topology leads to a leading jet  $p_T$  of  $\sum p_T/2$ , therefore, the  $p_T$  distributions give a peak at half of the lower edge of  $\sum p_T$ . Figure 7.8 shows the fifth leading jet  $p_T$  distributions of QCD events in  $1000 \text{ GeV} < \sum p_T < 1500 \text{ GeV}$  and  $2000 \text{ GeV} < \sum p_T < 3000 \text{ GeV}$ . The  $p_T$  of fifth leading jet is relatively small even for large  $\sum p_T$  events.

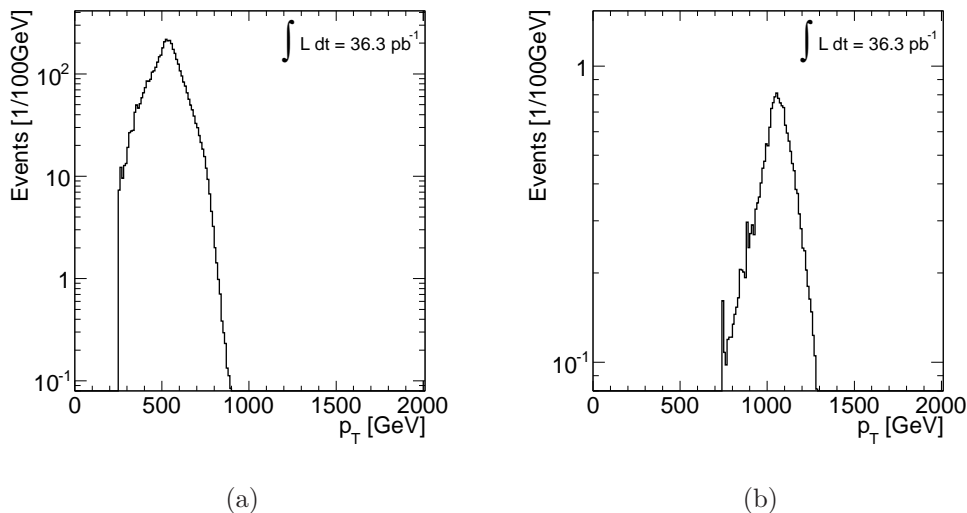


Figure 7.7: Leading jet  $p_T$  distributions of QCD MC events in  $1000 \text{ GeV} < \sum p_T < 1500 \text{ GeV}$  (a) and  $2000 \text{ GeV} < \sum p_T < 3000 \text{ GeV}$  (b)

Figure 7.9 shows the  $\sum p_T$  distributions of QCD MC events for each  $N_J$  bin. The distributions in 7.9(b) are normalized by the number of events in  $\sum p_T > 1000 \text{ GeV}$ . For QCD background events,  $\sum p_T$  distributions depend little on  $N_J$  by requiring  $\sum p_T > 1000 \text{ GeV}$ : the effect of jet  $p_T$  threshold on  $\sum p_T$  is small and  $\sum p_T$  of the event is represented by  $Q^2$  of the hard process. Therefore the ratio of  $\sum p_T$  distributions between  $N_J \geq 5$  and  $N_J < 5$  is stable for  $\sum p_T > 1000 \text{ GeV}$ , as shown in Figure 7.10.

Table 7.5 summarizes the numbers of events in  $N_J \geq 5$  and  $N_J < 5$ , and the ratio between them. The  $\sum p_T$  ranges are divided into 100 GeV-width bins. In the region of  $1100 \text{ GeV} < \sum p_T < 2700 \text{ GeV}$ , where the number of events is expected to be  $> 0.1$ , the ratio of  $N_J \geq 5/N_J < 5$  gives  $0.282 \pm 0.032$ . In this region the ratio is stable within 11.3%. Assuming this relation and no signal, the number of background events in the signal dominant region

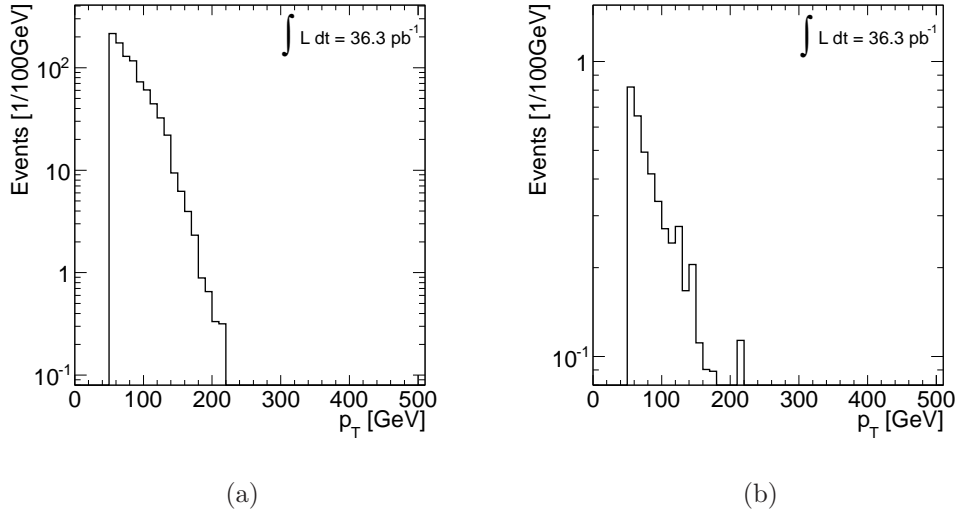


Figure 7.8: Fifth leading jet  $p_T$  distributions of QCD MC events in  $1000 \text{ GeV} < \sum p_T < 1500 \text{ GeV}$  (a) in  $2000 \text{ GeV} < \sum p_T < 3000 \text{ GeV}$  (b)

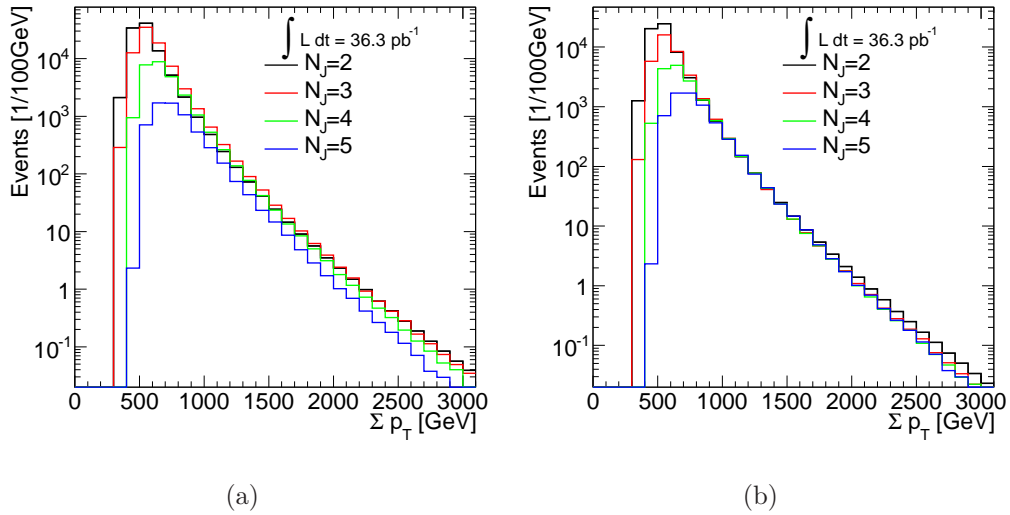


Figure 7.9:  $\sum p_T$  distributions of QCD background for  $N_J = 2 - 5$ . In (b), histograms are normalized by the number of events in  $\sum p_T > 1000 \text{ GeV}$ .

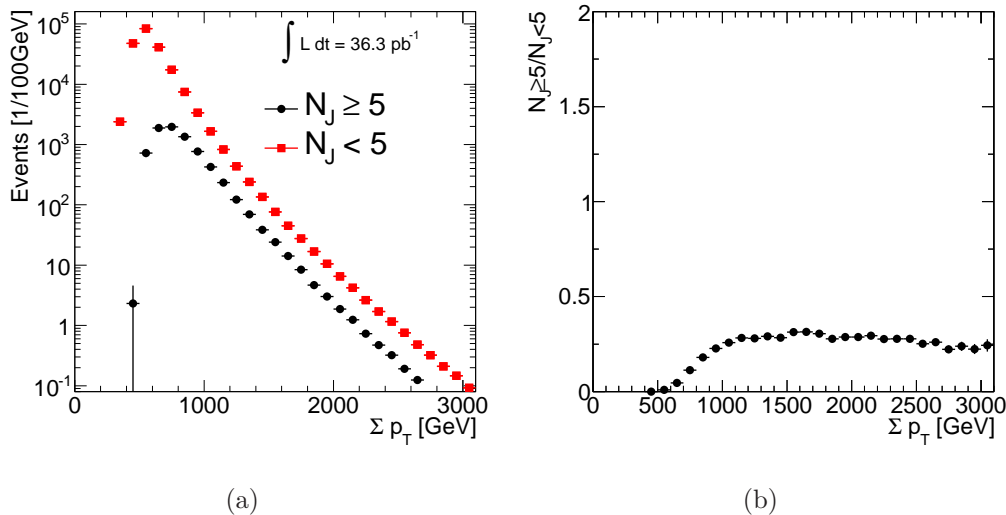


Figure 7.10:  $\sum p_T$  distributions of QCD PYTHIA MC (a) for  $N_J < 5$  (red rectangles) and  $N_J \geq 5$  (black circles), and the ratio of them:  $\sum p_T (N_J \geq 5) / \sum p_T (N_J < 5)$  (b)

given in Eq. 7.1 can be estimated as

$$\mathcal{N} \left( \sum p_T > 2 \text{ TeV}, N_J \geq 5 \right) = \mathcal{N} \left( \sum p_T > 2 \text{ TeV}, N_J < 5 \right) \frac{\mathcal{N} (1.1 < \sum p_T < 1.2 \text{ TeV}, N_J \geq 5)}{\mathcal{N} (1.1 < \sum p_T < 1.2 \text{ TeV}, N_J < 5)}, \quad (7.2)$$

where  $N$  represents the number of events with the criteria given in the bracket.

Figure 7.11 show  $\sum p_T$  distributions of QCD MC events in  $N_J \geq 5$  and  $N_J < 5$ . The histograms are normalized by the number of events in  $1100 < \sum p_T < 1200$  GeV. Two distributions show a reasonable agreement. Table 7.6 gives the numbers of events in  $N_J$ - $\sum p_T$  space. The number of remaining events in  $\sum p_T > 2000$  GeV and an estimation calculated by Eq. 7.2 are  $5.17 \pm 0.12$  and  $5.19 \pm 0.08$ , respectively. The numbers are normalized to  $36.3 \text{ pb}^{-1}$  and the errors show statistical uncertainties of MC events.

In summary,  $\sum p_T$  distributions of QCD events depend little on  $N_J$  in the region above 1100 GeV. In the next chapter, details of the signal extraction method based on this feature are given and mini black hole search is performed.

Table 7.5: The numbers of QCD MC events with  $N_J \geq 5$  and  $N_J < 5$ , and the ratio between them for each  $\sum p_T$  bin. The errors indicate statistical uncertainties of MC events.

$\sum p_T$ Range [GeV]	$N_J \geq 5$	$N_J < 5$	$N_J \geq 5/N_J < 5$
0-100	0.00±0.00	0.00±0.00	0.00±0.00
100-200	0.00±0.00	0.00±0.00	0.00±0.00
200-300	0.00±0.00	0.00±0.00	0.00±0.00
300-400	0.00±0.00	$2.40 \times 10^3 \pm 0.14 \times 10^3$	0.00±0.00
400-500	$2.32 \pm 2.26$	$4.77 \times 10^4 \pm 0.04 \times 10^4$	$4.87 \times 10^{-5} \pm 4.74 \times 10^{-5}$
500-600	$7.22 \times 10^2 \pm 1.04 \times 10^2$	$8.40 \times 10^4 \pm 0.04 \times 10^4$	$8.60 \times 10^{-3} \pm 1.24 \times 10^{-3}$
600-700	$1.88 \times 10^3 \pm 0.08 \times 10^3$	$4.11 \times 10^4 \pm 0.02 \times 10^4$	$4.57 \times 10^{-2} \pm 0.20 \times 10^{-2}$
700-800	$1.96 \times 10^3 \pm 0.05 \times 10^3$	$1.74 \times 10^4 \pm 0.01 \times 10^4$	0.113±0.003
800-900	$1.34 \times 10^3 \pm 0.04 \times 10^3$	$7.46 \times 10^3 \pm 47.4$	$0.18 \pm 5.13 \times 10^{-3}$
900-1000	$7.68 \times 10^2 \pm 0.22 \times 10^2$	$3.37 \times 10^3 \pm 0.02 \times 10^3$	0.228±0.007
1000-1100	$4.27 \times 10^2 \pm 0.12 \times 10^2$	$1.65 \times 10^3 \pm 0.01 \times 10^3$	0.258±0.008
1100-1200	$2.34 \times 10^2 \pm 0.07 \times 10^2$	$8.30 \times 10^2 \pm 0.06 \times 10^2$	0.282±0.009
1200-1300	$1.22 \times 10^2 \pm 0.03 \times 10^2$	$4.35 \times 10^2 \pm 0.03 \times 10^2$	0.28±0.006
1300-1400	$69.7 \pm 1.82$	$2.39 \times 10^2 \pm 0.02 \times 10^2$	0.291±0.008
1400-1500	$38.5 \pm 1.23$	$1.36 \times 10^2 \pm 0.01 \times 10^2$	0.283±0.009
1500-1600	$24 \pm 0.885$	$76.6 \pm 0.805$	0.314±0.012
1600-1700	$14.2 \pm 0.599$	$45 \pm 0.487$	0.314±0.014
1700-1800	$8.43 \pm 0.396$	$27.6 \pm 0.329$	0.305±0.014
1800-1900	$4.67 \pm 0.201$	$16.8 \pm 0.201$	0.277±0.012
1900-2000	$3.03 \pm 0.145$	$10.5 \pm 0.143$	0.288±0.014
2000-2100	$1.87 \pm 0.09$	$6.51 \pm 0.08$	0.288±0.015
2100-2200	$1.24 \pm 0.07$	$4.22 \pm 0.06$	0.294±0.017
2200-2300	$0.731 \pm 0.025$	$2.64 \pm 0.042$	0.277±0.011
2300-2400	$0.472 \pm 0.020$	$1.7 \pm 0.029$	0.277±0.013
2400-2500	$0.321 \pm 0.016$	$1.16 \pm 0.021$	0.278±0.015
2500-2600	$0.19 \pm 0.012$	$0.757 \pm 0.014$	0.251±0.016
2600-2700	$0.125 \pm 0.089$	$0.480 \pm 0.096$	0.261±0.019
2700-2800	$7.15 \times 10^{-2} \pm 0.61 \times 10^{-2}$	$0.321 \pm 0.007$	0.222±0.020
2800-2900	$5.00 \times 10^{-2} \pm 0.49 \times 10^{-2}$	$0.21 \pm 0.005$	0.238±0.024

Table 7.6: Number of expected events in each region for PYTHIA MC events. The errors represent statistical uncertainties of MC events.

$\sum p_T$ [GeV]	1100 to 1200	> 2000
$N_J \geq 5$	$2.34 \times 10^2 \pm 7$	$5.17 \pm 0.12$
$N_J < 5$	$8.30 \times 10^2 \pm 6$	$18.4 \pm 0.1$

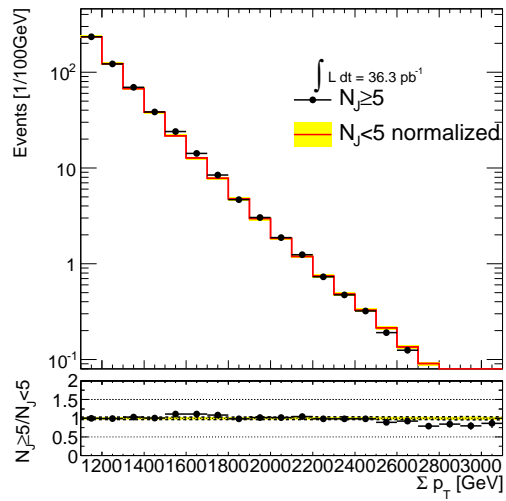


Figure 7.11:  $\sum p_T$  distributions of QCD PYTHIA MC for  $N_J < 5$  (circles) and  $N_J \geq 5$  (histogram). The histogram is normalized by events in  $1100 < \sum p_T < 1200$  GeV. The yellow error band represents a statistical uncertainty of MC events.

# Chapter 8

## Search for the Mini Black Hole

This chapter describes details of the mini black hole search in the multijet final state. First, observed events and QCD MC events are compared. Second, a method to measure the signal yield is described. Then, systematic uncertainties and validation results on the analysis method are summarized.

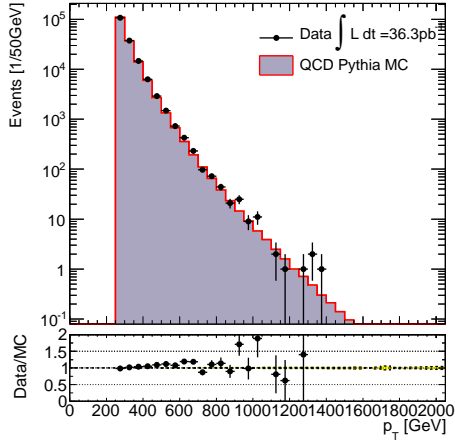
### 8.1 Jets in Observed Events

The QCD process primarily contributes to background events in the search with the multijet final states. The distributions of jets in observed events are compared to QCD MC events. All the histograms of QCD MC events are normalized to the numbers of observed events. In this section, the shapes related to jets in data events are compared to QCD MC events.

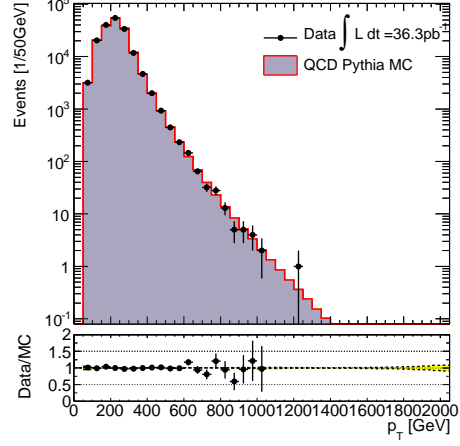
Figures 8.1-8.3 show  $p_T$  distributions of the leading five jets and  $N_J$  distributions for data and QCD PYTHIA MC events. The yellow error bands of histograms indicate statistical uncertainties of MC events. The data shows a reasonable agreement with QCD MC events in each figure.

Figure 8.4 shows  $\sum p_T$  distribution of data and QCD MC events in the region of  $N_J < 5$  in which QCD background events are expected to be dominated. They agree in statistical uncertainties.

All the shapes of jets and  $\sum p_T$  in observed events are consistent with QCD background expectations within the statistical uncertainties and no significant excess of signal was found. The next section describes the details of the method to measure the signal yield based on the shape of QCD events.

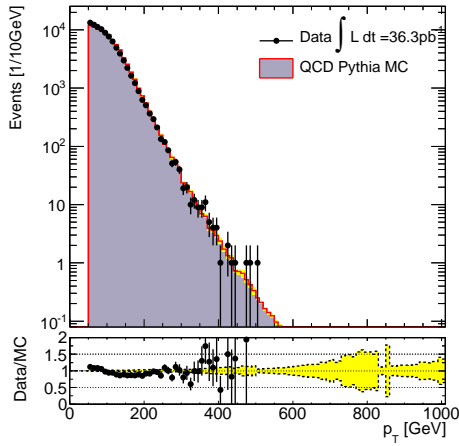


(a)

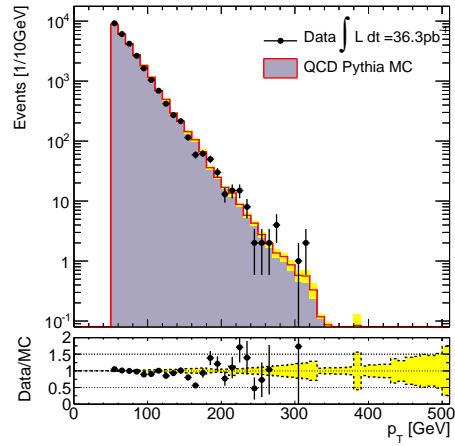


(b)

Figure 8.1:  $p_T$  distributions of leading jet (a) and second leading jet (b) for data and QCD MC events. Yellow error bands represent statistical uncertainties of MC events.



(a)



(b)

Figure 8.2:  $p_T$  distributions of third leading jet (a) and fourth leading jet (b) for data and QCD MC events. Yellow error bands represent statistical uncertainties of MC events.

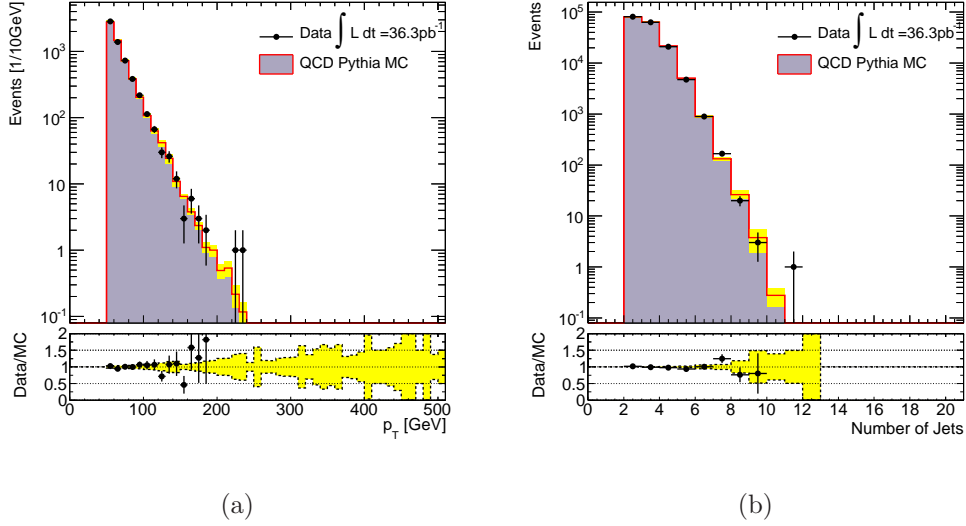


Figure 8.3:  $p_T$  distribution of fifth leading jet (a) and  $N_J$  distribution for data and QCD MC events. Yellow error bands represent statistical uncertainties of MC events.

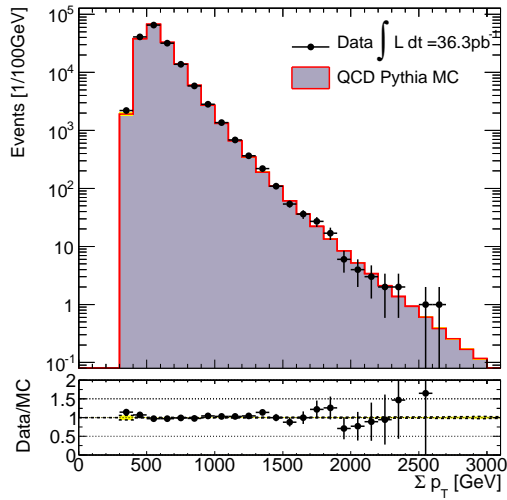


Figure 8.4:  $\sum p_T$  distributions of  $N_J < 5$  for data and QCD PYTHIA MC events. Yellow error bands represent statistical uncertainties of MC events.

## 8.2 Extraction of Signal Yield

As described in the previous chapter,  $N_J$  and  $\sum p_T$  gives a good discrimination performance between black hole signal and QCD background events; their yields are extracted with a simultaneous fit in different  $N_J$ - $\sum p_T$  regions. Four regions ( $\mathcal{R}_i; i = 0, 1, 2, 3$ ) in  $N_J$ - $\sum p_T$  plane are defined as follows:

$$\begin{aligned}
 \mathcal{R}_0 : & 1100 \text{ GeV} < \sum p_T < 1200 \text{ GeV}, \quad N_J < 5, \\
 \mathcal{R}_1 : & 1100 \text{ GeV} < \sum p_T < 1200 \text{ GeV}, \quad N_J \geq 5, \\
 \mathcal{R}_2 : & \sum p_T > 2000 \text{ GeV}, \quad N_J < 5, \\
 \mathcal{R}_3 : & \sum p_T > 2000 \text{ GeV}, \quad N_J \geq 5.
 \end{aligned} \tag{8.1}$$

Figure 8.5 shows an illustration of four regions. The number of observed events in  $\mathcal{R}_i$  is represented as  $d_i$ .

The expected number of events in each region,  $\mu_i$ , is written as follows

$$\mu_i = b_i + s_i, \tag{8.2}$$

where  $b_i$  and  $s_i$  are the numbers of expected background and signal events in  $\mathcal{R}_i$ , respectively.

As discussed in Section 7.3, the following expression is given under the assumption that the shape of  $\sum p_T$  spectrum does not depend on  $N_J$ :

$$\frac{b_1}{b_0} \simeq \frac{b_3}{b_2}. \tag{8.3}$$

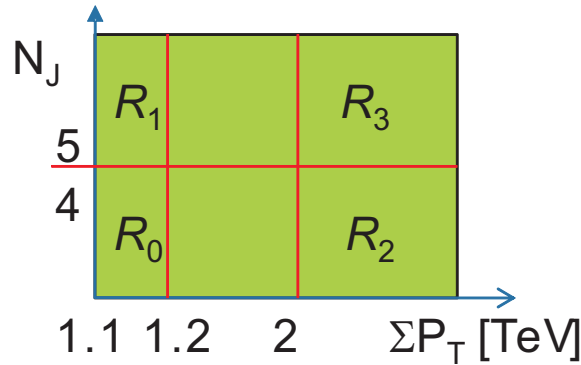


Figure 8.5: Illustration of four regions in  $N_J$  -  $\sum p_T$  plane

Assuming this relation,  $b_{1,2,3}$  is formed as

$$b_1 = f_1 b_0, \quad (8.4)$$

$$b_2 = f_2 b_0, \quad (8.5)$$

$$b_3 = f_1 f_2 b_0, \quad (8.6)$$

where  $f_1$  ( $f_2$ ) is the ratio of  $b_1$  ( $b_2$ ) to  $b_0$ . With incorporation of signal strength  $s'$ , the expected number of events in each region ( $\mu_i$ ) is represented as

$$\begin{aligned} \mu_0 &= b_0 + s' s_0^{\text{th}}, \\ \mu_1 &= f_1 b_0 + s' s_1^{\text{th}}, \\ \mu_2 &= f_2 b_0 + s' s_2^{\text{th}}, \\ \mu_3 &= f_1 f_2 b_0 + s' s_3^{\text{th}}. \end{aligned} \quad (8.7)$$

where  $s_i^{\text{th}}$  is the expected number of signal event in  $\mathcal{R}_i$  for a certain black hole model.

With variables described above, the likelihood function,  $\mathcal{L}$ , is constructed as

$$\mathcal{L} = \prod_{i=0}^3 \frac{(\mu_i)^{d_i}}{d_i!} \exp(-\mu_i). \quad (8.8)$$

In this formula,  $s'$  is the parameter of interest and  $b_0$ ,  $f_1$  and  $f_2$  are the nuisance parameters. In order to determine the signal yield, a statistical test is performed based on the profile likelihood ratio represented as

$$\lambda(s') = \frac{\mathcal{L}(s', \hat{\nu}(s'))}{\mathcal{L}(\hat{s}', \hat{\nu})}, \quad (8.9)$$

where  $\nu$  shows all of the nuisance parameters. Here  $\hat{\nu}$  in the numerator denotes the values of  $\nu$  that maximizes  $\mathcal{L}$  for a given  $s'$ . The denominator is the maximized likelihood function in which  $\hat{s}'$  and  $\hat{\nu}$  are their maximum likelihood estimators. With the test statistics,  $-\log \lambda(s')$ , an interval of  $s'$  for the required CL, 95 % for instance, is defined as an ensemble of  $s'$  satisfying the following:

$$-\log \lambda(s') < 1.92. \quad (8.10)$$

## 8.3 Incorporating Systematic Uncertainties

The QCD background shape of the data in  $\sum p_T$ - $N_J$  plane could differ from the MC expectation, which results in a partial invalidity of Eq. 8.6. In order to account for this effect, the uncertainty of QCD background shape is incorporated as follows:

$$b_3 = (1 + f^{\text{sys}}) f_1 f_2 b_0, \quad (8.11)$$

where  $f^{\text{sys}}$  is the systematic parameter of QCD background shape on  $f_1 f_2$ . The uncertainty of signal normalization is similarly incorporated as follows:

$$s_i = s' (1 + s_i^{\text{sys}}) s_i^{\text{th}}, \quad (8.12)$$

where  $s_i^{\text{sys}}$  is the systematic parameter on the signal normalization for each  $\mathcal{R}_i$ .

Incorporating all the systematic uncertainties, the resulting likelihood function is represented as

$$\mathcal{L} = \prod_{i=0}^3 \frac{(\mu_i)^{d_i}}{d_i!} \exp(-\mu_i) \cdot G(f^{\text{sys}}|0, \Delta f^{\text{sys}}) \cdot \prod_{i=0}^3 G(s_i^{\text{sys}}|0, \Delta s_i^{\text{sys}}), \quad (8.13)$$

where  $G(x|a, b)$  represents Gaussian function of  $x$  with mean  $a$  and variance  $b^2$ . Here  $\Delta f^{\text{sys}}$  and  $\Delta s_i^{\text{sys}}$  represent the total uncertainties on  $f_1 f_2$  and  $s'$ , respectively. Possible sources of systematic uncertainty are summarized in the following section.

## 8.4 Systematic Uncertainties

The systematic uncertainties of background shape and signal normalization are evaluated.

### 8.4.1 Uncertainties of background shape

The test statistics given in Eq 8.9 is calculated assuming the validity of the relation Eq 8.3. Therefore, the systematic uncertainties could originate from the description of QCD background process. This section covers the systematic uncertainties related to the QCD background shape.

#### $N_J \geq 5 / N_J < 5$ Ratio Stability

In Table 7.5 in Section 7.3, the ratio of events between  $N_J \geq 5$  and  $N_J < 5$  shows a stability of 11.3% for  $\sum p_T$  above 1100 GeV; this is assigned as a systematic uncertainty of QCD background shape.

## Jet Energy Scale Uncertainty

The jet energy scale is determined with an uncertainty smaller than 7% [120]. The numbers of events in  $\mathcal{R}_i$  is affected by the jet energy scale. This effect is checked by shifting the jet energies in QCD MC events within their uncertainties. Table 8.1 and 8.2 show the numbers of remaining events in each  $\mathcal{R}_i$ , and resulting  $\Delta f^{\text{sys}}$  estimated with positive and negative jet energy shifts, respectively. The  $\Delta f^{\text{sys}}$  changes by 2.0% at a maximum.

Table 8.1: Number of events in four regions estimated with the negative jet energy shift. The errors represent statistical uncertainties of MC events.

$\sum p_{\text{T}}$ [GeV]	1100 to 1200		> 2000	
$N_{\text{J}} \geq 5$	$1.40 \times 10^2$	$\pm 0.03 \times 10^2$	2.78	$\pm 0.05$
$N_{\text{J}} < 5$	$5.70 \times 10^2$	$\pm 0.04 \times 10^2$	11.2	$\pm 0.1$
$\Delta f^{\text{sys}} = 0.006$				

Table 8.2: Number of events in four regions estimated with the positive jet energy shift. The errors represent statistical uncertainties of MC events.

$\sum p_{\text{T}}$ [GeV]	1100 to 1200		> 2000	
$N_{\text{J}} \geq 5$	$3.53 \times 10^2$	$\pm 0.10 \times 10^2$	8.98	$\pm 0.19$
$N_{\text{J}} < 5$	$1.17 \times 10^3$	$\pm 0.01 \times 10^3$	29.2	$\pm 0.2$
$\Delta f^{\text{sys}} = 0.020$				

## Jet Energy Resolution Uncertainty

The jet energy resolutions estimated from the collision data are summarized in [119], which shows an agreement with the MC simulation within 14%. Table 8.3 shows the number of events in each  $\mathcal{R}_i$  with additional 14% resolution. The  $\Delta f^{\text{sys}}$  changes by 1.7%.

## Comparison with ALPGEN QCD MC

The PYTHIA MC sample does not contain any full higher-order matrix elements. The lowest-order matrix elements are combined with parton showers. On the other hand, QCD ALPGEN sample contains higher-order matrix elements. Here, the difference of two MC generators is assigned as a systematic

Table 8.3: Number of events in four regions estimated with additional 14 % resolution. The errors represent statistical uncertainties of MC events.

$\sum p_T$ [GeV]	1100 to 1200		> 2000	
$N_J \geq 5$	$2.45 \times 10^2$	$\pm 0.09 \times 10^2$	6.28	$\pm 0.19$
$N_J < 5$	$9.46 \times 10^2$	$\pm 0.08 \times 10^2$	23.8	$\pm 0.2$
$\Delta f^{\text{sys}} = 0.017$				

uncertainty related to the description of hard process. Table 8.4 shows the number of events in each  $\mathcal{R}_i$  and resulting  $\Delta f^{\text{sys}}$  for QCD ALPGEN MC events. Figure 8.6 shows  $\sum p_T$  distributions of QCD ALPGEN MC events in  $N_J \geq 5$  and  $N_J < 5$ . The distributions are normalized by the number of events in  $1100 < \sum p_T < 1200$  GeV. The yellow error band shows a statistical uncertainty of MC events. The uncertainty due to the description of hard process is estimated to be 23.5 %.

Table 8.4: Number of events in four regions of QCD ALPGEN MC sample. The errors represent statistical error of MC events.

$\sum p_T$ [GeV]	1100 to 1200		> 2000	
$N_J \geq 5$	$2.10 \times 10^2$	$\pm 0.17 \times 10^2$	5.67	$\pm 1.47$
$N_J < 5$	$7.73 \times 10^2$	$\pm 0.24 \times 10^2$	16.9	$\pm 2.6$
$\Delta f^{\text{sys}} = 0.235$				

### Uncertainty on PDFs

The MC generators adopt PDFs to simulate collision events. The MC events generated by PYTHIA are proceeded with PDFs of MRST2007. The PDFs of CTEQ66 have an error set while that of MRST2007 is not prepared. Therefore, the uncertainties are evaluated the central value of MRST2007 with the errors of CTEQ66. Figure 8.7 shows  $\sum p_T$  distributions of QCD PYTHIA MC events in  $N_J < 5$  and  $N_J \geq 5$ . A solid line shows PYTHIA QCD events with MRST2007/ Dashed and dot-dashed lines show the events generated with CTEQ66 and uncertainties estimated with its error set, respectively. Table 8.5 shows the number of events in each region and resulting  $\Delta f^{\text{sys}}$  obtained from QCD PYTHIA MC events with CTEQ66. An uncertainty of 14.0 % is estimated. With the CTEQ66 error set,  $f^{\text{sys}}$  changes by 4.2 %. Therefore, the total uncertainty on PDFs is quoted as 14.6 %.

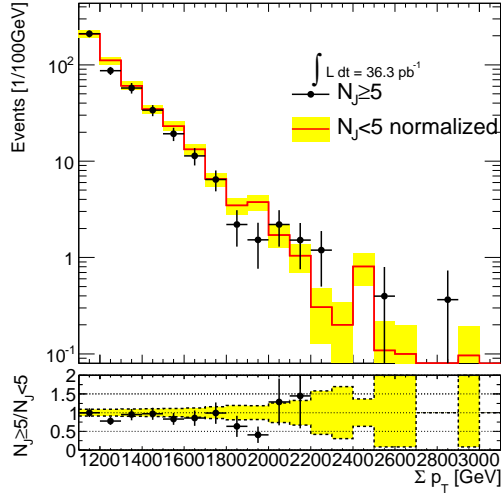


Figure 8.6:  $\sum p_T$  distributions of QCD ALPGEN MC for the event in  $N_J < 5$  (circles) and  $N_J \geq 5$  (histogram). The histograms are normalized by the number of events in  $1100 < \sum p_T < 1200$  GeV. The yellow error band represents a statistical uncertainty of MC events.

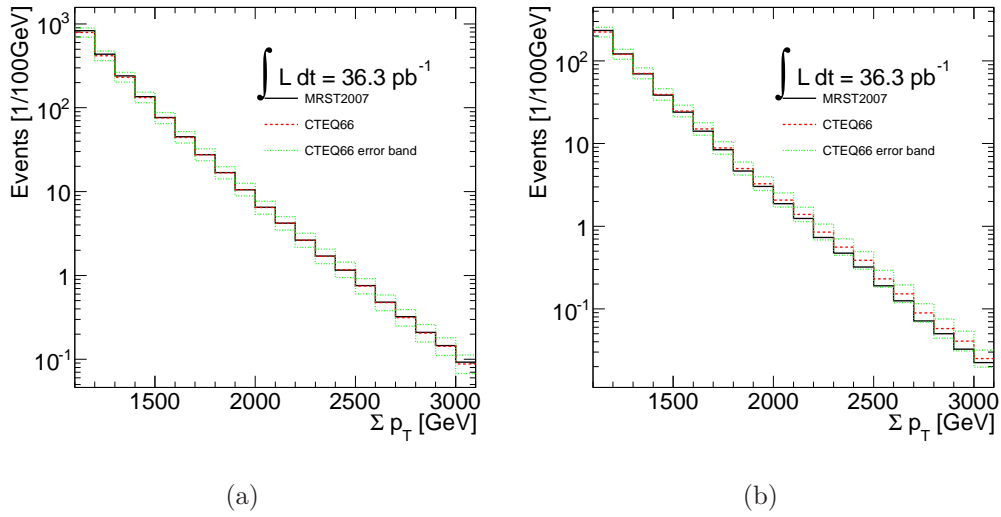


Figure 8.7:  $\sum p_T$  distributions in  $N_J < 5$  (a) and  $N_J \geq 5$  of QCD PYTHIA sample. A solid line shows the events generated with MRST2007, a dash line shows the events generated with CTEQ66 and dash-dot lines show the error band obtained from CTEQ66 error set.

Table 8.5: Number of events in four regions of QCD PYTHIA MC events with CTEQ66. The errors represent statistical errors of MC events.

$\sum p_T$ [GeV]	1100 to 1200	> 2000
$N_J \geq 5$	$2.23 \times 10^2 \pm 0.07 \times 10^2$	$5.91 \pm 0.13$
$N_J < 5$	$7.89 \times 10^2 \pm 0.06 \times 10^2$	$18.3 \pm 0.1$
$\Delta f^{\text{sys}} = 0.140$		

### Other Standard Model Backgrounds

The contributions of  $t\bar{t}$ ,  $Z + \text{jets}$  and  $W + \text{jets}$  processes are checked. Figure 8.8 shows  $\sum p_T$  distributions in  $N_J < 5$  (a) and  $N_J \geq 5$  (b) for QCD,  $t\bar{t}$ ,  $Z + \text{jets}$  and  $W + \text{jets}$  processes. Table 8.6 shows the number of events obtained from MC events including all SM processes. A change of 0.1% on  $f_1 f_2$  is estimated.

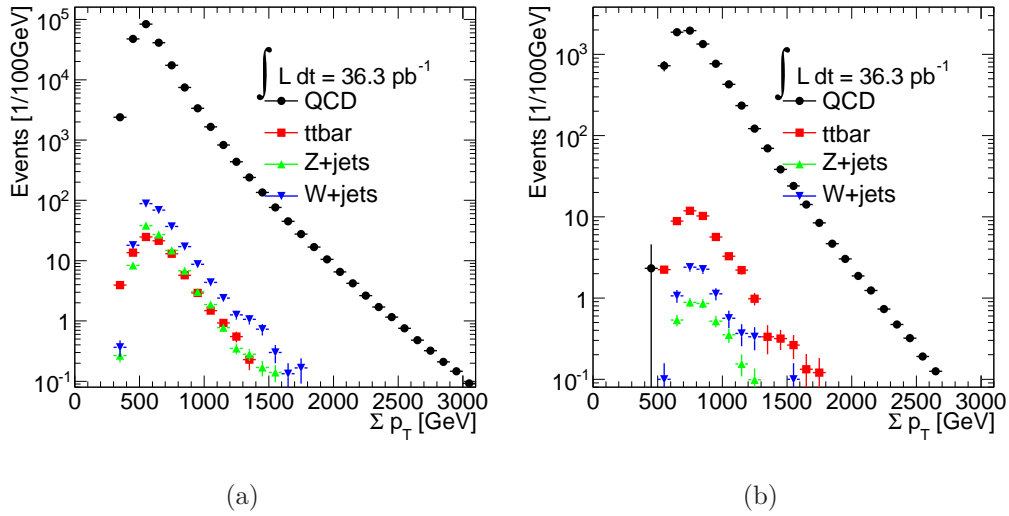


Figure 8.8:  $\sum p_T$  distributions in  $N_J < 5$  (a) and  $N_J \geq 5$  (b) for QCD,  $t\bar{t}$ ,  $Z + \text{jets}$  and  $W + \text{jets}$  processes

### Summary of the Background Shape Uncertainties

Table 8.7 shows the summary of the background shape uncertainties. In total, an uncertainty of 30.0% is quoted.

Table 8.6: Number of events in four regions. The MC events of QCD PYTHIA,  $t\bar{t}$ ,  $Z$  + jets and  $W$  + jets are summed.

$\sum p_T$ [GeV]	1100 to 1200	> 2000
$N_J \geq 5$	$2.37 \times 10^2 \pm 0.07 \times 10^2$	$5.28 \pm 0.13$
$N_J < 5$	$8.34 \times 10^2 \pm 0.06 \times 10^2$	$18.6 \pm 0.1$
$\Delta f^{\text{sys}} = -0.001$		

Table 8.7: Systematic uncertainties of the background shape

Source of Systematic Uncertainty	Uncertainty [%]
$\sum p_T$ dependence of ratio	11.3
Jet Energy Scale	2.0
Jet Energy Resolution	1.7
Physics model description	23.5
PDFs	14.6
Other background contribution	0.1
Total	30.0

## 8.4.2 Uncertainties in Signal Normalization

### Uncertainties in Acceptance

The acceptance of the mini black hole signal events could alter by the jet energy scale and resolution. These uncertainties are estimated in a similar way as described before. Systematic uncertainties in the signal acceptance are estimated by changing jet energy scales and resolutions within their uncertainties, including statistical uncertainties of MC events. Table 8.8-8.11 (8.12-8.15) show the expected number of events and their uncertainties for various signal points on the assumption of  $\lambda < r_s$  ( $\lambda < r_h$ ).

### Luminosity Uncertainty

The integrated luminosity is determined by the measurement with the LUCID detector as described in Section 3.7 and uncertainty is estimated to be 11.0% [91].

Table 8.8: Number of expected events in  $\mathcal{R}_0$  for each signal models on the assumption  $\lambda < r_s$ . The error indicates the uncertainty originating from the statistics of MC events, jet energy scale and jet resolution. The signal model corresponding to each abbreviation is given in Table 4.1.

Signal point	$s_{\text{th0}}$	MC Statistics	Jet Energy Scale	Jet Resolution
rs_2_800	0.381	$\pm 0.11$	$\pm 0.317$	$\pm 0.159$
rs_2_1000	$5.95 \times 10^{-3}$	$\pm 2.1 \times 10^{-3}$	$\pm 2.23 \times 10^{-3}$	$\pm 3.72 \times 10^{-3}$
rs_2_1200	$5.13 \times 10^{-5}$	$\pm 1.94 \times 10^{-5}$	$\pm 1.47 \times 10^{-5}$	$\pm 2.2 \times 10^{-5}$
rs_3_800	12	$\pm 2.2$	$\pm 3.3$	$\pm 0$
rs_3_1000	0.295	$\pm 0.089$	$\pm 0.187$	$\pm 0.054$
rs_3_1200	$1.63 \times 10^{-2}$	$\pm 0.47 \times 10^{-2}$	$\pm 0.68 \times 10^{-2}$	$\pm 0.82 \times 10^{-2}$
rs_3_1500	$1.07 \times 10^{-5}$	$\pm 0.75 \times 10^{-5}$	$\pm 3.73 \times 10^{-5}$	$\pm 1.6 \times 10^{-5}$
rs_4_800	85.7	$\pm 13.4$	$\pm 46$	$\pm 14.6$
rs_4_1000	5.39	$\pm 1.08$	$\pm 1.73$	$\pm 1.29$
rs_4_1200	0.396	$\pm 0.091$	$\pm 0.063$	$\pm 0.063$
rs_4_1500	$7.02 \times 10^{-3}$	$\pm 1.7 \times 10^{-3}$	$\pm 3.72 \times 10^{-3}$	$\pm 0.83 \times 10^{-3}$
rs_4_2000	$2.22 \times 10^{-7}$	$\pm 0.84 \times 10^{-7}$	$\pm 1.27 \times 10^{-7}$	$\pm 0.32 \times 10^{-7}$
rs_5_800	$4.29 \times 10^2$	$\pm 0.53 \times 10^2$	$\pm 0.19 \times 10^2$	$\pm 0.91 \times 10^2$
rs_5_1000	37.7	$\pm 5.8$	$\pm 5.4$	$\pm 3.6$
rs_5_1200	3.99	$\pm 0.69$	$\pm 0.97$	$\pm 0.24$
rs_5_1500	$9.97 \times 10^{-2}$	$\pm 2.29 \times 10^{-2}$	$\pm 1.57 \times 10^{-2}$	$\pm 2.1 \times 10^{-2}$
rs_5_2000	$7.73 \times 10^{-5}$	$\pm 2.44 \times 10^{-5}$	$\pm 2.32 \times 10^{-5}$	$\pm 3.09 \times 10^{-5}$
rs_6_800	$1.55 \times 10^3$	$\pm 0.16 \times 10^3$	$\pm 0.33 \times 10^3$	$\pm 0.02 \times 10^3$
rs_6_1000	$1.09 \times 10^2$	$\pm 0.17 \times 10^2$	$\pm 0.38 \times 10^2$	$\pm 0.15 \times 10^2$
rs_6_1200	22.4	$\pm 3.1$	$\pm 8.6$	$\pm 3.5$
rs_6_1500	0.627	$\pm 0.134$	$\pm 0.313$	$\pm 0.085$
rs_6_2000	$1.62 \times 10^{-3}$	$\pm 0.51 \times 10^{-3}$	$\pm 0.97 \times 10^{-3}$	$\pm 0.16 \times 10^{-3}$
rs_7_800	$3.95 \times 10^3$	$\pm 0.35 \times 10^3$	$\pm 1.03 \times 10^3$	$\pm 0.37 \times 10^3$
rs_7_1000	$4.61 \times 10^2$	$\pm 0.51 \times 10^2$	$\pm 1.01 \times 10^2$	$\pm 0.67 \times 10^2$
rs_7_1200	60.7	$\pm 8.3$	$\pm 12.4$	$\pm 7.9$
rs_7_1500	3.54	$\pm 0.6$	$\pm 0.81$	$\pm 0.4$
rs_7_2000	$1.62 \times 10^{-2}$	$\pm 0.45 \times 10^{-2}$	$\pm 0.75 \times 10^{-2}$	$\pm 0.37 \times 10^{-2}$

Table 8.9: Number of expected events in  $\mathcal{R}_1$  for each signal models on the assumption  $\lambda < r_s$ . The error indicates the uncertainty originating from the statistics of MC events, jet energy scale and jet resolution. The signal model corresponding to each abbreviation is given in Table 4.1.

Signal point	$s_{\text{th1}}$	MC Statistics	Jet Energy Scale	Jet Resolution
rs_2_800	0.317	$\pm 0.1$	$\pm 0.19$	$\pm 0.127$
rs_2_1000	$2.23 \times 10^{-3}$	$\pm 1.29 \times 10^{-3}$	$\pm 2.98 \times 10^{-3}$	$\pm 0 \times 10^{-3}$
rs_2_1200	$2.93 \times 10^{-5}$	$\pm 1.47 \times 10^{-5}$	$\pm 1.47 \times 10^{-5}$	$\pm 1.47 \times 10^{-5}$
rs_3_800	17.4	$\pm 2.7$	$\pm 7.1$	$\pm 0.4$
rs_3_1000	0.268	$\pm 0.085$	$\pm 0.214$	$\pm 0.268$
rs_3_1200	$2.72 \times 10^{-3}$	$\pm 1.92 \times 10^{-3}$	$\pm 5.44 \times 10^{-3}$	$\pm 0 \times 10^{-3}$
rs_3_1500	$1.6 \times 10^{-5}$	$\pm 0.92 \times 10^{-5}$	$\pm 1.07 \times 10^{-5}$	$\pm 0.53 \times 10^{-5}$
rs_4_800	$1.61 \times 10^2$	$\pm 0.18 \times 10^2$	$\pm 0.86 \times 10^2$	$\pm 0.25 \times 10^2$
rs_4_1000	8.2	$\pm 1.33$	$\pm 1.73$	$\pm 2.16$
rs_4_1200	0.229	$\pm 0.069$	$\pm 0.167$	$\pm 0.063$
rs_4_1500	$1.24 \times 10^{-3}$	$\pm 0.72 \times 10^{-3}$	$\pm 0 \times 10^{-3}$	$\pm 0 \times 10^{-3}$
rs_4_2000	$3.17 \times 10^{-8}$	$\pm 3.17 \times 10^{-8}$	$\pm 3.17 \times 10^{-8}$	$\pm 0 \times 10^{-8}$
rs_5_800	$7.34 \times 10^2$	$\pm 0.69 \times 10^2$	$\pm 2.27 \times 10^2$	$\pm 0.65 \times 10^2$
rs_5_1000	45.7	$\pm 6.4$	$\pm 12.6$	$\pm 3.6$
rs_5_1200	4.11	$\pm 0.7$	$\pm 0.97$	$\pm 0.12$
rs_5_1500	$4.72 \times 10^{-2}$	$\pm 1.57 \times 10^{-2}$	$\pm 2.62 \times 10^{-2}$	$\pm 0.52 \times 10^{-2}$
rs_5_2000	$1.55 \times 10^{-5}$	$\pm 1.09 \times 10^{-5}$	$\pm 1.55 \times 10^{-5}$	$\pm 0.77 \times 10^{-5}$
rs_6_800	$3.13 \times 10^3$	$\pm 0.22 \times 10^3$	$\pm 0.69 \times 10^3$	$\pm 0.02 \times 10^3$
rs_6_1000	$1.78 \times 10^2$	$\pm 0.21 \times 10^2$	$\pm 0.66 \times 10^2$	$\pm 0.46 \times 10^2$
rs_6_1200	19.4	$\pm 2.9$	$\pm 4.7$	$\pm 0.4$
rs_6_1500	0.228	$\pm 0.081$	$\pm 0.256$	$\pm 0.256$
rs_6_2000	$9.72 \times 10^{-4}$	$\pm 3.97 \times 10^{-4}$	$\pm 3.24 \times 10^{-4}$	$\pm 3.24 \times 10^{-4}$
rs_7_800	$7.49 \times 10^3$	$\pm 0.48 \times 10^3$	$\pm 1.46 \times 10^3$	$\pm 0.37 \times 10^3$
rs_7_1000	$7.03 \times 10^2$	$\pm 0.63 \times 10^2$	$\pm 2.19 \times 10^2$	$\pm 0.34 \times 10^2$
rs_7_1200	57.3	$\pm 8$	$\pm 14.6$	$\pm 4.5$
rs_7_1500	2.33	$\pm 0.48$	$\pm 1.82$	$\pm 0.1$
rs_7_2000	$8.71 \times 10^{-3}$	$\pm 3.29 \times 10^{-3}$	$\pm 2.49 \times 10^{-3}$	$\pm 0 \times 10^{-3}$

Table 8.10: Number of expected events in  $\mathcal{R}_2$  for each signal models on the assumption  $\lambda < r_s$ . The error indicates the uncertainty originating from the statistics of MC events, jet energy scale and jet resolution. The signal model corresponding to each abbreviation is given in Table 4.1.

Signal point	$s_{\text{th}2}$	MC Statistics	Jet Energy Scale	Jet Resolution
rs_2.800	11.4	$\pm 0.6$	$\pm 0.5$	$\pm 0.3$
rs_2.1000	0.35	$\pm 0.016$	$\pm 0.013$	$\pm 0.008$
rs_2.1200	$4.31 \times 10^{-3}$	$\pm 0.18 \times 10^{-3}$	$\pm 0.02 \times 10^{-3}$	$\pm 0.02 \times 10^{-3}$
rs_3.800	$1.71 \times 10^2$	$\pm 0.08 \times 10^2$	$\pm 0.11 \times 10^2$	$\pm 0.05 \times 10^2$
rs_3.1000	15.4	$\pm 0.6$	$\pm 0.1$	$\pm 0.1$
rs_3.1200	0.876	$\pm 0.035$	$\pm 0.023$	$\pm 0.012$
rs_3.1500	$4.17 \times 10^{-3}$	$\pm 0.15 \times 10^{-3}$	$\pm 0.07 \times 10^{-3}$	$\pm 0.005 \times 10^{-3}$
rs_4.800	$7.63 \times 10^2$	$\pm 0.4 \times 10^2$	$\pm 1.4 \times 10^2$	$\pm 0.1 \times 10^2$
rs_4.1000	$1.32 \times 10^2$	$\pm 0.05 \times 10^2$	$\pm 0.05 \times 10^2$	$\pm 0.009 \times 10^2$
rs_4.1200	15.4	$\pm 0.6$	$\pm 0.3$	$\pm 0.3$
rs_4.1500	0.35	$\pm 0.012$	$\pm 0.003$	$\pm 0.002$
rs_4.2000	$3.28 \times 10^{-5}$	$\pm 0.1 \times 10^{-5}$	$\pm 0.05 \times 10^{-5}$	$\pm 0.03 \times 10^{-5}$
rs_5.800	$1.72 \times 10^3$	$\pm 0.11 \times 10^3$	$\pm 0.53 \times 10^3$	$\pm 0.19 \times 10^3$
rs_5.1000	$4.87 \times 10^2$	$\pm 0.21 \times 10^2$	$\pm 0.58 \times 10^2$	$\pm 0.19 \times 10^2$
rs_5.1200	90.3	$\pm 3.3$	$\pm 3.9$	$\pm 1$
rs_5.1500	4.7	$\pm 0.16$	$\pm 0.06$	$\pm 0.05$
rs_5.2000	$8.57 \times 10^{-3}$	$\pm 0.26 \times 10^{-3}$	$\pm 0.14 \times 10^{-3}$	$\pm 0.12 \times 10^{-3}$
rs_6.800	$2.29 \times 10^3$	$\pm 0.19 \times 10^3$	$\pm 0.89 \times 10^3$	$\pm 0.13 \times 10^3$
rs_6.1000	$1.16 \times 10^3$	$\pm 0.05 \times 10^3$	$\pm 0.23 \times 10^3$	$\pm 0.003 \times 10^3$
rs_6.1200	$2.86 \times 10^2$	$\pm 0.11 \times 10^2$	$\pm 0.21 \times 10^2$	$\pm 0.02 \times 10^2$
rs_6.1500	25.4	$\pm 0.9$	$\pm 0.2$	$\pm 0.06$
rs_6.2000	0.189	$\pm 0.006$	$\pm 0.003$	$\pm 0.0003$
rs_7.800	$3.36 \times 10^3$	$\pm 0.32 \times 10^3$	$\pm 1.21 \times 10^3$	$\pm 0.53 \times 10^3$
rs_7.1000	$1.79 \times 10^3$	$\pm 0.1 \times 10^3$	$\pm 0.56 \times 10^3$	$\pm 2e - 08 \times 10^3$
rs_7.1200	$7.08 \times 10^2$	$\pm 0.28 \times 10^2$	$\pm 0.85 \times 10^2$	$\pm 0.03 \times 10^2$
rs_7.1500	89.2	$\pm 3$	$\pm 3.3$	$\pm 1.5$
rs_7.2000	1.44	$\pm 0.04$	$\pm 0.01$	$\pm 0.01$

Table 8.11: Number of expected events in  $\mathcal{R}_3$  for each signal models on the assumption  $\lambda < r_s$ . The error indicates the uncertainty originating from the statistics of MC events, jet energy scale and jet resolution. The signal model corresponding to each abbreviation is given in Table 4.1.

Signal point	$s_{\text{th3}}$	MC Statistics	Jet Energy Scale	Jet Resolution
rs_2.800	$1.02 \times 10^2$	$\pm 0.02 \times 10^2$	$\pm 0.08 \times 10^2$	$\pm 0.02 \times 10^2$
rs_2.1000	2.65	$\pm 0.04$	$\pm 0.09$	$\pm 0.02$
rs_2.1200	$2.68 \times 10^{-2}$	$\pm 0.04 \times 10^{-2}$	$\pm 0.03 \times 10^{-2}$	$\pm 0.001 \times 10^{-2}$
rs_3.800	$9.1 \times 10^2$	$\pm 0.19 \times 10^2$	$\pm 1.49 \times 10^2$	$\pm 0.17 \times 10^2$
rs_3.1000	81.8	$\pm 1.5$	$\pm 5.5$	$\pm 0.5$
rs_3.1200	4.63	$\pm 0.08$	$\pm 0.15$	$\pm 0.04$
rs_3.1500	$1.82 \times 10^{-2}$	$\pm 0.03 \times 10^{-2}$	$\pm 0.02 \times 10^{-2}$	$\pm 0.005 \times 10^{-2}$
rs_4.800	$2.84 \times 10^3$	$\pm 0.08 \times 10^3$	$\pm 0.78 \times 10^3$	$\pm 0.03 \times 10^3$
rs_4.1000	$5.09 \times 10^2$	$\pm 0.1 \times 10^2$	$\pm 0.63 \times 10^2$	$\pm 0.04 \times 10^2$
rs_4.1200	61.2	$\pm 1.1$	$\pm 4.3$	$\pm 0.8$
rs_4.1500	1.31	$\pm 0.02$	$\pm 0.04$	$\pm 0.005$
rs_4.2000	$1.03 \times 10^{-4}$	$\pm 0.02 \times 10^{-4}$	$\pm 0.02 \times 10^{-4}$	$\pm 0.007 \times 10^{-4}$
rs_5.800	$5.11 \times 10^3$	$\pm 0.18 \times 10^3$	$\pm 1.99 \times 10^3$	$\pm 7e - 08 \times 10^3$
rs_5.1000	$1.59 \times 10^3$	$\pm 0.04 \times 10^3$	$\pm 0.3 \times 10^3$	$\pm 0.02 \times 10^3$
rs_5.1200	$2.93 \times 10^2$	$\pm 0.06 \times 10^2$	$\pm 0.28 \times 10^2$	$\pm 0.02 \times 10^2$
rs_5.1500	15.6	$\pm 0.3$	$\pm 0.8$	$\pm 0.1$
rs_5.2000	$2.32 \times 10^{-2}$	$\pm 0.04 \times 10^{-2}$	$\pm 0.04 \times 10^{-2}$	$\pm 0.002 \times 10^{-2}$
rs_6.800	$6.68 \times 10^3$	$\pm 0.32 \times 10^3$	$\pm 3.21 \times 10^3$	$\pm 0.69 \times 10^3$
rs_6.1000	$3.07 \times 10^3$	$\pm 0.09 \times 10^3$	$\pm 0.87 \times 10^3$	$\pm 0.02 \times 10^3$
rs_6.1200	$8.78 \times 10^2$	$\pm 0.19 \times 10^2$	$\pm 1.36 \times 10^2$	$\pm 0.21 \times 10^2$
rs_6.1500	77.9	$\pm 1.5$	$\pm 6.4$	$\pm 2.2$
rs_6.2000	0.474	$\pm 0.009$	$\pm 0.013$	$\pm 0.002$
rs_7.800	$8.98 \times 10^3$	$\pm 0.53 \times 10^3$	$\pm 3.58 \times 10^3$	$\pm 0.37 \times 10^3$
rs_7.1000	$4.51 \times 10^3$	$\pm 0.16 \times 10^3$	$\pm 1.54 \times 10^3$	$\pm 0.11 \times 10^3$
rs_7.1200	$1.77 \times 10^3$	$\pm 0.04 \times 10^3$	$\pm 0.38 \times 10^3$	$\pm 0.03 \times 10^3$
rs_7.1500	$2.46 \times 10^2$	$\pm 0.05 \times 10^2$	$\pm 0.21 \times 10^2$	$\pm 0.05 \times 10^2$
rs_7.2000	3.54	$\pm 0.07$	$\pm 0.13$	$\pm 0.02$

Table 8.12: Number of expected events in  $\mathcal{R}_0$  for each signal models on the assumption  $\lambda < r_h$ . The error indicates the uncertainty originating from the statistics of MC events, jet energy scale and jet resolution. The signal model corresponding to each abbreviation is given in Table 4.1.

Signal point	$s_{\text{th0}}$	MC Statistics	Jet Energy Scale	Jet Resolution
rh_2.800	$2.37 \times 10^{-5}$	$\pm 2.37 \times 10^{-5}$	$\pm 2.37 \times 10^{-5}$	$\pm 4.74 \times 10^{-5}$
rh_3.800	$1.74 \times 10^{-2}$	$\pm 0.87 \times 10^{-2}$	$\pm 1.3 \times 10^{-2}$	$\pm 0.87 \times 10^{-2}$
rh_3.1000	$7.69 \times 10^{-5}$	$\pm 3.84 \times 10^{-5}$	$\pm 3.84 \times 10^{-5}$	$\pm 5.76 \times 10^{-5}$
rh_4.800	0.996	$\pm 0.266$	$\pm 0.356$	$\pm 0.071$
rh_4.1000	$8.16 \times 10^{-3}$	$\pm 3.65 \times 10^{-3}$	$\pm 3.26 \times 10^{-3}$	$\pm 3.26 \times 10^{-3}$
rh_4.1200	$3.03 \times 10^{-5}$	$\pm 2.15 \times 10^{-5}$	$\pm 3.03 \times 10^{-5}$	$\pm 4.55 \times 10^{-5}$
rh_5.800	10.2	$\pm 2.1$	$\pm 4$	$\pm 2.2$
rh_5.1000	0.188	$\pm 0.067$	$\pm 0.094$	$\pm 0.024$
rh_5.1200	$8.25 \times 10^{-3}$	$\pm 2.49 \times 10^{-3}$	$\pm 3 \times 10^{-3}$	$\pm 0.75 \times 10^{-3}$
rh_5.1500	0	$\pm 0$	$\pm 0$	$\pm 5e - 06$
rh_6.800	59.2	$\pm 9.9$	$\pm 21.4$	$\pm 1.6$
rh_6.1000	2.51	$\pm 0.58$	$\pm 1.19$	$\pm 0.26$
rh_6.1200	0.119	$\pm 0.032$	$\pm 0.042$	$\pm 0.034$
rh_6.1500	$7.98 \times 10^{-4}$	$\pm 2.3 \times 10^{-4}$	$\pm 5.32 \times 10^{-4}$	$\pm 4.65 \times 10^{-4}$
rh_7.800	$2.1 \times 10^2$	$\pm 0.31 \times 10^2$	$\pm 0.58 \times 10^2$	$\pm 0 \times 10^2$
rh_7.1000	14.1	$\pm 2.6$	$\pm 1.9$	$\pm 1.9$
rh_7.1200	0.692	$\pm 0.179$	$\pm 0.508$	$\pm 0.185$
rh_7.1500	$9.29 \times 10^{-3}$	$\pm 2.94 \times 10^{-3}$	$\pm 5.57 \times 10^{-3}$	$\pm 2.79 \times 10^{-3}$
rh_7.2000	$3 \times 10^{-7}$	$\pm 1.5 \times 10^{-7}$	$\pm 3 \times 10^{-7}$	$\pm 2.25 \times 10^{-7}$

Table 8.13: Number of expected events in  $\mathcal{R}_1$  for each signal models on the assumption  $\lambda < r_h$ . The error indicates the uncertainty originating from the statistics of MC events, jet energy scale and jet resolution. The signal model corresponding to each abbreviation is given in Table 4.1.

Signal point	$s_{th1}$	MC Statistics	Jet Energy Scale	Jet Resolution
rh_2.800	$2.37 \times 10^{-5}$	$\pm 2.37 \times 10^{-5}$	$\pm 0 \times 10^{-5}$	$\pm 0 \times 10^{-5}$
rh_3.800	$3.48 \times 10^{-2}$	$\pm 1.23 \times 10^{-2}$	$\pm 0.87 \times 10^{-2}$	$\pm 0.87 \times 10^{-2}$
rh_3.1000	$3.84 \times 10^{-5}$	$\pm 2.72 \times 10^{-5}$	$\pm 1.92 \times 10^{-5}$	$\pm 3.84 \times 10^{-5}$
rh_4.800	0.64	$\pm 0.213$	$\pm 0.64$	$\pm 0.213$
rh_4.1000	$6.53 \times 10^{-3}$	$\pm 3.26 \times 10^{-3}$	$\pm 1.63 \times 10^{-3}$	$\pm 1.63 \times 10^{-3}$
rh_4.1200	$3.03 \times 10^{-5}$	$\pm 2.15 \times 10^{-5}$	$\pm 3.03 \times 10^{-5}$	$\pm 0 \times 10^{-5}$
rh_5.800	10.2	$\pm 2.1$	$\pm 6.2$	$\pm 2.2$
rh_5.1000	0.259	$\pm 0.078$	$\pm 0.094$	$\pm 0.094$
rh_5.1200	$4.5 \times 10^{-3}$	$\pm 1.84 \times 10^{-3}$	$\pm 1.5 \times 10^{-3}$	$\pm 2.25 \times 10^{-3}$
rh_5.1500	$9.06 \times 10^{-7}$	$\pm 9.06 \times 10^{-7}$	$\pm 9.06 \times 10^{-7}$	$\pm 9.06 \times 10^{-7}$
rh_6.800	78.9	$\pm 11.4$	$\pm 23$	$\pm 9.9$
rh_6.1000	1.85	$\pm 0.49$	$\pm 0.66$	$\pm 0.4$
rh_6.1200	$6.79 \times 10^{-2}$	$\pm 2.4 \times 10^{-2}$	$\pm 1.7 \times 10^{-2}$	$\pm 1.7 \times 10^{-2}$
rh_6.1500	$1.99 \times 10^{-4}$	$\pm 1.15 \times 10^{-4}$	$\pm 1.99 \times 10^{-4}$	$\pm 0.66 \times 10^{-4}$
rh_7.800	$2.95 \times 10^2$	$\pm 0.36 \times 10^2$	$\pm 1.52 \times 10^2$	$\pm 0.76 \times 10^2$
rh_7.1000	13.2	$\pm 2.5$	$\pm 8$	$\pm 2.8$
rh_7.1200	0.646	$\pm 0.173$	$\pm 0.046$	$\pm 0$
rh_7.1500	$5.57 \times 10^{-3}$	$\pm 2.28 \times 10^{-3}$	$\pm 1.86 \times 10^{-3}$	$\pm 0 \times 10^{-3}$
rh_7.2000	0	$\pm 0$	$\pm 0$	$\pm 0$

Table 8.14: Number of expected events in  $\mathcal{R}_2$  for each signal models on the assumption  $\lambda < r_h$ . The error indicates the uncertainty originating from the statistics of MC events, jet energy scale and jet resolution. The signal model corresponding to each abbreviation is given in Table 4.1.

Signal point	$s_{\text{th}2}$	MC Statistics	Jet Energy Scale	Jet Resolution
rh_2.800	$4.5 \times 10^{-3}$	$\pm 0.33 \times 10^{-3}$	$\pm 0.07 \times 10^{-3}$	$\pm 0.17 \times 10^{-3}$
rh_3.800	1.56	$\pm 0.08$	$\pm 0.03$	$\pm 0.02$
rh_3.1000	$7.34 \times 10^{-3}$	$\pm 0.38 \times 10^{-3}$	$\pm 0.42 \times 10^{-3}$	$\pm 0.25 \times 10^{-3}$
rh_4.800	35.1	$\pm 1.6$	$\pm 0.2$	$\pm 0.6$
rh_4.1000	0.857	$\pm 0.037$	$\pm 0.013$	$\pm 0.003$
rh_4.1200	$8.95 \times 10^{-3}$	$\pm 0.37 \times 10^{-3}$	$\pm 0.18 \times 10^{-3}$	$\pm 0.06 \times 10^{-3}$
rh_5.800	$2.19 \times 10^2$	$\pm 0.1 \times 10^2$	$\pm 0.12 \times 10^2$	$\pm 0.09 \times 10^2$
rh_5.1000	14.1	$\pm 0.6$	$\pm 0.3$	$\pm 0.1$
rh_5.1200	0.518	$\pm 0.02$	$\pm 0.011$	$\pm 0.013$
rh_5.1500	$7.38 \times 10^{-4}$	$\pm 0.26 \times 10^{-4}$	$\pm 0.13 \times 10^{-4}$	$\pm 0.06 \times 10^{-4}$
rh_6.800	$8.02 \times 10^2$	$\pm 0.36 \times 10^2$	$\pm 0.86 \times 10^2$	$\pm 0.41 \times 10^2$
rh_6.1000	83.7	$\pm 3.3$	$\pm 1.6$	$\pm 0.4$
rh_6.1200	6.52	$\pm 0.24$	$\pm 0.08$	$\pm 0.04$
rh_6.1500	$5.48 \times 10^{-2}$	$\pm 0.19 \times 10^{-2}$	$\pm 0.1 \times 10^{-2}$	$\pm 0.06 \times 10^{-2}$
rh_7.800	$1.7 \times 10^3$	$\pm 0.09 \times 10^3$	$\pm 0.31 \times 10^3$	$\pm 0.03 \times 10^3$
rh_7.1000	$3.02 \times 10^2$	$\pm 0.12 \times 10^2$	$\pm 0.14 \times 10^2$	$\pm 0.06 \times 10^2$
rh_7.1200	33.9	$\pm 1.3$	$\pm 0.6$	$\pm 0.6$
rh_7.1500	0.809	$\pm 0.027$	$\pm 0.008$	$\pm 0.002$
rh_7.2000	$7.7 \times 10^{-5}$	$\pm 0.24 \times 10^{-5}$	$\pm 0.22 \times 10^{-5}$	$\pm 0.04 \times 10^{-5}$

Table 8.15: Number of expected events in  $\mathcal{R}_3$  for each signal models on the assumption  $\lambda < r_h$ . The error indicates the uncertainty originating from the statistics of MC events, jet energy scale and jet resolution. The signal model corresponding to each abbreviation is given in Table 4.1.

Signal point	$s_{\text{th}3}$	MC Statistics	Jet Energy Scale	Jet Resolution
rh_2_800	$9.68 \times 10^{-2}$	$\pm 0.15 \times 10^{-2}$	$\pm 0.05 \times 10^{-2}$	$\pm 0.04 \times 10^{-2}$
rh_3_800	16.2	$\pm 0.3$	$\pm 0.6$	$\pm 0.2$
rh_3_1000	$7.44 \times 10^{-2}$	$\pm 0.12 \times 10^{-2}$	$\pm 0.07 \times 10^{-2}$	$\pm 0.008 \times 10^{-2}$
rh_4_800	$2.21 \times 10^2$	$\pm 0.04 \times 10^2$	$\pm 0.15 \times 10^2$	$\pm 0.03 \times 10^2$
rh_4_1000	5.88	$\pm 0.1$	$\pm 0.19$	$\pm 0.04$
rh_4_1200	$5.52 \times 10^{-2}$	$\pm 0.09 \times 10^{-2}$	$\pm 0.07 \times 10^{-2}$	$\pm 0.03 \times 10^{-2}$
rh_5_800	$1.15 \times 10^3$	$\pm 0.02 \times 10^3$	$\pm 0.15 \times 10^3$	$\pm 0.03 \times 10^3$
rh_5_1000	71.7	$\pm 1.3$	$\pm 4.7$	$\pm 1$
rh_5_1200	2.56	$\pm 0.04$	$\pm 0.06$	$\pm 0.02$
rh_5_1500	$3.09 \times 10^{-3}$	$\pm 0.05 \times 10^{-3}$	$\pm 0.02 \times 10^{-3}$	$\pm 0.007 \times 10^{-3}$
rh_6_800	$3.28 \times 10^3$	$\pm 0.07 \times 10^3$	$\pm 0.68 \times 10^3$	$\pm 0.04 \times 10^3$
rh_6_1000	$3.67 \times 10^2$	$\pm 0.07 \times 10^2$	$\pm 0.31 \times 10^2$	$\pm 0.06 \times 10^2$
rh_6_1200	26.9	$\pm 0.5$	$\pm 1.2$	$\pm 0.2$
rh_6_1500	0.221	$\pm 0.004$	$\pm 0.004$	$\pm 0.001$
rh_7_800	$6.08 \times 10^3$	$\pm 0.16 \times 10^3$	$\pm 1.68 \times 10^3$	$\pm 0.08 \times 10^3$
rh_7_1000	$1.12 \times 10^3$	$\pm 0.02 \times 10^3$	$\pm 0.14 \times 10^3$	$\pm 0.02 \times 10^3$
rh_7_1200	$1.36 \times 10^2$	$\pm 0.03 \times 10^2$	$\pm 0.08 \times 10^2$	$\pm 0.02 \times 10^2$
rh_7_1500	2.93	$\pm 0.05$	$\pm 0.07$	$\pm 0.009$
rh_7_2000	$2.37 \times 10^{-4}$	$\pm 0.04 \times 10^{-4}$	$\pm 0.03 \times 10^{-4}$	$\pm 0.01 \times 10^{-4}$

## Uncertainties on Signal Cross Sections

Black hole signal events are generated by BlackMax with CTEQ66. Systematic uncertainties on signal cross sections are estimated with its PDFs error set. Table 8.16 and 8.17 show cross section uncertainties for each signal point.

## Total uncertainty on the signal

A total uncertainty in the signal normalization is estimated by the convolution of all the systematic uncertainties other than those of PDFs, accounting for the correlations between them. The systematic uncertainties on PDFs are incorporated into signal cross sections when obtained signal yields are compared to the theoretical predictions.

Table 8.16: Systematic uncertainties of signal cross sections for signal points on the assumption  $\lambda < r_s$  estimated by CTEQ66 error set

Signal point	Cross section	Uncertainty
rs_2_800	4.4	+1.71 -1.37
rs_2_1000	0.102	+0.059 -0.045
rs_2_1200	$1.02 \times 10^{-3}$	$+0.96 \times 10^{-3}$ $-0.66 \times 10^{-3}$
rs_3_800	57.6	+16.7 -14
rs_3_1000	3.72	+1.48 -1.19
rs_3_1200	0.188	+0.103 -0.079
rs_3_1500	$7.34 \times 10^{-4}$	$+7.24 \times 10^{-4}$ $-4.94 \times 10^{-4}$
rs_4_800	$2.89 \times 10^2$	$+0.67 \times 10^2$ $-0.58 \times 10^2$
rs_4_1000	29.9	+9.2 -7.6
rs_4_1200	2.89	+1.18 -0.94
rs_4_1500	$5.74 \times 10^{-2}$	$+3.54 \times 10^{-2}$ $-2.63 \times 10^{-2}$
rs_4_2000	$4.37 \times 10^{-6}$	$+7.28 \times 10^{-6}$ $-4.33 \times 10^{-6}$
rs_5_800	$9.02 \times 10^2$	$+1.85 \times 10^2$ $-1.59 \times 10^2$
rs_5_1000	$1.24 \times 10^2$	$+0.32 \times 10^2$ $-0.27 \times 10^2$
rs_5_1200	16.8	+5.5 -4.5
rs_5_1500	0.729	+0.343 -0.268
rs_5_2000	$1.05 \times 10^{-3}$	$+0.98 \times 10^{-3}$ $-0.68 \times 10^{-3}$
rs_6_800	$2.17 \times 10^3$	$+0.4 \times 10^3$ $-0.35 \times 10^3$
rs_6_1000	$3.51 \times 10^2$	$+0.79 \times 10^2$ $-0.68 \times 10^2$
rs_6_1200	59.7	+16.5 -14
rs_6_1500	3.96	+1.56 -1.25
rs_6_2000	$2.23 \times 10^{-2}$	$+1.53 \times 10^{-2}$ $-1.13 \times 10^{-2}$
rs_7_800	$4.3 \times 10^3$	$+0.73 \times 10^3$ $-0.64 \times 10^3$
rs_7_1000	$7.81 \times 10^2$	$+1.63 \times 10^2$ $-1.4 \times 10^2$
rs_7_1200	$1.55 \times 10^2$	$+0.38 \times 10^2$ $-0.33 \times 10^2$
rs_7_1500	14	+4.7 -3.8
rs_7_2000	0.171	+0.095 -0.072

Table 8.17: Systematic uncertainties of signal cross sections for signal points on the assumption  $\lambda < r_h$  estimated by CTEQ66 error set

Signal point	Cross section	Uncertainty
rh_2_800	$3.27 \times 10^{-3}$	$+3.03 \times 10^{-3}$ $-2.1 \times 10^{-3}$
rh_3_800	0.603	+0.332 -0.252
rh_3_1000	$2.66 \times 10^{-3}$	$+2.58 \times 10^{-3}$ $-1.75 \times 10^{-3}$
rh_4_800	9.88	+3.84 -3.09
rh_4_1000	0.227	+0.136 -0.101
rh_4_1200	$2.11 \times 10^{-3}$	$+1.98 \times 10^{-3}$ $-1.37 \times 10^{-3}$
rh_5_800	61.1	+19.2 -15.9
rh_5_1000	3.09	+1.35 -1.07
rh_5_1200	0.104	+0.065 -0.049
rh_5_1500	$1.26 \times 10^{-4}$	$+1.64 \times 10^{-4}$ $-1.04 \times 10^{-4}$
rh_6_800	$2.28 \times 10^2$	$+0.59 \times 10^2$ $-0.5 \times 10^2$
rh_6_1000	18	+6.5 -5.3
rh_6_1200	1.18	+0.58 -0.45
rh_6_1500	$9.14 \times 10^{-3}$	$+7.5 \times 10^{-3}$ $-5.32 \times 10^{-3}$
rh_7_800	$6.18 \times 10^2$	$+1.41 \times 10^2$ $-1.21 \times 10^2$
rh_7_1000	65.4	+19.5 -16.3
rh_7_1200	6.41	+2.59 -2.07
rh_7_1500	0.127	+0.078 -0.058
rh_7_2000	$1.03 \times 10^{-5}$	$+1.72 \times 10^{-5}$ $-1.01 \times 10^{-5}$

## 8.5 Validation of Signal Extraction Method with Pseudo Data

This section gives a validity check of the signal extraction method with pseudo data. The pseudo data of QCD background and signal events are simulated with PYTHIA and BlackMax, respectively.

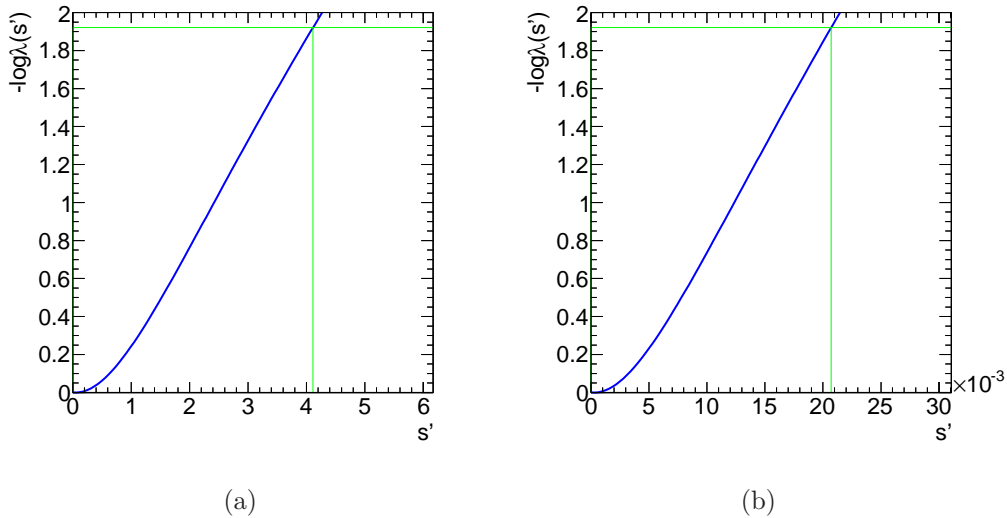


Figure 8.9: Test statistics,  $-\log \lambda(s')$ , as a function of  $s'$  for pseudo data without signal events. The results of hypothesis tests (a:rs\_2\_1000) and (b:rs\_4\_1000) are shown. The 95% CL boundaries are indicated by the lines.

First, the fitting is performed with pseudo data without mini black hole signal events. Figure 8.9 shows the result of hypothesis test for

$$\left\{ \begin{array}{l} \text{rs\_2\_1000(a)} : n = 2, M_D = 1000 \text{ GeV}, M_{\text{BHth}} = 4266 \text{ GeV}, \\ \quad \text{cross section} = 0.102^{+0.059}_{-0.045} \text{ pb}, \\ \text{rs\_4\_1000(b)} : n = 4, M_D = 1000 \text{ GeV}, M_{\text{BHth}} = 2923 \text{ GeV}, \\ \quad \text{cross section} = 29.9^{+8.2}_{-7.6} \text{ pb}. \end{array} \right.$$

The resulting signal yields are consistent with zero for both cases, as expected.

Second, the fitting is performed with pseudo data with signal events of a certain model. Figure 8.10 shows the results of hypothesis test on rs\_2\_1000 (a) and rs\_4\_1000 (b). Obtained values of signal strength are consistent with unity for both cases. Consequently, the introduced method has been

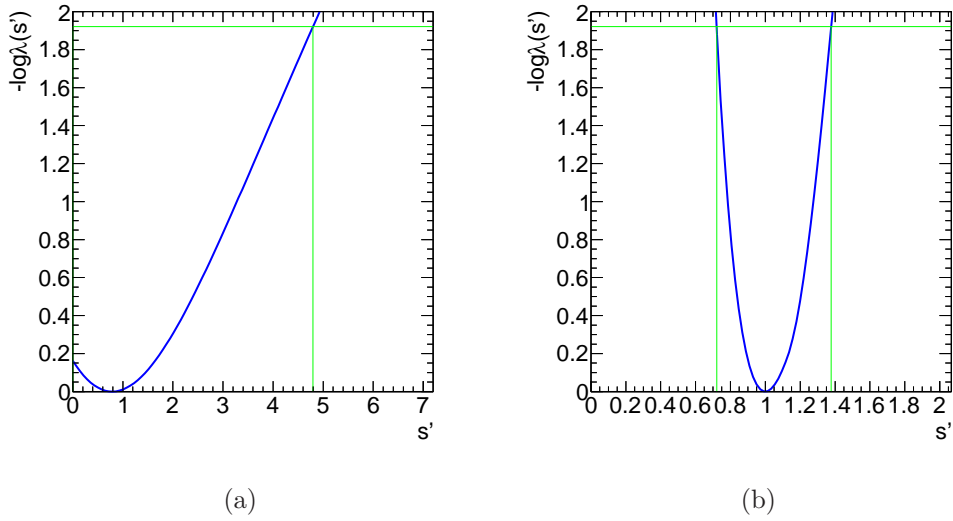


Figure 8.10: Test statistics,  $-\log \lambda(s')$ , as a function of  $s'$  for pseudo data with signal events. The results of hypothesis tests (a:rs\_2\_1000) and (b:rs\_4\_1000) are shown. The 95 % CL boundaries are indicated by the lines.

validated and works on data with and without signal events, and gives the correct values on the signal yield.

# Chapter 9

## Constraint on the Mini Black Hole Production

### 9.1 Limits on the Mini Black Hole Production Cross Sections

Figure 9.1 shows  $\sum p_T$  distributions of data. The filled circles show the observed events in  $N_J \geq 5$  and the histogram shows those in  $N_J < 5$  which is normalized by the number of events in  $1100 < \sum p_T < 1200$  GeV. The yellow error band includes the total uncertainty including statistical uncertainties in  $\mathcal{R}_{0,1,2}$  and systematic uncertainties given in Section 8.4.1. Two distributions show an agreement within the uncertainties.

The number of observed events in the regions defined by Eq. 8.1 are summarized in Table 9.1. With these numbers, the statistical tests with various signal hypotheses are performed with the method described in the previous chapter. Figure 9.2(a) and 9.2(b) show the resulting signal yields for rs\_2\_1000 and rs\_4\_1000, respectively; both of them show the results consistent with no signal events.

Table 9.1: Numbers of observed events for each  $\sum p_T$ - $N_J$  region

$\sum p_T$ [GeV]	1100 to 1200	> 2000
$N_J \geq 5$	194	7
$N_J < 5$	685	13

Table 9.2 (9.3) shows signal cross sections and obtained 95% CL limits on the cross section for each signal point on the assumption  $\lambda < r_s$  ( $r_h$ ).

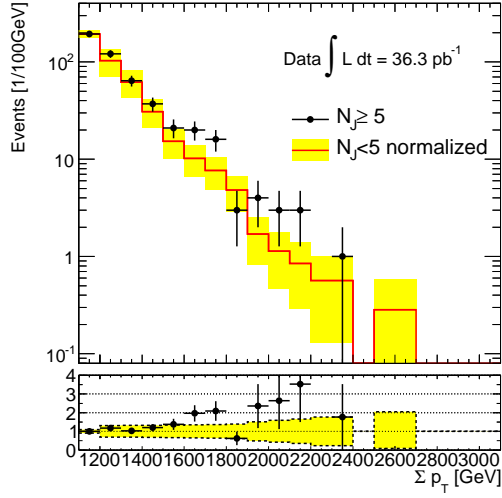


Figure 9.1:  $\sum p_T$  distributions of observed events for  $N_J \geq 5$  (filled circles) and  $N_J < 5$  (histogram). The histogram is normalized by the number of events in  $1100 < \sum p_T < 1200$  GeV. The yellow error band represents the total uncertainty including the statistical uncertainty in  $N_J < 5$  and the systematic uncertainties given in Section 8.4.1.

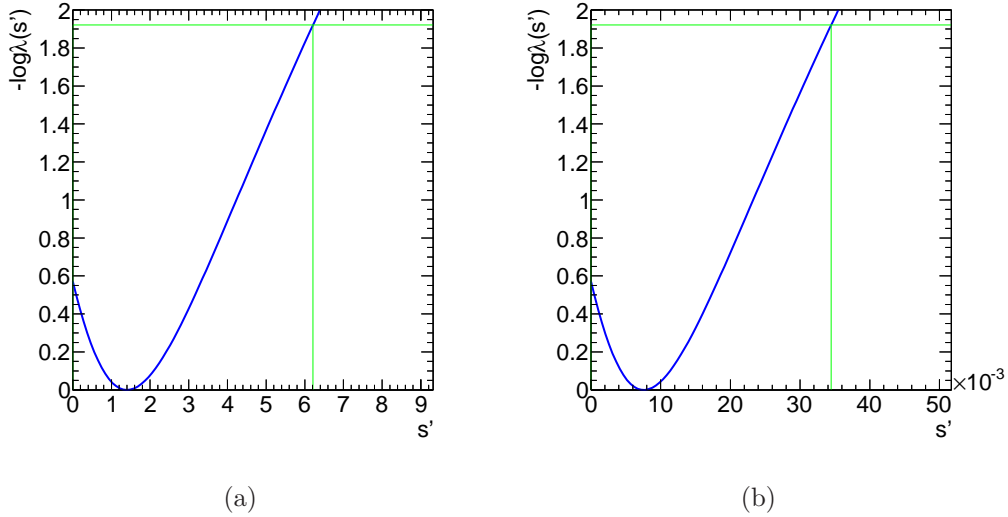


Figure 9.2: Test statistics ( $-\log \lambda(s')$ ) as a function of  $s'$  for observed events. The results of hypothesis tests for rs\_2\_1000 (a) and rs\_4\_1000 (b) are shown. The 95% CL boundaries are indicated by the lines.

Table 9.2: 95% CL limits on cross sections for each signal point on the assumption  $\lambda < r_s$

Signal point	Cross section $\pm$ Cross section uncertainty	95% CL Limits
rs_2_800	$4.4 \pm^{+1.71}_{-1.37}$	0.713
rs_2_1000	$0.102 \pm^{+0.059}_{-0.045}$	0.636
rs_2_1200	$1.02 \times 10^{-3} \pm^{+0.96 \times 10^{-3}}_{-0.66 \times 10^{-3}}$	0.630
rs_3_800	$57.6 \pm^{+16.7}_{-14}$	1.11
rs_3_1000	$3.72 \pm^{+1.48}_{-1.19}$	0.765
rs_3_1200	$0.188 \pm^{+0.103}_{-0.079}$	0.679
rs_3_1500	$7.34 \times 10^{-4} \pm^{+7.24 \times 10^{-4}}_{-4.94 \times 10^{-4}}$	0.683
rs_4_800	$2.89 \times 10^2 \pm^{+0.67 \times 10^2}_{-0.58 \times 10^2}$	2.08
rs_4_1000	$29.9 \pm^{+9.2}_{-7.6}$	1.03
rs_4_1200	$2.89 \pm^{+1.18}_{-0.94}$	0.811
rs_4_1500	$5.74 \times 10^{-2} \pm^{+3.54 \times 10^{-2}}_{-2.63 \times 10^{-2}}$	0.748
rs_4_2000	$4.37 \times 10^{-6} \pm^{+7.28 \times 10^{-6}}_{-4.33 \times 10^{-6}}$	0.737
rs_5_800	$9.02 \times 10^2 \pm^{+1.85 \times 10^2}_{-1.59 \times 10^2}$	7.07
rs_5_1000	$1.24 \times 10^2 \pm^{+0.32 \times 10^2}_{-0.27 \times 10^2}$	1.45
rs_5_1200	$16.8 \pm^{+5.5}_{-4.5}$	1.01
rs_5_1500	$0.729 \pm^{+0.343}_{-0.268}$	0.813
rs_5_2000	$1.05 \times 10^{-3} \pm^{+0.98 \times 10^{-3}}_{-0.68 \times 10^{-3}}$	0.802
rs_6_800	$2.17 \times 10^3 \pm^{+0.4 \times 10^3}_{-0.35 \times 10^3}$	21.5
rs_6_1000	$3.51 \times 10^2 \pm^{+0.79 \times 10^2}_{-0.68 \times 10^2}$	2.54
rs_6_1200	$59.7 \pm^{+16.5}_{-14}$	1.24
rs_6_1500	$3.96 \pm^{+1.56}_{-1.25}$	0.897
rs_6_2000	$2.23 \times 10^{-2} \pm^{+1.53 \times 10^{-2}}_{-1.13 \times 10^{-2}}$	0.840
rs_7_800	$4.3 \times 10^3 \pm^{+0.73 \times 10^3}_{-0.64 \times 10^3}$	20.3
rs_7_1000	$7.81 \times 10^2 \pm^{+1.63 \times 10^2}_{-1.4 \times 10^2}$	5.00
rs_7_1200	$1.55 \times 10^2 \pm^{+0.38 \times 10^2}_{-0.33 \times 10^2}$	1.74
rs_7_1500	$14 \pm^{+4.7}_{-3.8}$	1.02
rs_7_2000	$0.171 \pm^{+0.095}_{-0.072}$	0.866

Table 9.3: 95% CL limits on cross sections for each signal point on the assumption  $\lambda < r_h$

Signal point	Cross section $\pm$ Cross section uncertainty	95% CL Limits
rh_2.800	$3.27 \times 10^{-3} \pm \begin{matrix} +3.03 \times 10^{-3} \\ -2.1 \times 10^{-3} \end{matrix}$	0.542
rh_3.800	$0.603 \pm \begin{matrix} +0.332 \\ -0.252 \end{matrix}$	0.606
rh_3.1000	$2.66 \times 10^{-3} \pm \begin{matrix} +2.58 \times 10^{-3} \\ -1.75 \times 10^{-3} \end{matrix}$	0.582
rh_4.800	$9.88 \pm \begin{matrix} +3.84 \\ -3.09 \end{matrix}$	0.746
rh_4.1000	$0.227 \pm \begin{matrix} +0.136 \\ -0.101 \end{matrix}$	0.637
rh_4.1200	$2.11 \times 10^{-3} \pm \begin{matrix} +1.98 \times 10^{-3} \\ -1.37 \times 10^{-3} \end{matrix}$	0.632
rh_5.800	$61.1 \pm \begin{matrix} +19.2 \\ -15.9 \end{matrix}$	0.918
rh_5.1000	$3.09 \pm \begin{matrix} +1.35 \\ -1.07 \end{matrix}$	0.727
rh_5.1200	$0.104 \pm \begin{matrix} +0.065 \\ -0.049 \end{matrix}$	0.682
rh_5.1500	$1.26 \times 10^{-4} \pm \begin{matrix} +1.64 \times 10^{-4} \\ -1.04 \times 10^{-4} \end{matrix}$	0.690
rh_6.800	$2.28 \times 10^2 \pm \begin{matrix} +0.59 \times 10^2 \\ -0.5 \times 10^2 \end{matrix}$	1.29
rh_6.1000	$18 \pm \begin{matrix} +6.5 \\ -5.3 \end{matrix}$	0.838
rh_6.1200	$1.18 \pm \begin{matrix} +0.58 \\ -0.45 \end{matrix}$	0.746
rh_6.1500	$9.14 \times 10^{-3} \pm \begin{matrix} +7.5 \times 10^{-3} \\ -5.32 \times 10^{-3} \end{matrix}$	0.702
rh_7.800	$6.18 \times 10^2 \pm \begin{matrix} +1.41 \times 10^2 \\ -1.21 \times 10^2 \end{matrix}$	2.10
rh_7.1000	$65.4 \pm \begin{matrix} +19.5 \\ -16.3 \end{matrix}$	1.03
rh_7.1200	$6.41 \pm \begin{matrix} +2.59 \\ -2.07 \end{matrix}$	0.806
rh_7.1500	$0.127 \pm \begin{matrix} +0.078 \\ -0.058 \end{matrix}$	0.745
rh_7.2000	$1.03 \times 10^{-5} \pm \begin{matrix} +1.72 \times 10^{-5} \\ -1.01 \times 10^{-5} \end{matrix}$	0.754

Figure 9.3-9.5 (9.6-9.8) show the 95 % CL upper limits on the signal cross sections as a function of  $M_D$  for each signal point and  $n$  on the assumption of  $\lambda < r_s$  ( $r_h$ ). The observed limits, the theoretical cross sections and the expected limits for no signal are shown by rectangles, solid lines and dashed lines, respectively. The uncertainties on the theoretical cross sections and  $1\sigma$  ( $2\sigma$ ) counters of the expected limits are shown by green (yellow) error bands. The expected limits are obtained as follows:

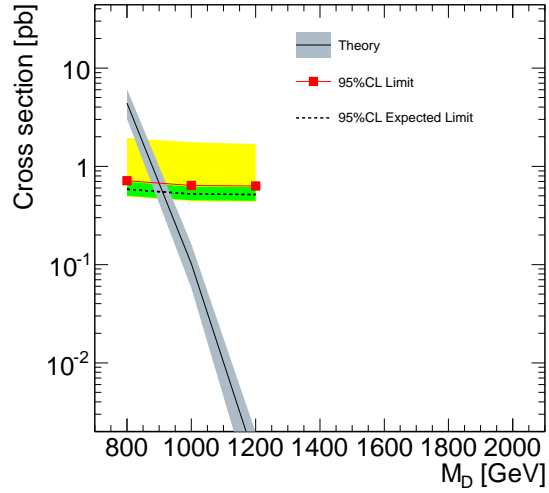
- Set the signal components as zero in Eq. 8.8 and find the parameters which maximize the likelihood function of Eq. 8.8. Obtained  $\mu_i, i = 1, 2, 3, 4$  is used for the seeds of pseudo data.
- Generate a set of pseudo data  $b_i, i = 1, 2, 3, 4$ . Under the constraint of Eq. 8.4, 8.5 and 8.11,  $b_i$  is randomly generated in the Poisson regime with the mean value  $\mu_i$ . Thousand set of pseudo data events are generated.
- Obtain 95 % CL limits on the cross section for each pseudo data.
- Find the median of the obtained 95 % CL limits.
- Define the  $1\sigma$  ( $2\sigma$ ) contour of the expected limit in which the limits are expected to line with a probability of 68.3 % (95.5 %.)

All obtained limits show consistent with expected limits.

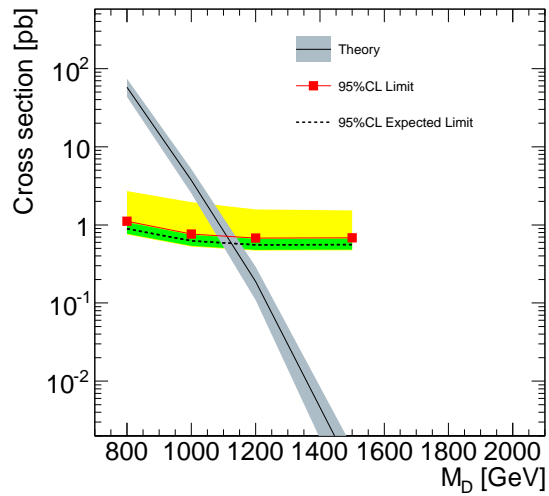
Table 9.4 lists the signal points excluded at 95 % CL and shows their values of  $M_D$ . For example, on the assumption of  $\lambda < r_s$ , signals of  $M_D$  up to 800(1500) GeV is excluded for  $n = 2(7)$ . On the assumption of  $\lambda < r_h$ , no signal point is excluded for  $n \leq 3$ , while signals of  $M_D$  up to 1200 GeV are excluded for  $n = 7$ .

Table 9.4: The highest  $M_D$  of excluded signal points at 95 % CL in same  $n$  and same assumption for  $M_{\text{BHth}}$

$n$	On the assumption of $\lambda < r_s$	On the assumption of $\lambda < r_h$
2	800 GeV	-
3	1000 GeV	-
4	1200 GeV	800 GeV
5	1200 GeV	1000 GeV
6	1500 GeV	1000 GeV
7	1500 GeV	1200 GeV

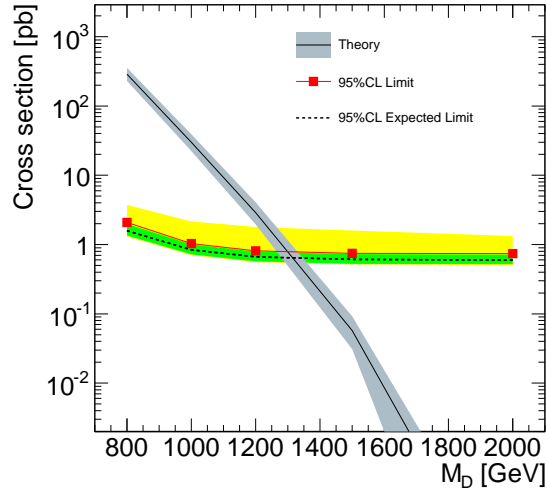


(a)

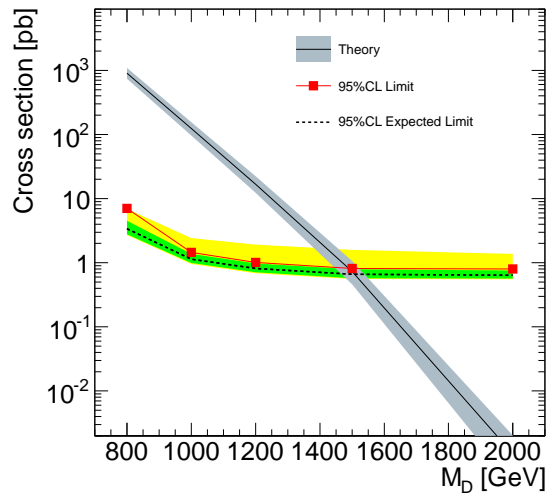


(b)

Figure 9.3: 95% CL upper limit on the cross section for  $n = 2$  (a) and  $n = 3$  (b) on the assumption of  $\lambda < r_s$ . The observed limit, the signal cross section and the expected limit are shown by rectangles, a solid line and dashed line, respectively. The PDF uncertainty on the theoretical cross section is shown by an error band and the  $1\sigma$  ( $2\sigma$ ) contour of the expected limit is shown in green (yellow).

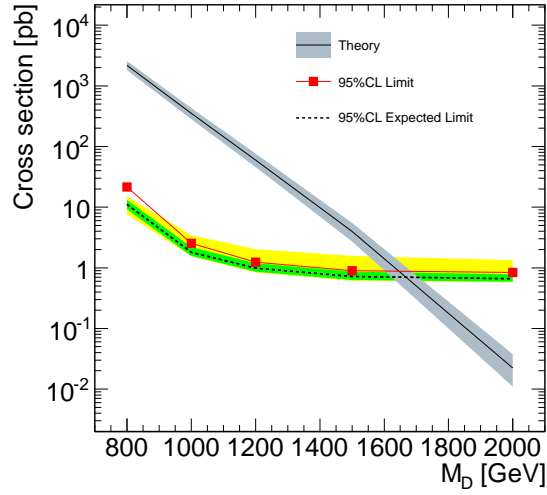


(a)

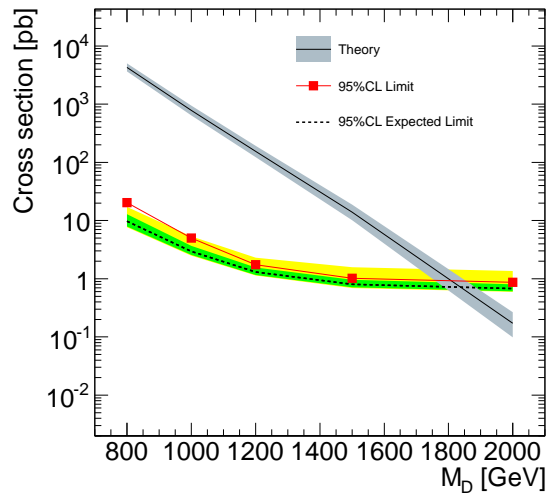


(b)

Figure 9.4: 95% CL upper limit on the cross section for  $n = 4$  (a) and  $n = 5$  (b) on the assumption of  $\lambda < r_s$ . The observed limit, the signal cross section and the expected limit are shown by rectangles, a solid line and dashed line, respectively. The PDF uncertainty on the theoretical cross section is shown by an error band and the  $1\sigma$  ( $2\sigma$ ) contour of the expected limit is shown in green (yellow).

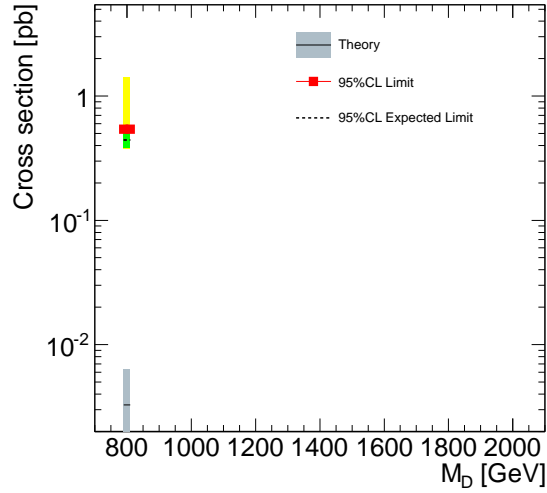


(a)

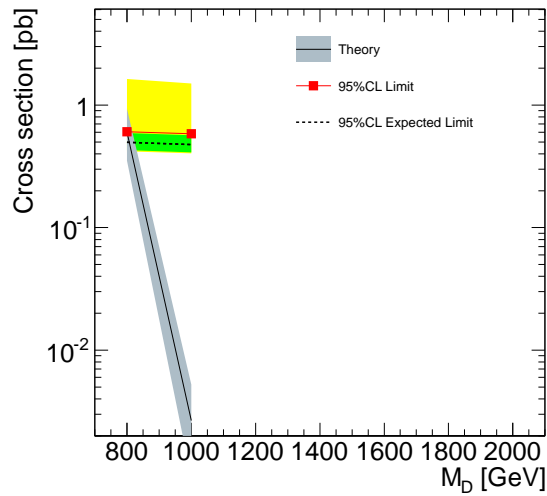


(b)

Figure 9.5: 95% CL upper limit on the cross section for  $n = 6$  (a) and  $n = 7$  (b) on the assumption of  $\lambda < r_s$ . The observed limit, the signal cross section and the expected limit are shown by rectangles, a solid line and dashed line, respectively. The PDF uncertainty on the theoretical cross section is shown by an error band and the  $1\sigma$  ( $2\sigma$ ) contour of the expected limit is shown in green (yellow).

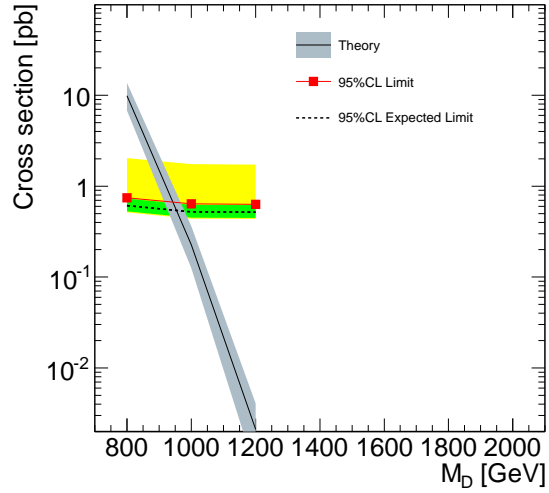


(a)

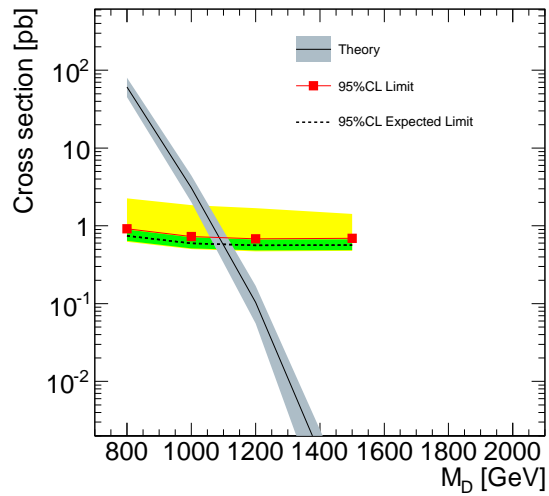


(b)

Figure 9.6: 95% CL upper limit on the cross section for  $n = 2$  (a) and  $n = 3$  (b) on the assumption of  $\lambda < r_h$ . The observed limit, the signal cross section and the expected limit are shown by rectangles, a solid line and dashed line, respectively. The PDF uncertainty on the theoretical cross section is shown by an error band and the  $1\sigma$  ( $2\sigma$ ) contour of the expected limit is shown in green (yellow).

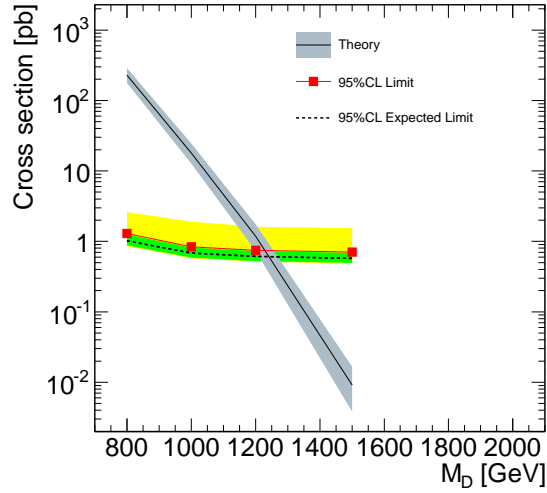


(a)

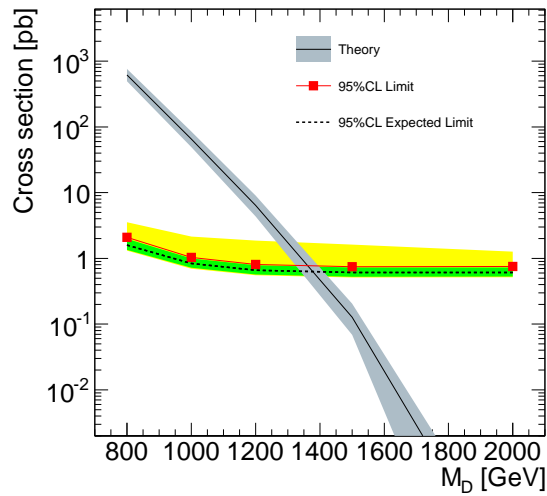


(b)

Figure 9.7: 95% CL upper limit on the cross section for  $n = 4$  (a) and  $n = 5$  (b) on the assumption of  $\lambda < r_h$ . The observed limit, the signal cross section and the expected limit are shown by rectangles, a solid line and dashed line, respectively. The PDF uncertainty on the theoretical cross section is shown by an error band and the  $1\sigma$  ( $2\sigma$ ) contour of the expected limit is shown in green (yellow).



(a)



(b)

Figure 9.8: 95% CL upper limit on the cross section for  $n = 6$  (a) and  $n = 7$  (b) on the assumption of  $\lambda < r_h$ . The observed limit, the signal cross section and the expected limit are shown by rectangles, a solid line and dashed line, respectively. The PDF uncertainty on the theoretical cross section is shown by an error band and the  $1\sigma$  ( $2\sigma$ ) contour of the expected limit is shown in green (yellow).

## 9.2 Lower Limits on the Planck Scale

Scanning along  $M_D$  and calculating upper limits on the production cross section for each  $n$ , the lower limits on  $M_D$  can be placed where the obtained cross section limits fall below the theoretical cross sections accounting for their uncertainties. Figure 9.2 shows the lower limits on  $M_D$  at 95% CL for  $n = i, 2 \leq i \leq 7$ , on the assumption of  $\lambda < r_s$  ( $r_h$ ). Table 9.5 summarizes the lower limits on  $M_D$  for each  $n$ .

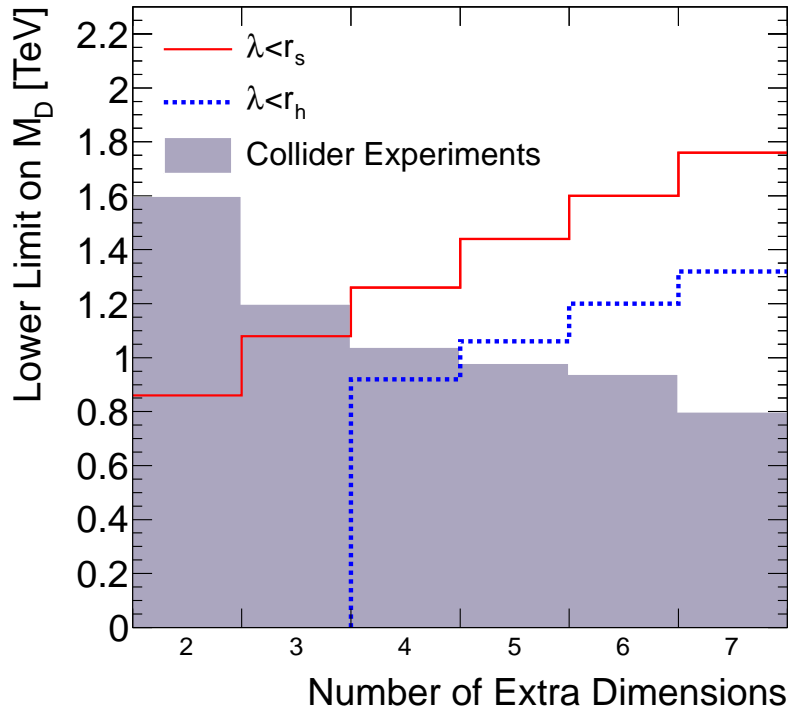


Figure 9.9: 95% CL lower limit on  $M_D$  as a function of number of extra dimension. A solid (dashed) line is the result on the assumption  $\lambda < r_s$  ( $\lambda < r_h$ ). Filled histogram shows the lower limit by the previous collider experiments [39, 40, 41].

For  $n = 2(3)$ , the most stringent limit of  $M_D > 1.60$  TeV(1.20 TeV) is reported by LEP and Tevatron experiments [39, 40, 41], showing an agreement with result of  $M_D > 0.86$  TeV(1.08 TeV) on the assumption  $\lambda < r_s$ . For  $n = 4$ , the limit on  $M_D$  is set as

$$M_D > 1.26 \text{ TeV} \quad (95\% \text{ CL}). \quad (9.1)$$

Table 9.5: Lower limits on  $M_D$ [TeV] at 95% CL on the assumption of  $\lambda < r_s$  ( $r_h$ ). The limits reported by the previous collider experiments [39, 40, 41] are given in the last column.

$n$	$\lambda < r_s$	$\lambda < r_h$	Previous Result
2	0.86	-	1.60
3	1.08	-	1.20
4	1.26	0.92	1.04
5	1.44	1.06	0.98
6	1.60	1.20	0.94
7	1.76	1.32	0.80

Currently, this is the strictest result on  $M_D$  by collider experiments. For  $n > 4$ , more stringent limits are set on  $M_D$ .

The limits on the assumption of  $\lambda < r_h$  also show an agreement with the results by the previous collider experiments up to  $n = 4$ . For  $n = 5$ , a limit is set as

$$M_D > 1.06 \text{ TeV} \quad (95\% \text{ CL}). \quad (9.2)$$

More stringent limits are placed for  $n > 5$  compared with the results by the previous collider experiments.

# Chapter 10

## Discussion

In this chapter, the resulting limits on black hole production and  $M_D$  are compared with those with a different selection boundary on  $\sum p_T$ . The results are also compared with astrophysical results. Finally, experimental sensitivities with increased statistics are discussed.

### 10.1 Setting Limits with Different $\sum p_T$ Range

In Figure 9.1, more outliers around  $\sum p_T \sim 1500$  GeV can be observed in  $N_J \geq 5$ , which could be a result of statistical fluctuations. These events are not taken into account in calculating signal yields. As a check of the obtained results, a comparison of fitting results with different  $\sum p_T$  boundaries is performed. An alternative fit is performed by changing the  $\sum p_T$  boundary of 2000 GeV to 1500 GeV. The regions of  $\mathcal{R}_2$  and  $\mathcal{R}_3$  are redefined as

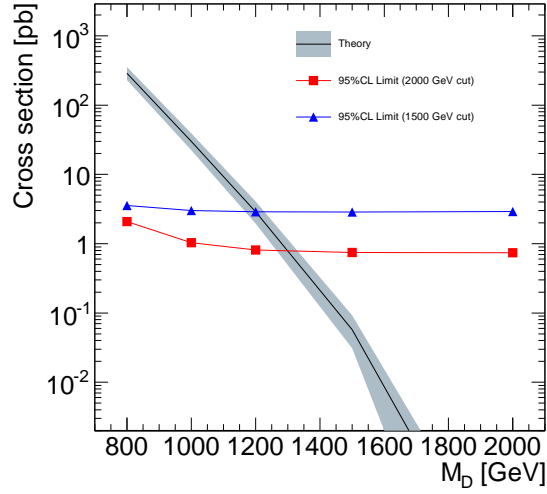
$$\begin{aligned}\mathcal{R}'_2 &: \sum p_T > 1500 \text{ GeV}, \quad N_J < 5, \\ \mathcal{R}'_3 &: \sum p_T > 1500 \text{ GeV}, \quad N_J \geq 5.\end{aligned}\tag{10.1}$$

Table 10.1 gives the number of observed events in each region.

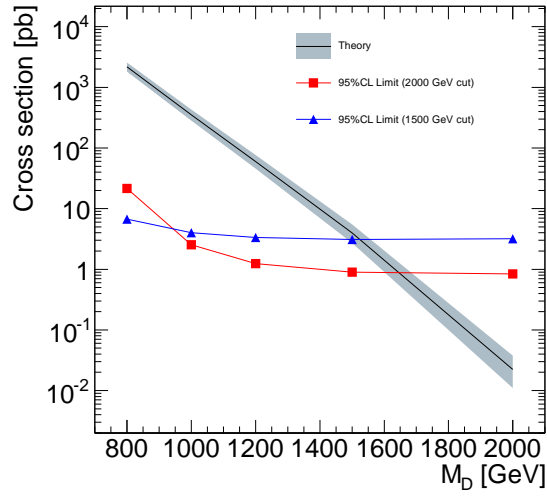
Table 10.1: Number of events in each region of the data

$\sum p_T$ [GeV]	1100 to 1200	> 1500
$N_J \geq 5$	194	71
$N_J < 5$	685	153

Figure 10.1, Table 10.2 and Table 10.3 give resulting upper limits on the black hole production with different  $\sum p_T$  boundaries. The results of



(a)



(b)

Figure 10.1: 95% CL upper limit on the cross section for  $n = 4$  (a) and  $n = 6$  (b) on the assumption of  $\lambda < r_s$ . The observed limit with  $\sum p_T$  cut of 1500 (2000) GeV and the signal cross section are shown by triangles (rectangles) and a solid line, respectively. The PDF uncertainty on the theoretical cross section is shown by an error band.

the  $\sum p_T$  boundary at 1500 GeV indicate slightly weaker limits on the cross sections, however, no significant change of the constraint on  $M_D$  can be found; the limit on  $M_D$  in case of  $n = 4$  is set to be 1.19 TeV, nearly equal to the result of Eq. 9.1.

Table 10.2: 95 % CL limits on cross sections for signal point on the assumption  $\lambda < r_s$

Signal point	Cross section $\pm$ Uncertainty	95 % CL Limits ( $\sum p_T$ cut of 2000 GeV)	95 % CL Limits ( $\sum p_T$ cut of 1500 GeV)
rs_2_800	$4.4 \pm^{+1.71}_{-1.37}$	0.713	2.44
rs_2_1000	$0.102 \pm^{+0.059}_{-0.045}$	0.636	2.44
rs_2_1200	$1.02 \times 10^{-3} \pm^{+0.96 \times 10^{-3}}_{-0.66 \times 10^{-3}}$	0.630	2.49
rs_3_800	$57.6 \pm^{+16.7}_{-14}$	1.11	2.93
rs_3_1000	$3.72 \pm^{+1.48}_{-1.19}$	0.765	2.67
rs_3_1200	$0.188 \pm^{+0.103}_{-0.079}$	0.679	2.59
rs_3_1500	$7.34 \times 10^{-4} \pm^{+7.24 \times 10^{-4}}_{-4.94 \times 10^{-4}}$	0.683	2.68
rs_4_800	$2.89 \times 10^2 \pm^{+0.67 \times 10^2}_{-0.58 \times 10^2}$	2.08	3.57
rs_4_1000	$29.9 \pm^{+9.2}_{-7.6}$	1.03	3.02
rs_4_1200	$2.89 \pm^{+1.18}_{-0.94}$	0.811	2.89
rs_4_1500	$5.74 \times 10^{-2} \pm^{+3.54 \times 10^{-2}}_{-2.63 \times 10^{-2}}$	0.748	2.86
rs_4_2000	$4.37 \times 10^{-6} \pm^{+7.28 \times 10^{-6}}_{-4.33 \times 10^{-6}}$	0.737	2.91
rs_5_800	$9.02 \times 10^2 \pm^{+1.85 \times 10^2}_{-1.59 \times 10^2}$	7.07	4.69
rs_5_1000	$1.24 \times 10^2 \pm^{+0.32 \times 10^2}_{-0.27 \times 10^2}$	1.45	3.31
rs_5_1200	$16.8 \pm^{+5.5}_{-4.5}$	1.01	3.18
rs_5_1500	$0.729 \pm^{+0.343}_{-0.268}$	0.813	2.99
rs_5_2000	$1.05 \times 10^{-3} \pm^{+0.98 \times 10^{-3}}_{-0.68 \times 10^{-3}}$	0.802	3.11
rs_6_800	$2.17 \times 10^3 \pm^{+0.4 \times 10^3}_{-0.35 \times 10^3}$	21.5	6.71
rs_6_1000	$3.51 \times 10^2 \pm^{+0.79 \times 10^2}_{-0.68 \times 10^2}$	2.54	4.00
rs_6_1200	$59.7 \pm^{+16.5}_{-14}$	1.24	3.36
rs_6_1500	$3.96 \pm^{+1.56}_{-1.25}$	0.897	3.11
rs_6_2000	$2.23 \times 10^{-2} \pm^{+1.53 \times 10^{-2}}_{-1.13 \times 10^{-2}}$	0.840	3.20
rs_7_800	$4.3 \times 10^3 \pm^{+0.73 \times 10^3}_{-0.64 \times 10^3}$	20.3	11.0
rs_7_1000	$7.81 \times 10^2 \pm^{+1.63 \times 10^2}_{-1.4 \times 10^2}$	5.00	4.94
rs_7_1200	$1.55 \times 10^2 \pm^{+0.38 \times 10^2}_{-0.33 \times 10^2}$	1.74	3.88
rs_7_1500	$14 \pm^{+4.7}_{-3.8}$	1.02	3.34
rs_7_2000	$0.171 \pm^{+0.095}_{-0.072}$	0.866	3.24

Table 10.3: 95 % CL limits on cross sections for signal point on the assumption  $\lambda < r_h$

Signal point	Cross section $\pm$ Uncertainty	95 % CL Limits ( $\sum p_T$ cut of 2000 GeV)	95 % CL Limits ( $\sum p_T$ cut of 1500 GeV)
rh_2_800	$3.27 \times 10^{-3} \pm^{+3.03 \times 10^{-3}}_{-2.1 \times 10^{-3}}$	0.542	2.18
rh_3_800	$0.603 \pm^{+0.332}_{-0.252}$	0.606	2.30
rh_3_1000	$2.66 \times 10^{-3} \pm^{+2.58 \times 10^{-3}}_{-1.75 \times 10^{-3}}$	0.582	2.32
rh_4_800	$9.88 \pm^{+3.84}_{-3.09}$	0.746	2.56
rh_4_1000	$0.227 \pm^{+0.136}_{-0.101}$	0.637	2.46
rh_4_1200	$2.11 \times 10^{-3} \pm^{+1.98 \times 10^{-3}}_{-1.37 \times 10^{-3}}$	0.632	2.52
rh_5_800	$61.1 \pm^{+19.2}_{-15.9}$	0.918	2.70
rh_5_1000	$3.09 \pm^{+1.35}_{-1.07}$	0.727	2.67
rh_5_1200	$0.104 \pm^{+0.065}_{-0.049}$	0.682	2.65
rh_5_1500	$1.26 \times 10^{-4} \pm^{+1.64 \times 10^{-4}}_{-1.04 \times 10^{-4}}$	0.690	2.73
rh_6_800	$2.28 \times 10^2 \pm^{+0.59 \times 10^2}_{-0.5 \times 10^2}$	1.29	3.09
rh_6_1000	$18 \pm^{+6.5}_{-5.3}$	0.838	2.81
rh_6_1200	$1.18 \pm^{+0.58}_{-0.45}$	0.746	2.77
rh_6_1500	$9.14 \times 10^{-3} \pm^{+7.5 \times 10^{-3}}_{-5.32 \times 10^{-3}}$	0.702	2.75
rh_7_800	$6.18 \times 10^2 \pm^{+1.41 \times 10^2}_{-1.21 \times 10^2}$	2.10	3.66
rh_7_1000	$65.4 \pm^{+19.5}_{-16.3}$	1.03	3.04
rh_7_1200	$6.41 \pm^{+2.59}_{-2.07}$	0.806	2.85
rh_7_1500	$0.127 \pm^{+0.078}_{-0.058}$	0.745	2.87
rh_7_2000	$1.03 \times 10^{-5} \pm^{+1.72 \times 10^{-5}}_{-1.01 \times 10^{-5}}$	0.754	2.97

## 10.2 Comparison with Astrophysical Results

Astrophysical observations also provide attractive results on  $M_D$ . The best existing limits on  $M_D$  for  $n \leq 3$  are given by the constraints on the KK graviton emission rate in supernova cores and neutron stars, which greatly exceed 1 TeV [44]. For larger values of  $n$ , resulting bounds by collider experiments are competitive and on solid theoretical footing: large theoretical uncertainties are involved in the calculation of the KK graviton emission probabilities, however, not incorporated in the limits. For  $n = 6$  and 7, the result of this thesis provides most strict constraints on  $M_D$ .

Further, the limits obtained from the mini black hole observation in collisions of ultra high-energy neutrino cosmic-rays with the atmosphere are reported in [45]. For  $n \geq 5$ , the  $M_D$  lower limits are 1.0 and 1.4 in case  $M_{\text{BHth}} = M_D$  and  $M_{\text{BHth}} = 3M_D$ , respectively. Corresponding result of this thesis, in case of  $M_D < M_{\text{BHth}} < 3M_D$ , shows a more strict limit of  $M_D > 2.08$  TeV for  $n \geq 5$ .

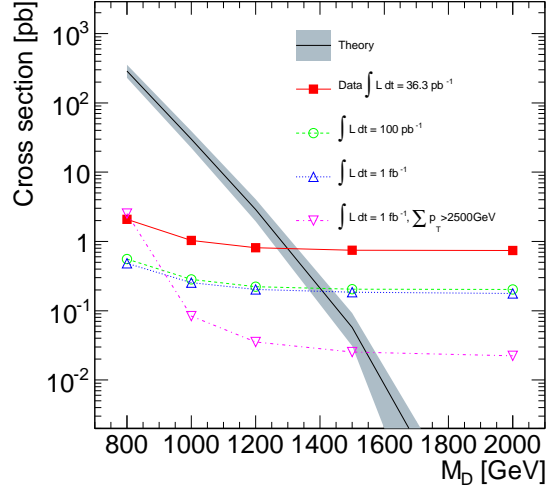
## 10.3 Expected limits with increased statistics

In 2011, the integrated luminosity is expected to achieve  $O(1)\text{fb}^{-1}$  at the center of mass energy of 7 TeV or 8 TeV. In this section, the experimental sensitivities of searching for the mini black hole are evaluated with increased statistics and high energy collisions above 7 TeV.

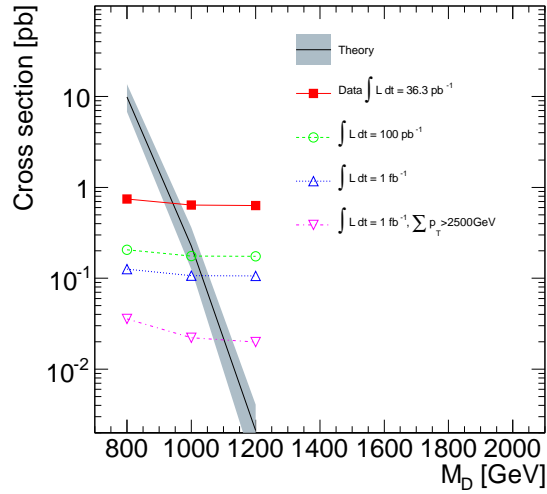
First, expected limits with data samples corresponding to  $100\text{pb}^{-1}$  and  $1\text{fb}^{-1}$  at  $\sqrt{s} = 7$  TeV are calculated with MC events. Here, a modified boundary of 2500 GeV on  $\sum p_T$  is also adopted to improve the experimental sensitivities with increased statistics. In the calculation, the number of QCD MC events is normalized by that of observed events in a data sample of  $36.3\text{pb}^{-1}$ .

Figure 10.2 shows expected limits on the black hole production cross sections for  $n = 4$ . On the assumption of  $\lambda < r_s$  ( $\lambda < r_h$ ), the lower limit on  $M_D$  is expected to reach beyond 1.5(1) TeV. Table 10.4 and 10.5 summarize the expected limits on  $M_D$  with each statistics on the assumption of  $\lambda < r_s$  and  $\lambda < r_h$ , respectively. An improvement of limit on  $M_D$  by 0.2 TeV is expected with a data sample of  $1\text{fb}^{-1}$ , however, a large amount of data corresponding to  $O(1)\text{ab}^{-1}$  is required to test a signal model of  $M_D \sim 2$  TeV.

The production cross sections of high mass black holes are largely increased in higher energy collisions. Figure 10.4 shows cross sections for three different parameter sets as a function of  $\sqrt{s}$ . Black, red and blue lines represent signals of  $M_{\text{BHth}} = 2.9, 5.9$  and  $8.6$  TeV, respectively. Corresponding

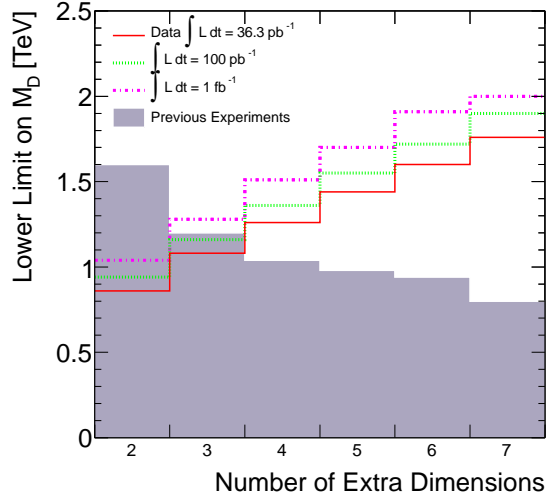


(a)

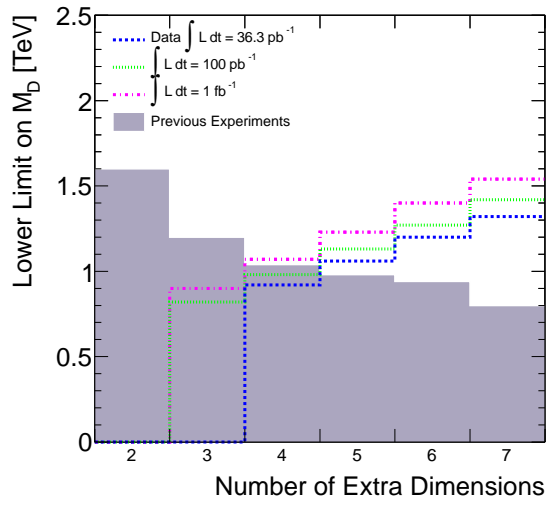


(b)

Figure 10.2: Expected 95% CL upper limit on cross section with theoretical cross section for  $n = 4$  on the assumption  $\lambda < r_s$  (a) and on the assumption  $\lambda < r_h$  (b). The observed upper limits on the signal cross section with  $36.3 \text{ pb}^{-1}$  are shown by rectangles. The theoretical cross sections are represented by solid lines. The error band for theoretical cross section represents the cross section uncertainty estimated by CTEQ66 error set. Circles and Triangles are expected limits for the integrated luminosity of  $100 \text{ pb}^{-1}$  and  $1 \text{ fb}^{-1}$ , respectively. Inverted triangles represent expected limits with  $\sum p_T$  cut of  $2500 \text{ GeV}$  for regions of  $\mathcal{R}_{2,3}$  with  $1 \text{ fb}^{-1}$  data.



(a)



(b)

Figure 10.3: Expected lower limits on  $M_D$  for on the assumption of  $\lambda < r_s$  (a) and  $\lambda < r_h$  (b). Red and blue lines shows the limits for the data of  $36.3\text{pb}^{-1}$  on the assumption of  $\lambda < r_s$  and  $\lambda < r_h$ , respectively. Green and pink lines in both figures represent expected limits for  $100\text{pb}^{-1}$  and for  $1\text{fb}^{-1}$  with  $\sum p_T$  cut of  $2500\text{GeV}$ , respectively.

Table 10.4: Expected 95 % CL Limits on  $M_D$  [TeV] on the assumption  $\lambda < r_s$ . The obtained limits with data of  $36.3 \text{ pb}^{-1}$ , expected limits for  $100 \text{ pb}^{-1}$  and expected limits for  $1 \text{ pb}^{-1}$  with  $\sum p_T$  cut of  $2500 \text{ GeV}$  are listed. The limits reported from the previous collider experiments are shown in the last column.

$n$	Data $36.3 \text{ pb}^{-1}$	Expected $100 \text{ pb}^{-1}$	Expected $1 \text{ fb}^{-1}$ $\sum p_T > 2500 \text{ GeV}$	Previous Result
2	0.86	0.94	1.04	1.60
3	1.08	1.16	1.28	1.20
4	1.26	1.36	1.51	1.04
5	1.44	1.55	1.70	0.98
6	1.60	1.72	1.91	0.94
7	1.76	1.90	>2.00	0.80

Table 10.5: Expected 95 % CL Limits on  $M_D$  [TeV] on the assumption  $\lambda < r_h$ . The obtained limits with data of  $36.3 \text{ pb}^{-1}$ , expected limits for  $100 \text{ pb}^{-1}$  and expected limits for  $1 \text{ pb}^{-1}$  with  $\sum p_T$  cut of  $2500 \text{ GeV}$  are listed. The limits reported from the previous collider experiments are shown in the last column.

$n$	Data $36.3 \text{ pb}^{-1}$	Expected $100 \text{ pb}^{-1}$	Expected $1 \text{ fb}^{-1}$ $\sum p_T > 2500 \text{ GeV}$	Previous Result
2	-	-	-	1.60
3	-	0.82	0.90	1.20
4	0.92	0.98	1.07	1.04
5	1.06	1.13	1.23	0.98
6	1.20	1.27	1.40	0.94
7	1.32	1.42	1.54	0.80

signal points at 7 TeV for these parameter sets are rs\_4\_1000, rs\_4\_2000 and rh\_4\_2000 for black, red and blue lines, respectively. In case  $M_{\text{BHth}} = 2.9$  TeV, the cross section increases threefold by changing  $\sqrt{s}$  from 7 TeV to 8 TeV, and about 100 times by changing  $\sqrt{s}$  from 7 TeV to 14 TeV. On the other hand, the cross section of  $(n, M_D, M_{\text{BHth}})=(4, 2 \text{ TeV}, 5.9 \text{ TeV})$  (red line) at  $\sqrt{s} = 8$  TeV is  $8 \times 10^{-3}$  pb, which is  $\sim 100$  times higher than the cross section at  $\sqrt{s} = 7$  TeV. In case  $\sqrt{s} = 8$  TeV, more than 10 events are expected with data of  $20 \text{ fb}^{-1}$ . For  $M_{\text{BHth}} = 8.6$  TeV, the collision energy is not enough to produce black holes; such model of a higher mass could be tested with collision data of  $\sqrt{s} = 14$  TeV where the cross section would increase up to 0.04 pb.

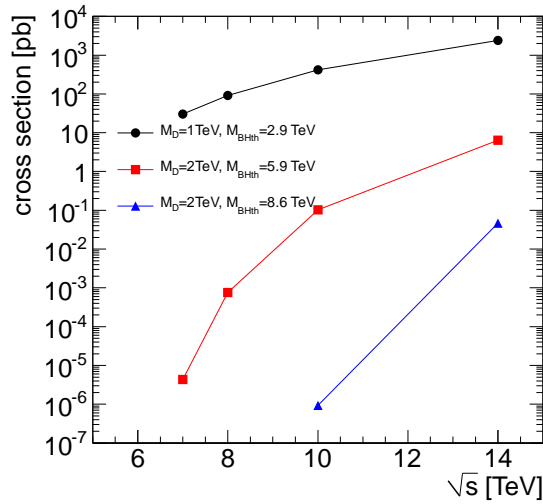


Figure 10.4: Cross sections for three different parameter sets of  $(M_D, M_{\text{BHth}})$  as a function of  $\sqrt{s}$ . Black, red, and blue lines represent parameter sets of  $(1 \text{ TeV}, 2.9 \text{ TeV})$ ,  $(2 \text{ TeV}, 5.9 \text{ TeV})$  and  $(2 \text{ TeV}, 8.6 \text{ TeV})$ , respectively.

In summary, the experimental sensitivities to  $M_D$  do not change to a great extent with increased statistics. Hopefully, in near future, a new search with 14 TeV collisions will address black holes with higher masses and improve the constraint on  $M_D$ .

# Chapter 11

## Conclusions

A theory introducing extra dimensions is one of the solutions for the hierarchy problem in which the Planck scale is vastly large compared with the electroweak scale. In the theory of extra dimensions, the gravitational field can propagate into all dimensions while all the other Standard Model particles are localized in the 3+1 space-time dimensions. Therefore, only a part of the gravitational force is measured in 3 + 1 space-time dimensions and it is reduced from the fundamental gravitational force. This could lead the fundamental Planck scale of  $O(1)$  TeV and solve the hierarchy problem. Black hole events are one of the signatures of extra dimensions because if there are such extra dimensions, the mini black holes with masses of  $O(1)$  TeV could be produced in particle collisions with the sufficient energy. In 2010, 3.5 TeV proton beams are provided by LHC and the collision data at  $\sqrt{s} = 7$  TeV were recorded by the ATLAS detector. The mini black hole events were searched with the entire data sample corresponding to the integrated luminosity of  $36.3\text{pb}^{-1}$ .

Black hole events are characterized as high- $p_T$  and high multijet events. With the classification of high- $p_T$  multijet signature, the dominant background contribution comes from the QCD process. The observables of the number of jets,  $N_J$ , and the scalar sum of  $p_T$  of jets,  $\sum p_T$ , gives a good discrimination performance between mini black hole and QCD background events. In this thesis, a data driven method to estimate the QCD background contribution was developed based on the  $\sum p_T$ - $N_J$  two-dimensional distribution and a series of limits were set on the mini black hole production.

For mini black hole signals, two assumptions for the production mass of black holes with the Schwarzschild radius ( $r_s$ ) and horizon radius ( $r_h$ ) are considered; black holes are produced if the Compton wave length ( $\lambda$ ) is equal to or less than the Schwarzschild (horizon) radius. These assumptions give fixed mass threshold for each  $n$  and  $M_D$ . No graviton emission model is used

in this thesis. In case Planck Phase where  $M_{\text{BH}} < M_D$ , the burst model, which makes multi-body decay at this phase, is adopted.

Extracted signal yields are consistent with zero and cross section upper limits are set on the cross sections of the mini black holes. On the assumption of  $\lambda < r_s$  ( $r_h$ ), a lower limit on the Planck scale at 95 % CL was set as

$$M_D > 1.26 (1.06) \text{ TeV} \quad \text{for } n = 4 (5),$$

and more strict limits for larger  $n$  were obtained. Currently, these results are the most stringent limits on  $M_D$  by the collider experiments.

# Appendix A

## Parameters for BlackMax

This is the one of the example of the parameter file for BlackMax ( $n = 4$ ,  $M_D = 1000$  GeV,  $M_{\text{BHth}} = 2923$  GeV)

```
Number_of_simulations
6200
incoming_particle (1: pp-2: ppbar-3: ee+)
1
Center_of_mass_energy_of_incoming_particle
7000.
M_pl(GeV)
1000
definition_of_M_pl:(1:M.D.2:M.p-3:M.DL.4: put_in_by_hand)
1
if_definition==4
1.
Choose_a_case:(1:tensionless_nonrotating-2:tension_nonrotating-3:rotating_nonsplit-4:
  Lisa_two_particles_final_states)
3
number_of_extra_dimensions
4
number_of_splitting_dimensions
0
size_of_brane (1/Mpl)
0.0
extradimension_size (1/Mpl)
10.
tension (parameter_of_deficit_angle:1_to_0)
1.0
choose_a_pdf_file (200_to_240.cteq6) Or_>10000.for.LHAPDF
10550
Chose_events_by_center_of_mass_energy_or_by_initial_black_hole_mass (1:center_of_mass-2:
  black_hole.mass)
2
Minimum.mass (GeV)
2923
Maximum.mass (GeV)
7000.
Include_string_ball:(1:no-2:yes)
1
String_scale (M_s) (GeV)
0
string_coupling (g_s)
0
The_minimum_mass_of_a_string_ball_or_black_hole (in_unit_Mpl)
1.
fix_time_step (1:fix-2:no)
2
time_step (1/GeV)
1.e-5
other_definition_of_cross_section (0:no-1:yoshino-2:pi*r^2-3:4pi*r^2)
2
calculate_the_cross_section_according_to (0:the_radius_of_initial_black_hole-1:
  centre_of_mass_energy)
1
calculate_angular_eigen_value (0:calculate-1:fitting_result)
0
Mass_loss_factor (0~1.0)
```

```

0.
momentum_loss_factor (0~1.0)
0.
Angular_momentum_loss_factor (0~1.0)
0.
turn_on_graviton (0: off_1 : on)
0
Seed
RAND
Write_LHA_Output_Record?_0=NO_1=Yes_2=More_Detailed_output
2
L_suppression (1: none_2: delta_area_3: anular_momentum_4: delta_angular_momentum)
1
angular_momentum_suppression_factor
1
charge_suppression (1: none_2: do)
1
charge_suppression_factor
1
color_suppression_factor
20
split_fermion_width (1/Mpl) _and_location (from -15to15) ( up_to_9extradimensions)
u_quark_Right (Note: do_not_insert_blank_spaces)
1.0
10.0,0.0,0.0,0.0,0.0,0.0,0.0,0.0,0.0,0.0
u_quark_Left (Note: do_not_insert_blank_spaces)
1.0
10.0,0.0,0.0,0.0,0.0,0.0,0.0,0.0,0.0,0.0
u_bar_quark_Right (Note: do_not_insert_blank_spaces)
1.0
10.0,0.0,0.0,0.0,0.0,0.0,0.0,0.0,0.0,0.0
u_bar_quark_Left (Note: do_not_insert_blank_spaces)
1.0
10.0,0.0,0.0,0.0,0.0,0.0,0.0,0.0,0.0,0.0
d_quark_Right (Note: do_not_insert_blank_spaces)
1.0
10.0,0.0,0.0,0.0,0.0,0.0,0.0,0.0,0.0,0.0
d_quark_Left (Note: do_not_insert_blank_spaces)
1.0
10.0,0.0,0.0,0.0,0.0,0.0,0.0,0.0,0.0,0.0
d_bar_quark_Right (Note: do_not_insert_blank_spaces)
1.0
10.0,0.0,0.0,0.0,0.0,0.0,0.0,0.0,0.0,0.0
d_bar_quark_Left (Note: do_not_insert_blank_spaces)
1.0
10.0,0.0,0.0,0.0,0.0,0.0,0.0,0.0,0.0,0.0
s_quark_Right (Note: do_not_insert_blank_spaces)
1.0
10.0,0.0,0.0,0.0,0.0,0.0,0.0,0.0,0.0,0.0
s_quark_Left (Note: do_not_insert_blank_spaces)
1.0
10.0,0.0,0.0,0.0,0.0,0.0,0.0,0.0,0.0,0.0
s_bar_quark_Right (Note: do_not_insert_blank_spaces)
1.0
10.0,0.0,0.0,0.0,0.0,0.0,0.0,0.0,0.0,0.0
s_bar_quark_Left (Note: do_not_insert_blank_spaces)
1.0
10.0,0.0,0.0,0.0,0.0,0.0,0.0,0.0,0.0,0.0
c_quark_Right (Note: do_not_insert_blank_spaces)
1.0
10.0,0.0,0.0,0.0,0.0,0.0,0.0,0.0,0.0,0.0
c_quark_Left (Note: do_not_insert_blank_spaces)
1.0
10.0,0.0,0.0,0.0,0.0,0.0,0.0,0.0,0.0,0.0
c_bar_quark_Right (Note: do_not_insert_blank_spaces)
1.0
10.0,0.0,0.0,0.0,0.0,0.0,0.0,0.0,0.0,0.0
c_bar_quark_Left (Note: do_not_insert_blank_spaces)
1.0
10.0,0.0,0.0,0.0,0.0,0.0,0.0,0.0,0.0,0.0
b_quark_Right (Note: do_not_insert_blank_spaces)
1.0
10.0,0.0,0.0,0.0,0.0,0.0,0.0,0.0,0.0,0.0
b_quark_Left (Note: do_not_insert_blank_spaces)
1.0
10.0,0.0,0.0,0.0,0.0,0.0,0.0,0.0,0.0,0.0
b_bar_quark_Right (Note: do_not_insert_blank_spaces)
1.0
10.0,0.0,0.0,0.0,0.0,0.0,0.0,0.0,0.0,0.0
b_bar_quark_Left (Note: do_not_insert_blank_spaces)
1.0
10.0,0.0,0.0,0.0,0.0,0.0,0.0,0.0,0.0,0.0
t_quark_Right (Note: do_not_insert_blank_spaces)

```

```

1.0
10.0,0.0,0.0,0.0,0.0,0.0,0.0,0.0,0.0,0.0
t_quark_Left (Note: do_not_insert_blank_spaces)
1.0
10.0,0.0,0.0,0.0,0.0,0.0,0.0,0.0,0.0,0.0
t_bar_quark_Right (Note: do_not_insert_blank_spaces)
1.0
10.0,0.0,0.0,0.0,0.0,0.0,0.0,0.0,0.0,0.0
t_bar_quark_Left (Note: do_not_insert_blank_spaces)
1.0
10.0,0.0,0.0,0.0,0.0,0.0,0.0,0.0,0.0,0.0
e_-_Left (Note: do_not_insert_blank_spaces)
1.0
-10.0,0.0,0.0,0.0,0.0,0.0,0.0,0.0,0.0,0.0
e_-_Right (Note: do_not_insert_blank_spaces)
1.0
-10.0,0.0,0.0,0.0,0.0,0.0,0.0,0.0,0.0,0.0
e+_Left (Note: do_not_insert_blank_spaces)
1.0
-10.0,0.0,0.0,0.0,0.0,0.0,0.0,0.0,0.0,0.0
e+_Right (Note: do_not_insert_blank_spaces)
1.0
-10.0,0.0,0.0,0.0,0.0,0.0,0.0,0.0,0.0,0.0
mu_-_Left (Note: do_not_insert_blank_spaces)
1.0
-10.0,0.0,0.0,0.0,0.0,0.0,0.0,0.0,0.0,0.0
mu_-_Right (Note: do_not_insert_blank_spaces)
1.0
-10.0,0.0,0.0,0.0,0.0,0.0,0.0,0.0,0.0,0.0
mu+_Left (Note: do_not_insert_blank_spaces)
1.0
-10.0,0.0,0.0,0.0,0.0,0.0,0.0,0.0,0.0,0.0
mu+_Right (Note: do_not_insert_blank_spaces)
1.0
-10.0,0.0,0.0,0.0,0.0,0.0,0.0,0.0,0.0,0.0
tau_-_Left (Note: do_not_insert_blank_spaces)
1.0
-10.0,0.0,0.0,0.0,0.0,0.0,0.0,0.0,0.0,0.0
tau_-_Right (Note: do_not_insert_blank_spaces)
1.0
-10.0,0.0,0.0,0.0,0.0,0.0,0.0,0.0,0.0,0.0
tau+_Left (Note: do_not_insert_blank_spaces)
1.0
-10.0,0.0,0.0,0.0,0.0,0.0,0.0,0.0,0.0,0.0
tau+_Right (Note: do_not_insert_blank_spaces)
1.0
-10.0,0.0,0.0,0.0,0.0,0.0,0.0,0.0,0.0,0.0
neutrino_e-(Note: do_not_insert_blank_spaces)
1.0
-10.0,0.0,0.0,0.0,0.0,0.0,0.0,0.0,0.0,0.0
neutrino_e+(Note: do_not_insert_blank_spaces)
1.0
-10.0,0.0,0.0,0.0,0.0,0.0,0.0,0.0,0.0,0.0
neutrino_mu-(Note: do_not_insert_blank_spaces)
1.0
-10.0,0.0,0.0,0.0,0.0,0.0,0.0,0.0,0.0,0.0
neutrino_mu+(Note: do_not_insert_blank_spaces)
1.0
-10.0,0.0,0.0,0.0,0.0,0.0,0.0,0.0,0.0,0.0
neutrino_tau-(Note: do_not_insert_blank_spaces)
1.0
-10.0,0.0,0.0,0.0,0.0,0.0,0.0,0.0,0.0,0.0
neutrino_tau+(Note: do_not_insert_blank_spaces)
1.0
-10.0,0.0,0.0,0.0,0.0,0.0,0.0,0.0,0.0,0.0
number_of_conservation
2
d,s,b,u,c,t,e,mu,tau,nu_e,nu_mu,nu_tau
1,1,1,1,1,1,0,0,0,0,0,0
0,0,0,0,0,0,1,1,1,1,1,1
1,1,1,1,1,1,-3,-3,-3,-3,-3,-3
0,0,0,0,0,0,0,0,0,0,0,0
0,0,0,0,0,0,0,0,0,0,0,0
0,0,0,0,0,0,0,0,0,0,0,0
0,0,0,0,0,0,0,0,0,0,0,0

```

# Appendix B

## Mass Reconstruction of the Mini Black Hole

If all particles emitted by the mini black hole can be detected, the mass of the mini black hole is reconstructed as

$$p_{\text{BH}} = \sum_{i=\text{particles}} p_i, \quad (\text{B.1})$$

$$M_{\text{BH}} = \sqrt{p_{\text{BH}}^2}. \quad (\text{B.2})$$

The mini black hole events are dominated by jets. Therefore the particles in Eq. B.1 can be replaced by jets. In addition, the momentum of the transverse direction can be assumed to be conserved before and after the mini black hole production by particle collisions. Hence,  $E_{\text{T}}^{\text{miss}}$  in the event can be considered as a part of momentum of particles emitted by the mini black hole. With jets and  $E_{\text{T}}^{\text{miss}}$ , Eq B.1 is rewritten as

$$p_{\text{BH}} = \sum_{i=\text{jets}} p_i + (E_{\text{x}}^{\text{miss}}, E_{\text{y}}^{\text{miss}}, 0, E_{\text{T}}^{\text{miss}}), \quad (\text{B.3})$$

where  $E_{\text{x}(y)}^{\text{miss}}$  is the  $E_{\text{T}}^{\text{miss}}$  component along  $x(y)$ -axis. Here,  $E_{\text{T}}^{\text{miss}}$  is reconstructed from jets as:

$$(E_{\text{x}}^{\text{miss}}, E_{\text{y}}^{\text{miss}}, 0, E_{\text{T}}^{\text{miss}}) = \sum_{\text{jets}} \left( -p_x, -p_y, 0, \sqrt{p_x^2 + p_y^2} \right) \quad (\text{B.4})$$

where  $p_{x(y)}$  is the momentum of jets along  $x(y)$ -axis.

Figure B.1(a) shows mass spectrum of the mini black hole of signal point rs.2.1000 ( $n = 2$ ,  $M_D = 1000$  GeV,  $M_{\text{BHth}} = 4266$  GeV). Dashed line shows truth mass of which lower edge is 4266 GeV. Green line shows the mass

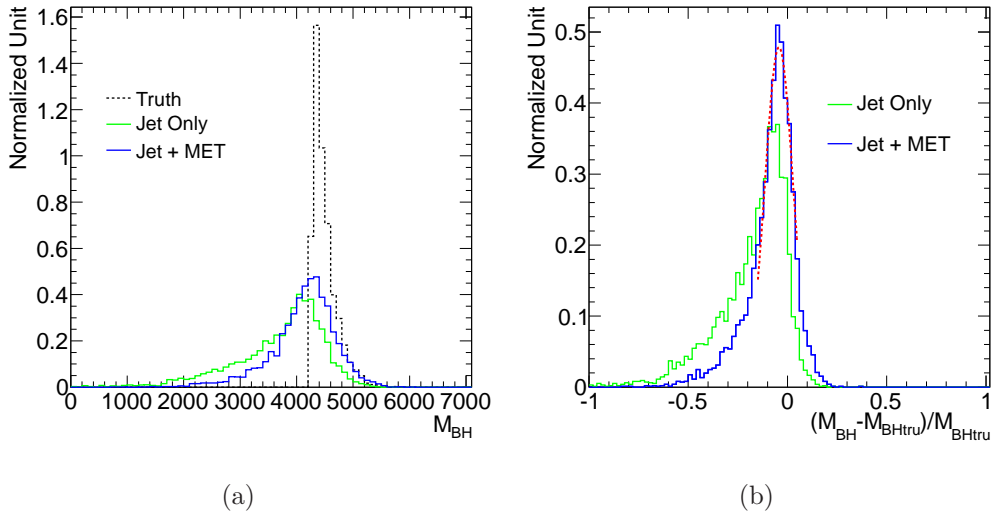


Figure B.1: The mass spectrum (a) and the resolution (b) of the mini black hole. Signal point  $rs\_2\_1000$  ( $n = 2$ ,  $M_D = 1000$  GeV,  $M_{\text{BHth}} = 4266$  GeV) is used. Dashed line in (a) shows truth mass distribution. Green and blue lines show the mass distributions reconstructed from only jets and jets and  $E_T^{\text{miss}}$ , respectively.  $E_T^{\text{miss}}$  is calculated from jets. Red line represent Gaussian function fitted to Jet + MET distribution. The fitted function shows the mean value equal to  $-0.0427$  and the deviation equal to  $0.0701$ .

reconstructed from only jets and jets +  $E_T^{\text{miss}}$ , respectively. The tail in the lower region is reduced by addition of  $E_T^{\text{miss}}$ . Figure B.1(b) shows resolutions for the mass reconstructed from only jets and jets +  $E_T^{\text{miss}}$ . Red line shows a Gaussian function fitted to the distribution of jets +  $E_T^{\text{miss}}$ . The fitted function shows the scale shift of -4.27 % and the resolution of 7.01 %. The generated mass spectrum of the mini black hole have sharp peak at  $M_{\text{BHth}}$ , therefore reconstructed mass shows peak at  $M_{\text{BHth}}$ .

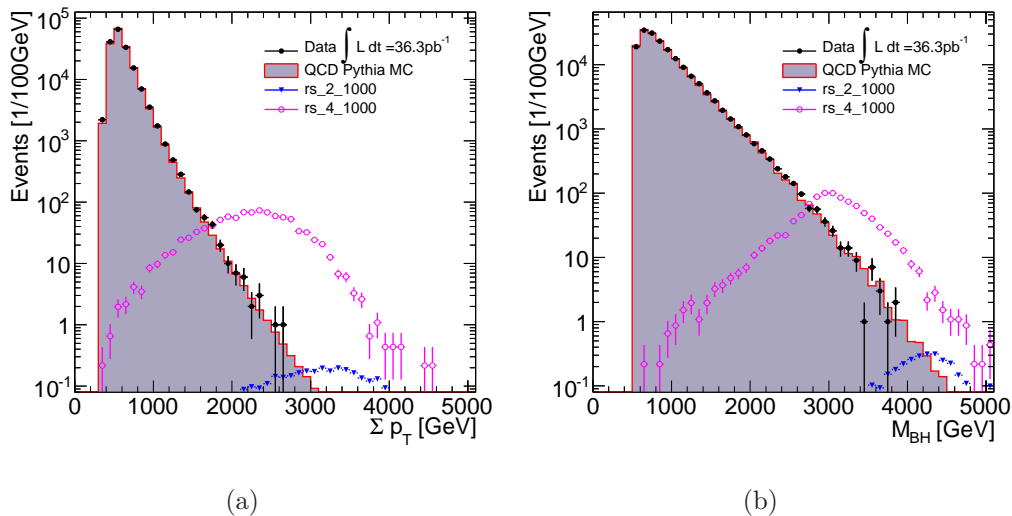


Figure B.2:  $\sum p_T$  distributions (a) and  $M_{\text{BH}}$  distributions (b) for the events required all preselection cut and the second leading jet  $p_T > 50$  GeV. The data is represented by black points. The histogram shows QCD PYTHIA MC events which is normalized by the number of total events of the data. Circles and inverted triangles represent signal points of rs\_2\_1000 and rs\_4\_1000, respectively.

Figure B.2 shows  $\sum p_T$  and  $M_{\text{BH}}$  distributions for the events required all preselection cut and the second leading jet  $p_T > 50$  GeV. Black points show the data events and the histogram shows QCD PYTHIA MC events. The histogram is normalized by the number of total events of the data. Circles and inverted triangles show signal points of rs\_2\_1000 and rs\_4\_1000, respectively. The data points in both histograms show consistent with QCD MC events within statistical uncertainty. The mass threshold of signal point for rs\_2\_1000 (rs\_4\_1000) is 4266 GeV (2923 GeV). The peak of  $M_{\text{BH}}$  distributions for signals are around the mass threshold while QCD events show smooth line from low  $M_{\text{BH}}$  region. Therefore, this variable is also good variables to

discriminate signal and QCD events.

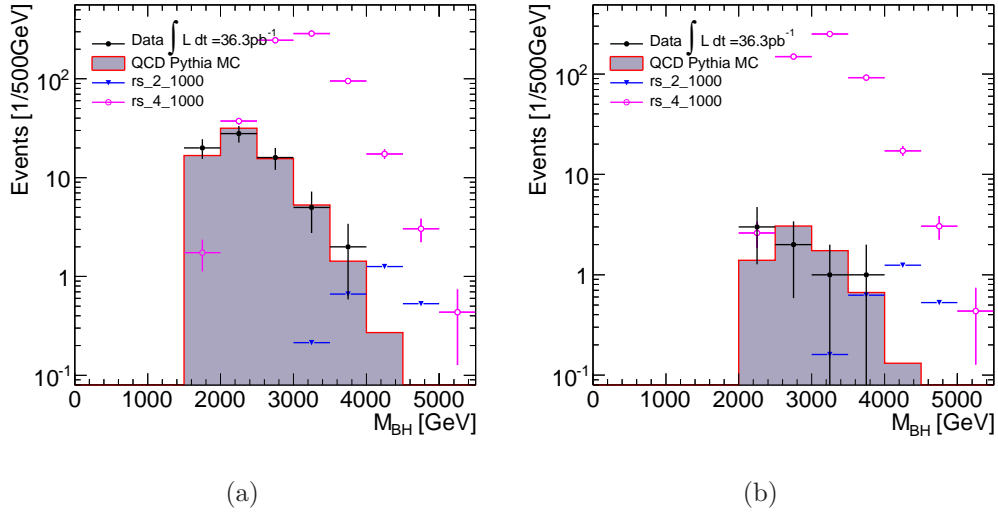


Figure B.3:  $M_{\text{BH}}$  distributions for events of  $N_J \geq 5$  with  $\sum p_T$  cut of 1500 GeV (a) and 2000 GeV (b). The data is represented by black points. The histogram shows QCD PYTHIA MC events which is normalized by the number of total events of the data. Circles and inverted triangles represent signal points of rs\_2\_1000 and rs\_4\_1000, respectively.

Figure B.3(a) and B.3(b) show  $M_{\text{BH}}$  distributions for the events of  $N_J \geq 5$  with  $\sum p_T$  cut of 1500 GeV and 2000 GeV, respectively. The definitions of the plots are same as Figure B.2. The data events shows consistent with the shape of QCD PYTHIA MC events and signal like events are not observed.

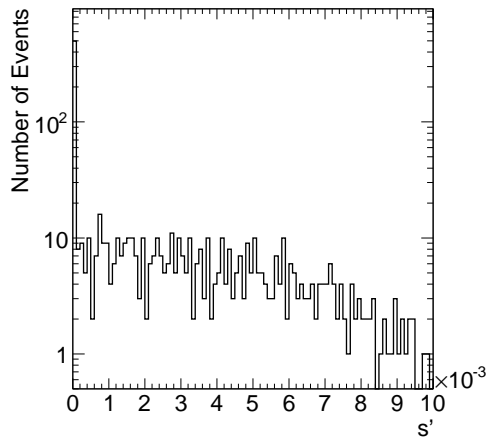
# Appendix C

## Further Validation of Signal Extraction

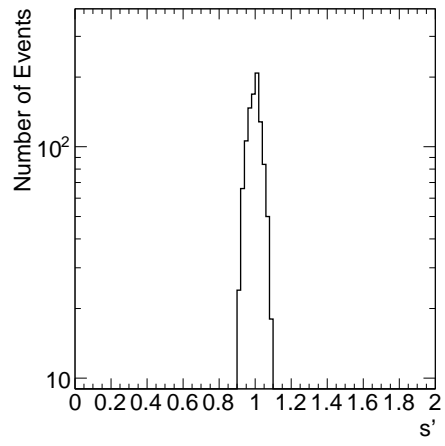
This appendix describes the validation of extraction method described in Chapter 8 in addition to Section 8.5.

Figure 8.9 shows zero consistent for only QCD background pseudo data, and Figure 8.10 shows consistent with unity for pseudo data with signal events.

To check them, thousand set of pseudo data events are generated in the Poisson regime under the constraint of Eq. 8.7, 8.11 and 8.12, using input data set for above figures as the mean value,  $\mu_i$ . For each pseudo data set, a best fit value for  $s'$  which maximizes likelihood function of Eq 8.13 is obtained. Figure C.1(a) (C.1(b)) shows the best fit value of  $s'$  for the pseudo data without (with) signal events for signal point of  $rs_4_{1000}$ . As expected, Figure C.1(a) shows localization around zero while C.1(b) shows the distribution around unity.



(a)



(b)

Figure C.1:

# Bibliography

- [1] S. Weinberg, *A Model of Leptons*, *Phys. Rev. Lett.* **19** (1967) 1264–1266.
- [2] A. Salam, *Weak and Electromagnetic Interactions*, . Originally printed in \*Svartholm: Elementary Particle Theory, Proceedings Of The Nobel Symposium Held 1968 At Lerum, Sweden\*, Stockholm 1968, 367-377.
- [3] H. D. Politzer, *RELIABLE PERTURBATIVE RESULTS FOR STRONG INTERACTIONS?*, *Phys. Rev. Lett.* **30** (1973) 1346–1349.
- [4] D. J. Gross and F. Wilczek, *ULTRAVIOLET BEHAVIOR OF NON-ABELIAN GAUGE THEORIES*, *Phys. Rev. Lett.* **30** (1973) 1343–1346.
- [5] H. Fritzsch, M. Gell-Mann, and H. Leutwyler, *Advantages of the Color Octet Gluon Picture*, *Phys. Lett.* **B47** (1973) 365–368.
- [6] P. W. Higgs, *Spontaneous Symmetry Breakdown without Massless Bosons*, *Phys. Rev.* **145** (1966) 1156–1163.
- [7] Y. Nambu and G. Jona-Lasinio, *Dynamical model of elementary particles based on an analogy with superconductivity. I*, *Phys. Rev.* **122** (1961) 345–358.
- [8] UA1 Collaboration, G. Arnison et al., *Experimental observation of isolated large transverse energy electrons with associated missing energy at  $s^{*}(1/2) = 540\text{-GeV}$* , *Phys. Lett.* **B122** (1983) 103–116.
- [9] UA2 Collaboration, M. Banner et al., *Observation of single isolated electrons of high transverse momentum in events with missing transverse energy at the CERN anti-p p collider*, *Phys. Lett.* **B122** (1983) 476–485.

- [10] UA1 Collaboration, G. Arnison et al., *Experimental observation of lepton pairs of invariant mass around 95-GeV/c\*\*2 at the CERN SPS collider*, *Phys. Lett.* **B126** (1983) 398–410.
- [11] UA2 Collaboration, P. Bagnaia et al., *Evidence for  $Z^0 \rightarrow e^+ e^-$  at the CERN anti-p p collider*, *Phys. Lett.* **B129** (1983) 130–140.
- [12] LEP Working Group for Higgs boson searches Collaboration, R. Barate et al., *Search for the standard model Higgs boson at LEP*, *Phys. Lett.* **B565** (2003) 61–75, [arXiv:hep-ex/0306033](#).
- [13] LEP Collaboration, *A Combination of preliminary electroweak measurements and constraints on the standard model*, [arXiv:hep-ex/0312023](#).
- [14] CDF and D0 Collaboration, *Combined CDF and D0 Upper Limits on Standard Model Higgs- Boson Production with up to 6.7 fb<sup>-1</sup> of Data*, [arXiv:1007.4587 \[hep-ex\]](#).
- [15] C. ATLAS, *ATLAS Sensitivity Prospects for 1 Higgs Boson Production at the LHC Running at 7, 8 or 9 TeV*, Tech. Rep. ATL-PHYS-PUB-2010-015, CERN, Geneva, Nov, 2010.
- [16] D. V. Volkov and V. P. Akulov, *Is the Neutrino a Goldstone Particle?*, *Phys. Lett.* **B46** (1973) 109–110.
- [17] J. Wess and B. Zumino, *Supergauge Transformations in Four-Dimensions*, *Nucl. Phys.* **B70** (1974) 39–50.
- [18] S. P. Martin, *A Supersymmetry Primer*, [arXiv:hep-ph/9709356](#).
- [19] D. I. Kazakov, *Beyond the standard model (in search of supersymmetry)*, [arXiv:hep-ph/0012288](#).
- [20] U. Amaldi, W. de Boer, and H. Furstenau, *Comparison of grand unified theories with electroweak and strong coupling constants measured at LEP*, *Phys. Lett.* **B260** (1991) 447–455.
- [21] J. R. Ellis, J. S. Hagelin, D. V. Nanopoulos, K. A. Olive, and M. Srednicki, *Supersymmetric relics from the big bang*, *Nucl. Phys.* **B238** (1984) 453–476.
- [22] G. Noardström, *Über die Möglichkeit, das elektromagnetische Feld und das Gravitationsfeld zu vereinigen*, *Phys. Z.* **15** (1914) 504 – 506.

- [23] A. Einstein, *Die Grundlage der allgemeinen Relativitätstheorie*, *Annalen der Physik* **345** (1916) 769 – 822.
- [24] T. Kaluza, *Zum unitätsproblem in der physik*, Preuss. Akad. Wiss. Berlin (1921) 966 – 972.
- [25] O. Klein, *Quantentheorie und funfdimensionale relativitätstheorie*, *Z. Phys* (1926) 895 – 906.
- [26] E. Cremmer, B. Julia, and J. Scherk, *Supergravity theory in 11 dimensions*, *Phys. Lett.* **B76** (1978) 409–412.
- [27] M. B. Green and J. H. Schwarz, *Supersymmetrical String Theories*, *Phys. Lett.* **B109** (1982) 444–448.
- [28] J. Polchinski, *Lectures on D-branes*, [arXiv:hep-th/9611050](https://arxiv.org/abs/hep-th/9611050).
- [29] N. Arkani-Hamed, S. Dimopoulos, and G. R. Dvali, *The hierarchy problem and new dimensions at a millimeter*, *Phys. Lett.* **B429** (1998) 263–272, [arXiv:hep-ph/9803315](https://arxiv.org/abs/hep-ph/9803315).
- [30] I. Antoniadis, N. Arkani-Hamed, S. Dimopoulos, and G. R. Dvali, *New dimensions at a millimeter to a Fermi and superstrings at a TeV*, *Phys. Lett.* **B436** (1998) 257–263, [arXiv:hep-ph/9804398](https://arxiv.org/abs/hep-ph/9804398).
- [31] N. Arkani-Hamed, S. Dimopoulos, and G. R. Dvali, *Phenomenology, astrophysics and cosmology of theories with sub-millimeter dimensions and TeV scale quantum gravity*, *Phys. Rev.* **D59** (1999) 086004, [arXiv:hep-ph/9807344](https://arxiv.org/abs/hep-ph/9807344).
- [32] Particle Data Group Collaboration, K. Nakamura, *Review of particle physics*, *J. Phys.* **G37** (2010) 075021.
- [33] G. F. Giudice, R. Rattazzi, and J. D. Wells, *Quantum gravity and extra dimensions at high-energy colliders*, *Nucl. Phys.* **B544** (1999) 3–38, [arXiv:hep-ph/9811291](https://arxiv.org/abs/hep-ph/9811291).
- [34] M. E. Peskin, *Theoretical summary lecture for EPS HEP99*, [arXiv:hep-ph/0002041](https://arxiv.org/abs/hep-ph/0002041).
- [35] S. B. Giddings and S. D. Thomas, *High energy colliders as black hole factories: The end of short distance physics*, *Phys. Rev.* **D65** (2002) 056010, [arXiv:hep-ph/0106219](https://arxiv.org/abs/hep-ph/0106219).

- [36] S. Dimopoulos and G. L. Landsberg, *Black Holes at the LHC*, *Phys. Rev. Lett.* **87** (2001) 161602, [arXiv:hep-ph/0106295](#).
- [37] ATLAS Collaboration, N. D. Brett et al., *Discovery reach for black hole production*, . ATL-PHYS-PUB-2009-074.
- [38] D. J. Kapner et al., *Tests of the gravitational inverse-square law below the dark-energy length scale*, *Phys. Rev. Lett.* **98** (2007) 021101, [arXiv:hep-ph/0611184](#).
- [39] S. Ask, *Search for extra dimensions at LEP*, [arXiv:hep-ex/0410004](#).
- [40] CDF Collaboration, T. Aaltonen et al., *Search for large extra dimensions in final states containing one photon or jet and large missing transverse energy produced in  $p\bar{p}$  collisions at  $\sqrt{s} = 1.96$ -TeV*, *Phys. Rev. Lett.* **101** (2008) 181602, [arXiv:0807.3132 \[hep-ex\]](#).
- [41] D0 Collaboration, V. M. Abazov et al., *Search for large extra dimensions via single photon plus missing energy final states at  $\sqrt{s} = 1.96$ -TeV*, *Phys. Rev. Lett.* **101** (2008) 011601, [arXiv:0803.2137 \[hep-ex\]](#).
- [42] C. Hanhart, J. A. Pons, D. R. Phillips, and S. Reddy, *The likelihood of GODs' existence: Improving the SN1987a constraint on the size of large compact dimensions*, *Phys. Lett.* **B509** (2001) 1–9, [arXiv:astro-ph/0102063](#).
- [43] S. Hannestad and G. Raffelt, *New supernova limit on large extra dimensions*, *Phys. Rev. Lett.* **87** (2001) 051301, [arXiv:hep-ph/0103201](#).
- [44] S. Hannestad and G. G. Raffelt, *Supernova and neutron-star limits on large extra dimensions reexamined*, *Phys. Rev.* **D67** (2003) 125008, [arXiv:hep-ph/0304029](#).
- [45] L. A. Anchordoqui, J. L. Feng, H. Goldberg, and A. D. Shapere, *Updated limits on TeV-scale gravity from absence of neutrino cosmic ray showers mediated by black holes*, *Phys. Rev.* **D68** (2003) 104025, [arXiv:hep-ph/0307228](#).
- [46] L. Randall and R. Sundrum, *A large mass hierarchy from a small extra dimension*, *Phys. Rev. Lett.* **83** (1999) 3370–3373, [arXiv:hep-ph/9905221](#).

- [47] W. D. Goldberger and M. B. Wise, *Modulus stabilization with bulk fields*, *Phys. Rev. Lett.* **83** (1999) 4922–4925, [arXiv:hep-ph/9907447](#).
- [48] H. Davoudiasl, J. L. Hewett, and T. G. Rizzo, *Experimental probes of localized gravity: On and off the wall*, *Phys. Rev.* **D63** (2001) 075004, [arXiv:hep-ph/0006041](#).
- [49] The D0 Collaboration, V. M. Abazov et al., *Search for Randall-Sundrum gravitons in the dielectron and diphoton final states with 5.4 fb<sup>-1</sup> of data from ppbar collisions at sqrt(s)=1.96 TeV*, *Phys. Rev. Lett.* **104** (2010) 241802, [arXiv:1004.1826 \[hep-ex\]](#).
- [50] J. Tanaka, T. Yamamura, S. Asai, and J. Kanzaki, *Study of black holes with the ATLAS detector at the LHC*, *Eur. Phys. J.* **C41** (2005) 19–33, [arXiv:hep-ph/0411095](#).
- [51] P. Kanti, *Black holes in theories with large extra dimensions: A Review*, *Int. J. Mod. Phys.* **A19** (2004) 4899–4951, [arXiv:hep-ph/0402168](#).
- [52] D. Ida, K.-y. Oda, and S. C. Park, *Rotating black holes at future colliders*, [arXiv:hep-ph/0312385](#).
- [53] S. W. Hawking, *Particle Creation by Black Holes*, *Commun. Math. Phys.* **43** (1975) 199–220.
- [54] D.-C. Dai et al., *BlackMax: A black-hole event generator with rotation, recoil, split branes and brane tension*, *Phys. Rev.* **D77** (2008) 076007, [arXiv:0711.3012 \[hep-ph\]](#).
- [55] M. Casals, S. R. Dolan, P. Kanti, and E. Winstanley, *Brane decay of a (4+n)-dimensional rotating black hole. III: Spin-1/2 particles*, *JHEP* **03** (2007) 019, [arXiv:hep-th/0608193](#).
- [56] D. Ida, K.-y. Oda, and S. C. Park, *Rotating black holes at future colliders. III: Determination of black hole evolution*, *Phys. Rev.* **D73** (2006) 124022, [arXiv:hep-th/0602188](#).
- [57] M. Casals, P. Kanti, and E. Winstanley, *Brane decay of a (4+n)-dimensional rotating black hole. II: Spin-1 particles*, *JHEP* **02** (2006) 051, [arXiv:hep-th/0511163](#).

- [58] G. Duffy, C. Harris, P. Kanti, and E. Winstanley, *Brane decay of a  $(4+n)$ -dimensional rotating black hole: Spin-0 particles*, *JHEP* **09** (2005) 049, [arXiv:hep-th/0507274](#).
- [59] C. M. Harris and P. Kanti, *Hawking radiation from a  $(4+n)$ -dimensional rotating black hole*, *Phys. Lett.* **B633** (2006) 106–110, [arXiv:hep-th/0503010](#).
- [60] J. A. Frost et al., *Phenomenology of Production and Decay of Spinning Extra- Dimensional Black Holes at Hadron Colliders*, *JHEP* **10** (2009) 014, [arXiv:0904.0979](#) [[hep-ph](#)].
- [61] J. D. Bekenstein and V. F. Mukhanov, *Spectroscopy of the quantum black hole*, *Phys. Lett.* **B360** (1995) 7–12, [arXiv:gr-qc/9505012](#).
- [62] B. Koch, M. Bleicher, and S. Hossenfelder, *Black hole remnants at the LHC*, *JHEP* **10** (2005) 053, [arXiv:hep-ph/0507138](#).
- [63] H. Stoecker, *Stable TeV - black hole remnants at the LHC: Discovery through di-jet suppression, mono-jet emission and a supersonic boom in the quark-gluon plasma*, *Int. J. Mod. Phys.* **D16** (2007) 185–205, [arXiv:hep-ph/0605062](#).
- [64] F. Scardigli, *Glimpses on the micro black hole Planck phase*, [arXiv:0809.1832](#) [[hep-th](#)].
- [65] S. R. Coleman, J. Preskill, and F. Wilczek, *Quantum hair on black holes*, *Nucl. Phys.* **B378** (1992) 175–246, [arXiv:hep-th/9201059](#).
- [66] J. Preskill, P. Schwarz, A. D. Shapere, S. Trivedi, and F. Wilczek, *Limitations on the statistical description of black holes*, *Mod. Phys. Lett.* **A6** (1991) 2353–2362.
- [67] L. A. Anchordoqui, J. L. Feng, H. Goldberg, and A. D. Shapere, *Inelastic black hole production and large extra dimensions*, *Phys. Lett.* **B594** (2004) 363–367, [arXiv:hep-ph/0311365](#).
- [68] P. Meade and L. Randall, *Black Holes and Quantum Gravity at the LHC*, *JHEP* **05** (2008) 003, [arXiv:0708.3017](#) [[hep-ph](#)].
- [69] D.-C. Dai et al., *Manual of BlackMax, a black-hole event generator with rotation, recoil, split branes, and brane tension*, [arXiv:0902.3577](#) [[hep-ph](#)].

- [70] L. Evans, (ed. ) and P. Bryant, (ed. ), *LHC Machine*, [JINST \*\*3\*\* \(2008\) S08001](#).
- [71] ATLAS Collaboration, G. Aad et al., *The ATLAS Experiment at the CERN Large Hadron Collider*, [JINST \*\*3\*\* \(2008\) S08003](#).
- [72] CMS Collaboration, R. Adolphi et al., *The CMS experiment at the CERN LHC*, [JINST \*\*3\*\* \(2008\) S08004](#).
- [73] LHCb Collaboration, A. A. Alves et al., *The LHCb Detector at the LHC*, [JINST \*\*3\*\* \(2008\) S08005](#).
- [74] ALICE Collaboration, K. Aamodt et al., *The ALICE experiment at the CERN LHC*, [JINST \*\*3\*\* \(2008\) S08002](#).
- [75] *ATLAS: Detector and physics performance technical design report. Volume 1*, . CERN-LHCC-99-14.
- [76] *ATLAS detector and physics performance. Technical design report. Vol. 2*, . CERN-LHCC-99-15.
- [77] A. Yamamoto et al., *The ATLAS central solenoid*, [Nucl. Instrum. Meth. \*\*A584\*\* \(2008\) 53–74](#).
- [78] A. Yamamoto et al., *Progress in ATLAS central solenoid magnet*, [IEEE Trans. Appl. Supercond. \*\*10\*\* \(2000\) 353–356](#).
- [79] G. Aad et al., *ATLAS pixel detector electronics and sensors*, [JINST \*\*3\*\* \(2008\) P07007](#).
- [80] A. Ahmad et al., *The Silicon microstrip sensors of the ATLAS semiconductor tracker*, [Nucl. Instrum. Meth. \*\*A578\*\* \(2007\) 98–118](#).
- [81] ATLAS TRT Collaboration, E. Abat et al., *The ATLAS Transition Radiation Tracker (TRT) proportional drift tube: Design and performance*, [JINST \*\*3\*\* \(2008\) P02013](#).
- [82] ATLAS Collaboration, *ATLAS liquid argon calorimeter: Technical design report*, . CERN-LHCC-96-41.
- [83] ATLAS Collaboration, *ATLAS tile calorimeter: Technical design report*, . CERN-LHCC-96-42.

- [84] ATLAS Electromagnetic Barrel Calorimeter Collaboration, M. Aharrouche et al., *Energy linearity and resolution of the ATLAS electromagnetic barrel calorimeter in an electron test- beam*, [Nucl. Instrum. Meth. \*\*A568\*\* \(2006\) 601–623](#), [arXiv:physics/0608012](#).
- [85] D. M. Gingrich et al., *Construction, assembly and testing of the ATLAS hadronic end-cap calorimeter*, [JINST \*\*2\*\* \(2007\) P05005](#).
- [86] ATLAS Liquid Argon HEC Collaboration, A. E. Kiryunin, *Performance of the ATLAS hadronic end-cap calorimeter in beam tests*, . Prepared for 10th International Conference on Calorimetry in High Energy Physics (CALOR 2002), Pasadena, California, 25-30 Mar 2002.
- [87] J. P. Archambault et al., *Energy calibration of the ATLAS liquid argon forward calorimeter*, [JINST \*\*3\*\* \(2008\) P02002](#).
- [88] ATLAS Collaboration, *ATLAS muon spectrometer: Technical design report*, . CERN-LHCC-97-22.
- [89] M. Bruschi, *The ATLAS luminosity monitor*, [Nucl. Instrum. Meth. \*\*A623\*\* \(2010\) 371–373](#).
- [90] S. van der Meer, *Calibration of the effective beam height in the ISR*. [oai:cds.cern.ch:296752](#), Tech. Rep. CERN-ISR-PO-68-31. ISR-PO-68-31, CERN, Geneva, 1968.
- [91] *Luminosity Determination Using the ATLAS Detector*, Tech. Rep. ATLAS-CONF-2010-060, CERN, Geneva, Jul, 2010.
- [92] R. Achenbach et al., *The ATLAS level-1 calorimeter trigger*, [JINST \*\*3\*\* \(2008\) P03001](#).
- [93] E. F. Eisenhandler, *ATLAS Level-1 Calorimeter Trigger Algorithms*, Tech. Rep. ATL-DAQ-2004-011. CERN-ATL-DAQ-2004-011, CERN, Geneva, Sep, 2004.
- [94] ATLAS Collaboration, G. Duckeck, (Ed. ) et al., *ATLAS computing: Technical design report*, . CERN-LHCC-2005-022.
- [95] M. Asai, *Geant4-a simulation toolkit*, [Trans. Amer. Nucl. Soc. \*\*95\*\* \(2006\) 757](#).
- [96] J. Allison et al., *Geant4 developments and applications*, [IEEE Trans. Nucl. Sci. \*\*53\*\* \(2006\) 270](#).

- [97] P. M. Nadolsky et al., *Implications of CTEQ global analysis for collider observables*, *Phys. Rev.* **D78** (2008) 013004, [arXiv:0802.0007 \[hep-ph\]](#).
- [98] T. Sjostrand, S. Mrenna, and P. Z. Skands, *PYTHIA 6.4 Physics and Manual*, *JHEP* **05** (2006) 026, [arXiv:hep-ph/0603175](#).
- [99] X. Artru and G. Mennessier, *String model and multiproduction*, *Nucl. Phys.* **B70** (1974) 93–115.
- [100] M. G. Bowler,  *$e+ e-$  Production of Heavy Quarks in the String Model*, *Zeit. Phys.* **C11** (1981) 169.
- [101] B. Andersson, G. Gustafson, and B. Soderberg, *A General Model for Jet Fragmentation*, *Z. Phys.* **C20** (1983) 317.
- [102] B. Andersson, G. Gustafson, and B. Soderberg, *A PROBABILITY MEASURE ON PARTON AND STRING STATES*, *Nucl. Phys.* **B264** (1986) 29.
- [103] M. R. Whalley, D. Bourilkov, and R. C. Group, *The Les Houches Accord PDFs (LHAPDF) and Lhaglué*, [arXiv:hep-ph/0508110](#).
- [104] A. Sherstnev and R. S. Thorne, *Parton Distributions for LO Generators*, *Eur. Phys. J.* **C55** (2008) 553–575, [arXiv:0711.2473 \[hep-ph\]](#).
- [105] G. Corcella et al., *HERWIG 6.5 release note*, [arXiv:hep-ph/0210213](#).
- [106] G. Marchesini and B. R. Webber, *Simulation of QCD Jets Including Soft Gluon Interference*, *Nucl. Phys.* **B238** (1984) 1.
- [107] J. M. Butterworth, J. R. Forshaw, and M. H. Seymour, *Multiparton interactions in photoproduction at HERA*, *Z. Phys.* **C72** (1996) 637–646, [arXiv:hep-ph/9601371](#).
- [108] M. L. Mangano, M. Moretti, F. Piccinini, R. Pittau, and A. D. Polosa, *ALPGEN, a generator for hard multiparton processes in hadronic collisions*, *JHEP* **07** (2003) 001, [arXiv:hep-ph/0206293](#).
- [109] S. Frixione and B. R. Webber, *Matching NLO QCD computations and parton shower simulations*, *JHEP* **06** (2002) 029, [arXiv:hep-ph/0204244](#).

- [110] S. Frixione, P. Nason, and B. R. Webber, *Matching NLO QCD and parton showers in heavy flavour production*, JHEP **08** (2003) 007, [arXiv:hep-ph/0305252](#).
- [111] J. Pumplin et al., *New generation of parton distributions with uncertainties from global QCD analysis*, JHEP **07** (2002) 012, [arXiv:hep-ph/0201195](#).
- [112] J. Alwall et al., *Comparative study of various algorithms for the merging of parton showers and matrix elements in hadronic collisions*, Eur. Phys. J. **C53** (2008) 473–500, [arXiv:0706.2569 \[hep-ph\]](#).
- [113] *ATLAS Monte Carlo tunes for MC09*, Tech. Rep. ATL-PHYS-PUB-2010-002, CERN, Geneva, Mar, 2010.
- [114] W. Lampl et al., *Calorimeter clustering algorithms: Description and performance*, . ATL-LARG-PUB-2008-002.
- [115] M. Aleksa, M. Delmastro, M. Fanti, R. Lafaye, W. Lampl, S. Laplace, D. Prieur, F. Tarrade, and I. Wingerter-Seez, *ATLAS Combined Testbeam: Computation and Validation of the Electronic Calibration Constants for the Electromagnetic Calorimeter*, Tech. Rep. ATL-LARG-PUB-2006-003. ATL-COM-LARG-2006-003, CERN, Geneva, Apr, 2006.
- [116] M. H. Seymour, *Searches for new particles using cone and cluster jet algorithms: A Comparative study*, Z. Phys. **C62** (1994) 127–138.
- [117] ATLAS Collaboration, and others, *Readiness of the ATLAS Tile Calorimeter for LHC collisions*, [arXiv:1007.5423 \[physics.ins-det\]](#).
- [118] ATLAS Collaboration, and others, *Measurement of inclusive jet and dijet cross sections in proton-proton collisions at 7 TeV centre-of-mass energy with the ATLAS detector*, [arXiv:1009.5908 \[hep-ex\]](#).
- [119] *Jet energy resolution and selection efficiency relative to track jets from in-situ techniques with the ATLAS Detector Using Proton-Proton Collisions at a Center of Mass Energy  $\sqrt{s} = 7$  TeV*, Tech. Rep. ATLAS-CONF-2010-054, CERN, Geneva, Jul, 2010.
- [120] *Jet energy scale and its systematic uncertainty for jets produced in proton-proton collisions at  $\sqrt{s} = 7$  TeV and measured with the ATLAS detector*, Tech. Rep. ATLAS-CONF-2010-056, CERN, Geneva, Jul, 2010.

- [121] A. Buckley, H. Hoeth, H. Lacker, H. Schulz, and J. E. von Seggern, *Systematic event generator tuning for the LHC*, [Eur. Phys. J. C65 \(2010\) 331–357](#), [arXiv:0907.2973 \[hep-ph\]](#).
- [122] G. Folger and J. P. Wellisch, *String parton models in Geant4*, [arXiv:nucl-th/0306007](#).
- [123] H. W. Bertini, *Intranuclear-cascade calculation of the secondary nucleon spectra from nucleon-nucleus interactions in the energy range 340 to 2900 mev and comparisons with experiment*, [Phys. Rev. 188 \(1969\) 1711–1730](#).
- [124] *In-situ pseudo-rapidity inter-calibration to evaluate jet energy scale uncertainty and calorimeter performance in the forward region*, Tech. Rep. ATLAS-CONF-2010-055, CERN, Geneva, Jul, 2010.
- [125] The ATLAS Collaboration, G. Aad et al., *Expected Performance of the ATLAS Experiment - Detector, Trigger and Physics*, [arXiv:0901.0512 \[hep-ex\]](#).